DUBLIN CITY UNIVERSITY

IMAGING AND SPECTROSCOPY OF LASER-PRODUCED COLLIDING PLASMAS

A thesis submitted for the degree of

DOCTOR *of* PHILOSOPHY

Presented to

School of Physical Sciences

Submitted by

KEVIN D KAVANAGH

B Sc MInstP

Supervisor

Prof John T Costello

29 August 2006

DECLARATION

I hereby certify that this material which I now submit for assessment on the programme of study leading to the award of Doctor of Philosophy is entirely my own work and has not been taken from others save and to the extent that it has been cited and acknowledged within the text of my work

Kevin Kavanagh, 29th August 2006
Student Number 98519450

To my family

He ladens his prose with allusions to his academic and literary credentials, including that upper-crust tic of lapsing into French or Latin when the going gets delicate

– *Simon Jenkins, 10th September 2006*

CONTENTS

List of Figures

List of Tables

ACKNOWLEDGEMENTS

First and foremost I must sincerely thank my supervisor Prof John Costello for his continual support and encouragement over the past four years Without his energy, enthusiasm and guidance this thesis would never have been completed or probably even started Despite his busy schedule his door was always open for physics discussions or just a chat

I would also like to thank the rest of the academic staff in the CLPR Prof Eugene Kennedy, Dr Jean-Paul Mosnier and Paul van Kampen They have been a great source of advice and assistance to me over the years Thanks also to Prof Michael Mansfield, Dr Vince Ruddy and Dr Enda McGlynn for their contributions to my viva-voce, in particular to Vince for the epigraph!

My time spent in DCU was made bearable by the postgrads and postdocs in the physics department I would like to thank all of them for the many blurred memories of extra-curricular activities spent in various fine establishments around Dublin In particular I'd like to mention Eoin O'Leary, Oisin McDonald and Deirdre McCabe who've been at this physics game with me since the very beginning, eight years ago! From the long departed old school of jedi masters, I'd like to thank John Hirsch, Mark Stapleton and Pat Yeates From the new school of padawan learners, thanks to John Dardis, Phil Smyth and Caroline Banahan

Special thanks to Hugo de Luna for working closely with me on this project, he contributed significantly to the quality of the results obtained, good luck with the baby! To our local Fine Gael representative Des Lavelle, thanks for all of the excellent constructions, over the years and for all of the laughs in the workshop

Thanks to my flatmates Ricky and Trevor, for all their help, support and cups of tea along the way Also thanks to Lisa for her encouragement and patience during the seemingly never-ending final three months of thesis writing I'd also like to thank all my friends that are not in DCU for putting up with my anti-social behaviour over the last year Finally, I'd like to acknowledge financial support under the Embark initiative scholarship scheme 2002, funded by the Irish Research Council for Science, Engineering and Technology (IRCSET)

ABSTRACT

Laser-produced plasmas are formed when short pulse, high power lasers are focused onto a surface Applications range from VUV / X-ray sources for lithography, microscopy and radiography to X-ray lasers, thin film deposition, analytical spectroscopy and electron / ion beam generation A battery of particle and optical techniques are currently being used to fully characterise the properties of laser-produced plasmas

Over the past forty years much experimental and theoretical / computational work has focussed on the generation and expansion of LPP's in vacuum Recently however, the dynamics of LPP's expanding into background gasses has received increased interest This has been driven by the need to control the growth conditions of thin films produced using pulsed laser deposition The dynamics of LPP's expanding into background gasses are very different from that of the vacuum case and leads to plume splitting and sharpening effects

Although much is known about the properties of laser-produced plasmas expanding in vacuum and into background gasses, very little is known about the expansion and interaction of a LPP into another LPP The aim of this project is the study of this system, colliding laser-produced plasmas Colliding plasma experiments may be cast as a model system for atmospheric and / or astrophysical colliding systems, for example when tracer elements are injected into supersonic winds at high altitude or collisionless plasma interaction in young supernova remnants Colliding plasmas have also been considered as a possible solution to the problem of particulate deposition in PLD

In order to study colliding plasmas in this work we have used, primarily, three diagnostic techniques VUV photoabsorption imaging was used in order to track the evolution of dark plume matter, or non-emitting plasma species residing in ground and metastable states We have also performed combined conventional gated CCD imaging and imaging spectroscopy to study excited species in the interaction region

CHAPTER 1

INTRODUCTION

1.1 Thesis Structure

This thesis has been divided into eight chapters A short description of the contents of each chapter is given below to aid the reader in navigating this thesis

Chapter One gives a brief overview of the motivations for studying colliding laser-produced plasmas A short survey of the important papers published to date on colliding plasmas has been provided

Chapter Two discusses all of the relevant theoretical background required for the analysis and discussion of the experimental and computational results presented in the results chapters of the thesis Basic atomic processes in plasmas and thermodynamic equilibrium models are outlined

Chapter Three outlines the specific theory relating to the plasma diagnostics used in this work A broad introduction to plasma diagnostics is followed by a detailed description of photoabsorption imaging as well as the theory behind the extraction of plasma parameters from such images A discussion on spectral line broadening mechanisms and methods for extracting plasma parameters from spectroscopic measurements has been presented

Chapter Four provides a detailed description of the experimental systems used during this work The VUV photoabsorption imaging facility (VPIF), spec-

trally filtered time-resolved emission imaging and time-resolved imaging spectroscopy setups are discussed The capabilities and limitations of these system are outlined

Chapter Five presents results and analysis of VUV photoabsorption imaging studies of single and colliding laser-produced plasmas Equivalent width images and column density maps are calculated and discussed Data acquisition procedures using the VPIF are also outlined

Chapter Six presents time and space-resolved imaging spectroscopy results of the interaction region between colliding calcium plasmas Results from spectrally filtered time-resolved ICCD imaging of the evolution and interaction dynamics are also presented, discussed and analysed

Chapter Seven describes in detail the implementation and application of a radiation transport model developed to explain spectroscopic results obtained during this work and presented in chapter six

Chapter Eight concludes the work by providing a summary of all of the results presented in the thesis Suggestions for possible future experimental and computational work are discussed

Appendix A provides reference material to aid the reader A list of all notation used in this thesis along with a description of their meaning and the location of the first instance of their use A list of abbreviations used in this thesis and their meanings is also provided

1.2 Review of Colliding Laser-Produced Plasmas

Plasmas produced by the focussing of laser beams onto solid targets have been the object of intensive theoretical and experimental work since the development of high-power lasers in the early 1960's This research is still vigorous to this day and is fuelled both by the fundamental physics interest in laser-solid / laser-plasma interactions and by the more recent applied requirements of materials processing technology The number of applications of laser-produced plasma's (LPP's) has steadily grown throughout the years and now ranges from Vacuum Ultraviolet (VUV) / X-ray sources for lithography, microscopy and radiography to X-ray lasers, thin film deposition, analytical spectroscopy, electron / ion beam generation and quantitative elemental analysis of samples [1, 2, 3, 4, 5]

As the number of applications of LPP's grew so too did the list of particle and optical diagnostic techniques available to study their characteristics, these include emission / absorption spectroscopy, laser-induced fluorescence, mass spectrometry, Langmuir probes, interferometry, Thompson scattering and a host of imaging techniques [6, 7, 8]

In spite of these developments the majority of the research carried out on LPP's to date has been on the study of single element, single plasma expansion in vacuum Even though considerable effort has been spent on this specific system the expansion dynamics of laser-produced plasmas remains incompletely understood This is due mainly to the transient nature of laser-produced plasmas, whose characteristics evolve quickly and are strongly dependent on irradiation conditions such as laser intensity, wavelength, pulse length and spot size, as well as the number of mechanisms that are involved in the laser-solid / laser-plasma interaction and subsequent plume expansion These mechanisms include laser absorption, heating, melting, evaporation, expansion, ionisation, radiation, recombination and condensation

Improvements in laser technology throughout the 60's and 70's shifted the theoretical and experimental research focus from the moderate energy regime ($10^6 - 10^{10}$ Wcm^{-2}) to the ultra-intense ($> 10^{15}$ Wcm^{-2}) driven primarily by fusion experiments [6] and more recently by X-ray lasers [3] However since the early 90's the growth in the semiconductor industry and the need to manufacture thin films has generated strong interest in Pulsed Laser Deposition (PLD) of thin films, which

predominantly uses plasmas generated with moderate energy nanosecond pulses [9] A detailed understanding of the processes involved in the generation, expansion and deposition of plasmas in this energy regime is critically important to control and optimise the processing of these films

PLD has also recently focussed attention on the interaction of laser-produced plasmas with a background gas due to the need in PLD to tailor the composition of the thin films and control the conditions under which the films are grown The expansion dynamics of a laser-produced plasma expanding into a background gas is very different to that of a plasma expanding *in vacuo* and is poorly understood Ablation into a gas results in shock waves and expansion fronts as well as plume splitting and sharpening effects [10] that are not seen in expansion into vacuum Although little work has been done on the expansion of laser-produced plasmas into a background gas, considerably less work has been carried out on the interaction of plasmas expanding into other plasmas During this collision process, the plasmas do not merge and decay in a simple manner, instead a dramatic configurational transformation is observed during which increased emission from the overlap or interaction region is recorded [11] This plasma-plasma interaction is a major focus of this work and this thesis

Colliding plasmas occur in very many situations, predominantly astrophysical but recently a number of possible applications of colliding laser-produced plasmas have emerged These include, in the design of indirect drive inertial confinement fusion hohlraums [12], in the field of X-ray lasers [3] and as a possible solution to cluster formation and deposition problems in PLD [13]

Astrophysically, the free expansion of stellar ejecta into interstellar media is a naturally occurring colliding plasma phenomenon that has been subject to high resolution astronomical observation The scale and complexity of the events involved make them a significant challenge for current numerical simulation, making a direct experimental approach particularly helpful [14] Although the absolute physical scales (lengths, times, densities) of these astrophysical phenomena differ greatly from that of colliding laser-produced plasmas the relevance and ability of laboratory experiments to simulate these events rests on detailed scaling analysis of specific properties of the plasmas Recently Woolsey *et al* [14] published results of just such experiments in which they address specific aspects of collisionless plasma interaction in a young supernova remnant using millimetre-scale counter

streaming colliding laser-produced plasmas

Initial experiments on colliding plasmas were performed in the late 1960's and early 1970's Rumsby *et al* [15] published the first significant paper on colliding plasma plumes during this period in 1974 They investigated the expansion and interaction of two laterally colliding carbon plasma plumes generated next to each other on a flat surface Time-integrated photographs and photon scattering techniques were used to study the expansion dynamics and the plasma parameters from the interaction region for different plume separations

After this paper very little was published on colliding plasmas until the early 1990's Since then there has been considerably increased experimental and computational interest in the field of colliding laser-produced plasmas Numerous target configurations and diagnostic techniques have been employed to elucidate the interaction dynamics of plasmas initiated with various irradiance conditions In what follows, results of the most important of these papers are summarised

In 1992 Begimkulov *et al* [16] investigated the collision of two plasmas generated next to each other on a flat surface in vacuum and at various background gas pressures They generated the plasmas by splitting a high-power (8 J in 8 ns) ruby laser into two parts by placing a glass wedge prism into the beam, deflecting a portion at a slight angle before focussing the two beams onto beryllium and aluminium targets They recorded time and wavelength (visible) integrated photographs of the colliding plumes as well as charge specific spectroheliograms to track the distribution of selected ion stages Figure 1 1 shows an example image set taken from this paper in which they vary the separation (Δr) between the two beryllium plasmas, to examine the effect it has on the interaction region formed between the two plumes Their main concern however was the angular scatter pattern of ions of different multiplicity within the interaction region and they developed a numerical model which gave good agreement with the pattern observed in their experiments

The following year Vick *et al* [12] used the technique of buried tracer layers and an X-ray pinhole camera as well as X-ray spectroscopy to study the interaction of aluminium plasmas The aluminium target was buried beneath layers of parylene (CH) of varying thickness The Nd-YAG laser (9 6 J in 900 ps) needed to ablate the CH overcoat before reaching the aluminium target, hence by varying the overcoat thickness the time history of the evolution could be studied with a time-integrated

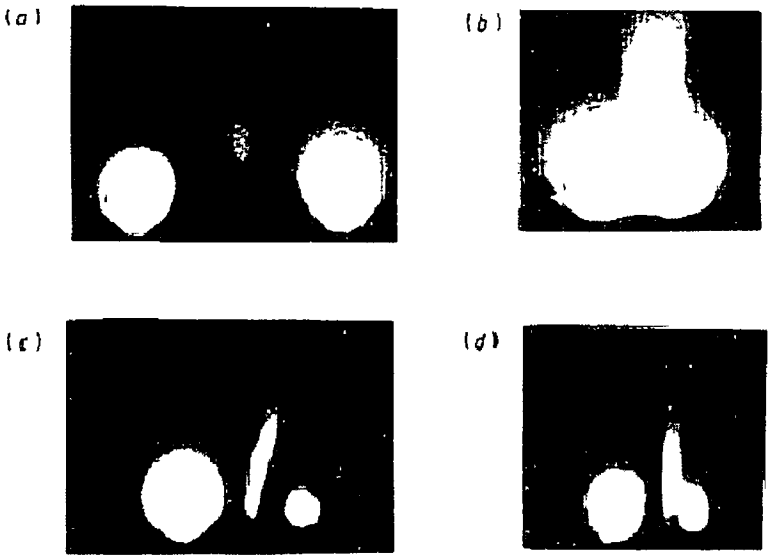

Figure 1 1 Region of interaction of Be plasma flows (a) Δr = 6 mm, (c) Δr = 4 mm, (b) and (d) Δr = 2 5 mm (beam energies differ) (After Begimkulov *et al* [16])

camera Emission from the CH overcoat was filtered out using a beryllium filter Figure 1 2 shows a sequence of images taken from this paper in which targets with varying overcoat thickness were used X-ray spectra were recorded (5 5 – 8 Å) from the region between the two plasmas Theoretical spectra were fitted to the experimental spectra using the RATION code, yielding electron temperatures of $\sim$ 580 eV and densities of the order of 10^{20} cm^{-3} A 2-D single fluid hydrodynamic code (IZANAMI) was used to model the expansion of a single plasma under the same conditions and was compared with the recorded images

The most active group in the field of colliding laser-produced plasmas is located in the Institut fur Experimentaphysik Ruhr-Universat in Bochum Germany Between 1997 and 2001 they produced eight papers on colliding plasmas The first of these papers Ruhl *et al* [17] examined the possibility that charge-exchange collisions during the interaction of a "hot" (C (VII)) and "cold" (C (III)) plasma could be responsible for enhanced emission from the C (VI) Balmer-alpha line The premise of their experiment was based on the fact that for certain collision processes, theoretical calculations predict large charge exchange cross-sections in spite of strong Coulomb repulsion for highly charged ions These cross-sections are only large if the relative collision velocities of the ions is very high ($\sim$ 10^7 cms^{-1}) Counter streaming laser-produced plasmas provided the high collision velocities required, thereby providing an ideal scenario to test these theoretical

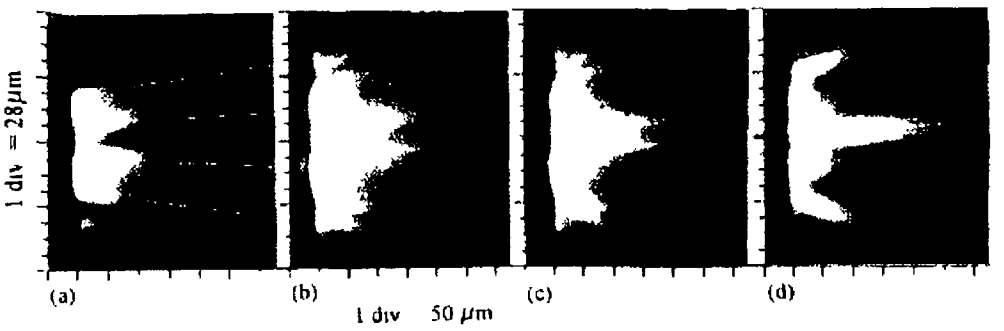

Figure 1 2 Time-integrated x-ray pinhole images from four CH-Al-CH layered targets irradiated by a nonuniform laser beam of spatial periodicity 112 μm The x-ray emission originates primarily from the aluminium layer buried at depths of 0 54, 0 24, 0 12 and 0 0 μm for targets (a)-(d) respectively (After Vick *et al* [12])

predictions Time-integrated XUV spectroscopy ($6-24$ nm) of the collision region was used as a diagnostic and increased emission was observed from the C (VI) Balmer-alpha line from the collision region when compared with spectra obtained from single plasma expansion This paper was followed by five more papers on charge-exchange collisions in colliding LPP's

The second paper in 1998 by Henč-Bartolic *et al* [18] examined the lateral collision of two boron-nitride plasmas using time-integrated VUV spectroscopy ($16-34$ nm) Intensities of nitrogen and boron lines were compared between colliding and non-colliding plasmas generated using the same irradiance conditions The authors observed a significant decrease in the intensity of boron emission, while no effect was witnessed in the nitrogen lines The authors ruled opacity out as a possible explanation for this observation, as the line profiles do not show pronounced symptoms of optical thickness A slight enhancement however was observed in the emission from the B (V) Balmer-alpha line, which was interpreted as a sign of charge-exchange between fully ionised boron and B (III) ions

In the third paper by the Bochum group on colliding laser-produced plasmas, charge-exchange collisions between a "hot" dense and a "cold" rarefied Al plasmas were studied In an addition to the previous experiments time-resolved XUV pinhole photography was performed on the colliding plasmas, as well as XUV spectroscopy A head-on collision between the two plasmas was enabled by a novel target configuration A narrow capillary was drilled through a 1 mm thick Al plate with a diameter equal to the beam waist of the laser A second Al plate was

placed 2 mm behind it A cold plasma is generated at the edges of the capillary as the laser passes through and strikes the back plate Electron temperatures were estimated to be 60, 15 and 18 eV for the hot, cold and collision region respectively No evidence of charge-exchange was observed in the collision region from analysis of line intensity ratios

The next three papers Aschke *et al* [19], Harilal *et al* [20] and Harilal *et al* [21], used the same experimental setups and diagnostic techniques Time-resolved XUV pinhole imaging and time-resolved XUV spectroscopy were used to search for charge-exchange collisions In all three cases the plasmas were generated using a 6 J in 15 ns ruby laser, that was focussed onto an angled target configuration thereby producing orthogonally colliding plasmas

Aschke *et al* [19] again attempted to confirm theoretical predictions of very high cross-sections for charge-exchange collisions, this time however between He-like aluminium and Al (IV) ions Intensity comparisons were made between the sum of the individual spectra of the non-colliding plasmas with the spectra obtained from the collision region A significant increase in the intensity of emission from the $n = 3$ level of Al (XI) was observed at early time-scales, when the plasmas first collide, as was predicted by the charge-exchange calculations [19]

Two papers by Harilal *et al* [20, 21] in 2001 both explored the interaction of "hot" and "cold" magnesium plasmas XUV pinhole images and spectra of the collision region were presented in both papers Figure 1 3 shows an image set taken from Harilal *et al* [20], and represents the highest quality sequence of images published on colliding plasmas to date Time-resolved spectra showed selective enhancement of certain transitions at short time delays and general enhancements at longer time delays, leading the authors to conclude that the plasmas interpenetrate at short time delays and stagnate at longer time delays enhancing emission purely due to density build-up at the stagnation front

The final two papers by the Bochum group, Harilal *et al* [11] and Atwee *et al* [22] concentrate on the characterisation of the collision region between colliding plasma plumes Harilal *et al* [11] use time-resolved XUV pin-hole imaging only to study the interaction between counter-propagating magnesium plasmas In particular they studied the effect that two different target geometries had on the interaction region produced In the first case pulses from a Ruby laser (6 J, 15 ns) were

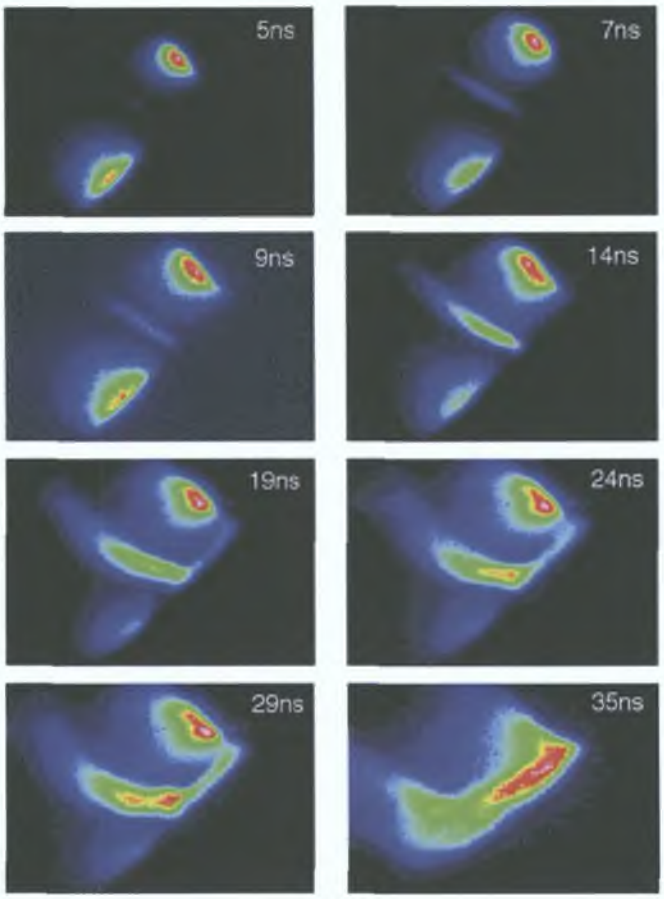

Figure 1.3: Time evolution of colliding plasmas recorded using a 50 μm pinhole camera. The time given in the pictures is the delay of the gate pulse after the laser pulse maximum. The gate width was set at 5 ns. The foci were separated by a distance of 0.75 mm. (After Harilal *et al* [20])

split in two using a moveable glass wedge and focussed to two spots on a flat magnesium slab, allowing the plasmas to collide laterally. In the second case, two magnesium slabs were positioned at 90° to each other, allowing the plasmas to collide orthogonally. The separation between the plumes was varied using two glass wedges with different acute angles, providing distances of 0.75 and 1.5 mm between the spot positions. XUV emission from the plasmas was limited to times < 100 ns. A jet-like interaction region was observed between the two plasma plumes using both target configurations. Varying the spot separation appeared only to vary the time delay at which the interaction region was formed, due to the increased transit time before interaction. The lifetime of the interaction region was found to be longer than the lifetime of the primary "feeding" plasmas in all cases.

Atwee *et al* [22] continued the exploration of XUV emission from colliding plasmas

by performing time-integrated XUV pinhole imaging and time-integrated XUV spectroscopy on orthogonally colliding boron-nitride plasmas Electron temperatures were calculated using relative line intensities in the case of orthogonally colliding and single plasma expansion on a flat surface A temperature increase of up to 50% was observed in the collision region for certain distances from the target surface The conversion of directed kinetic energy into thermal energy as the plasmas slow down and stagnate is considered to be the most probable reason for the observed temperature enhancement

The most serious attempt made to date at computational modelling of the interaction region between colliding laser-produced plasmas was performed at the Lawrence Livermore National Laboratory in the U S A Rambo and Denavit [23] developed a one-dimensional multi-fluid hydrodynamics model to study the transition regime between stagnation and interpenetration Stagnation was said to occur at the interface between the two plasmas if the ion-ion mean-free path λ_{ii} was much smaller than the gradient scale length D of the colliding fronts ($\lambda_{ii} \ll D$), which in this case is taken to be the inter-target separation In this situation the interaction takes place over a narrow interface region between the two plasmas, resulting in large temperature increases and the formation of shock waves On the other hand interpenetration was said to occur when the ion-ion mean-free path was much greater than the characteristic scale length ($\lambda_{ii} \gg D$) Here, the plasmas interpenetrate considerably and interact over a large extended spatial region Rambo and Denavit [23] endeavoured to study the intermediate regime where $\lambda_{ii} \approx D$, in this situation partial interpenetration followed by a moderate stagnation occurs A collisionality parameter ζ was defined to relate the two factors that dictate the form the interaction will most likely take, ($\zeta = D/\lambda_{ii}$) The higher the value of the collisionality parameter the more likely it is that stagnation will occur at the plasma interface Changing the collisionality of a system experimentally may be performed in a number of ways The two most important of these are (i) changing the separation between the plasmas, (ii) changing the particle number density in the plume by varying the on-target irradiance

The Rambo and Denavit [23] paper of 1994 was followed up in 1995 by a paper by Rambo and Procassini [24] in which direct comparisons were made between the multifluid model previously developed and a kinetic Monte-Carlo Particle-In-Cell (MC-PIC) code The two differing approaches to modelling colliding plasmas

were in substantial agreement on the dominant output features, typically within $10 - 20\%$ of each other

The final two papers of note on colliding laser-produced plasmas were led by a French group at Laboratoire pour l'Utilisation des Lasers Intenses, CNRS, Ecole Polytechnique, Palaiseau Cedex

Rancu *et al* [25] studied the collision of laser-exploded Al / Al and Al / Mg foils using X-ray spectroscopy A very flexible target geometry was used in these experiments, plasmas are produced at the rear side of two thin foils placed in close proximity to each other This configuration allows easy and accurate manipulation of the inter-target separation This allowed the authors to precisely vary the velocity and density with which the plasmas collide, giving them complete control over the colhsionality of the system Thus allowed them explore the boundary between interpenetration and stagnation regimes Two X-ray spectrometers, with differing spectral resolutions simultaneously observed the interaction region between the foils Ion temperatures were inferred from the recorded spectra by fitting them with simulated spectra generated by the collisional radiative code FLY Ion temperatures of the order of $20 - 27$ keV were determined and electron densities of $> 10^{22}$ cm^{-3} were calculated for laser irradiances of 5×10^{13} Wcm^{-2}

Finally Chenais-Popovics *et al* [26] (1996) studied in greater detail the interaction of Al / Al and Al / Mg foils with the same X-ray spectrometers Monochromatic X-ray imaging of the interaction region was also employed as well as multi-fluid modelling using the MULTIF code They observed that when the inter-target separation is large (i e the relative collision velocity is large) the plasmas interpenetrate considerably leading to a broad collision region The larger the separation the more efficient the interpenetration due to the almost linear relationship between the inter-target separation and the relative collision velocities For low velocities and high densities the plasmas did not interpenetrate and the ion kinetic energy was converted very locally in time and space into thermal energy, generating shock fronts that propagate back into the plasmas [26]

In this work we have examined a parameter space that has been largely over-looked in the literature to date The majority of the work published on colliding plasmas has focussed on the study of X-ray and XUV emission from the interaction region Emission in these spectral ranges enables authors to study the dynamics of hot,

dense, highly charged regions of the plumes at short time delays after plasma initiation and interaction We have concentrated our efforts on the interaction of low density, low temperature PLD-like plasma plumes using predominantly diagnostic techniques in the visible spectral range and over relatively long time-scales (< 1 μs)

We have performed spectrally filtered time-resolved visible emission imaging and spatially and temporally-resolved visible imaging spectroscopy on the interaction between counter-streaming colliding calcium plasmas We have also performed VUV photoabsorption imaging of single and colliding calcium plumes in order to determine the spatial distribution of ground state non-emitting plume species During the course of our spectroscopic work we encountered very strong radiation trapping in the $3p^6 4s(^2S_{1/2})$-$3p^6 4p(^2P_{3/2,1/2})$ Ca^+ doublet at 393 36 and 396 68 nm A computational model was implemented to simulate this effect and was subsequently used as a diagnostic tool to extract plasma parameters from spectra obtained from the interaction region between colliding calcium plasmas

Bibliography

[1] J S Hirsch, E T Kennedy, A Neogi, and J T Costello Vacuum-ultraviolet photoabsorption imaging system for laser plasma plume diagnostics *Review of Scientific Instruments*, 74 2992–2998, 2003

[2] J S Hirsch, K D Kavanagh, E T Kennedy, P Nicolosi, L Poletto, and J T Costello Tracking ground state Ba^+ ions in an expanding laser plasma plume using Vacuum-UV photoionization imaging *Laser and Particle Beams*, 2004

[3] R W Clark, J Davis, A L Velikovich, and K G Whitney X-ray lasing in colliding plasmas *Physics of Plasmas*, 4 3718–3724, 1997

[4] J B Greenwood, G F Collins, J Pedregosa-Gutierrez, J McKenna, A Murphy, and J T Costello Double ionization of atomic negative ions in an intense laser field *Journal of Physics B Atomic, Molecular and Optical Physics*, 36(16) L235–L240, 2003

[5] M A Khater, P van Kampen, J T Costello, J-P Mosnier, and E T Kennedy Time-integrated laser-induced plasma spectroscopy in the vacuum ultraviolet for the quantitative elemental characterization of steel alloys *Journal of Physics D Applied Physics*, 33 2252–2262, 2000

[6] P K Carroll and E T Kennedy Laser-produced plasmas *Contemporary Physics*, 22 61–96, 1981

[7] E T Kennedy Plasmas and intense laser-light *Contemporary Physics*, 25 31–58, 1984

[8] A S Wan, T W Barbee, R Cauble, P Celliers, L B Da Silva, J C Moreno, P W Rambo, G F Stone, J E Trebes, and F Weber Electron density measurement of a colliding plasma using soft-x-ray laser interferometry *Phys Rev E*, 55 6293–6296, 1997

[9] B N Chichkov, C Momma, S Nolte, F von Alvensleben, and A Tunnermann Femtosecond, picosecond and nanosecond laser ablation of solids *Applied Physics A*, 63 109–115, 1996

[10] S S Harilal, C V Bindhu, M S Tillack, F Najmabadi, and A C Gaeris

Plume splitting and sharpening in laser-produced aluminium plasma *Journal of Physics D Applied Physics*, 35 2935–2938, 2002

[11] S S Harilal, C V Bindhu, and H -J Kunzea Time evolution of colliding laser produced magnesium plasmas investigated using a pinhole camera *Journal of Applied Physics*, 89 4737–4740, 2001

[12] D Vick, M Kado, H Yamamoto, A Nishiguchi, K A Tanaka, K A Tanaka, A A Offenberger, C E Capjack, and S Nakai Hydrodynamics of collisional structures in laser-produced plasmas *Phys Rev E*, 48 2308–2311, 1993

[13] E Camps and L Escobar-Alarcon Interaction of two laser ablation plumes *Sociedad Mexicana de Ciencia de Superficies y de Vacio*, 14 21–25, July 2002

[14] N C Woolsey, C Courtois, and R O Dendy Laboratory plasma astrophysics simulation experiments using lasers *Plasma Phys Control Fusion*, 46 B397–B405, 2004

[15] P T Rumsby, J W M Paul, and M M Masoud Interactions between two colliding laser produced plasmas *Plasma Physics*, 16 969–975, 1974

[16] U Sh Begimkulov, B A Bryunetkm, V M Dyakin, G A Koldashov, A Yu Repin, E L Stupitsky, and A Ya Faenov Interaction of laser-produced plasma clouds in vacuum and background medium *Journal of Physics D Applied Physics*, 25 1583–1590, 1992

[17] F Ruhl, L Aschke, and H -J Kunze Selective population of the $n = 3$ level of hydrogen-like carbon in two colliding laser-produced plasmas *Physics Letters A*, 225 107–112, 1997

[18] V Henč-Bartolic, Z Andreic, D Gracin, L Aschke, F Ruhl, and H -J Kunze Spectral line enhancement in laterally colliding boron-nitride plasmas *Physica Scripta*, T75 279–299, 1998

[19] L Aschke Selective population of the n = 3 levels of lithium like aluminium in interpenetrating plasmas *Contrib Plasma Phys* , 40 72–76, 2000

[20] S S Harilal, C V Bindhu, V P Shevelko, and H-J Kunze Xuv diagnostics of colliding laser-produced magnesium plasmas *Journal of Physics B Atomic,*

Molecular and Optical Physics, 34 3717–3726, 2001

[21] S S Harilal, C V Bindhu, V P Shevelko, and H -J Kunze Charge-exchange collisions in interpenetrating laser-produced magnesium plasmas *Laser and Particle Beams*, 19 99–103, 2001

[22] T Atwee and H-J Kunze Spectroscopic investigation of two equal colliding plasma plumes of boron nitride *Journal of Physics D Applied Physics*, 35 524–528, 2002

[23] P W Rambo and J Denavit Interpenetration and ion separation in colliding plasmas *Physics of Plasmas*, 1 4050–4060, 1994

[24] P W Rambo and R J Procassini A comparison of kinetic and multifluid simulations of laser-produced colliding plasmas *Physics of Plasmas*, 2 3130–3145, 1995

[25] O Rancu, P Renaudin, C Chenais-Popovics, H Kawagashi, J C Gauthier, M Dirksmoller, T Missalla, I Uschmann, E Forster, O Larroche, O Peyrusse, O Renner, E Krousky, H Pepin, and T Shepard Experimental evidence of interpenetration and high ion temperature in colliding plasmas *Phys Rev Lett* , 75 3854–3857, 1995

[26] C Chenais-Popovics, P Renaudin, O Rancu, F Gilleron, J -C Gauthier, O Larroche, O Peyrusse, M Dirksmoller, P Sondhauss, T Missalla, I Uschmann, E Forster, O Renner, and E Krousky Kinetic to thermal energy transfer and interpenetration in the collision of laser-produced plasmas *Physics of Plasmas*, 4 190–208, 1997

CHAPTER 2

THEORETICAL BACKGROUND

2.1 Plasma Definition

Plasma is matter in a state of partial or complete ionisation Ionisation occurs when electrons are removed from neutral atoms during the absorption of energy from an external source The resultant assembly of electrons and ions needs to satisfy certain criteria in order that it be defined as being plasma One such criterion stipulates that the electrons and ions maintain overall electrical neutrality for the lifetime of the plasma such that

$$n_e = \sum_z n_z z \tag{2 1}$$

where n_e is the electron density and n_z is the density of ions of charge z [1] Another defining characteristic of a plasma is its "collective response" to perturbing agents This is due to the fact that the Coulombic forces between charged particles in plasmas are strong and long-range By this we mean that each particle interacts and has influence over many of its near neighbours, whereas neutral (gas) particles interact weakly and only over short distances Collective phenomena may be regarded as the basic defining criterion [1] for plasmas The distance beyond which collective influences dominate over Coulombic force due to an individual ion is known as the Debye length λ_D

$$\lambda_D = \sqrt{\left(\frac{\epsilon_0 k_B T}{n_e e^2}\right)} \tag{2 2}$$

where ϵ_0 is the permitivity of free space, k_B is the Boltzmann's constant, T is the plasma temperature and e is the electron charge In order to satisfy the collective response criterion [1], the length of the plasma L, must be at least one order of magnitude greater than the Debye length [2]

$$L > 10\lambda_D \tag{2 3}$$

An extension of the Debye length definition is the concept of the Debye sphere N_D It states that the number of particles contained within a sphere of radius λ_D must be much larger than unity

$$N_D = \frac{4\pi n_e}{3}\lambda_D^3 \gg 1 \tag{2 4}$$

An ion can only influence and be influenced by the ions that reside within its Debye sphere This is the case for most plasmas but at extremely high ion densities the relationship (equation 2 4) may break down due to the fact that the Debye length decreases with increasing ion density and may become smaller than the ion sphere radius [2] The most important collective characteristic of plasmas are the wavelike motions that are superimposed onto the random motions of individual particles The electron wave is the most basic of these and oscillates at the plasma frequency ω_p given by

$$\omega_p^2 = \frac{n_e e^2}{m_e \epsilon_0} \tag{2 5}$$

where m_e and e are the electron mass and charge Such plasma waves are due to electrons oscillating in unison relative to the comparably static ion background [3] The plasma frequency plays a critical role in the laser-plasma interaction, as will be discussed in section 2 2 2

2.2 Plasma Initiation

Laser produced plasmas are formed when high intensity laser light interacts with a target The properties and expansion dynamics of the plasmas produced are very sensitive to the conditions used to generate them Laser pulse length, wavelength, spot size, intensity, even pulse shape are all important factors, equally so are the properties of the target material such as, atomic weight, density, surface reflectivity, conductivity, melting and boiling points The generation of LPP's with high irradiance pulses can be divided into three distinct regimes

(i) The interaction of laser light with the target material, causing heating, melting and evaporation

(ii) The interaction of laser light with the evaporated material as well as an isothermal expansion, perpendicular to the target surface

(iii) An adiabatic expansion of the plume in vacuum

The first two of these regimes take place during the laser pulse, while the third begins at its termination The following two sub-sections will deal with the laser-solid and laser-plasma interaction *ab initio*, while in section 2 3 we will discuss plasma expansion dynamics during and after the laser pulse

2 2 1 Laser-Solid Interaction

When laser light impinges on a metallic target some fraction of the radiation is reflected at the surface while the rest penetrates to a distance known as the skin depth δ

$$\delta = \sqrt{\frac{2}{\omega\mu\sigma}} \tag{2 6}$$

where ω is the angular frequency of the radiation, μ is the target's magnetic permeability and σ is its conductivity [4] The skin depth is typically a small fraction of the wavelength of the incident radiation

During the rising edge of the laser pulse, radiation is absorbed by electrons in the skin depth layer, raising them to higher energy states in the conduction band These electrons then pass this energy on to the lattice during collisions [4], which quickly heat and melt the surface This results in a decreased reflectivity of the surface, thereby increasing the proportion of the laser-light that is absorbed by the target For nanosecond time-scale pulses a significant amount of heat is conducted from the skin depth layer into the bulk of the material, to a depth known as the heat penetration depth L_{th}

$$L_{th} \approx \sqrt{(2D_f\tau_p)} \tag{2 7}$$

where $D_f = k_B/\rho c$, (ρ = mass density, c = speed of light) is the heat diffusion coefficient and τ_p is the laser pulse length [5] For nanosecond pulses the heat

penetration depth is much larger than the skin depth

$$L_{th} \gg \delta \tag{2 8}$$

This relationship does not however hold true for pico or femto-second pulses, because at very short time-scales there is insufficient time for thermal conduction into the target to take place [5] This means that the heated zone runs only to the skin depth Plasmas generated with these ultrashort pulses are considered to have undergone a solid-vapour only transition as opposed to the nanosecond solid-liquid-vapour path [5] For this reason short-pulse lasers are more efficient at generating plasmas from the incident radiation, because energy losses while heating the bulk material are negligble

Due to the fact that metals require substantially more energy to vaporise them than to melt them, evaporation of the molten metal layer occurs when the energy absorbed by the skm depth becomes larger than the latent heat of evaporation This leads to an evaporation or ablation depth ΔZ_ν

$$\Delta Z_\nu \approx \frac{A_s(F_L - F_{th})}{\rho L_\nu} \tag{2 9}$$

where F_L is the laser fluence[1], L_ν is the latent heat per unit mass and F_{th} is the threshold fluence above which significant evaporation occurs and A_s is the surface absorbance [5]

During the vaporisation stage, electrons are stripped from atoms by direct and multi-photon ionisation The free electrons so produced further absorb laser radiation by the process of Inverse Bremsstrahlung (IB) (see section 2 4 3) This dramatically improves the absorption rate of incident photons The electrons subsequently transfer their increased kinetic energy to the atoms and ions through colhsional ionisation and excitation processes These ionisation processes increase the electron density thereby further enhancing the absorption of incident radiation The increasing ion density allows us to now refer to the vaporised material as plasma

[1] fluence = energy applied per unit area (Jcm^{-2})

2 2 2 Laser-Plasma Interaction

Despite the fact that the initial plasma vapour generated by the rising edge of the laser pulse may not have a very high density of free electrons, the efficiency of IB absorption of photons (especially in the infrared (IR)) means that it is difficult to effectively couple energy to the target surface [6] For this reason the ablated vapour density and ablation depth remain low for short pulses, even at high intensities Visible (VIS) and Ultra-violet (UV) photons are less efficiently absorbed by the IB process, therefore are not as prone to this form of target shielding, allowing them access denser regions of the plume [5] The absorption coefficient K_{IB} [7] due to inverse Bremsstrahlung may be calculated using the following

$$K_{IB} = 7\,8 \times 10^{-9} \frac{z n_e^2 ln\Lambda(\omega)}{\omega^2 (k_B T_e)^{3/2}} \frac{1}{(1 - (\omega_p^2/\omega^2))^{1/2}} \tag{2 10}$$

where ω and ω_p are the laser and plasma frequency respectively and $ln\Lambda(\omega)$ is the "Coulomb logarithm" for particle collisions, which typically has a value between 5 and 10 for laser-produced plasmas [1, 8, 9]

Another form of plasma shielding of the target arises from the plasma frequency ω_p (equation 2 5) and the dispersion relation for an electromagnetic wave travelling in a plasma

$$\omega^2 = \omega_p^2 + c^2 k_p^2 \tag{2 11}$$

where c is the speed of light in vacuum and k_p ($=2\pi/\lambda$, λ=wavelength) is the wave's propagation constant If $\omega_p < \omega$, then k_p is real, allowing the wave to propagate, on the other hand when $\omega_p > \omega$, k_p is imaginary, and the wave cannot propagate As was shown in equation 2 5, ω_p varies linearly with electron density An incident electromagnetic wave travelling in a plasma will propagate until it reaches an electron density sufficiently large that ω_p becomes greater than ω At this boundary where the wave is reflected, this electron density is known as the critical electron density n_c [1] and is given by

$$n_c = \frac{\epsilon_0 m_e \omega^2}{e^2} \tag{2 12}$$

this gives us a value of $\approx 2 \times 10^{19}$ cm^{-3} for the fundamental wavelength of the Nd YAG lasers (λ = 1064 nm) used in this work As the plasma expands, the electron density decreases and drops below n_c This once again allows radiation

to reach and ablate the surface, which again increases the electron density to the critical level, where shielding of the target surface re-occurs This dynamic "self-regulation" of the ablation process continues until the termination of the laser pulse While most of the laser's energy is being deposited in the thin layer around the critical density boundary (deflagration zone) the plasma in front of this zone expands isothermally, relatively transparent to the laser light due to its lower electron density The expansion can be considered to be isothermal at this stage because the plasma still has a small velocity and volume Therefore it can thermalise faster than the characteristic plasma expansion time [10]

2.3 Plasma Expansion

Following the termination of the laser pulse the plasma expands rapidly into its surroundings The expansion velocity of the electrons far exceeds that of the heavier ions This leads to the generation of a strong electric field caused by the steep spatial distribution of charged particles as the electrons try to separate from the ions The electric field serves to slow the electrons while accelerating the ions

Ablation of solid targets in vacuum with low intensities and very low material vaporisation rates results in the formation of a colhsionless low-density vapour in front of the target surface In this situation the angular and velocity distributions of the expanding vapour can be described by a simple $\cos(\theta)$ law [5, 10] However, at the irradiances used in this work the expansion dynamics are considerably different As mentioned previously during the laser pulse the plasma can be described by an isothermal expansion Another mechanism supporting this isothermal expansion is the dynamic equilibrium that exists between the absorption of incident radiation and the rapid conversion of thermal to kinetic energy The *isothermal* expansion of the plasma plume is given by [10]

$$\begin{aligned} X(t)\left(\frac{1}{t}\frac{dX}{dt}+\frac{d^2X}{dt^2}\right) &= Y(t)\left(\frac{1}{t}\frac{dY}{dt}+\frac{d^2Y}{dt^2}\right) \\ &= Z(t)\left(\frac{1}{t}\frac{dZ}{dt}+\frac{d^2Z}{dt^2}\right) \\ &= \frac{k_BT}{m} \end{aligned} \tag{2 13}$$

where T is the plasma temperature, $X(t)$, $Y(t)$ and $Z(t)$ are the plume dimensions as a function of time, on the x, y, z coordinate system, with the z-axis normal to

the target surface and m is the particle mass From the termination of the pulse onwards the plume is best described by an *adiabatic* expansion (*in vacuo*) given by [10]

$$X(t)\frac{d^2X}{dt^2} = Y(t)\frac{d^2Y}{dt^2} = Z(t)\frac{d^2Z}{dt^2} = \left(\frac{k_B T_0}{m}\right)\left(\frac{X_0 Y_0 Z_0}{XYZ}\right)^{\gamma-1} \qquad (2\ 14)$$

where γ is the ratio of specific heat capacities at constant pressure and volume, T_0 is the plasma temperature at the end of the laser pulse and X_0, Y_0 and Z_0 are the values of X, Y and Z at the termination of the laser pulse

Equation 2 14 is a gas dynamics model, used to calculate expansion velocities of the plume It depends on the initial dimensions, temperature and atomic weight of the plasma species, but it does not discriminate between ions of differing charge states, whose velocity profiles can be quite different from each other The model more accurately describes the expansion of a high pressure, high temperature neutral gas in vacuum but it is found in practice that it predicts the motion of the overall material in the plasma quite well The plasma expansion velocity is extremely rapid at the leading edge of the plasma due to very large pressure gradients between the plasma and the vacuum Plume front velocities up to 10^6 cm/s are common for LPP's generated using medium irradiance pulses (typically 10^{10} W/cm^2)

2.4 Atomic Processes

The manner in which radiation is absorbed by, transported within and emitted from plasmas is governed by atomic processes within the plasma The relative importance of each of these processes at any given time depends on local plasma conditions Parameters such as temperature, ionisation stage, electron / ion / photon densities all influence what processes dominate

In this section we will discuss the twelve most important atomic processes relating to laser-produced plasmas Six of the twelve are excitation processes and the other six are their inverse de-excitation processes The twelve can be divided up into three distinct categories bound–bound, bound–free and free–free We will discuss four bound–bound, six bound–free and two free–free processes, which will involve electrons, ions and photons Table 2 1 shows all of the processes in their various sub-categories It should be noted from table 2 1 that each process has been further described to be either collisional or radiative, depending on the main method of energy transfer in the process

Table 2 1 Classification of the main atomic processes in laser-produced plasmas (B$\Longleftrightarrow$B Bound-Bound, B$\Longleftrightarrow$F Bound-Free F$\Longleftrightarrow$F Free-Free)

Process	Excitation	De-Excitation	Type
B$\Longleftrightarrow$B	Impact Excitation	Impact De-Excitation	Collisional
B$\Longleftrightarrow$B	Photoabsorption	Spontaneous Decay	Radiative
B$\Longleftrightarrow$F	Impact Ionisation	3-Body Recombination	Collisional
B$\Longleftrightarrow$F	Photoionisation	Radiative Recombination	Radiative
F$\Longleftrightarrow$F	—	Inverse Bremsstrahlung	Radiative
F$\Longleftrightarrow$F	Bremsstrahlung	—	Collisional
B$\Longleftrightarrow$F	Autoionisation	Dielectronic Recombination	Special

In the forthcoming sub-sections we will discuss in detail the three classes of transitions and their relative importance under different plasma conditions In each category collisional processes will be discussed first, then radiative ones The processes have been numbered (i through xii) and are discussed individually below

2.4 1 Bound–Bound Processes

A bound–bound transition occurs when an electron occupying a discrete energy level in an atom or ion, is promoted or demoted to another discrete energy level during a collision with another electron or by the absorption or emission of a photon

As mentioned in the previous section there are four processes that fall under the heading of bound-bound processes Two of these processes are considered collisional and two radiative Likewise two are excitations and two are de-excitations

Bound–Bound Collisional Pathways

(i) **Electron-impact excitation** of an ion occurs when an electron moving near the ion induces a transition of a bound electron to a higher excited bound state The free electron looses kinetic energy equal to the energy difference between the upper (j) and lower (i) bound states This is graphically represented by the left-hand side of figure 2 1 [2] and symbolically by the left-to-right reaction in the balance equation 2 15 [2], where A^z represents an ion of charge z, and e_1 and e_2 the incident and scattered free electrons

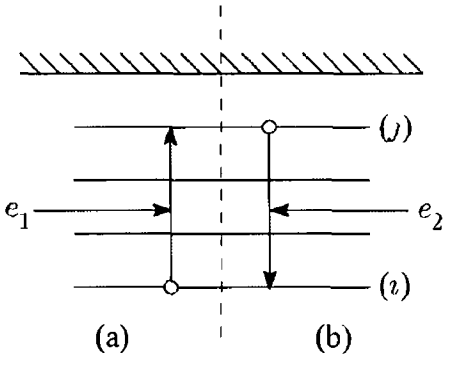

Figure 2 1 Electron impact excitation and de-excitation

(ii) **Electron-impact de-excitation** is the second bound-bound process It is the inverse of electron-impact excitation and is also described by equation 2 15 but from right-to-left, it is graphically depicted on the right-hand side of figure 2 1 Electron-impact de-excitation occurs when a free electron

induces a downward transition of an excited bound electron in a nearby ion to a lower bound state, converting the excess energy into increased kinetic energy for the free electron

$$A_i^z + e_1 \Longleftrightarrow A_j^z + e_2 \qquad (e_1 > e_2) \tag{2 15}$$

Bound–Bound Radiative Pathways

(iii) **Spontaneous decay** is the first radiative bound–bound transition to be discussed It is one of only two of the processes discussed here in which, there is no interaction with any other particle or field In this process a photon is emitted stochastically in a completely spontaneous transition from an excited energy level to a lower discrete energy level, as is shown on the left of figure 2 2 and left-to-right in equation 2 16

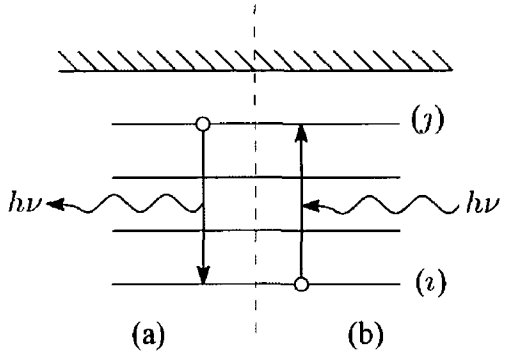

Figure 2 2 Spontaneous decay and resonant photoabsorption

(iv) **Resonant photoabsorption** is the inverse process of spontaneous decay It occurs when an electron in a bound state of an atom or ion is excited to a higher discrete state by absorbing a photon whose energy ($h\nu = |E_i - E_j|$) matches the difference between the initial (i) and final (j) state Resonant photoabsorption is given by the right-to-left reaction in equation 2 16 and depicted by process on the right-hand side of figure 2 2

$$A_j^z \Longleftrightarrow A_i^z + h\nu \tag{2 16}$$

2 4 2 Bound–Free Processes

Bound–free processes occur when an ion either receives enough energy to eject one of its bound electrons into the continuum, thereby incrementing its ionisation state by one, or an electron in the continuum loses energy and falls into a discrete energy level of an ion thereby reducing its ionisation state by one

There are six atomic processes of interest that can be categorised as being bound–free, three of these are collisional and three are radiative

Bound–Free Collisional Pathways

(v) **Electron-impact ionisation** is extremely important in "low density" optically thin plasmas, whereas its inverse process is important only in high density plasmas It occurs when a free electron collides with an atom or ion and provides enough energy to ionise it, thus releasing a bound electron from the atom or ion into the continuum This process is shown (left-to-right) in equation 2 17 and by the left-hand side of figure 2 3

$$A^z + e_1 \Longleftrightarrow A^{z+1} + e_2 + e_3 \qquad (e_1 > e_2) \tag{2 17}$$

where e_1 is the energy of the incoming electron, e_2 denotes its energy after the interaction and e_3 is the energy of the newly liberated free-electron

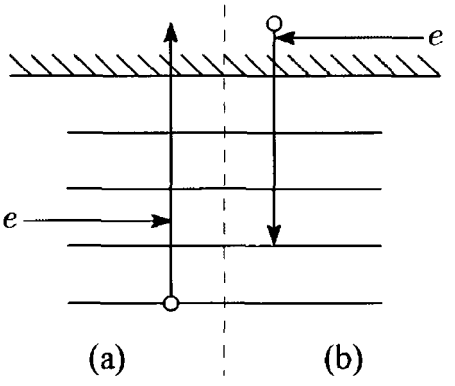

Figure 2 3 Electron impact ionisation and 3-body recombination

(vi) **Three-body recombination** occurs when two free electrons simultaneously enter the Debye sphere of an ion, one of the two is captured into a bound

state, while the other takes up the surplus energy as kinetic energy This process is only favoured in high density regimes because it requires that two electrons be present in the vicinity of an ion at the same time Three-body recombination is the inverse process of electron-impact ionisation It is shown from right-to-left in equation 2 17 and on the right-hand side of figure 2 3

Bound–Free Radiative Pathways

(vii) **Photoionisation** is a bound-free radiative excitation process It is the process by which an absorbed photon promotes a bound electron into the continuum, thereby ionising the atom or ion Photoionisation is an important process in hot plasmas, only if the incident photon density is high enough to induce photoionisation on a scale comparable with electron impact ionisation This is usually only the case in optically thick plasmas, where the

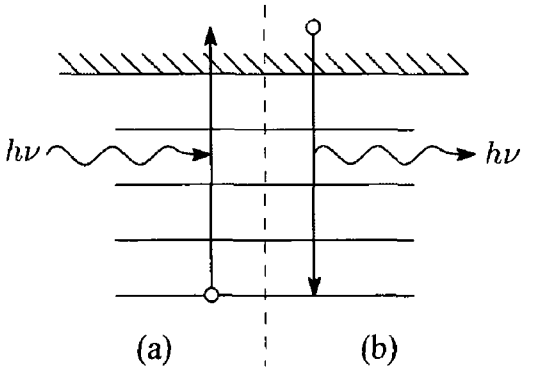

Figure 2 4 Photoionisation and radiative recombination

photon mean-free path (m f p) is short relative to the plasma dimensions See the left-to-right reaction in equation 2 18 and the left-hand side of figure 2 4

$$A^z + h\nu \Longleftrightarrow A^{z+1} + e \qquad (2\ 18)$$

(viii) **Radiative recombination** is a two body recombination process and has its largest influence in low density plasmas, where it is not rendered insignificant by collisional processes It is the inverse process to photoionisation and it occurs when a free electron in the continuum emits a photon "$h\nu$" and falls into a discrete energy level of an ion, thus decrementing the ionisation state by one, as shown in the right-to-left reaction of equation 2 18 and the right-hand side of figure 2 4

2.4.3 Free–Free Processes

The final group of transitions are called free–free transitions There are only two processes in this category, one of which is collisional (Bremsstrahlung) and one radiative (Inverse-Bremsstrahlung)

Free–free transitions are associated with the loss or gain of energy by an electron in the field of an ion They are photon-electron interaction processes Both free–free processes are extremely important in laser-produced plasmas Inverse-Bremsstrahlung is the most important method of plasma heating by laser radiation in the energy regimes of this work, and Bremsstrahlung is the main contributing factor to the continuum radiation observed in the spectra of hot plasmas

Free–Free Collisional Pathways

(ix) **Bremsstrahlung** occurs when a free electron moving close to an ion is accelerated by the ion's Coulomb field, thereby emitting a photon Bremsstrahlung is the main radiation process in low-z plasmas and is also very important in highly ionised high-z ones When a high-z plasma is less ionised Bremsstrahlung provides a low background continuum beneath the line emission The Bremsstrahlung process is represented by the left-to-right reaction in equation 2 19 and the left-hand side of figure 2 5

$$A^z + e_1 \Longleftrightarrow A^z + e_2 + h\nu \qquad (e_1 > e_2) \tag{2 19}$$

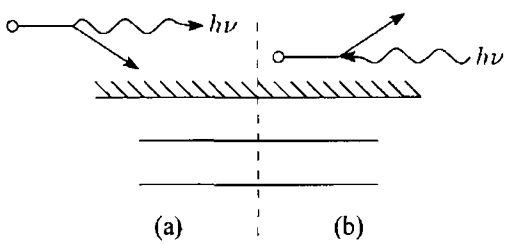

Figure 2 5 Bremsstrahlung and Inverse Bremsstrahlung

Free–Free Radiative Pathways

(x) **Inverse–Bremsstrahlung** occurs when a free electron in the continuum travelling near an ion absorbs a photon, thereby increasing its kinetic energy In order that momentum be conserved in this process, it can only take place in the presence of an ion, so that the ion may carry away the extra momentum IB is shown from right-to-left in the reaction equation 2 19 and the right-hand side of figure 2 5

2 4 4 'Special Case' Bound–Free Processes

(xi) **Autoionising** states are formed when high energy photons or electrons are resonantly scattered by atoms and ions In this process, either inner-shell excited or multiply-excited states, with an energy above the ionisation limit of the atom or ion, are formed These states are clearly unstable against ionisation and so decay rapidly (femtosecond time scale) by the emission of one or more electrons

Hence, autoionisation decay can be viewed as the second process in which there is no interaction with any external particle although the state itself has to be excited by collisions with photons or particles It begins with a doubly excited ion, two electrons occupying excited energy levels (i and i') One of these electrons decays to a lower state (j), while the excess energy ejects the second electron into the continuum Autoionisation can only occur if the sum of the energies of the initial electrons is greater than the ionisation energy of the ion [2] The reaction balance equation for autoionisation is given by (left-to-right) equation 2 20 and is represented by the left-hand-side of figure 2 6

$$A^z + (h\nu \text{ or } e) \Longleftrightarrow A^{z*} \Longleftrightarrow A^{z+1} + ne \qquad (n \geq 1) \qquad (2\ 20)$$

(xii) **Dielectronic recombination** occurs when an electron is captured from the continuum by an ion into an excited state The excess energy of the electron is used to promote another bound electron into an excited state, thereby resulting in a doubly excited ion Dielectronic recombination is considered the inverse process of autoionisation but it is not exactly so Dielectronic

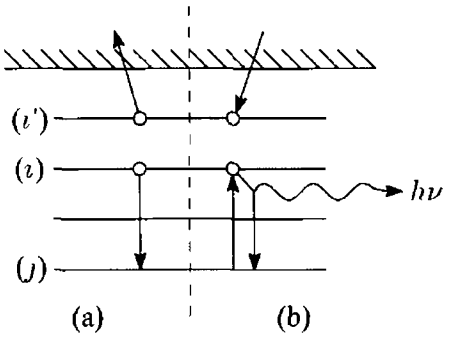

Figure 2 6 Autoionisation and dielectronic recombination

recombination is a two step process, the first of which is the inverse of autoionisation and results in the doubly excited ion as discussed above After that the doubly excited ion can either decay through autoionisation, returning the system to its initial state Alternatively it can radiatively decay, as represented by the right-to-left reaction in equation 2 17 and by the right hand side of figure 2 6

2 5 Equilibrium in Plasmas

A plasma can be said to be in a state of *complete thermodynamic equilibrium* (CT) if all of the following validity conditions are satisfied [1]

(i) All particles, electrons, atoms and ions have a Maxwell velocity distribution

(ii) The population distributions over the states of any atom or ion are given by the Boltzmann relation

(iii) The ratio of ions of charge (z) to those of charge $(z-1)$ is given by the Saha equation

(iv) The radiation intensity distribution as a function of frequency and temperature is given by the Planck formula

It is very rare that laboratory plasmas approach a state of CT equilibrium The very fact that plasmas radiate and are optically thin at most frequencies [11], continually losing energy to their surroundings prevents this from happening [1] It is for this reason that more practical models, with less stringent validity require-

ments have been developed to better describe laboratory plasmas The three most

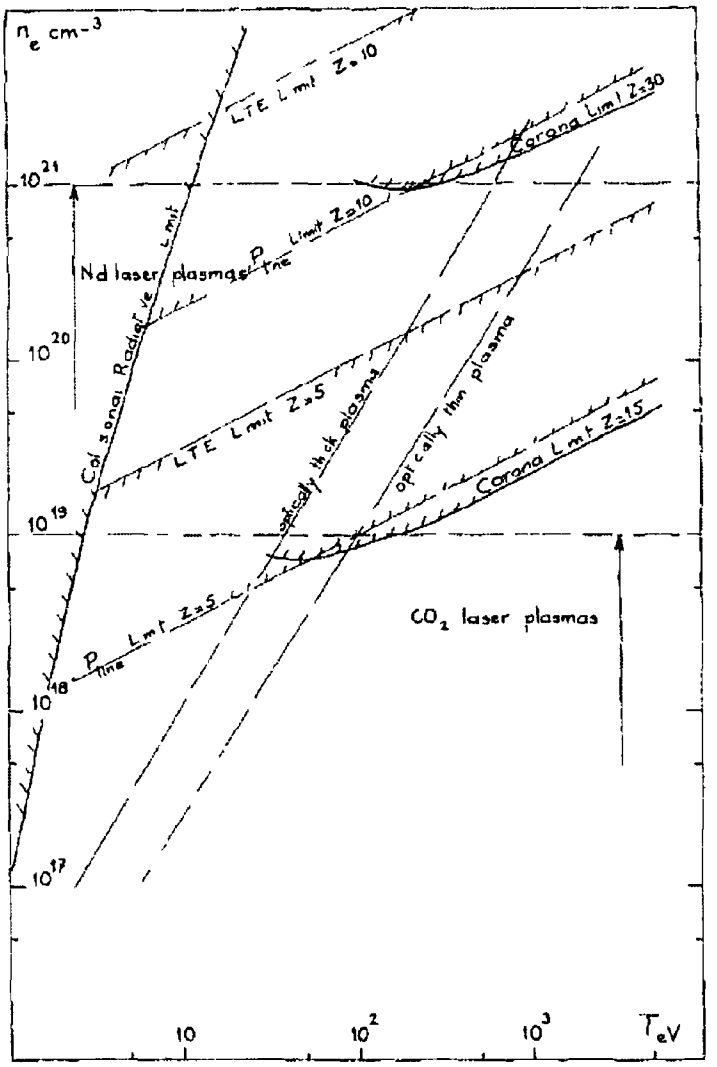

Figure 2 7 Validity ranges of thermodynamic models (After Colombant and Tonon [12])

commonly used thermodynamic models in plasma physics are

(i) Local Thermodynamic Equilibrium (LTE)

(ii) Coronal Equilibrium (CE)

(iii) Collisional Radiative Equilibrium (CR)

The LTE model is very close to CT and is applicable to high density, hot plasmas, such as solar interiors The CE model deals with low density plasmas, such as the solar corona, hence its name, and finally the CR model describes the intermediate or medium density regime and overlaps with LTE and CE at its high and low den-

sity limits Figure 2 7 shows the electron density requirements for valid application of the three equilibrium models as a function of temperature (after Colombant and Tonon [12])

2 5 1 Local Thermodynamic Equilibrium

LTE describes a type of equilibrium in which collisional processes dominate over radiative ones In order for this to be the case a plasma must have a high electron density, such that the collision frequency is high One criterion for the applicability of LTE is that the electron density be sufficiently high such that the rate of collisional de-excitation be at least one order of magnitude larger than that for radiative decay for all transitions [12] Achieving this will ensure that there is less than a 10% departure from LTE [13] This density requirement will be met if

$$n_e \geq 8 \times 10^{11}\, T_e^{\frac{1}{2}} \chi_{max}^3 \quad cm^{-3} \tag{2 21}$$

where χ_{max} is the highest ionisation energy of any atoms or ions present and T_e is the electron temperature [14] In complete thermodynamic equilibrium all three particles electrons, ions and photons are in mutual equilibrium In LTE the electrons and ions are in equilibrium with each other but the photons are not A detailed balancing of all excitation / ionisation and de-excitation / recombination processes must exist to sustain equilibrium Radiation processes are not balanced in an LTE plasma because the mean-free path of the photons is larger than the plasma dimensions, leading to a larger proportion of radiative emission processes than photoabsorption, resulting in a dilution of the radiation field [11], and energy losses to the surroundings

The most important validity condition for LTE application is that the rate of energy-conserving collisional processes be much higher than the rate of energy-dissipating radiative processes This minimises the amount of energy that is lost to the surroundings In optically thick plasmas equation 2 21 can be somewhat relaxed because re-absorption of radiation effectively suppresses the radiative decay rate, minimising energy loses In LTE all particles can be described by a Maxwellian velocity distribution, a Boltzmann population distribution within each ion stage and a Saha ionisation balance The Saha equation is given by [15]

$$\frac{n_e n_{z+1}}{n_z} = \frac{2U_{z+1}(T)}{U_z(T)} \left[\frac{2\pi m_e k_B T}{h^2}\right]^{\frac{3}{2}} exp\left(\frac{-I_z^{eff}}{k_B T}\right) \quad z = 0, 1, \quad (Z_{max} - 1) \tag{2 22}$$

where z is the ionisation stage, $U_z(T)$ is the temperature dependent partition function for the ion stage z and I_z^{eff} is the effective ionisation energy for the ionisation process $z \rightarrow (z+1)$.

An important advantage of LTE over the other equilibrium models is the fact that the ionisation balance can be computed without knowing any of the transition rates. CR and CE required the calculation of some transition probabilities. Solving equation 2.22 for Ca, the ionisation balance as a function of temperature can be computed [16]. Figure 2.8 shows the result of this calculation including only the first eight charge stages.

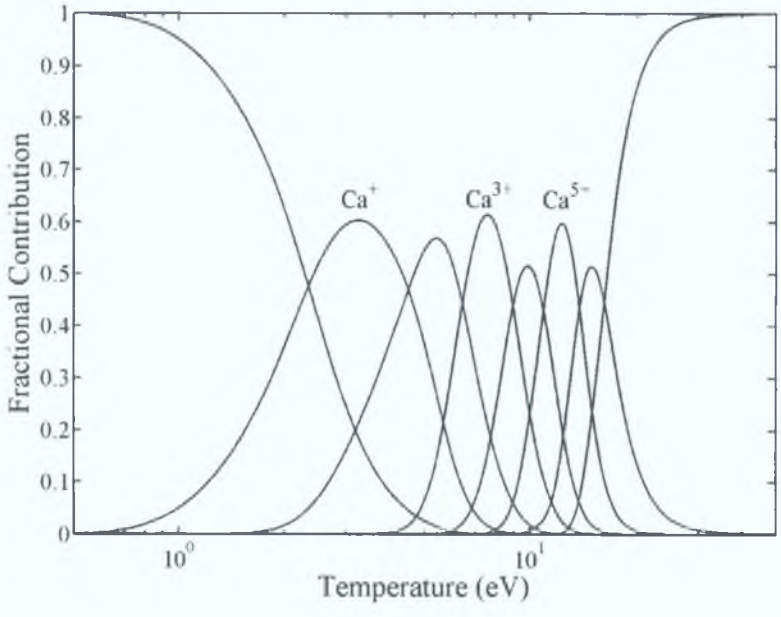

Figure 2.8: Ionisation balance of a Ca plasma as a function of temperature assuming a state of local thermodynamic equilibrium, calculated in this work using equation 2.22.

By combining the Saha and Boltzmann equations, one may relate the number density of neutral atoms in state j ($n_{a,j}$) to the number density of ions in state k ($n_{i,k}$). The equation is known as the Saha-Boltzmann equation and is given by [17]

$$\frac{n_e n_{i,k}}{n_{a,j}} = \frac{2(2\pi m k_B T)^{3/2}}{h^3} \frac{g_{i,k}}{g_{a,j}} exp\left(\frac{-I_z^{eff}}{k_B T}\right) \tag{2.23}$$

where g denotes the degeneracy of the level. Using this equation, one may calculate the relative population of a specific level from any charge stage.

2 5 2 Coronal Equilibrium

Coronal equilibrium is at the other density extreme to LTE It is used to describe low density, optically thin plasmas Such plasmas occur frequently in astrophysical situations such as interstellar nebulae and solar coronas, as well as in the laboratory, in tokamaks and other discharge plasmas and in the extended low density portions of plumes of laser-produced plasmas

Unlike LTE, where detailed balancing of each process and its inverse mostly exists, no process is balanced by its inverse counterpart in CE plasmas The upward excitation rate caused by collisions is so low relative to spontaneous decay that it is safe to assume that an excited electron will spontaneously undergo a transition to a lower state before another collision occurs [2] Most ions therefore reside in the ground state Collisional de-excitation can be totally ignored Due to the fact that CE plasmas are optically thin, the photon m f p is long, leading to very low photoionisation and photoexcitation rates The ionisation equilibrium (shown in figure 2 9) is a balance between electron impact ionisation $S(Z,T_e)$ and radiative recombination $\alpha_r(z,T_e)$ [13]

$$\frac{n_{z+1}}{n_z} = \frac{S(Z,T_e)}{\alpha_r(z+1,T_e)} \tag{2 24}$$

where the electron impact ionisation rate $S(z,T_e)$ in $cm^{-3}s^{-1}$ is given by

$$S(z,T_e) = \frac{9\times10^{-6}\xi_z(T_e/\chi_z)^{1/2}}{\chi_z^{3/2}(4\,88+T_e/\chi_z)} exp\left(\frac{-\chi_z}{T_e}\right) \tag{2 25}$$

χ_z is the ionisation potential of charge stage z and ξ_z is the number of electrons in the outermost shell The radiative recombination rate $\alpha_r(z,T_e)$ in $cm^{-3}s^{-1}$ is given by

$$\alpha_r(z,T_e) = 5\,2\times10^{-14}\left(\frac{\chi_z}{T_e}\right)^{\frac{1}{2}} Z\left[0\,43+\frac{1}{2}log\left(\frac{\chi_z}{T_e}\right)+0\,47\left(\frac{T_e}{\chi_z}\right)^{\frac{1}{2}}\right] \tag{2 26}$$

The maximum electron density allowable before the CE model starts to break down is when collisions begin to interfere with the assumption that there is only one decay mechanism, radiative decay [13] This electron density is given by

$$n_e \leq 1\,5\times10^{10}(k_BT_e)\chi^{-\frac{1}{2}} \tag{2 27}$$

where χ(eV) is the ionisation potential of the ion Z [18]

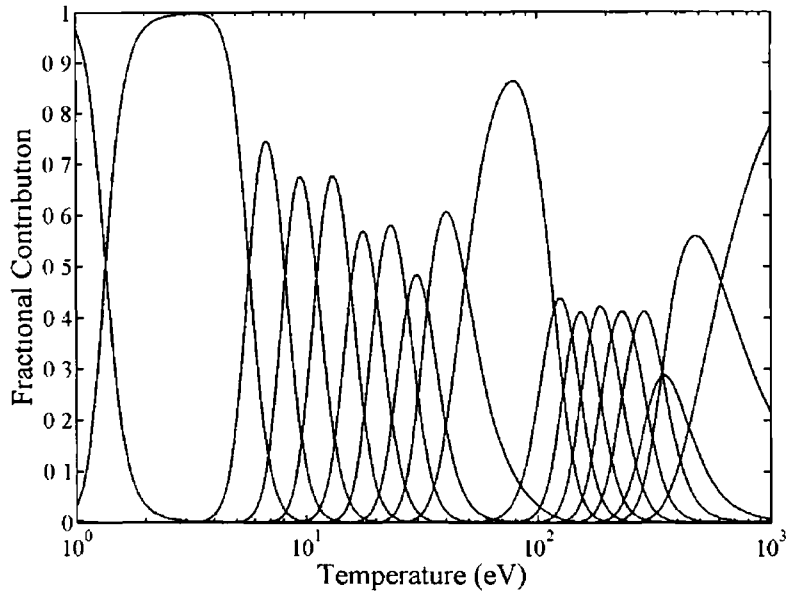

Figure 2 9 Ionisation balance of a Ca plasma as a function of temperature assuming a state of coronal equilibrium, calculated in this work using equation 2 24

2 5 3 Collisional Radiative Equilibrium

Collisional radiative equilibrium is applicable in the intermediate density regime between LTE and CE, i e typically electron densities between $\approx 10^{19}$-10^{21} cm^{-3} CR is an extension of the CE model and it includes electron collision processes causing transitions between excited state levels, including three-body recombination [13]

In CR it is assumed that a Maxwellian electron velocity distribution pertains and that the plasma is optically thin Using these assumptions the rate equation for a given ionisation stage is

$$\frac{dn_{z+1}}{dt} = n_e n_z S(z,T_e) - n_e n_{z+1}[S(z+1,T_e) + \alpha_r(z+1,T_e) + n_e\alpha_{3b}(z+1,T_e)] + n_e n_{z+2}[\alpha_r(z+2,T_e) + n_e\alpha_{3b}(z+2,T_e)] \quad (2\ 28)$$

where $S(z,T_e)$ is given by equation 2 25, $\alpha_r(z,T_e)$ by equation 2 26 and $\alpha_{3b}(z,T_e)$ the three-body recombination coefficient (s^{-1}) is given by

$$\alpha_{3b}(z,T_e) = \frac{2\ 97 \times 10^{-27}\xi_z}{T_e\chi_z^2(4\ 88 + T_e/\chi_z)} \quad (2\ 29)$$

Equation 2 28 is computationally very difficult to solve, however if one assumes a stationary state then the ionisation balance for successive stages is given by

$$\frac{n_{z+1}}{n_z} = \frac{S(z,T_e)}{\alpha_r(z+1,T_e) + n_e\alpha_{3b}(z+1,T_e)} \quad (2\ 30)$$

Using equation 2 30 one can calculate the ratio of each individual charge stage population to the total population n_T of all charge stages using the simple relationship

$$\frac{n_z}{n_T} = n_z / \sum_{k=1}^{Z} n_k \tag{2 31}$$

Figure 2 10 shows the ionisation balance for Ca plasma in collisional radiative equilibrium, calculated from equation 2 30

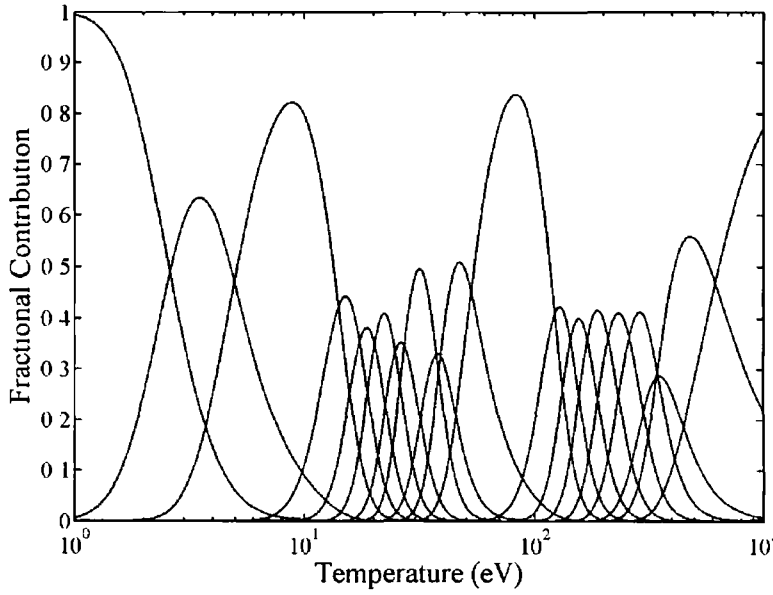

Figure 2 10 Ionisation balance of a Ca plasma as a function of temperature assuming a state of collisional radiative equilibrium, calculated in this work using equation 2 30

2.6 Radiation Transport

Radiation transport is the redistribution of energy within a medium through the emission and absorption of photons [19] In this section we are going to discuss the equation of radiative transfer with particular reference to two situations of importance for this work In the first case we will derive the general solution of the radiative transfer equation, which will be an important result in our emission spectroscopy studies The second case will be the photoionisation of atoms and ions, which is important for our photoabsorption imaging studies

We will begin by describing a two level energy system, from which we will obtain

the Einstein emission and absorption coefficients Using these coefficients we will define spatial and frequency dependent emission and absorption coefficients that will contain within them information about population distributions and densities as well as spectral distributions We will develop the general equation of radiative transfer and present, using the emission and absorption coefficients a particular solution relevant to photoionisation

2 6 1 Einstein Coefficients

Let us begin by considering a two level energy system as is shown in figure 2 11 Einstein was the first to derive the relationship between the probabilities of emission and absorption processes in this system Three processes are taken into con-

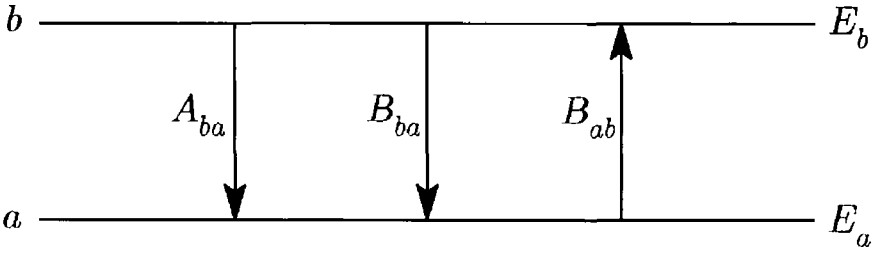

Figure 2 11 Einstein coefficient two-level energy system

sideration A_{ba} (in figure 2 11) is the Einstein coefficient for spontaneous emission, B_{ba} denotes the coefficient for stimulated emission and B_{ab} is the absorption coefficient The Einstein absorption coefficient can be related to the oscillator strength f_{ab} and transition frequency ω_{ba} by [20]

$$B_{ab} = \frac{2\pi^2 e^2 f_{ab}}{\epsilon_0 \hbar \omega_{ba} c} \tag{2 32}$$

where $\hbar$ is Planck's constant divided by 2π The absorption coefficient B_{ab} can then be related to the stimulated emission coefficient B_{ba}, by

$$g_a B_{ab} = g_b B_{ba} \tag{2 33}$$

where g_b and g_a are the upper and lower state degeneracies respectively Finally the spontaneous emission coefficient A_{ba} can be calculated from the stimulated emission coefficient B_{ba} by [21]

$$A_{ba} = \left(\frac{\hbar \omega_{ba}^3}{\pi^2 c^3}\right) B_{ba} \tag{2 34}$$

2 6 2 Emission and Absorption Coefficients

The building blocks of the equation of radiative transfer are the spectral emission $\epsilon(x,\nu)$ and absorption $\kappa(x\ \nu)$ coefficients The Einstein coefficients are combined with a spectral distribution function $f(x\ \nu)$ and level population distributions $n(x)$ to generate these functions The spatially dependent emission coefficient is given by

$$\epsilon(r,\nu) = \frac{A_{ba} n_b(x) h\nu f(x,\nu)}{4\pi} \tag{2 35}$$

where n_b is the excited state population distribution The absorption coefficient is given by

$$\kappa(x,\nu) = \frac{[B_{ab} n_a(x) - B_{ba} n_b(x)] h\nu f(x,\nu)}{c} \tag{2 36}$$

where n_a is the lower state population distribution and can be described as the fractional rate of absorption of radiation per unit path length as a function of frequency [22] The spectral distribution function $f(x,\nu)$ is a normalised shape function, characteristic of the lifetimes of the states and is broadened and shifted by the plasma electron density and temperature distribution

2 6 3 Equation of Radiative Transport

The equation of radiative transfer determines the change of intensity of a beam of radiation as it propagates through a material

We consider a beam of collimated radiation confined within a small solid angle, which is passed through a cylindrical volume of plasma (figure 2 12) The frequency of the radiation ν is chosen such that the photon energy lies close to the energy difference between our two states $E_b - E_a$ (figure 2 11), and has a small finite bandwidth $d\nu$ and small divergence $d\Omega$ The transfer equation is determined by considering the change in radiant energy contained within the frequency $d\nu$ as the beam passes through a cylindrical volume element of cross section dS and length dx

$$(I(x_0 + dr,\nu) - I(x_0\ \nu))d\nu dS d\Omega \ = \ \frac{dI(x,\nu)}{dx} dx d\nu dS d\Omega \tag{2 37}$$

Along the length of the cylinder the intensity of the beam will be augmented by spontaneous emission into the solid angle $d\Omega$ It could also, in principle, be

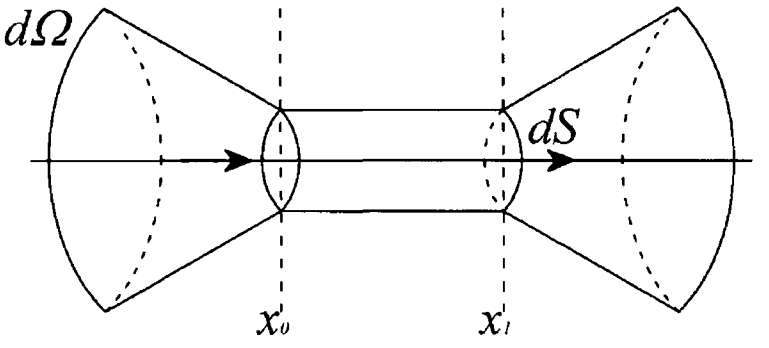

Figure 2 12 Radiation transport geometry (After Corney [20])

augmented by stimulated emission into $d\Omega$ induced by the incident beam and by stimulated emission into $d\Omega$ caused by spontaneous emission into 4π, this however is very unlikely in our situation, without a population inversion but should be mentioned here while describing the general case The spontaneous emission component of this enhancement is contained within the emission coefficient $\epsilon(x,\nu)$ whereas the stimulated emission term acts on the absorption coefficient $\kappa(x,\nu)$, reducing its overall value

Hence the intensity of the incident beam and its additional photons are diminished along the length of the cylinder by the absorption of photons, which excite electrons into the upper level If the system is in equilibrium the rates of emission and absorption processes will equal each other

A more concise way of saying this would be, the specific intensity of the incident beam along the cylinder increases in proportion to the local emission coefficient, but is attenuated at a rate equal to its product with the local absorption coefficient [19] This change of intensity of the beam can therefore be written as

$$\frac{dI(\nu)}{dx} = \epsilon(x,\nu) - \kappa(x,\nu)I(\nu) \tag{2 38}$$

which is the general form of the equation of radiative transfer

2 6 4 General Solution of Equation of Radiative Transport

Knowing the values of the emission and absorption coefficients the general formal solution to equation 2 38 is given by

$$I(\nu)_{x_1} = I(\nu)_{x_0} e^{-\tau_\nu(0)} + \int_{x_0}^{x_1} \epsilon(x,\nu) e^{-\tau_\nu(x)} dx \tag{2 39}$$

where the optical depth $\tau_\nu(x)$ between x_0 and x_1 (figure 2 12) is defined by

$$\tau_\nu(x) = \int_{x_0}^{x_1} \kappa(x,\nu) dx \tag{2 40}$$

when $\tau_\nu(x) \gg 1$ the cylinder is said to be optically thick [22] The first term on the right hand side of the equation 2 39 represents the exponential attenuation of the incident beam along the path between x_0 and x_1 The second term describes the local emission and absorption processes along the path that augment and attenuate the beam, depending on the values of the coefficients We will be using this general solution later in this work to aid in the description of self-absorption observed in some calcium spectra

2 6 5 Solution of Equation of Radiative Transport for Photoionisation

There are two major simplifying assumptions that may be made to the equation of radiative transfer when dealing specifically with the case of photoionisation

The first assumption is that the spontaneous emission term A_{ba} may be neglected This is so because in the case of photoionisation we are not dealing with bound–bound transitions, the absorbed VUV radiation is almost exclusively used to generate photoelectrons This is particularly true for resonant photoionisation where almost all absorbed photons are converted into electrons since autoionisation / Auger rates can be many orders of magnitude greater than radiative rates (e g radiative recombination)

The second assumption is that the stimulated emission term may also be neglected since the branching ratio for fluorescence to electron emission processes tends to be less than 10^{-4} [23, 24]

As a result a simplified version of the equation of radiative transfer can be used

$$\frac{dI(\nu)}{dx} = -\kappa(\lambda, \nu)I(\nu) \tag{2 41}$$

the solution of which is given by

$$I = I_0 \exp(-\kappa(\tau, \nu)) \tag{2 42}$$

this result [20] will be discussed further and used when dealing with the Vacuum ultraviolet Photoabsorption Imaging Facility (VPIF) in chapter 5

2.7 Summary

In this chapter we have discussed the basic theory used during the remainder of this work The fundamental plasma processes were described as well as plasma formation and expansion due to the interaction of laser radiation with matter Thermodynamic equilibrium models have been discussed as well as radiation transport within plasmas

In the next chapter we will discuss the theory and application of the plasma diagnostics used in this work We will discuss how VUV photoabsorption imaging, spectrally filtered time-resolved emission imaging and time and space-resolved emission imaging spectroscopy may be used to determine information about laser-produced plasmas

Bibliography

[1] P K Carroll and E T Kennedy Laser-produced plasmas *Contemporary Physics*, 22 61–96, 1981

[2] D Salzmann *Atomic Physics in Hot Plasmas* Oxford University Press, New York, 1998

[3] E T Kennedy Plasmas and intense laser-light *Contemporary Physics*, 25 31–58, 1984

[4] J F Ready *Effects of high-power laser radiation* Academic Press, Florida, 1971

[5] S Amoruso, R Bruzzese, N Spinelli, and R Velotta Characterization of laser-ablation plasmas *Journal of Physics B Atomic, Molecular and Optical Physics*, 32 131–172, 1999

[6] Y F Lu, M H Hong, and T S Low Laser plasma interaction at an early stage of laser ablation *Journal of Applied Physics*, 85 2899–2903, 1999

[7] T W Johnston and J M Dawson Correct values for high-frequency power absorption by inverse bremsstrahlung in plasmas *Physics of Fluids*, 16 722–722, 1973

[8] C Chenais-Popovics, P Renaudin, O Rancu, F Gilleron, J -C Gauthier, O Larroche, O Peyrusse, M Dirksmoller, P Sondhauss, T Missalla, I Uschmann, E Forster, O Renner, and E Krousky Kinetic to thermal energy transfer and interpenetration in the collision of laser-produced plasmas *Physics of Plasmas*, 4 190–208, 1997

[9] Andy Gray *XUV photoabsorption studies of calcium and the neon isoelectronic sequence* PhD thesis, School of Physical Sciences, Dublin City University, 1999

[10] R K Singh and J Narayan Pulsed-laser evaporation technique for deposition of thin films Physics and theoretical model *Physical Review B*, 41 8843–8859, 1990

[11] W Lochte-Holtgreven *Plasma diagnostics* AIP Press, New York, 1995

[12] D Colombant and G F Tonon X-ray emission in laser produced plasmas *Journal of Applied Physics*, 44 3524–3537, 1973

[13] R H Huddlestone and S L Leonard *Plasma diagnostic techniques* Academic Press, New York, 1965

[14] T P Hughes *Plasmas and laser light* Hilger, Bristol, 1975

[15] M R Zaghloul, M A Bourham, and J M Doster A simple formulation and solution strategy of the saha equation for ideal and nonideal plasmas *Journal of Physics D Applied Physics*, 33 977–984, 2000

[16] Mofreh R Zaghloul Ionization equilibrium and partition functions of high-temperature weakly non-ideal Flibe gas much of this work has been presented at the 15th ans topical meeting on the technology of fusion energy (tofe) (washington, dc, november 2002) *Journal of Physics D Applied Physics*, 36 2249–2254, 2003

[17] Anne P Thorne *Spectrophysics* Chapman and Hall, 1988

[18] C McGuinness *The XUV Photoabsorption and Photoionisation Spectra of Selected Ions Techniques, Results and Theory* PhD thesis, University College Dublin, 1996

[19] J P Apruzese, J Davis, K G Whitney, J W Thornhill, P C Kepple, and R W Clark The physics of radiation transport in dense plasmas *Physics of Plasmas*, 9 2411–2419, 2002

[20] A Corney *Atomic and laser spectroscopy* Clarendon Press, New York, 1977

[21] B H Bransden and C J Joacham *Physics of atoms and molecules* Longman, New York, 1983

[22] I H Hutchinson *Principles of plasma diagnostics* Cambridge University Press, Cambridgeshire, 1987

[23] J S Hirsch *Photoabsorption Imaging of Laser Produced Plasmas* PhD thesis, School of Physical Sciences, Dublin City University, 2003

[24] V Schmidt Photoionization of atoms using synchrotron radiation *Reports on Progress in Physics*, 55 1483–1659, 1992

CHAPTER 3

PLASMA DIAGNOSTICS

3.1 Introduction

The overall objective of plasma diagnostics is to deduce information about the state of the plasma from experimental observations [1] A battery of optical and particle diagnostic techniques are currently being deployed in order to characterise laser-produced plasmas The number of techniques stems from the desire for 'complete" spatio-temporal parametrisation of plasma plumes, and is fuelled by the increasing number of applications of laser-produced plasmas Another reason for the strong interest in the characterisation of LPP's is that laser-produced plasmas provide an easily accessible system for the study of fundamental atomic physics

Complete characterisation of LPP's is extremely difficult due to the number of processes involved and by the number of parameters that have the ability to alter the plume properties As has been mentioned previously, altering any of the properties of the initiating laser pulse wavelength, intensity, duration, or spot-size can have dramatic effects Similarly, changing the properties of the target material or the ambient background, can produce significant alterations to the plume The number of parameters that can be measured, and used to describe these changes are also numerous These include electron, ion and atom densities, electron and ion temperatures, velocity distributions, charge stage distributions, electric and magnetic field strengths

Unfortunately, there is no one plasma diagnostic that can measure all of these parameters at all times and positions, for all possible values, and to an acceptable degree of accuracy Most diagnostic techniques are only applicable over a specific range of values, where theoretical assumptions are valid, and can be applied to the experimentally recorded data, thereby allowing the inference of the desired parameter It is for this reason that the thermodynamic models discussed in section 2 5 were developed If a plasma can be justifiably placed into the parameter space applicable to one of these models, by satisfying certain entry requirements, such as a minimum electron density, one can assume other properties of the plasma, such as population or velocity distributions that can aid in the quantitative description of the plasma

In LPP's the two most important characteristic parameters are the electron density and electron temperature This is so because electrons are the most active plasma constituent, they affect every aspect of the plume initiation and expansion All of the atomic processes discussed in section 2 4, such as the emission of line and continuum radiation result from changes in electron energies The rates at which all of these atomic processes take place are dictated by the density and temperature of the electrons The most reliable way of measuring electron densities and temperatures in LPP's are laser interferomety and Thompson scattering, closely followed by emission spectroscopy

In Thompson scattering the electric field of low intensity laser light impinging on a plasma accelerates electrons, the accelerated electrons scatter the radiation in a manner related to the thermal velocity distribution of the electrons, allowing the determination of the electron temperature Additionally, the intensity of the light scattered is proportional to the number of scatterers, thereby allowing the calculation of the electron density [1, 2, 3] This technique however can be very difficult to execute since the Thompson signal can be difficult to detect over the much stronger Rayleigh scattering signal

In interferometry the phase difference between a beam of light that traverses an LPP and a reference beam is recorded The phase of the traversing beam is altered by variations in refractive index in the plasma which is caused by electron density gradients By analysing the interference pattern between the two beams, the electron density and temperatures can be determined [4]

The final technique mentioned above, which is widely used for obtaining electron temperatures and densities is emission spectroscopy Spectroscopy is usually a less accurate method of obtaining n_e and T_e as it relies on the validity of quite a few assumptions, accuracy is diminished further because it relies on the detailed analysis of the shape and width of spectral lines that can be altered by numerous mechanisms

However, the slight accuracy deficit inherent in using spectroscopy as opposed to interferometry or scattering is outweighed by its ease of use and additional diagnostic abilities Using spectroscopy one can specifically study continuum or line emission, determine the elemental composition of the plasma, measure velocity distributions of various charge states (space and time-resolved spectroscopy) and determine relative population distributions In addition different temperature and density regimes can be accessed by measuring and analysing spectra from the infrared to the VUV or X-ray There are a number of other diagnostics techniques that measure parameters other than n_e and T_e that are worth noting in relation to laser-produced plasmas

The attenuation of radiation passing through an atomic or ionic, vapour or plasma column is an important system for the study of the interaction of radiation with free atoms Photoabsorption spectroscopy is an important diagnostic for studying this system, in which the attenuation of radiation, caused during excitation and ionisation processes is recorded The absorbance $\sigma_a = \log_{10}(I_0/I)$ of a length of plasma can be related to the column density $NL = \int_0^L n(l)dl$ (where n, the number density, is integrated along the absorbing column of length l) [5] If one knows "L" a species density N may be determined Additionally since ratios (I_0/I) are used absolute values of intensity are not required

The most basic and earliest plasma diagnostics were electrostatic and magnetic probes Probes have been used since the mid 1920's to determine plasma parameters such as electron density, electron temperature, ion densities and ion temperatures [6, 7] They are primarily deployed in the study of discharge plasmas but have also been applied to LPP's [8]

Electrostatic, or Langmuir probes are the most commonly used of the two probe types They basically consist of a small metallic electrode that is inserted into the plasma The bias on the probe is then varied relative to that of the plasma and

information about the local plasma conditions can be obtained by examining the current collected by the probe There are however many drawbacks to using probes as a diagnostic for LPP's Probes can only be used at relatively long time delays when the volume of the plasma is large enough to accommodate the probe Also the invasive nature of probing may perturb the plasma and affect the measured plasma parameters

There are various photographic / imaging techniques that provide information about the macroscopic temporal evolution of the emitting and non-emitting species in the plume Photographic techniques have been used for many years to image primarily steady-state or slowly varying discharge plasmas However LPP's, whose luminosity varies rapidly with time, could only be imaged by integrating over the life-time of the plasma This changed however with the advent of high-speed shutters, allowing for exposure times of just a few nanoseconds These have enabled the detailed study of the evolution of LPP's and comparisons with hydrodynamical models

In this work emission imaging and spectroscopy as well as photoabsorption imaging was used to study the interaction of two laser-produced plasmas In the next three sections we will discuss the principles behind these diagnostic methods and in the next chapter we will deal with their experimental details

3.2 VUV Photoabsorption Imaging

Many time-resolved imaging and spectroscopy experiments have been undertaken on the radiation emitted by excited species in plasmas Conversely, little work has been done to study the non-emitting ground state species in plasmas [9] Tuneable lasers have been used to study these "dark" species in plasmas [10] but their usefulness is limited by their inability to produce appreciable photon fluxes in the VUV where the resonance lines of many moderately charged ions, likely to be present in a plasma, reside Hence tuneable lasers are severely restricted in their application to the absorption spectroscopy of laser plasmas

The DLP technique mentioned in section 3 1 does not suffer from this problem, and it can access resonance lines of almost all atoms and ions in the VUV and

XUV. DLP is used to measure photoabsorption spectra of atoms and ions. In DLP spectroscopy two plasmas are generated, one of which acts as a backlighting (VUV / XUV) continuum source [11]. Radiation from the source is passed through the other "sample" plasma, which selectively absorbs the continuum. The radiation that is not absorbed by the sample is then dispersed by a spectrometer and recorded on a VUV sensitive CCD.

Time-resolved photoabsorption spectra can be obtained by varying the time delay between the generation of the source and sample plasma. Spatially-resolved photoabsorption spectra can be obtained by sequentially probing narrow slices of the sample plume at one time delay, gradually building a spatial picture [12].

An extension of the DLP technique that removes the need for sequential probing, and can capture in a single shot the complete spatial distribution of the dark non-emitting plasma species is known as photoabsorption imaging [13]. In order to achieve single shot spatial resolution the experimental configuration must be altered from that of traditional DLP setups where the "sample" and "light source" plasmas are located side by side in close proximity. In DLP a broadband diverging point source is used whereas in photoabsorption imaging the radiation from the source plasma is monochromatised and collimated before being passed through the sample plasma. Additionally the treatment of the transmitted radiation differs between the two techniques. In DLP the radiation is dispersed by a spectrometer before detection whereas in photoabsorption imaging the radiation footprint is recorded directly onto a VUV sensitive two-dimensional CCD array.

In photoabsorption imaging the monochromatic and collimated VUV radiation from the source can be tuned to access resonance lines of all atoms and lowly charged ions. Probing LPP's with VUV radiation has the advantage that refraction due to density gradients in the plasma is considerably less than that of visible radiation, due to the fact that the probe beam deviation scales with the square of the wavelength of the probe, λ^2_{probe} [9].

Using VUV radiation from a laser-produced plasma as the source for photoabsorption imaging has further advantages. The size and effective relative bandwidth of a laser plasma source means that it is essentially incoherent, meaning that the photoabsorption image analysis is not complicated by interference patterns. The most significant advantage of operation in the VUV is that VUV radiation can be

used to photoionise atoms or ions in the sample plasma Almost all photons in the probe beam that are absorbed in the plasma are converted to electrons For this reason opacity effects due to absorption / re-emission cycles can be ignored, freeing the analysis of the images from the usual radiation transport problems As was discussed in section 2 6, this reduces the interpretation of the attenuation of the probe beam to a simple Beer-Lambert law description

One final advantage of the source configuration is the collimation of monochromatic radiation prior to transmission through the sample plasma, this simplifies the geometrical interpretation of the absorption images VUV photoabsorption imaging is one of the primary diagnostic techniques used in this work to characterise the expansion and interaction of LPP's The system is known as the Vacuum-ultraviolet Photoabsorption Imaging Facility (VPIF) and it was constructed in collaboration with the University of Padua, Italy The specific details of the operation of the VPIF will be discussed later in section 4 4 Images recorded using the VPIF are related to fundamental plasma parameters using the equivalent width of an absorption line and the plasma column density

3.2 1 Equivalent Width

Equivalent width W_λ is an important parameter in the description of absorption profiles It is the width of a rectangle, whose area is equal to that of the area of the absorption line but for which the transmission is 0% across its profile or equivalently the absorption is fully 100% across W_λ This is shown graphically in figure 3 1 The equivalent width gives us a measure of how much absorption is taking place in the plasma It is related to our recorded images by

$$W_\lambda = \Delta\lambda \left(\frac{\int_{\Delta\lambda} [I_\lambda(0) - I_\lambda(L)] d\lambda}{\int_{\Delta\lambda} I_\lambda(0) d\lambda} \right) \tag{3 1}$$

where $\Delta\lambda$ is the bandwidth of the probe beam, $I_\lambda(0)$ is the intensity of the unattenuated probe beam and $I_\lambda(L)$ is the intensity of the probe beam attenuated by a length of plasma L Using equation 3 1, maps of equivalent width of single and colliding plasmas will be extracted and presented later in chapter 5

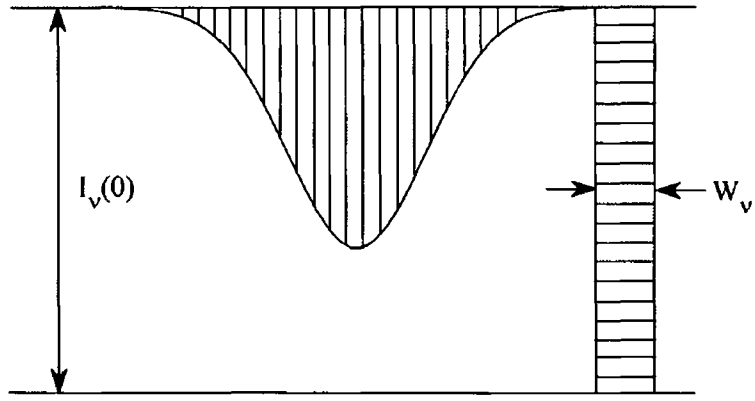

Figure 3 1 Equivalent width of an absorption profile (After Corney [14])

3 2 2 Column Densities

The spatial distribution of plasma column densities (NL) can be calculated from maps of equivalent width (W_λ), if the absolute photoionisation cross sections (σ_λ) of the transition in question is known If I_0 is constant across the wavelength interval of a spectral feature then we can write that the equivalent width is related to column density by [13]

$$W_\lambda = \int_{\Delta\lambda} (1 - e^{-NL \int_{\Delta\lambda} \sigma_\lambda d\lambda}) d\lambda \qquad (3\,2)$$

Calcium has been used in this work primarily because its absolute photoionisation cross-section has been measured in the VUV for the first ionisation stage (Ca^+) Knowing the absolute cross-section for a particular transition, we can convert maps of equivalent width into column density maps

3.3 Spectrally Resolved Emission Imaging

Emission imaging is a complementary diagnostic tool to the photoabsorption studies that have been undertaken It provides us with corresponding spatial distribution maps of excited state emitting species within the plasma

The emission imaging setup provided (i) spectral, (ii) spatial, and (iii) temporal resolution

(i) **Spectral** filtering of the radiation emitted by the plasmas, allows us to image

specific charge states independently of each other, for example choosing a narrowband filter which isolates a particular transition or transitions (e g 393 and 396 nm transitions of Ca^+) We can track the bulk motion of the plasma using broadband filters by capturing the total emission from a plasma and taking it to be proportional to the total amount of hot matter in the plasma

(ii) **Spatial** resolution is obtained by stigmatically imaging the plasma plume onto a two-dimensional CCD array

(iii) **Temporal** resolution is obtained by using an electronic shutter, to gate the CCD array This allows us to follow the plasma expansion dynamics, *ab ovo* until it eventually fades away

Emission imaging is not only used as a comparison with the absorption studies, it also serves other functions It provides expansion velocities and dimensions for comparison with hydrodynamic models Emission images are also used as an aid to spectroscopic measurements, to accurately determine the positions, times and dimensions of the plasma plumes, or in the case of colliding plasmas the collision region Additionally emission images are used to determine whether interpenetration or stagnation layers are constructed in the interaction region between two colliding plasmas (chapter 6) The specific experimental details relating to the emission imaging setup will be discussed in section 4 9

3.4 Emission Spectroscopy

The most important diagnostic tool in the study of laser-produced plasmas is the spectroscopic analysis of the radiation that they emit A wealth of information about the plasma parameters as well as the constituents of the plasma is contained within this radiation

The radiation emitted by plasmas falls into two main categories, continuous and line radiation Line radiation is emitted during bound-bound radiative processes and continuous radiation by bound-free and free-free radiative processes (as was discussed in section 2 4) The relative contribution of continuous and line radiation to a particular spectrum depends on temperature, target material, spectral range,

integration time and many other factors

In this section we will be discussing the radiation emitted by plasmas and how spectra obtained from this radiation is used as a diagnostic tool We will begin by discussing spectral line profiles and the mechanisms that broaden them We will then discuss how electron densities and temperatures can be determined from recorded spectra

3 4 1 Line Profiles

The profile of every spectral line has a finite width and shape that is determined by the local plasma conditions such as density and temperature that exist in the source These conditions can be determined by accounting for the various mechanisms that can broaden spectral lines

We will be discussing in detail the three main broadening mechanisms, natural, pressure and Doppler broadening Each of these broadening mechanisms reflects a fundamental property of the emitting species, in the case of the three mechanisms above, they are transition probability, collision frequency and thermal velocity [15] Of these line broadening mechanisms, Doppler and pressure broadening have become very useful processes for diagnosing plasma parameters

3 4 2 Natural Broadening

Let us begin by considering two discrete energy levels a and b, where the energy of level b is greater than that of level a, $E_a < E_b$ (as in figure 2 11, section 2 6 1) The angular frequency (ω_{ba}) of radiation that can be emitted or absorbed during electron transitions between these two states should be exactly the difference in energy between the two states

$$\omega_{ba} = (E_b - E_a)/\hbar \tag{3 3}$$

leading to an infinitely sharp spectral line This however cannot be the case since the Uncertainty Principle prevents the exact determination of the energy of such a level, leading to a spread of possible energies of the order of $\hbar/\tau$ where τ is the lifetime of the state Therefore there is a finite probability that photons will be

emitted with energies in an interval centered about $(E_b - E_a)$ of width $(\hbar/\tau_a + \hbar/\tau_b)$ where τ_a and τ_b are the lifetimes of the states a and b [16] This broadening due to the lifetimes of the states is referred to as *Natural Broadening* and leads to a Lorentzian intensity distribution function $\mathcal{L}(\omega)$, given by

$$\mathcal{L}(\omega) = \frac{\Gamma^2/4\hbar^2}{(\omega - \omega_{ba})^2 + (\Gamma)^2/4\hbar^2} \quad (3\,4)$$

where $\Gamma = h/\tau$ Natural broadening is the minimum possible spectral line width that can be observed from this transition It is however extremely difficult to do so because of other more significant broadening mechanisms Also, the natural width of a line is beyond the resolution of most typical laboratory spectrometers (but not all)

3 4 3 Pressure Broadening

Pressure broadening of a spectral line caused by interactions between the emitter and surrounding particles may be sub-divided into three categories (i) resonance, (ii) Van der Waals and (iii) Stark broadening, depending on whether the interaction with the emitter is caused by (i) the same type of atom (ii) a different type of atom or (iii) a charged particle

The form of pressure broadening that we are most concerned with is Stark broadening, because the majority of particles in a plasma are by definition charged Stark broadening occurs as a result of collisions between the emitter and nearby charged particles There are two components that contribute to the Stark broadened width of a spectral line the first is caused by electron-emitter collisions, the second by ion-emitter collisions

Electron-emitter collisions occur on a very short time-scale, much shorter than both the natural lifetime of the excited state and the time between electron-emitter collisions, electron-emitter collisions make the greatest contribution to the Stark broadening of a spectral line On the other hand, ion-emitter collisions take place over a much longer period, longer than that of the natural lifetime of the state, and longer than the time between ion-emitter collisions Such collisions are therefore known as the quasi-static component of the Stark broadening effect

The half width of a Stark-broadened spectral line is given by [17],

$$\Delta\lambda_{width} = 2w\left(\frac{n_e}{10^{16}}\right) + 3.5A_i\left(\frac{n_e}{10^{16}}\right)^{\frac{1}{4}}\left[1 - 1.2N_D^{-\frac{1}{3}}\right] w\left(\frac{n_e}{10^{16}}\right) \tag{3.5}$$

the first term on the right-hand side of equation 3.5 describes the contribution due to electron-emitter collisions, where w is the electron-impact parameter [18]. The second term on the right-hand side is the ion-emitter contribution to the broadening and is determined by the value of A_i, the ion broadening parameter. In

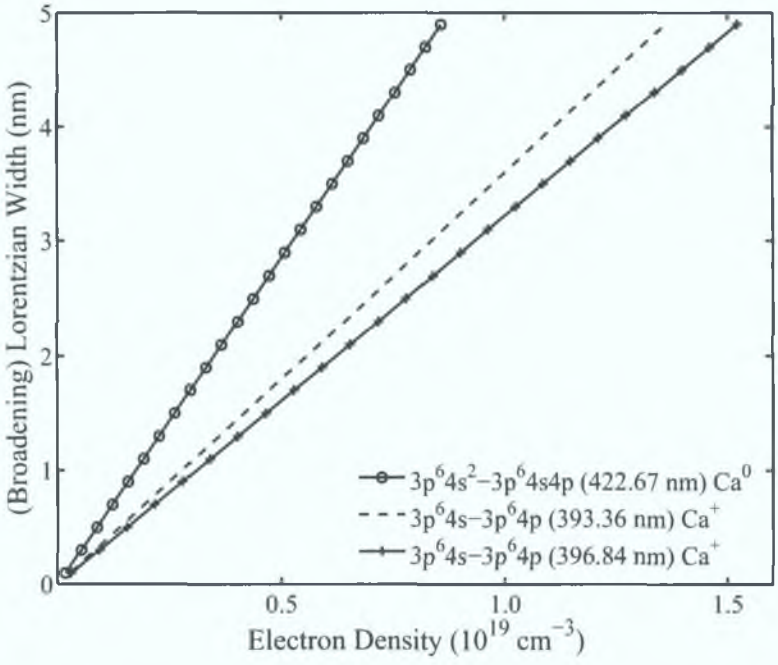

Figure 3.2: Stark widths as a function of n_e for selected calcium transitions, calculated during this work.

a hot dense plasma, emission lines are broadened due to the electron / ion collisions with the emitter but they are also shifted due to the Stark-shift of the energy levels involved in the transitions. Electric fields from nearby particles perturb the energy levels of the emitter, thereby shifting the wavelength of the photons emitted.

$$\Delta\lambda_{shift} = d\left(\frac{n_e}{10^{16}}\right) + 2A_i\left(\frac{n_e}{10^{16}}\right)^{\frac{1}{4}}\left[1 - 1.2N_D^{-\frac{1}{3}}\right] w\left(\frac{n_e}{10^{16}}\right) \tag{3.6}$$

where d is a calculated shift parameter [19] and w and A_i have the same meaning as in equation 3.5. Equations 3.5 and 3.6 can only be applied if the number of particles within the Debye sphere is > 2 and $A(n_e/10^{16}) < 0.5$. Stark broadening of lines in lowly ionised species is dominated by electron collisions. This allows the ion broadening term to be omitted in many cases, but the ion contribution

to the Stark shift plays a more significant role (in this case) Figure 3 2 shows how the width of three calcium spectral lines of interest in this work, change as the electron density is increased Only the electron's contribution has been used in equation 3 5, the electron-impact parameter has been obtained from literature [18]

3 4 4 Doppler Broadening

The observed wavelength of a line emitted by a moving atom is shifted by the Doppler effect, to shorter wavelengths if the emitter is moving towards the observer and to longer wavelengths if moving away The observed wavelength is given by

$$\lambda_{observed} = \lambda_0 \left(1 \pm \frac{v_x}{c}\right) \tag{3 7}$$

where v_x is the non-relativistic velocity of the emitter and λ_0 is the rest wavelength

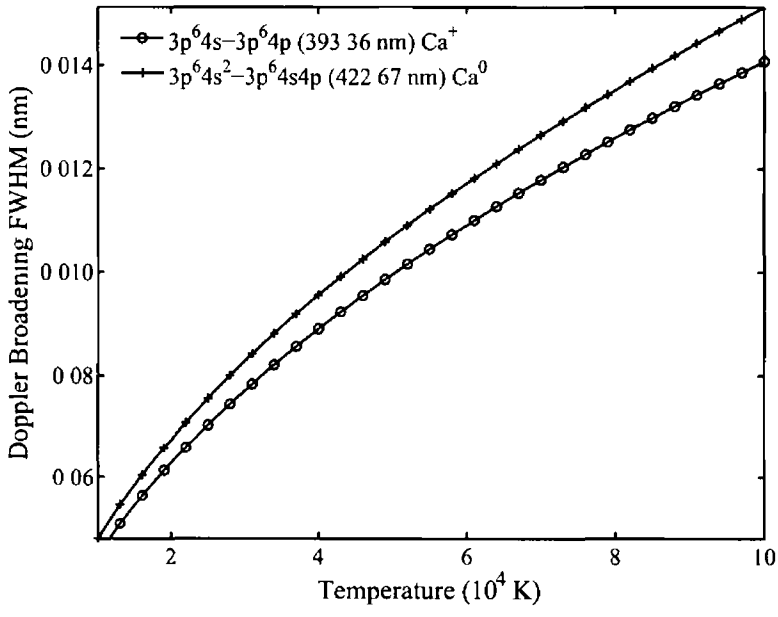

Figure 3 3 Doppler broadening as a function of temperature for selected calcium transitions, calculated during this work

The ± signs indicate whether the emitter is approaching or moving away from the observer The Doppler effect spreads the wavelength distribution observed and is related to the velocity distribution of the emitting particles If we are assuming a state of coronal equilibrium, collisional radiative equilibrium or local thermodynamic equilibrium we must assume a Maxwellian velocity distribution

This leads us to a Gaussian profile $\mathcal{G}(\omega)$ for the spectral line of the form [20]

$$\mathcal{G}(\omega) = \frac{1}{\sqrt{2\pi\sigma}} exp\left[-\frac{1}{2}\left(\frac{\omega-\omega_0}{\sigma}\right)^2\right] \tag{3 8}$$

Doppler broadening contributes more to width of spectral lines at high temperatures and in low-z elements where the velocities of the emitters are usually greater The full width at half maximum (FWHM) of a Gaussian due to Doppler broadening is given by

$$\Delta\lambda_{D_{\frac{1}{2}}} = 7\ 16 \times 10^{-6}\lambda_0\sqrt{\frac{T}{m}} \tag{3 9}$$

where m is the atomic weight, λ_0 is the centre wavelength in nm and T is the temperature (K) of the Maxwellian velocity distribution of the emitters [7]

Figure 3 3 shows how Doppler broadening affects the linewidth of a neutral and singly charged calcium line of interest in this work for a range plausible of temperatures

3 4 5 Gaussian, Lorentzian and Voigt Profiles

As was mentioned in the previous sub-sections a spectral line broadened by natural or Stark broadening leads to a Lorentzian shape, whereas thermal / Doppler broadening leads to a Gaussian profile for the line The result of the combination of the Lorentzian and Gaussian broadening profiles is that most spectral lines are best fitted by a Voigt profile A Voigt profile $\mathcal{V}(\omega)$ is generated by convoluting a Lorentzian with a Gaussian profile [20]

$$\mathcal{V}(\omega) = \mathcal{L}(\omega_0 - \omega) \otimes \mathcal{G}(\omega_0 - \omega) \tag{3 10}$$

where $\mathcal{L}(\omega)$ and $\mathcal{G}(\omega)$ are given by equation 3 4 and 3 8 respectively and $\otimes$ is a convolution operator Voigt profiles are approximately Gaussian around the central frequency ω_0 but tend towards a Lorentzian shape in the wings of the profile

Figure 3 4 shows a plot of the three line profiles, where the area under each profile is the same It can be seen that the Gaussian profile tends to zero with greater rapidity than the other two, the Voigt and Lorentzian have a much broader frequency spread Although Voigt profiles cannot be expressed analytically, analytical approximations have been developed [21] for computational efficiency In order to

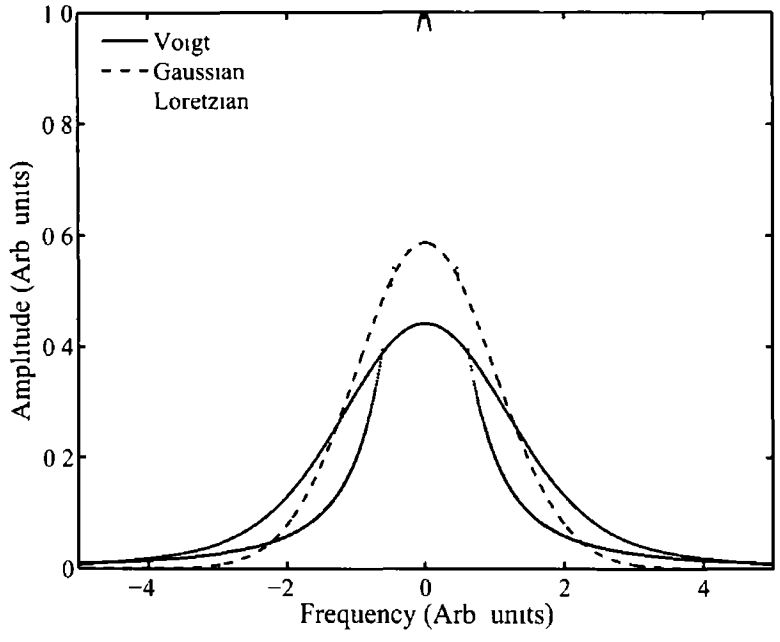

Figure 3 4 Gaussian, Lorentzian and Voigt Profiles, calculated during this work

determine the relative contributions of the two dominant broadening mechanisms (Doppler and Stark) it is necessary to analyse the experimentally determined profile

We will not use these analytic expressions in this work because we strive to resolve the Gaussian and Lorentzian components of the measured Voigt profiles so that we may determine the contributions of various broadening mechanisms

3 4 6 Instrument Function

When analysing recorded spectra, a further broadening contribution must be taken into account When using spectroscopic instruments with resolving powers comparable with the width of the line under examination, it is necessary to consider the effect of the optical system on the width of the observed line [16] Broadening caused by the instrument can take a number of forms (e g trapezoidal, rectangular, Gaussian, etc) and should be experimentally determined before being unfolded from the measured spectra We will discuss the instrumental function further in section 4 10

3 4 7 Electron Densities

There are many spectroscopic methods of determining electron densities in plasmas All of these methods require an approximate knowledge of the plasma temperature Electron densities can be calculated from the interpretation of the following spectroscopic measurements Stark widths or Stark shifts, relative line intensities, and absolute continuum intensities [22]

In this work we will concentrate on using Stark widths and shifts of spectral lines, from which the electron density can be calculated using either equation 3 5 or 3 6 Significant care should be exercised in the application of either technique The main difficulty with using Stark broadening to calculate the electron density is the deconvolution of the profile which is also affected by Doppler and instrument broadening Also when the electron density is relatively low and the temperature high Doppler broadening may dominate the overall width of the spectral line, leading to significant inaccuracies m the calculation of n_e Hence we are confined to applying the technique to plasmas at a relatively early stage in their evolution where the electron density is high and Stark broadening dominates any thermal broadening On the other-hand, using the Stark shift has been shown to be unreliable in cases where the magnitude of the shift is less than the FWHM of the line [23]

3.4 8 Electron Temperatures

There are many methods to determine the electron temperature of a plasma A quick, yet crude way of estimating T_e can be achieved by examining the spectrum of the plasma and noting the maximum ionisation stage of any of the transitions present Bremsstrahlung radiation can also be used to calculate electron temperature A plot of continuum photon energy (in eV) versus the logarithm of the intensity of the continuum should yield a straight line graph, provided there are no bound-bound or bound-free features, the slope of this graph provides a value for the electron temperature [1]

In the XUV or X-ray regions continuum radiation can also be used to calculate the electron temperature, using a method known as the foil absorption technique In this technique the relative intensity of the transmission through two different foils

of known density is calculated The transmission ratio of the foils can be related to the plasma temperature [24]

Another method for determining the electron temperature is to evaluate the widths of Doppler broadened spectral lines As was mentioned in section 3 4 4 the Gaussian half-width of a Doppler broadened line can be related to the electron temperature (equation 3 9) The plasma must be optically thin at the frequencies around the transition and the lines used should be negligibly affected by Stark broadening [7] However, the most common spectroscopic methods for determining electron temperature are based on intensity ratios The three most widely used ratio techniques are line-to-line, from the same ionisation stage, line-to-line from successive ionisation stages, and finally line-to-continuum These three methods will be discussed separately in the following sub-sections It should be mentioned before discussing these techniques that most spectroscopic methods for the determination of plasma tempereratures require approximate knowledge of the electron density It is therefore preferable to use an iterative approach to determining either parameter

Line-to-Line Ratios from the Same Charge State

In an optically thin plasma the integrated intensity of a line (I_{ab}) can be related to the excited state population distribution N_b and the length of the line of sight, l_{sight} by

$$I_{ab} \approx \frac{\hbar\omega_{ba}}{4\pi} A_{ab} N_b l_{sight} \tag{3 11}$$

where A_{ab} is the oscillator strength of the transition and ω_{ba} is the frequency As we are assuming a state of LTE the population distribution of any two states can be related by the Boltzmann factor

$$\frac{N_a}{N_b} = \frac{g_a}{g_b} exp\left(-\frac{E_a - E_b}{k_B T}\right) \tag{3 12}$$

Relating our integrated intensities in the same manner one obtains

$$\frac{I_1}{I_2} \approx \left(\frac{\omega_1 A_1 g_{b1}}{\omega_2 A_2 g_{b2}}\right) exp\left(\frac{E_{b1} - E_{b2}}{k_B T}\right) \tag{3 13}$$

where 1 and 2 refer to two individual spectral lines Measuring the ratio of intensities (I_1/I_2) of two experimentally observed lines, one can calculate a value for the

plasma temperature T_e It is very difficult even under ideal situations to obtain electron temperatures with errors < 10 %, using this method The accuracy of this method can be improved by measuring line ratios along some spectral series The logarithm of the intensity ratios, versus the excitation energies of the upper levels, should produce a straight line The reciprocal of the slope of this line will yield a more accurate value of k_BT

Significant deviation from a straight line plot may signal that the plasma was not in, or sufficiently close to LTE It may also signal errors in the integration of the line profiles caused by underlying continuum emission

Line-to-Line Ratios from Successive Charge Stages

The accuracy of the line-to-line intensity ratio technique can also be improved by increasing the energy difference between the two excited levels

An effective way of maximising this energy difference is to use lines from successive ionisation stages This introduces an additional energy gap E_∞, the ionisation energy, that usually leads to an energy separation of the levels larger than k_BT Instead of relating the integrated intensity ratios using the Boltzmann equation as was done in the previous method, it is now necessary to relate the intensities using the Saha equation The ratio of the integrated line profiles becomes

$$\frac{I'}{I} = \frac{\omega' A' g'}{\sqrt{\pi}\omega A g}(4\pi a_0^3)^{-1}\left(\frac{kT}{E_H}\right)^{\frac{3}{2}} exp\left(-\frac{E' + E_\infty - E - \Delta_\infty}{k_BT}\right) \qquad (3\ 14)$$

E and E' are the excitation energies of the transitions of interest in the successive ion stages, E_∞ is the ionisation energy of the lower of the two ion stages and ΔE_∞ is a high density correction factor that lowers the ionisation energy due to the presence of strong electric fields [22]

Relative Intensities of Line-to-Continuum

At short time delays after the plasma initiation, line intensity measurements are complicated by large background continuum radiation, resulting in significant measurement errors The relative line-to-continuum method uses the ratio of integrated line profiles to that of adjacent or underlying continuum, with the same bandwidth

or wavelength interval

$$\frac{\epsilon_l}{\epsilon_c}(\lambda) = C_r \frac{A_{21}}{U_i} \frac{\lambda_c^2}{\lambda_l T_e} exp\left(\frac{E_\infty - E_2 - \Delta E_\infty}{k_B T_e}\right) \times \left[\xi\left(1 - exp\left(\frac{-hc}{\lambda k_B T_e}\right)\right) + G\left(exp\left(\frac{-hc}{\lambda k_B T_e}\right)\right)\right]^{-1} \quad (3\ 15)$$

where $C_r = 2\,005 \times 10^{-5}$ (sK), ϵ_c is the continuum emission coefficient and ϵ_l integrated emission coefficient over the line profile λ_c and λ_l are the continuum centre wavelength and the centre wavelength of the line E_∞, E_2 and ΔE_∞ are the ionisation potential, upper level energy and the lowering of the ionisation potential in the field of the ions U_i is the partition function of the ion of interest G is the free-free Gaunt factor and ξ is the free-bound continuum correction factor [25, 26]

The relative line-to-continuum technique only yields accurate results when the intensity of the continuum and the line emission are comparable This gives the technique a range of applicability from approximately 30-100 ns It becomes a complementary technique to the other relative intensity techniques that have already been mentioned that require well defined line profiles for accurate results

Extracting temperatures from equation 3 15 is less straight forward than the other techniques The partition function U_i has a non-negligible temperature dependence and would be more accurately denoted by $U_i(T)$, and ξ the continuum correction factor is not known for most situations and must be determined by comparing the line-to-continuum ratios of two lines, this gives two equations in two unknowns ξ and T_e

3.5 Summary

In this chapter we have discussed all of the diagnostic methods used during the course of this work A general discussion on plasma diagnostics was followed by the theory employed by the VUV photoabsorption imaging facility to extract useful plasma parameters Spectral line profiles and the most important mechanisms involved in their broadening have been discussed Methods used to determine electron density and temperature from spectroscopic measurements were outlined The underlying assumptions and limitations of these techniques has also been mentioned

In the next chapter we will discuss in detail the experimental systems used to record VUV photoabsorption images, spectrally filtered time-resolved emission images and time and space-resolved spectroscopic images of single and colliding laser-produced plasmas The capabilities and limitations of these experimental systems will be presented

Bibliography

[1] I H Hutchinson *Principles of plasma diagnostics* Cambridge University Press, Cambridgeshire, 1987

[2] Yu Quan-Zhi, Zhang Jie, Li Yu-Tong, Zheng Jun, Yan Fei, Lu Xin, Wang Zhe-Bin, Zheng Jian, Yu Chang-Xuan, Jiang Xiao-Hua, Li Wen-Hong, Liu Shen-Ye, and Zheng Zhi-Jian Thomson scattering process in laser-produced plasmas *Chinese Physics Letters*, 22 1717–1720, 2005

[3] S H Glenzer, C A Back, K G Estabrook, and B J MacGowan Thomson scattering in the corona of laser-produced gold plasmas In *Review of Scientific Instruments*, volume 68, pages 668–671 AIP, 1997

[4] H Schittenhelm, G Callies, P Berger, and H Hugel Two-wavelength interferometry on excimer laser induced vapour plasma plumes during the laser pulse *Applied Surface Science*, 127-129 922–927, 1998

[5] P van Kampen, Ch Gerth, M Martins, P K Carroll, J Hirsch, E T Kennedy, O Meighan, J -P Mosnier, P Zimmermann, and J T Costello Photoabsorption and photoion spectroscopy of atomic uranium in the region of $6p$ and $5d$ excitations *Phys Rev A*, 61 062706, 2000

[6] P Yeates *A spectroscopic and diagnostic study of laser plasma generation and evolution under multi-variable target conditioning* PhD thesis, School of Physical Sciences, Dublin City University, 2004

[7] W Lochte-Holtgreven *Plasma diagnostics* AIP Press, New York, 1995

[8] C T Chang, M Hashmi, and H C Pant Study of a laser-produced plasma by langmuir probes *Plasma Physics*, 19 1129–1138, 1977

[9] J S Hirsch, E T Kennedy, A Neogi, and J T Costello Vacuum-ultraviolet photoabsorption imaging system for laser plasma plume diagnostics *Review of Scientific Instruments*, 74 2992–2998, 2003

[10] T P Williamson, G W Martin, A H El-Astal, A Al-Khateeb, I Weaver, D Riley, M J Lamb, T Morrow, and C L S Lewis An investigation of neutral and ion number densities within laser-produced titanium plasmas in vacuum and

ambient environments *Applied Physics A Materials Science & Processing*, 69 S859–S863, 1999

[11] J T Costello, E T Kennedy, B F Sonntag, and C L Cromer Xuv photoabsorption of laser-generated w and pt vapours *Journal of Physics B Atomic, Molecular and Optical Physics*, 24 5063–5069, 1991

[12] P Yeates, E T Kennedy, J-P Mosnier, P van Kampen, M W D Mansfield, J Pedregosa-Gutierrez, J B Greenwood, Ph V Demekhin, I D Petrov, B M Lagutin, V L Sukhorukov, L A Demekhina, and J T Costello Theoretical and experimental study of the extreme ultraviolet photoabsorption spectrum of triply ionized yttrium *Journal of Physics B Atomic, Molecular and Optical Physics*, 37(23) 4663–4680, 2004

[13] J S Hirsch, O Meighan, J-P Mosnier, P van Kampen, W W Whitty, and J T Costello Vacuum-ultraviolet resonant photoabsorption imaging of laser produced plasmas *Journal of Applied Physics*, 88 4953–4960, 2000

[14] A Corney *Atomic and laser spectroscopy* Clarendon Press, New York, 1977

[15] K Muraoka and M Maeda *Laser-aided diagnostics of plasmas and gases* Institute of Physics Publishing, 2001

[16] J F Ready *Effects of high-power laser radiation* Academic Press, Florida, 1971

[17] M A Hafez, M A Khedr, F F Elaksher, and Y E Gamal Characteristics of Cu plasma produced by a laser interaction with a solid target *Pasma Sources Science And Technology*, 12 185–198, 2003

[18] N Konjevic and W L Wiese Experimental stark widths and shifts for spectral lines of neutral and ionized atoms *Journal of Physical Chemistry and Reference Data*, 19 1307, 1990

[19] T McCormack and G O'Sullivan Spatially resolved spectra of resonantly pumped laser produced plasmas of lithium *Review of Scientific Instruments*, 70 2674–2680, 1999

[20] D Salzmann *Atomic Physics in Hot Plasmas* Oxford University Press, New

York, 1998

[21] A B McLean, C E J Mitchell, and D M Swanston Implementation of an efficient analytical approximation to the Voigt function for photoemission lineshape analysis *Journal of Electron Spectroscopy and Related Phenomena*, 69 125–132, 1994

[22] H R Griem *Principles of plasma spectroscopy* Cambridge monographs on plasma physics Cambridge University Press, New York, 1997

[23] R H Huddlestone and S L Leonard *Plasma diagnostic techniques* Academic Press, New York, 1965

[24] T P Donaldson Theory of foil-absorption techniques for plasma x-ray continuum measurements *Plasma Physics*, 20 1279–1289, 1978

[25] H C Liu, X L Mao, J H Yoo, and R E Russo Early phase laser induced plasma diagnostics and mass removal during single-pulse laser ablation of silicon *Spectrochimica Acta Part B Atomic Spectroscopy*, 54 1607–1624, 1999

[26] Xianzhong Zeng, Samuel S Mao, Chunyi Liu, Xianglei Mao, Ralph Greif, and Richard E Russo Laser-induced plasmas in micromachined fused silica cavities *Applied Physics Letters*, 83 240–242, 2003

CHAPTER 4

EXPERIMENTAL SYSTEMS

4.1 Introduction

The transient nature of laser-produced plasmas, with steep density and temperature gradients and high expansion velocities make them challenging entities to study in the laboratory In order to track the evolution of laser-produced plasmas, significant demands are placed on the experimental equipment, high temporal, spatial and spectral resolution is required, especially during early phase (< 100 ns) expansion dynamics

In this chapter we will present and discuss the operation of the experimental systems used in this work to characterise laser-produced plasmas We will begin by discussing the three laser systems used, followed by the Vacuum ultraviolet Photoabsorption Imaging Facility (VPIF) and the emission imaging and imaging spectroscopy systems

4.2 Surelite Laser Systems

Two Continuum Surelite Q-switched laser systems were used during the course of this work (series I and III) The lasing medium in both lasers is a rod of crystalline yttrium aluminium garnet ($Y_2Al_{12}O_{12}$) that has been doped with neodymium ions (Nd^{3+}), leading to the abbreviation Nd YAG

Figure 4 1 shows a schematic diagram of the Surelite I laser system The particular series III system used by the VPIF does not include the frequency doubling crystals shown in figure 4 1, therefore it is limited to operation at 1064nm

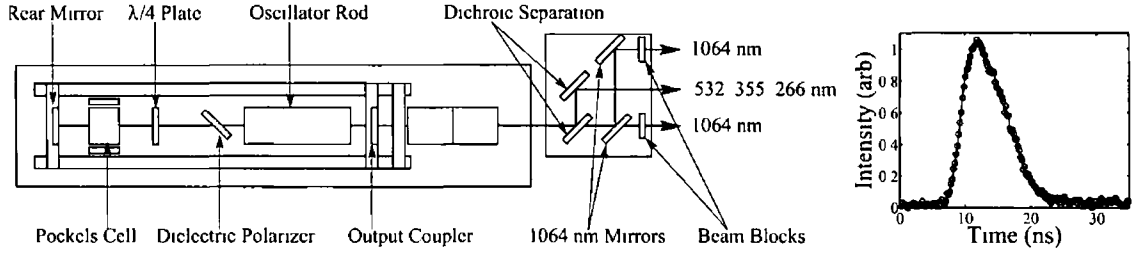

(a) Schematic of laser layout (b) Diode Trace

Figure 4 1 Schematic diagram of the Surelite laser system and a fast diode trace of the output pulse recorded on a Tektronix (TDS2400) oscilloscope

The flashlamp and Pockels cell of the Surelite lasers may be internally or externally triggered, producing a shot-to-shot jitter of < 10 ns or < 1 ns respectively, both lasers have been externally triggered using delay generators during this work The

Table 4 1 Specifications of the Surelite laser systems

	Surelite I	Surelite III
Lasing Medium	Nd YAG	Nd YAG
Wavelength	1064, 532, 355, 266 nm	1064 nm
Energy	450, 200, 100, 60 mJ	800 mJ
Pulse length	6 ns (FWHM)	6 ns (FWHM)
Repetition rate	10 Hz	10 Hz
Trigger jitter	< 1 ns	< 1 ns

series I laser system could be operated at 1064, 532, 355 and 266 nm producing up to 450, 200, 100 and 60 mJ respectively in 6ns (at 1064 nm) The pulse duration was 1 to 2 ns shorter when using the harmonics Figure 4 1 (b) shows a typical diode trace from the Surelite I system recorded using a fast diode and a Tektronix (TDS2400) oscilloscope The FWHM of a Gaussian fit to the diode trace is ≈ 6 ns

The series III Surelite, produces 800 mJ in 6 ns at a repetition rate of 10 Hz, operating at its fundamental wavelength 1064 nm The output from both lasers is linearly polarised with a Gaussian intensity profile (in the far field, > 1 m) while

the beam divergence of both lasers is 0 6 mrad The important parameters relating to both lasers have been summarised in table 4 1

4.3 Spectron Laser System

The Spectron SL-404 is a Q-switched Nd YAG laser system, producing 300 mJ in $\sim$ 16 ns, operating at 10 Hz Figure 4 2 (a) shows a schematic of the general optical layout of the Spectron SL range Figure 4 2 (b) shows a fast diode trace of

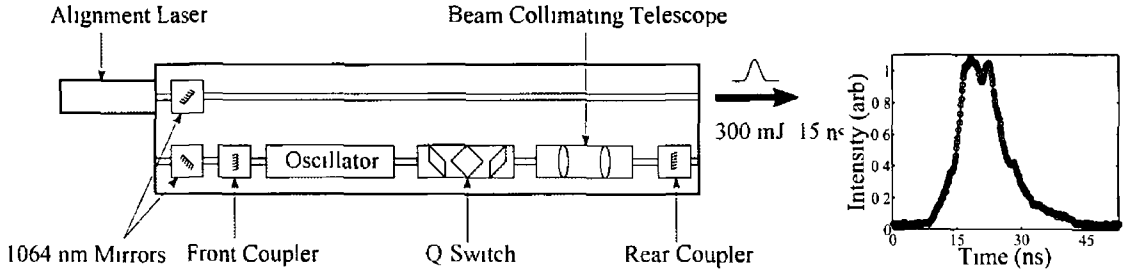

(a) Schematic of laser layout (b) Diode Trace

Figure 4 2 Schematic of the Spectron SL-404 laser system [1]

the SL-404 recorded on a Tektronix oscilloscope The FWHM of a Gaussian fit to the (somewhat asymmetric) diode trace is $\sim$ 16 ns

The SL-404 is an oscillator only system that also produces a linearly polarised output with a Gaussian intensity distribution The output beam divergence is between 0 8 and 2 mrad The flashlamps and Pockels cell can be externally triggered producing a shot-to-shot jitter of $<$ 1 ns Table 4 2 summarises the important parameters relating to the SL-404

Table 4 2 Spectron SL-400 specifications

Lasing Medium	Nd YAG
Wavelength	1064 nm
Energy	300 mJ
Pulse length	16 ns (FWHM)
Repetition rate	10 Hz
Trigger jitter	$<$ 1 ns

4.4 VUV Photoabsorption Imaging Facility

There are five main components to the vacuum ultraviolet photoabsorption imaging facility Each of these components will be discussed individually in the following sub-sections, they are

(i) The source plasma

(ii) The focussing / collimating toroidal mirrors

(iii) The monochromator

(iv) The sample plasma

(v) The CCD camera / optical filtering

A schematic diagram of the VPIF is shown in figure 4 3 and a photograph of the system is shown in figure 4 4 The entire system is evacuated to a minimum pressure of 10^{-5} mbar to avoid strong attenuation due to the high absorbance of molecular oxygen and nitrogen below 200 nm [2] There are five vacuum systems

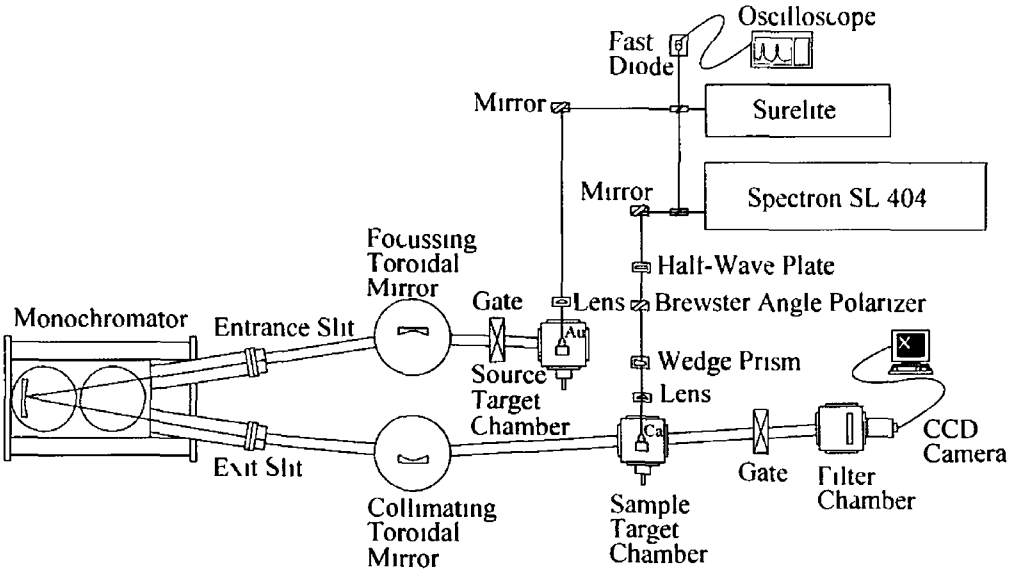

Figure 4 3 The Vacuum Ultraviolet Photoabsorption Imaging Facility (VPIF)

on the VPIF that can be independently controlled and monitored Two gate valves and a valve on the entrance and exit slit of the monochromator are used to isolate these sections as shown in figure 4 3

The first gate valve is located between the source target chamber and the focussing toroidal mirror chamber (see figure 4 3) Closing that valve allows us to isolate the target chamber for routine activities such as window and target replacement The target chamber is evacuated using a Leybold PT-50 turbomolecular pump (50 litres/sec) and is backed by a Leybold TRIVAC-E rotary vane pump The pressure in the chamber is monitored using a Leybold THERMOVAC gauge for pressures in the range 10^3-10^{-3} mbar A Leybold PENNINGVAC gauge was used for pressures below 10^{-2} mbar The next vacuum section, the VUV focussing

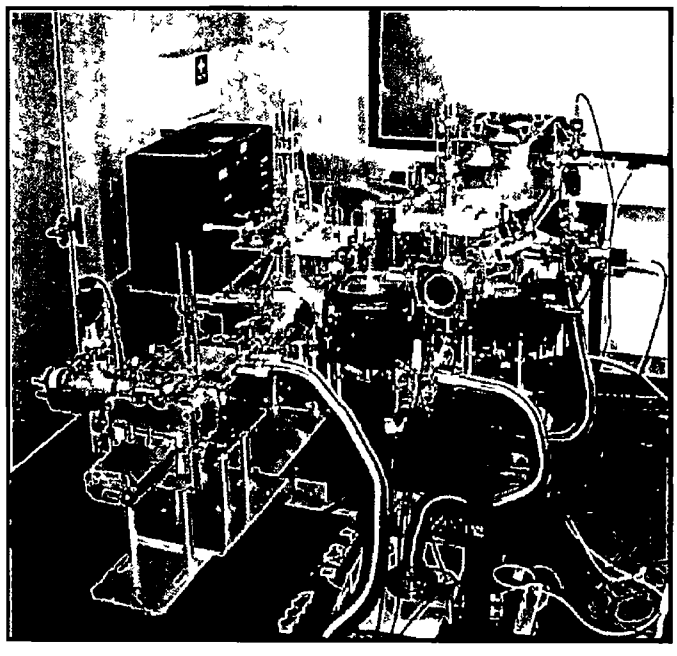

Figure 4 4 Photograph of the Vacuum Ultraviolet Photoabsorption Imaging Facility (VPIF) [3]

mirror chamber, located between the source target chamber and the entrance slit of the monochromator is similarly equipped and also uses a rotary backed PT-50 with the same model gauges The monochromator is evacuated using a Leybold PT-360 turbo with a 360 litres/sec flow rate, backed by a Leybold TRIVAC-B rotary

The final two independently evacuated sections (collimating mirror and sample chambers) are separated by a gate valve located between the sample target chamber and the filter chamber This permits easy access to the sample chamber on a regular basis while keeping the delicate filter and CCD camera under vacuum Both sections are evacuated and monitored using similar pumping rigs and gauges as the source target chamber

4 4 1 Continuum Source

The back-lighting source used in this dual-laser plasma experiment is produced by focusing the series III Continuum Surelite Nd YAG laser onto a solid gold target This produces a virtually line-free continuum in the VUV spectral range High-Z materials such as gold have been used for many years as VUV continuum sources for DLP absorption experiments [4]

The VUV spectrum of gold is shown in figure 4 5 in the spectral range extending from 30 to 100 nm This spectrum was taken using the same model monochromator as employed with the VPIF (Acton Research VM-521) but operating in spectrometer mode, i e, without an exit slit and with CCD readout In the initial VPIF design tungsten was used as the VUV source plasma because it has been extensively studied [5, 6] However, tungsten plasma debris from the source began coating the gold-coated toroidal mirrors, severely reducing their reflectivity in the VUV Moving to a gold source target eliminated this problem

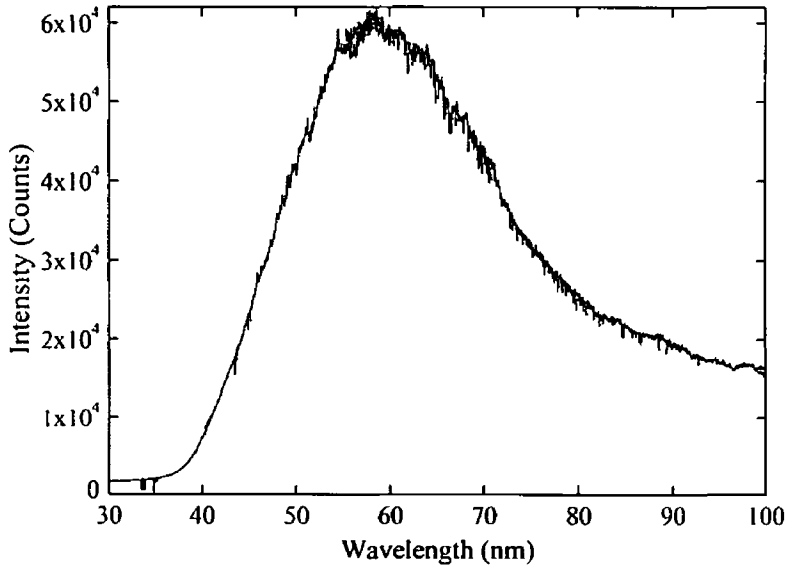

Figure 4 5 Time-integrated vacuum ultraviolet emission spectrum of gold (recorded by E O'Leary)

The time-resolution of the VPIF is dictated by the duration of the VUV emission from the source This duration is in turn determined by the length of the laser pulse generating the plasma as well as other factors such as the laser irradiance and the wavelength under observation Mosnier *et al* [7] observed XUV (10 nm) continuum emission from a series of high-Z targets (including Au), with pulse

durations of $\sim$ 20 ns FWHM using a 15 ns, 0 5 J Nd YAG laser [1] The shorter the wavelength of the emission observed the shorter the pulse duration In the X-ray region the emission duration at medium to high laser irradiances, may be some fraction of the laser pulse duration In the XUV, the emission duration is comparable to the laser pulse-length, as was observed by Mosnier *et al* In the VUV the emission duration is typically some multiple of the laser pulse length In the case of the VPIF operating at 35 nm, using a 6 ns pulse, the VUV emission duration was measured by Hirsch *et al* [8] to be $\sim$ 30 ns The main factor underlying the

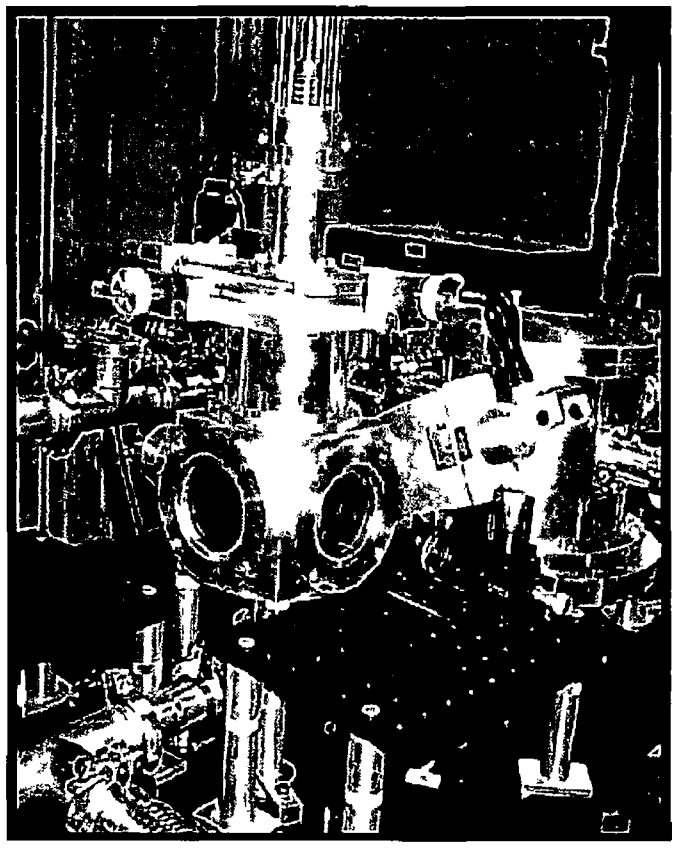

Figure 4 6 Photograph of the "source" target chamber [3]

above trend is the plasma temperature X-ray emission is observed only when the plasma temperature is highest, usually just after the peak of the laser pulse and only remains sufficiently high for a short time after that hence the X-ray emission is shortened to a fraction of the laser pulse duration At lower photon energies, the required plasma temperature is lower and stays above the minimum threshold for longer, hence the emission pulse duration increases on moving from X-ray $\rightarrow$ XUV $\rightarrow$ VUV $\rightarrow$ UV/VIS The temporal resolution of the VPIF could be improved to sub-nanosecond levels by using a laser yielding pulses of $\leq$ 0 2 ns such as the

EKSPLA 312P system now available in the laboratory

Figure 4 6 shows a photograph of the source target chamber, where the source plasma is generated The focussed Surelite laser beam produces an on target irradiance of $\sim 2 \times 10^{11}$ Wcm^{-2} For incompletely ionised targets and small radiation losses the initial plasma temperature can be related to the incident laser flux using the $3/5^{\text{ths}}$ power law given by Colombant and Tonon [10] This assumes a state of collisional radiative equilibrium as discussed in section 2 5 3, which is usually valid during the laser pulse [10] and is given by

$$T_e = 5\,2 \times 10^{-6} A_n^{1/5} [\lambda^2 \phi]^{3/5} \tag{4 1}$$

where A_n is the atomic number, λ is the laser wavelength (in μm) and ϕ is the on target irradiance (in Wcm^{-2}) From this we estimate the initial plasma temperature to be $\sim$ 80 eV Colombant and Tonon [10] also provide an expression for the average charge stage z, present in the plasma as a function of electron temperature T_e and the atomic weight Z This approximation is given in equation 4 2 but is only valid for a temperature $>$ 30 eV [10]

$$z \approx \frac{2}{3}[A_n T_e]^{1/3} \tag{4 2}$$

Figure 4 7 shows a plot of the average charge z vs T_e the electron temperature

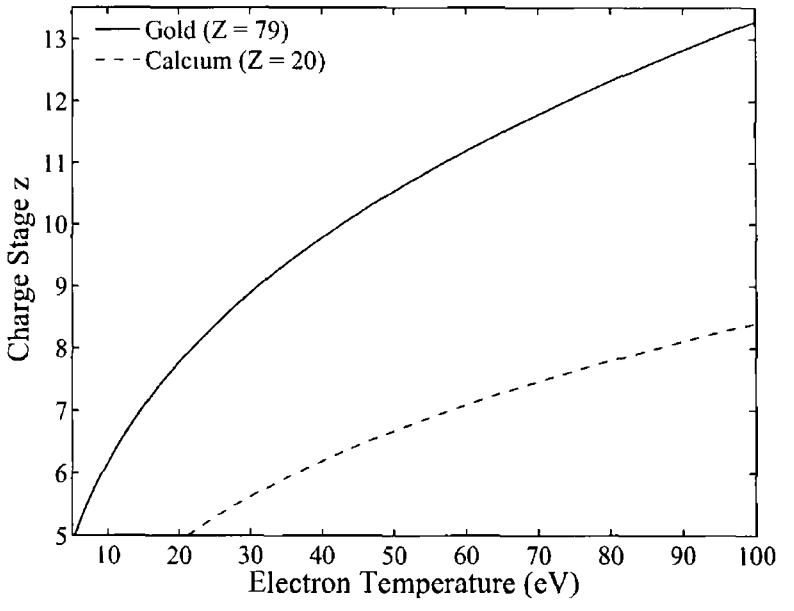

Figure 4 7 Average ion stage as a function of temperature for a Au plasma generated with an on target irradiance of 2×10^{11} Wcm^2, calculated during this work

for the source gold plasma Figure 4 7 also shows the average ion stage for Ca as a function of T_e to demonstrate how the atomic number A_n affects the result Figure 4 7 indicates that the dominant ionisation stages within the source plasma during the first 30 ns is between 10 to 15 times ionised

4 4 2 Focusing Toroidal Mirror

Light emanating from the gold (source) plasma is collected and focused onto the entrance slit of a monochromator using a specially designed gold-coated toroidal mirror The angle of incidence of the toroidal mirror is 85 degrees in order to maximise the reflectivity of gold in the VUV region and is located 400 mm from the source plasma The grazing incidence reflectivity of gold in the VUV is shown in figure 4 8 It can be seen that the reflectivity of gold is high (between 70 and 80%) at grazing incidence and low (between 5 and 40%) at normal incidence However

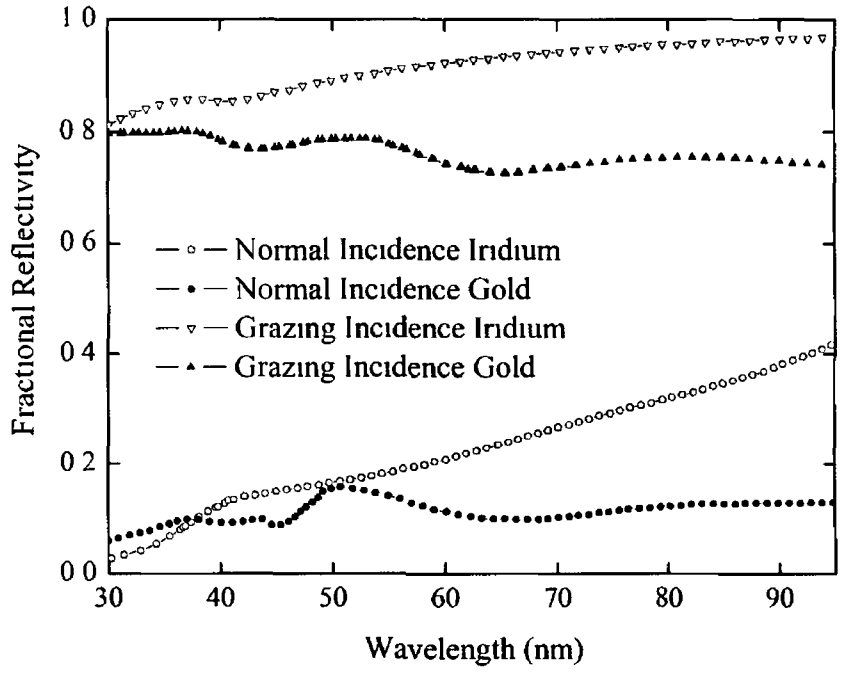

Figure 4 8 Grazing and normal incidence reflectivity of gold and iridium (Calculated using the "Multi-Ray" ray tracing code from the University of Padua, Italy [3])

the benefits in terms of increased light collection efficiency provided by operating at grazing incidence must be balanced against increased optical aberrations produced by operating at shallow angles of incidence The tangential and sagittal radii of the toroidal mirror are 2303 mm and 69 mm respectively and it images the plasma

source onto the entrance slit of the monochromator, the toroidal mirror radii were specially chosen with the aid of ray tracing codes in order to minimise aberrations caused by working at grazing incidence

4 4 3 Monochromator

The monochromator used in this system is an Acton Research VM-521 one metre near normal incidence configuration, operated at a pressure of typically 10^{-7} mBar The monochromator is equipped with a 1200 grooves / mm spherical concave, iridium coated Bausch and Lomb grating and covers the spectral range from 30 to 325 nm, the diffraction grating is blazed at an angle of 2 75°, resulting in a maximum conversion efficiency of incident radiation into first order light at 80 nm [3]

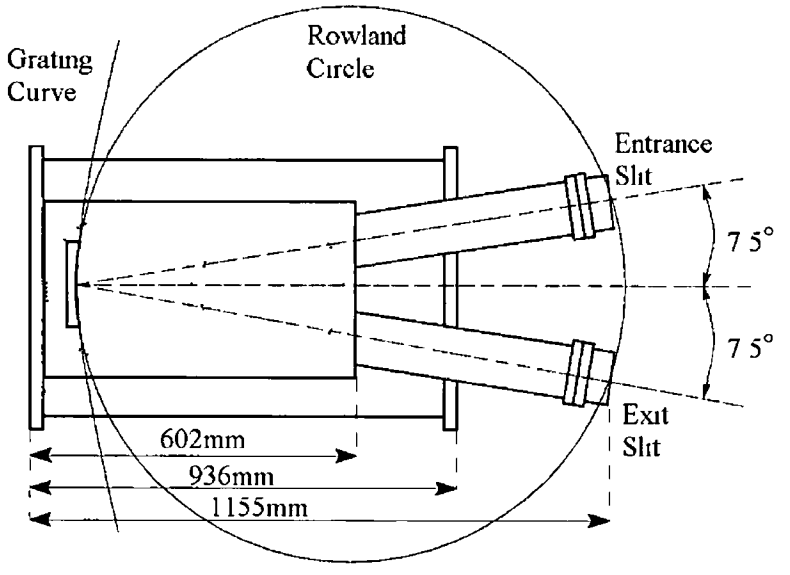

Figure 4 9 Acton Research VM-521 VUV Monochromator [11]

The monochromator operates on a Rowland circle configuration, meaning that the entrance slit, exit slit and diffraction grating all lie on a circle whose diameter equals the radius of curvature of the concave grating

The spherical concave diffraction grating combines the dispersive properties of a ruled grating surface with the focusing capability of a concave mirror [11] This has the effect of reducing the number of reflecting surfaces required in the spectrometer

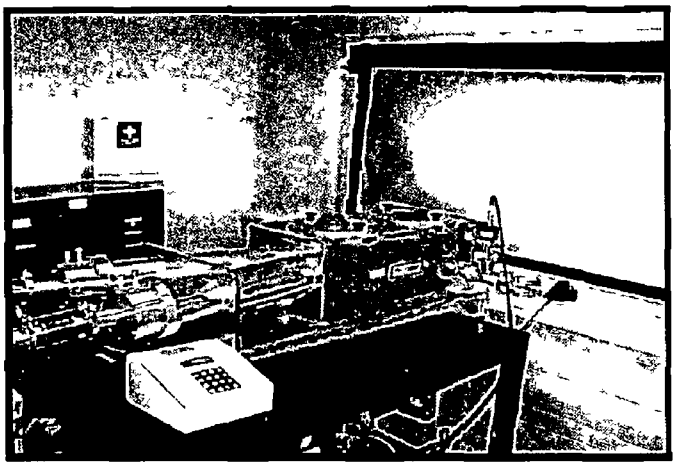

Figure 4 10 Photograph of the Acton Research 1-metre normal incidence monochromator [3]

which is important in the VUV where the normal incidence reflectivity of metals and dielectric coatings is very low, leading to large flux losses [12] The normal incidence reflectivity of the iridium coated grating used is very low for wavelengths shorter than $\sim$ 30 nm This leaves a region stretching from $\sim$ 35 to 70 nm that is free from second order light [1] The reflection efficiency of the grating tails off gradually at the long wavelength end of its range Figure 4 8 shows the normal and grazing incidence reflectivities of iridium in the VUV, calculated using the "Multi-Ray" ray tracing code from the University of Padua, Italy [3] Figure 4 9 shows a schematic of the Acton Research monochromator used including the Rowland circle and figure 4 10 shows a photograph of the monochromator The bandwidth $\Delta\lambda$ of the quasi-monochromatic radiation exiting the monochromator is determined by the width of the entrance and exit slits A bandwidth of $\sim$ 0 1 nm is achieved

Table 4 3 Acton Research (VM-502) monochromator specifications

Operating Range	30 – 325 nm
Focal Length	1000 mm
Configuration	Near normal incidence (7 5°)
Dispersion	0 83 nm/mm
Grating	1200 lines/mm, concave iridium coated
Aperture Ratio	F/10 4 (tangential plane)
	F/17 5 (sagittal plane)

for 100 μm wide slits at a wavelength of 50 nm [3] Table 4 3 summarises the important monochromator specifications

4 4 4 Collimating Toroidal Mirror

A second toroidal mirror is located 200 mm from the exit slit of the monochromator The function of this mirror is to collimate the monochromatised radiation emanating from the exit slit, so that a parallel beam with an approximately square (4×4 mm) cross section is created The tangential radius of the mirror is 2303 mm and the sagittal radius is 66 mm It is operated at an incident angle of 80 degrees Beyond the collimating mirror, a pulsed tunable (30 - 100 nm) approximately

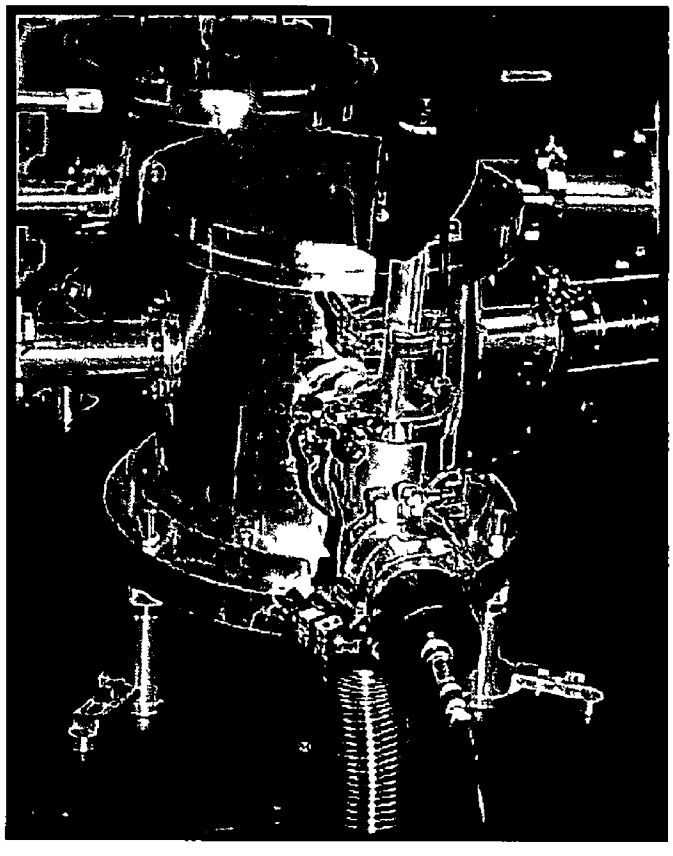

Figure 4 11 Photograph of the toroidal mirror chambers [3]

square VUV beam is available to probe both static (e g , thin films) and dynamic (e g , expanding plasma plumes) samples Figure 4 11 shows a photograph of both toroidal mirror chambers The next stage of the system is the generation of the sample plasma

4 4 5 Sample Plasma

The sample plasma is generated by focussing the Spectron SL-404 laser onto a solid Ca (metal) block The laser light is focused onto the sample using a cylindrical lens that generates a line plasma of approximately 8 mm in length times 0 2 mm in height The expansion of the plasma is set perpendicular to the propagation direction of the collimated VUV beam Increasing the length of the sample plasma increases its opacity along the line of sight of the VUV probe beam and hence increases the amount of VUV radiation that is absorbed by the sample The laser energy on the target was varied using a combination of a Brewster angle polariser and a half-wave plate The Brewster angle polariser and half-wave plate were mounted on rotational stages and can be accurately adjusted to give a desired energy with the same state of polarisation The ability to vary the on-target

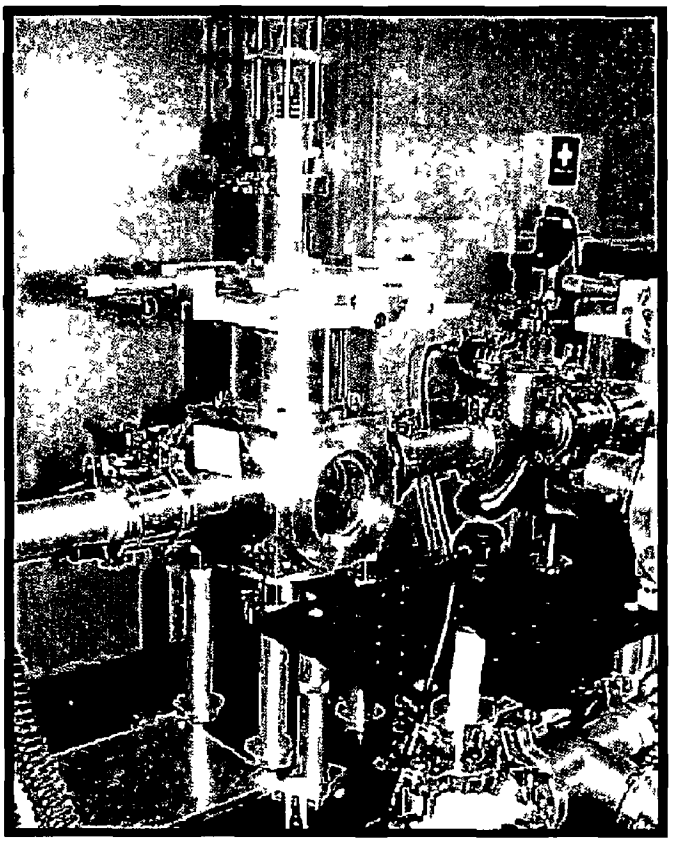

Figure 4 12 Photograph of the "sample" target chamber and beam line [3]

irradiance is very important so that absorption may be maximised by generating a large plasma of sufficient density, while keeping the sample plasma emission in the VUV as low as possible, as this radiation can fall directly onto the CCD

Figure 4 12 shows a photograph of the sample target chamber

The expansion dynamics of plasmas generated using three sample target geometries were studied during the course of this work The first and most straight forward concerned a single line or point plasma generated on a flat surface The second geometry involved the generation of two point or line plasmas next to each other on a flat surface This was achieved by splitting a laser beam in two using a wedge prism and subsequently focussing the beams onto the target surface, as shown in figure 4 13 (a) By varying the angle of the wedge prism we could vary the separation between the two plasmas, hence changing the conditions and times at which interaction occurs The third configuration used involved the generation of

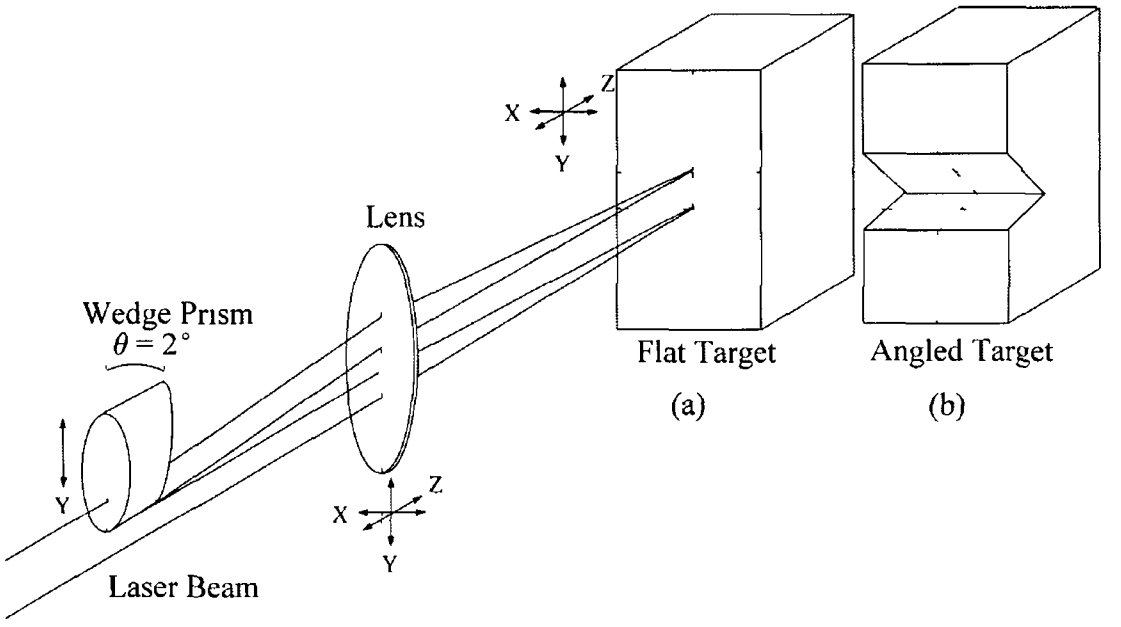

Figure 4 13 Schematic diagram of the wedge prism used to split the incident laser beam as well as the two colliding plasma target geometries

line and point plasmas on a 90° wedge obtained by making precise cuts at 45° to the target surface normal (figure 4 13 (b)) This geometry increases the intensity of the plasma interaction because the plasmas are directed along a collinear path and collide with a larger component of their faster, forward expansion velocity

4.4 6 Optical filter and CCD

Radiation that is transmitted through (and passes by) the sample plasma falls on a CCD where the beam footprint is recorded Sample (or front plasma) emission

is significantly reduced by inserting a knife edge between the plasma core and the CCD thereby shielding the detector from the brightest part of the plasma Residual visible / UV radiation is rejected by a thin (200 μm thick) Al metal filter placed in front of the CCD The knife edge is located in the sample target chamber and may be positioned precisely using a micrometer driven translational stage

The self-supported 5 × 5 mm, aluminium filter acts as a VUV bandpass filter, which blocks all radiation below ~ 18 nm (XUV / soft X-rays) and above ~ 80 nm (Deep UV to IR), as is shown in figure 4 14 The aluminum filter serves a second purpose in that it protects the CCD camera from debris generated by the sample plasma Directly behind the filter chamber the VUV footprint or 'shadowgrams"

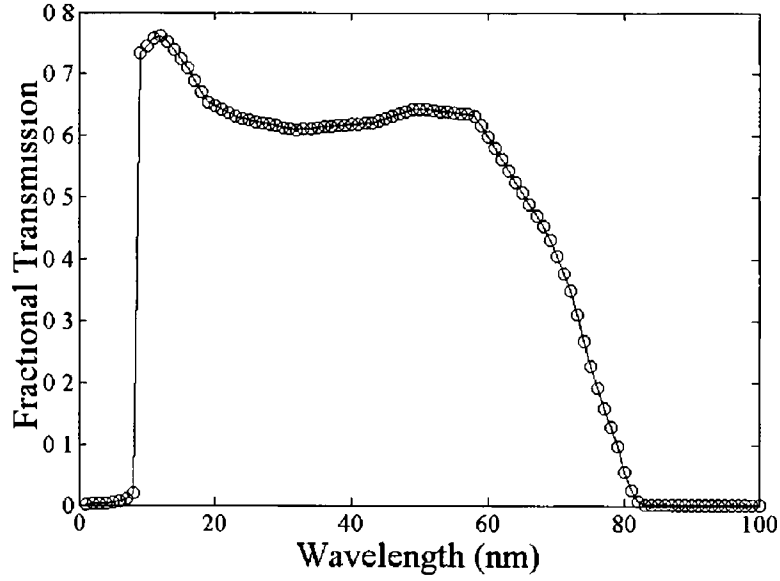

Figure 4 14 Transmission curve of a 0 2 μm Al filter in the VUV (Source data Centre for X-ray Optics website, http //www cxro lbl gov/optical_constants/)

are recorded on a 2048 × 512 pixel back-thinned Andor Technology DU440 CCD camera with a pixel size of 13 × 13 μm, providing a total imaging area of 27 6 × 6 9 mm The CCD pixels are generally binned 6 × 6 in order to improve signal to noise ratio (SNR), resulting in 78 μm square "superpixels"

The quantum efficiency Q_E of the CCD chip has been measured by the CCD manufacturer for our specific detector to be 22% at 50 nm operating with a gain of 1 4 From these values we may calculate the number of counts N_C per detected photon

$$N_C = Q_E \frac{E_{photon}}{3\,65 \times Gain} \tag{4 3}$$

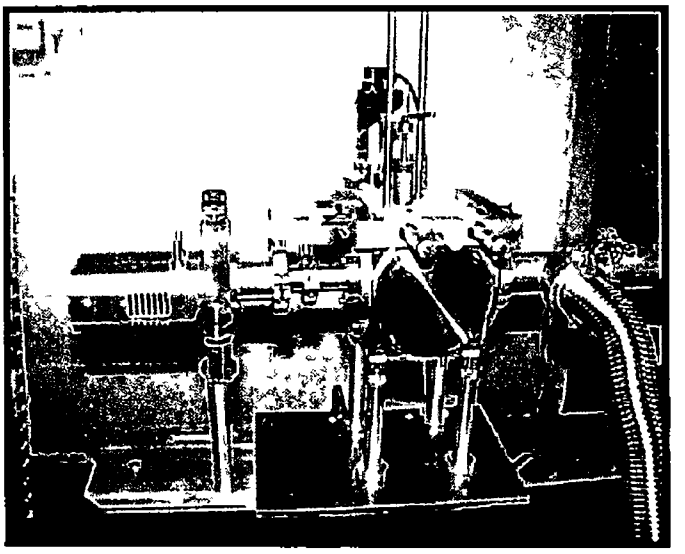

Figure 4 15 Photograph of the "Al filter" chamber and back illuminated Andor technology CCD [3]

where E_{photon} is the energy of the incident photon (in eV) [3, private communication (2002)] An image is recorded by averaging frames from ten laser shots, but this process will be discussed in more detail later, in section 5 2 Figure 4 15 shows a photograph of the filter chamber and the back illuminated Andor technology CCD camera

4 4 7 VPIF Synchronisation

The Spectron SL-404 and the Continuum lasers were synchronised using two Stanford DG-535 delay generators controlled by the Andor Technology CCD detector software The first delay generator constituted the master oscillator, it generated a reference pulse T_0 at 10 Hz This pulse was used to trigger the flashlamps of both lasers A 10 μs wide TTL pulse, was used to trigger the flashlamps of the Surelite laser while the flashlamp of the Spectron laser required amplification to 15 V, 10 μs wide pulses for reliable triggering The flashlamps of both lasers were continuously triggered at 10 Hz to stabilise the temperature of the laser rods, as recommended by the respective manufacturers

The T_0 reference pulse from the first generator was used to seed the second delay generator using a short (0 3 m) BNC cable ensuring time synchronisation (to < 1 ns) Two output pulses from the second generator were delayed by 180 μs, the

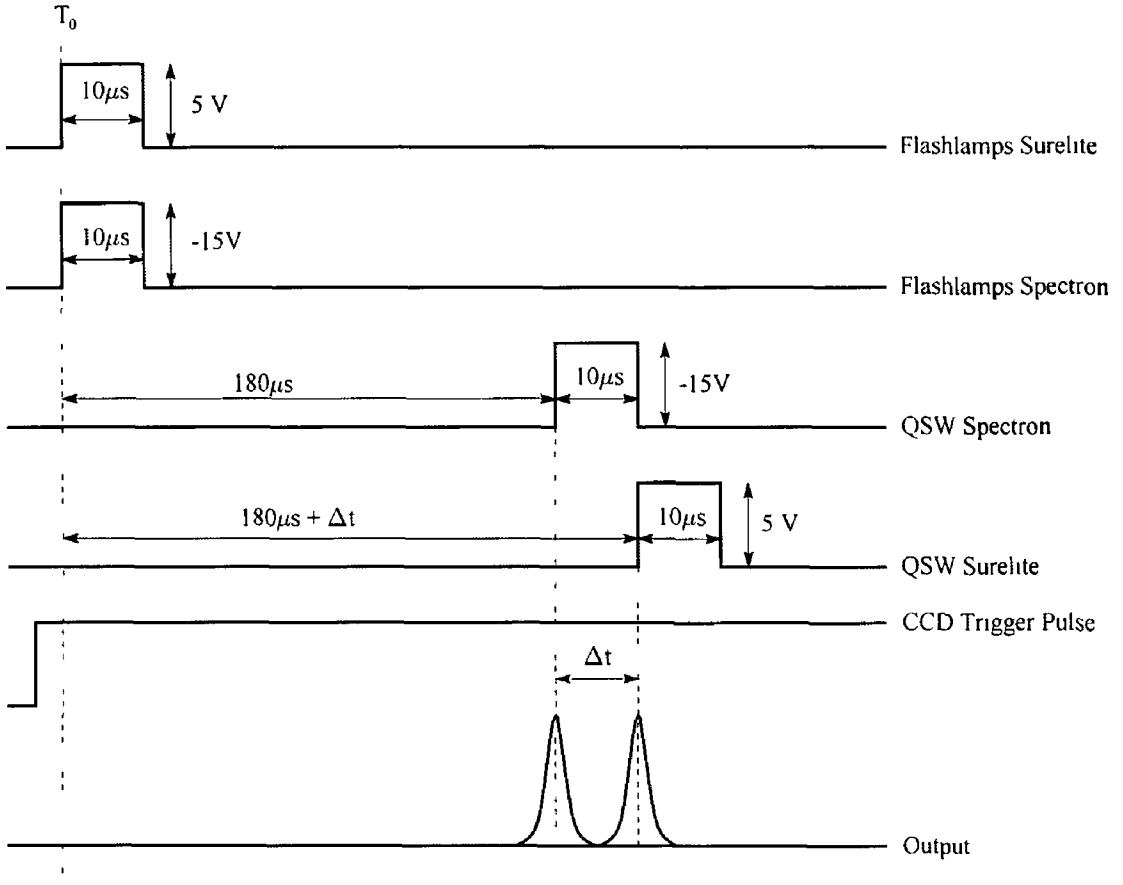

Figure 4 16 Timing diagram used to synchronise the source and sample laser systems

optimum delay between the laser flashlamp and Pockels cell trigger, and connected to the respective Pockels cells of the two lasers The output pulse connected to the SL-404 Pockels cell trigger had to be amplified to 15 V A variable delay was inserted between the two lasers, with a jitter of < 1 ns, providing time delays between 0 ns (overlapped pulses) and a few microseconds These two outputs were connected to the Pockels cells of the lasers via an "AND" gate controlled by the CCD camera software When the CCD camera exposure begins, a pulse relayed by a trigger box connected to the PC is sent to the "AND" gate The "AND" gate is then opened for the duration of the exposure time, permitting the Pockels cell of both lasers to be triggered Both lasers subsequently fire at a repetition rate of 10 Hz until the exposure time lapses In this configuration, the number of shots is determined by the exposure time set with the CCD camera software A timing diagram illustrating this sequence is shown in figure 4 16

In the next two sections the spectral and spatial resolution of the VPIF are discussed A detailed description of these parameters has been presented previously

by Hirsch [13] For this reason only a brief treatment, highlighting the salient features, will be presented here

4.5 Spectral Resolution

The spectral resolution of the VPIF is determined by the bandwidth $\Delta\lambda$ of the monochromatised VUV beam The bandwidth of the VUV beam is determined by the dispersion of the grating and the entrance and exit slit widths of the monochromator

The spectral resolution of the VPIF was experimentally determined by performing absorption spectroscopy on the He $1s^2(^1S_0)$-$1s2p(^1P_1)$ resonance at 58 43 nm Helium was held in the "sample" target chamber at a pressure between 0 17 and 0 19 mbar The helium absorbing column length was $\sim$ 900 mm The wavelength of the VUV beam was then scanned across the resonance transition from 58 2 to 58 5 nm in steps of 0 01 nm The CCD pixels were binned 64 × 64 resulting in

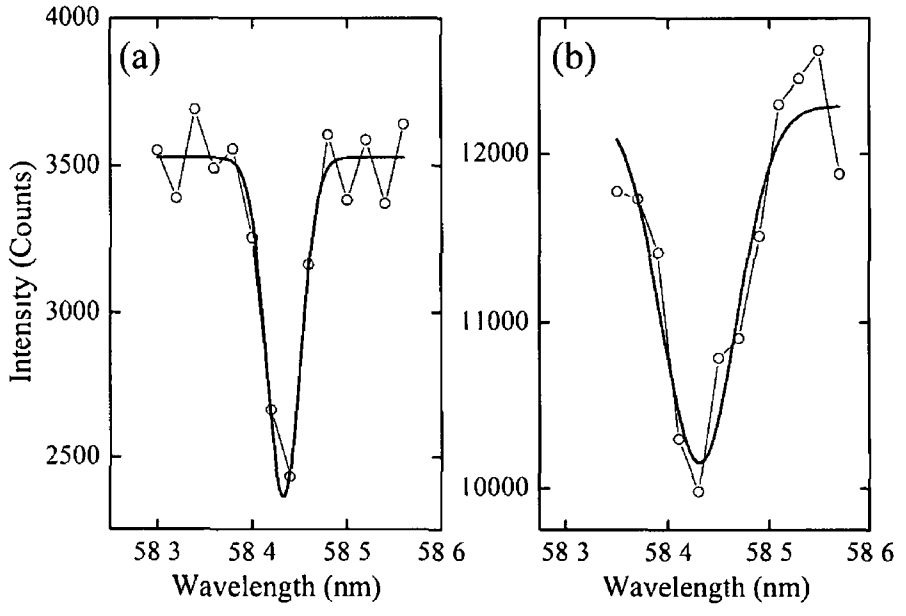

Figure 4 17 Measured spectral resolution using the He $1s^2(^1S_0)$-$1s2p(^1P_1)$ resonance line at 58 43 nm, with (a) 50μm / 50μm entrance / exit slit and (b) 100μm / 100μm entrance / exit slit [13]

0 832 × 0 832 mm pixels The intensity on four of these "superpixels" (containing the beam footprint) were summed and plotted as a function of wavelength This

m essence operates the imaging system as a spectrometer

Two monochromator entrance and exit slit configurations were used to measure the spectral resolution In the first case both slits were set to 50 μm, m the second both slits were set to 100 μm Figure 4 17 (a) shows the absorption profile of the He transition for the 50 μm slit and figure 4 17 (b) shows the absorption profile for 100 μm slits A Gaussian fit to the data-sets yields a FWHM of $0\ 05 \pm 0\ 01$ nm for the 50 μm slits and $0\ 08 \pm 0\ 01$ nm for the 100 μm slits From these values we obtain resolving powers of 730 and 1170 at 58 43 nm These values are in good agreement with ray tracing calculations performed at the University of Padua, Italy, in which resolving powers of 650 and 1200 were determined

4.6 Spatial Resolution

The horizontal and vertical spatial resolution of the VUV probe beam was determined using the edge trace technique described by Williams [14] The edge trace

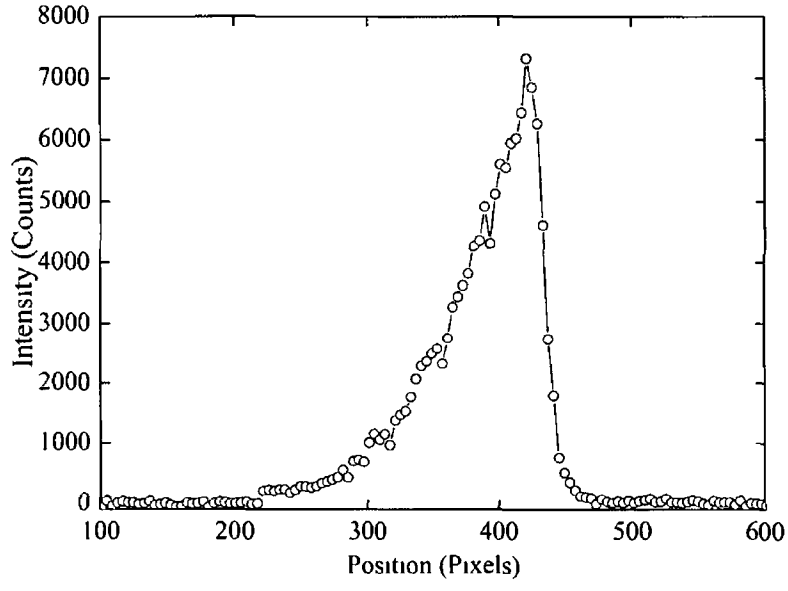

Figure 4 18 Horizontal edge trace of the VUV probe beam of the VPIF [13]

of the system was obtained by inserting a knife edge into the VUV beam (blocking half of it) for different combinations of the entrance and exit slits The edge trace is the integral of the line spread function of the system, which determines the system's overall spatial resolution

Figure 4 18 shows the edge trace of one row of pixels As can be seen the intensity recorded on the CCD does not drop immediately to zero when blocked by the knife edge, instead it drops gradually over approximately 15 pixels, this is due to diffraction at the knife edge

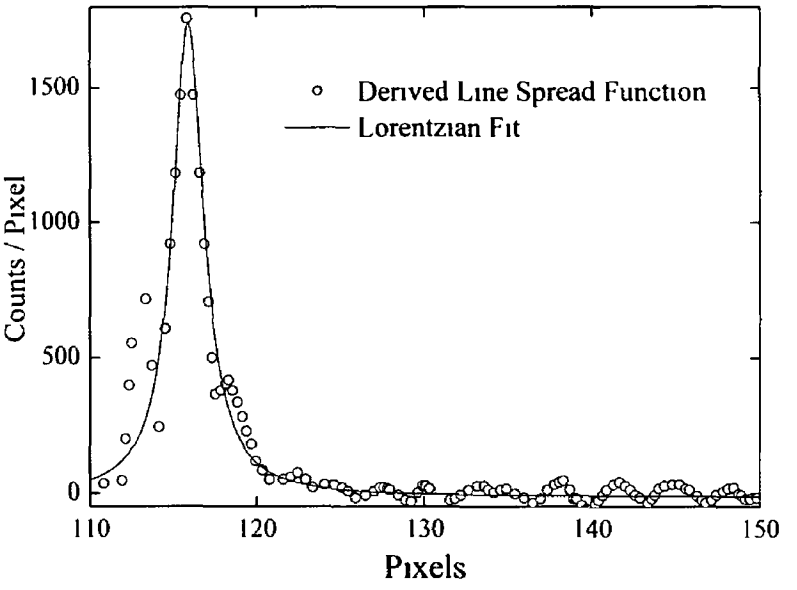

Figure 4 19 Experimentally determined line spread function of the VUV probe beam generated by the VPIF [13]

The line spread function W_l can be determined from the edge trace W_e from [14]

$$W_e(x) = \int_{-\infty}^{x} W_l(x')dx' \tag{4 4}$$

Figure 4 19 shows the resulting line spread function as well as a Lorentzian fit to the data The FWHM of the Lorentzian profile is 135 ± 30 μm, which is the horizontal spatial resolution of the system

The vertical spatial resolution was measured with a horizontal knife edge using the same procedure The FWHM of the Lorentzian fit to the vertical line spread function was 160 ± 30 μm

4.7 Probe Beam Characterisation

In an attempt to further characterise the VUV probe beam a single slit diffraction experiment was performed as part of the current work. A variable width slit was placed on the translational stage used to insert the knife edge into the beam. The slit was orientated vertically i.e. in the saggital plane. The width of the slit was estimated to be 80 ± 15 μm by examining the diffraction pattern formed by irradiating the slit with a He-Ne laser.

The distance from the slit to the CCD was estimated to be 500 ± 5 mm. The slit was moved into the centre of the beam and the wavelength of the beam was then varied from 30 to 150 nm in 10 nm steps. An image of the slit was taken at each wavelength interval without binning of the CCD pixels. Figure 4.20 shows a

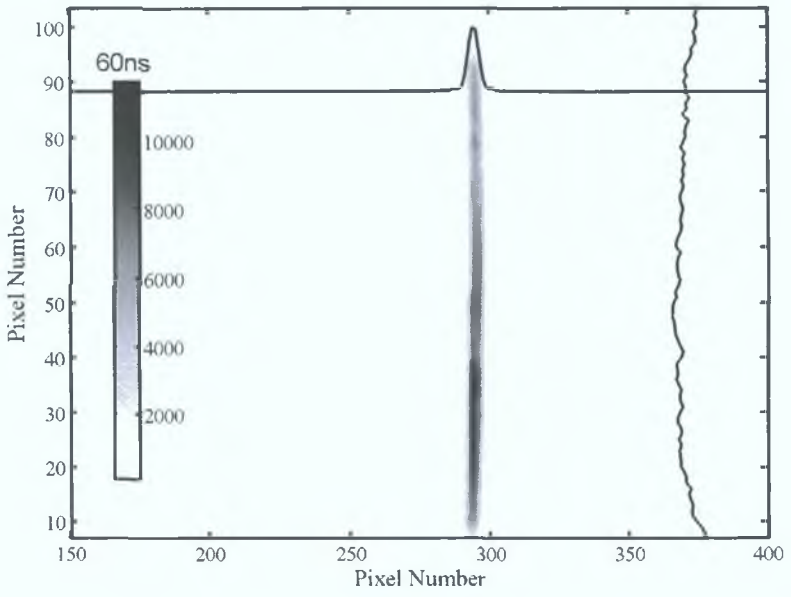

Figure 4.20: Image from the single slit diffraction experiment taken at a monochromator wavelength of 50 nm.

sample image taken with the monochromator set to 50 nm central wavelength and using 100 μm entrance and exit slits. The horizontal profile shown near the top of the image shows the fully vertically binned (FVB) trace of the image; the vertical profile shown on the right hand side of the image shows the fully horizontally binned (FHB) trace of the image. The FVB trace is re-plotted in figure 4.21.

The diffraction pattern observed is in fact a direct measurement of the line spread function of the optical system described in section 4.6. In section 4.6 the line

spread function was derived from the edge trace measurements obtained using a knife edge According to Williams *et al* [14] the line spread function for a diffraction limited system is in fact described by a first order Struve function In mathematical terms Struve functions are associated with Bessel functions, and tabulated values of Struve functions may usually be found in Bessel tables [14]

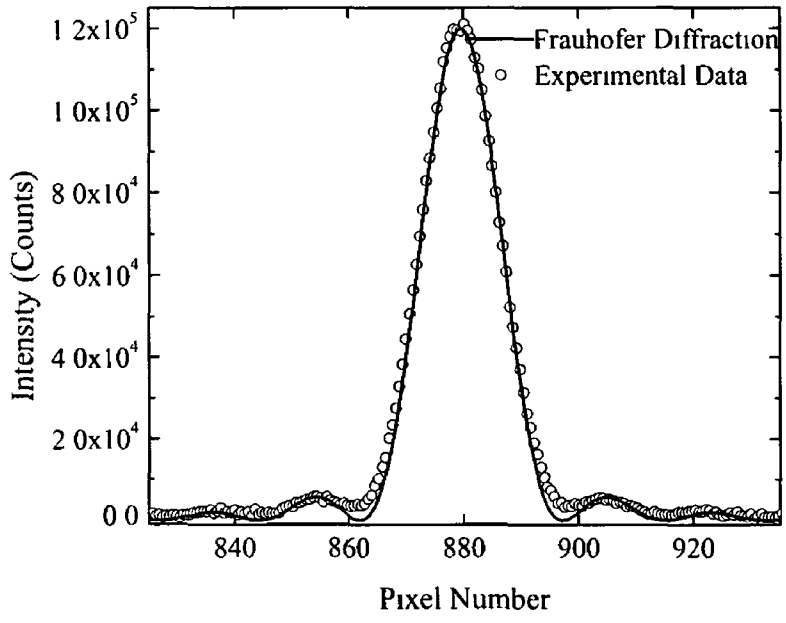

Figure 4 21 Comparison between single slit experimental data (FVB trace of figure 4 20) with a single slit Fraunhofer diffraction model

In order to make a simple but reasonably accurate determination of the FWHM of the central lobe, a basic single slit diffraction trace was fitted to the experimental data shown in figure 4 21 The diffraction pattern intensity I was calculated using equation 4 5

$$I = I_0 \frac{\sin^2(\pi a y/\lambda D_{sc})}{(\pi a y/\lambda D_{sc})^2} \tag{4 5}$$

where I_0 was normalised to the experimental intensity, a was the slit width, λ the wavelength, y the position along the CCD and D_{sc} the distance from the slit to the CCD

During the fitting process the actual slit width determined by the model was 68 ± 1 μm, which was within our measurement error from the HeNe The FWHM of the central lobe of the diffraction pattern was determined to be 13 15 $\pm$ 0 02 pixels which translates into 170 9 $\pm$ 0 3 μm In terms of the fit shown in figure 4 21, the

slight departure of the fit from the experimental data between the central and first order lobes would be corrected for in the implementation of a Struve diffraction pattern

The end result of this experiment is that a new more accurate value of the spatial resolution of the system can be determined through the direct measurement of the line spread function The previous calculation using the edge trace technique supplied a value for the horizontal spatial resolution of 135 ± 30 μm for 100 μm entrance and exit slits, whereas the direct measurement of the line spread function indicates a value just above the upper error limit, of $170\ 9 \pm 0\ 3$ μm

4.8 System Improvements

In order to improve the quality of the photoabsorption images obtained, numerous modifications were made to the VPIF to improve the signal-to-noise ratio The actual process used to calculate the photoabsorption images will be discussed in section 5 2

Two major difficulties hindered the ability of the system to record quality images The first was that one photoabsorption image requires 100 laser shots to be fired at the source target and 50 shots at the sample target Figure 4 22 shows the effect that cratering, caused by the laser radiation ablating the target surface, has on the VUV flux The traces shown in figure 4 22 are fully vertically binned images of the VUV probe beam after differing numbers of laser shots The reason for the step like structure in the traces is that the CCD pixels in the images have been binned 6×6

If this drop in flux from the source is not carefully considered when obtaining photoabsorption images it will produce an "apparent" absorption of the beam when the ratio of the source (I_0) to the sample (I) images are calculated For this reason reproducibility of the source and sample plasmas was a very important factor when attempting to improve the system All of the optical mounts and translational stages were upgraded to facilitate the regular movements to "fresh" source and sample surfaces while improving the reproducibility of the probe beam

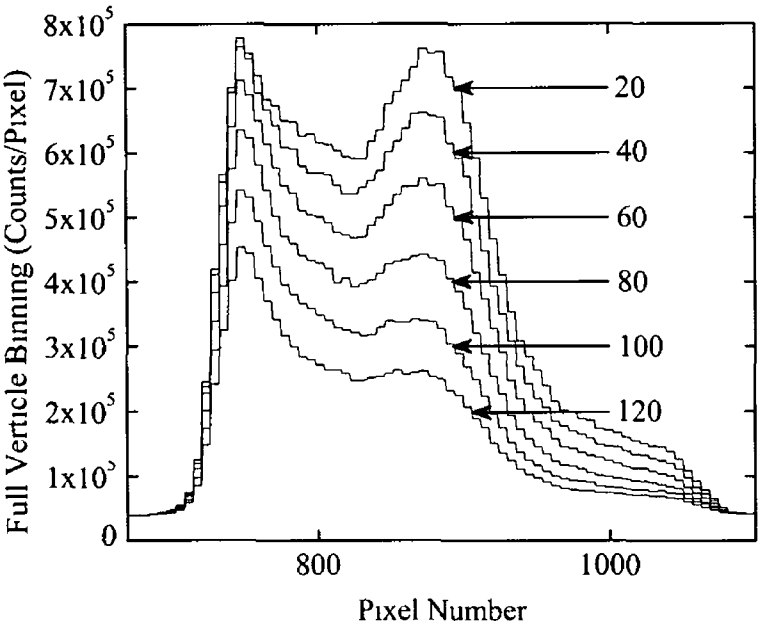

Figure 4 22 Full vertical binning of the VUV beam source at 37 3 nm

The second major difficulty was the background detection noise level This was tackled on a number of fronts The first was the introduction of the Brewster angle polariser and half-wave plate setup (section 4 4 5) This allowed us to vary precisely the energy supplied to the sample plasma This is required in order to limit the emission from the sample plasma to wavelengths longer than $\sim$ 80 nm Any strong emission with wavelengths shorter than this would penetrate the Al filter and saturate the camera However a balance must be found between low emission and reasonable volumes of ablated material for good absorption signals

To further reduce the front plasma emission from reaching the CCD camera, two 10 mm wide by 20 mm long slit apertures were placed inside the beamline, approximately 350 mm apart, this was done to minimise reflections from VUV emission located behind the knife edge from the inside wall of the KF-40 vacuum tubing This made the alignment of the system difficult as the apertures could only be manoeuvered while that section of the system was at atmospheric pressure

Another way to reduce the detection noise was to reduce the thermal noise on the detector The back-illuminated Andor Technology CCD contains a Peltier cooler with two fans, that allowed it to be cooled to 0° C However, it also had the facility to be cooled down to -80° C using flowing mains water to assist the Peltier cooler Figure 4 23 shows the effect that cooling the CCD chip has on the average thermal

background counts The traces shown in figure 4 23 are again images that have been fully vertically binned The entire width of the CCD chip (2048 pixels) is shown The temperature was varied from +10° C to -40° C All of the images recorded during the course of this work have been taken with a CCD temperature of -20° C

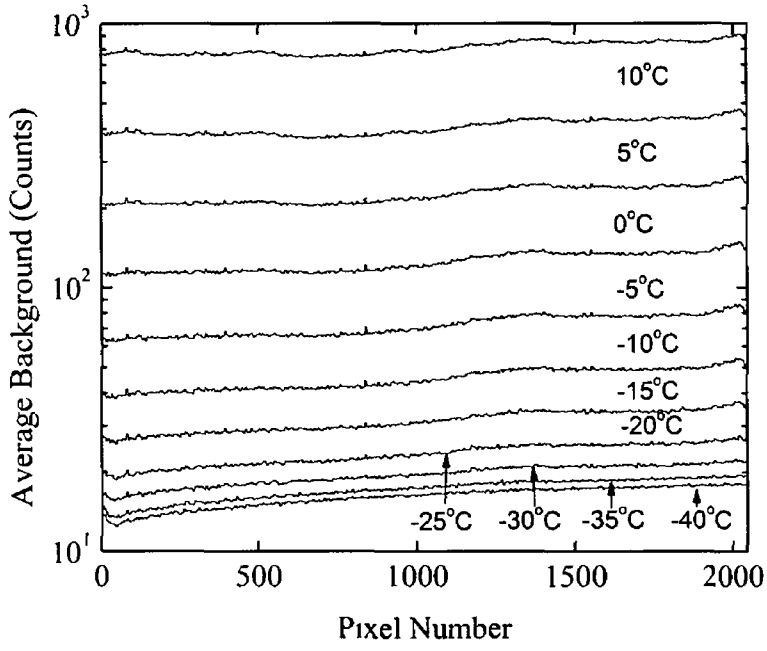

Figure 4 23 CCD thermal background noise as a function of CCD temperature

Figure 4 24 shows the effect that these improvements had on the quality of the photoabsorption images obtainable using the VPIF The image set shown on the top of figure 4 24 were taken before the improvements mentioned here and the image set at the bottom was taken after

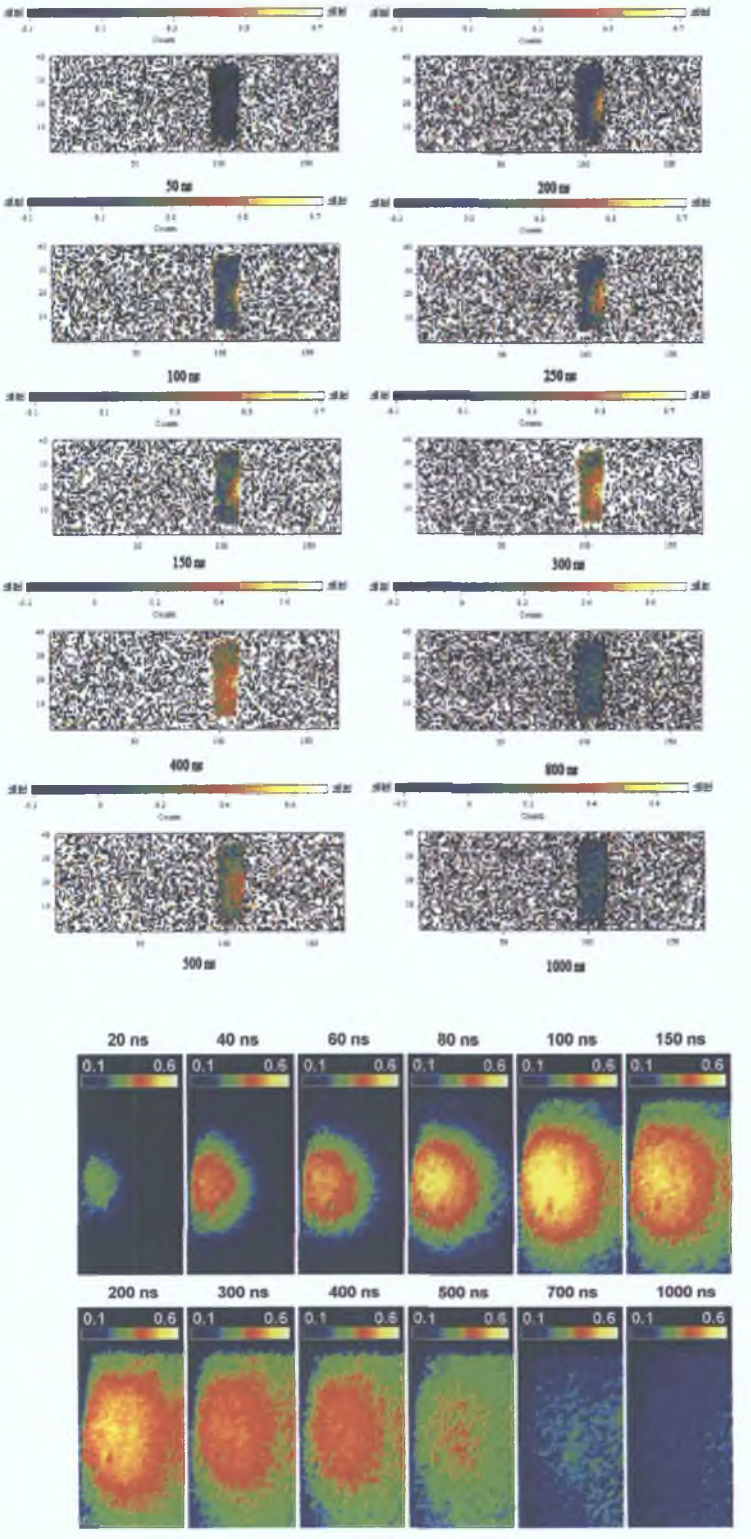

Figure 4.24: Comparison of VUV Photoabsorption Images taken during this work with images from John Hirsch's PhD Thesis [3].

4.9 Spectrally Resolved Emission Imaging

A schematic of the system used to record time, space and spectrally resolved visible emission images of expanding LPP's is shown in figure 4 25 There are three main components in the emission imaging setup the lasers, interference filters and the ICCD camera The plasmas were generated using either the Spectron SL-404 or

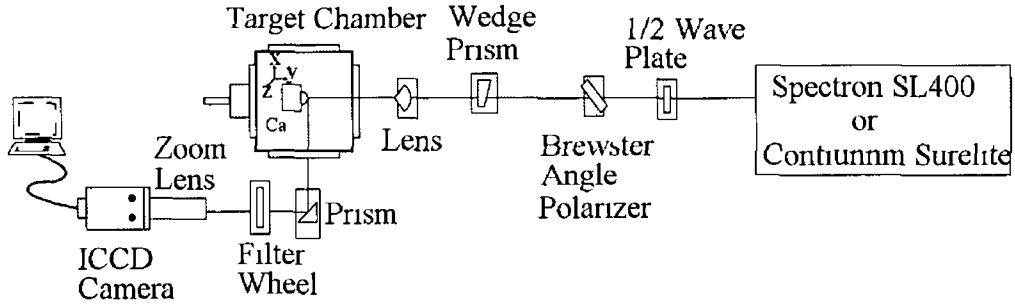

Figure 4 25 Experimental setup used to acquire time-resolved spectrally filtered emission images

Continuum Surelite laser systems as discussed previously in sections 4 3 and 4 2 The energy supplied to the target surface was controlled using the half-wave plate and Brewster angle polariser setup used by the VPIF Cylindrical lenses were used to generate low density, low temperature line plasmas under the same conditions as the photoabsorption experiments Spherical lenses were used to generate high density, high temperature point plasmas where strong interaction between the plasmas could be observed for synchronous spectroscopic and imaging experiments

The two components of the imaging setup that have not been discussed previously the interference filters and the ICCD camera, will be discussed individually in sections 4 9 1 and 4 9 2

4 9 1 Interference Filters

Radiation emitted by the sample plasma exits the target chamber through a glass window and is redirected using a 90° prism, as shown in figure 4 25 Before the radiation is allowed to enter the aperture of the ICCD camera it is passed through a narrow bandpass interference filter so that we can track a specific emission line of a desired charge state The two main transitions used were the $4s^2(^1S_0)$-$4s4p(^1P_1)$

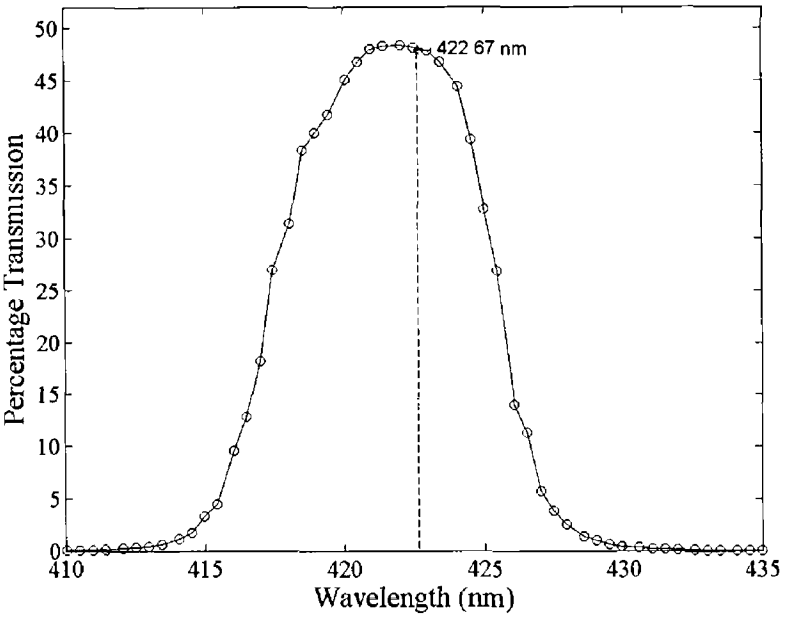

Figure 4 26 Transmission curve for the interference filter centered at 420 nm Used to track the $4s^2(^1S_0)$-$4s4p(^1P_1)$ Ca^0 line at 422 67 nm

neutral calcium line at 422 67 nm and the $4s(^2S_{1/2})$-$4p(^2P_{3/2,1/2})$ singly ionised calcium doublet at 393 36 and 396 85 nm Two bandpass filters were used to select these emission lines, the transmission curves for these interference filters centered 420 and 390 nm are shown in figures 4 26 and 4 27 respectively The location of the

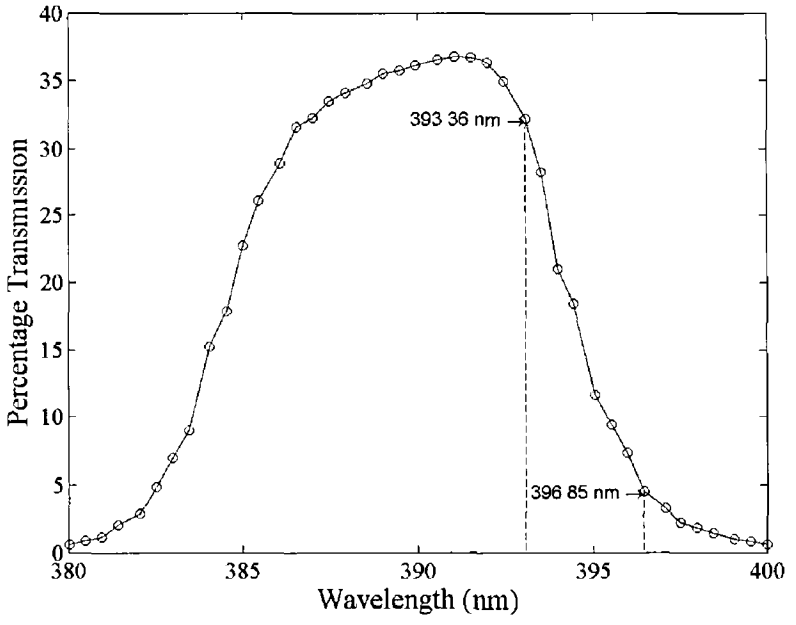

Figure 4 27 Transmission curve for the interference filter centered at 390 nm Used to track the $4s(^2S_{1/2})$-$4p(^2P_{3/2,1/2})$ Ca^+ lines at 393 36 and 396 85 nm

relevant Ca transitions has been indicated by dotted vertical lines in both figures

A number of other bandpass filters were used during the course of this work with similar transmission curves A broadband short-pass interference filter was also used to take "white" light images of the bulk plasma motion This filter blocked all radiation with wavelengths longer than 950 nm, thereby eliminating (fundamental) Nd YAG laser scatter whilst also protecting the CCD sensor

4 9 2 ICCD Camera

The ICCD camera that was used in the emission imaging setup was an Andor Technology DH5H7 The camera has 24 μm square pixels arranged in a 512×512 2-D array This array is coupled via a fibre optic coupler to a gated image intensifier

The image intensifier is placed before the CCD chip and serves two purposes The first purpose is to amplify incoming light in order to extend the intensity range over which the CCD chip is effective The second is that the intensifier can be used as an extremely fast shutter, as it can be switched rapidly on and off The fastest shutter speed, or gate width achievable with this intensifier is ~ 3 ns

The image intensifier consists of three components

(i) A photocathode, which is coated onto the back of the input window

(ii) A Micro-Channel Plate (MCP), which is a 1 mm thick glass capillary array

(iii) A phosphor screen

An incoming photon (figure 4 28), which enters the input window, will strike the photocathode and release an electron This electron is drawn to the MCP across a small path ($\sim$ 0 15 mm) by a 150 to 200 V electric potential The electron then enters one of the capillaries (or channels) of the MCP and is accelerated further by a larger potential difference, 500 to 1000 V As the electron traverses the MCP channel it collides with the walls of the capillary and creates secondary electrons (see inset of figure 4 28) These secondary electrons release more electrons during collisions with the walls resulting in a burst / pulse of electrons exiting the MCP channel for one input electron Amplifications of up to 10^4 can be achieved in this manner Varying the voltage across the MCP provides control over the number of

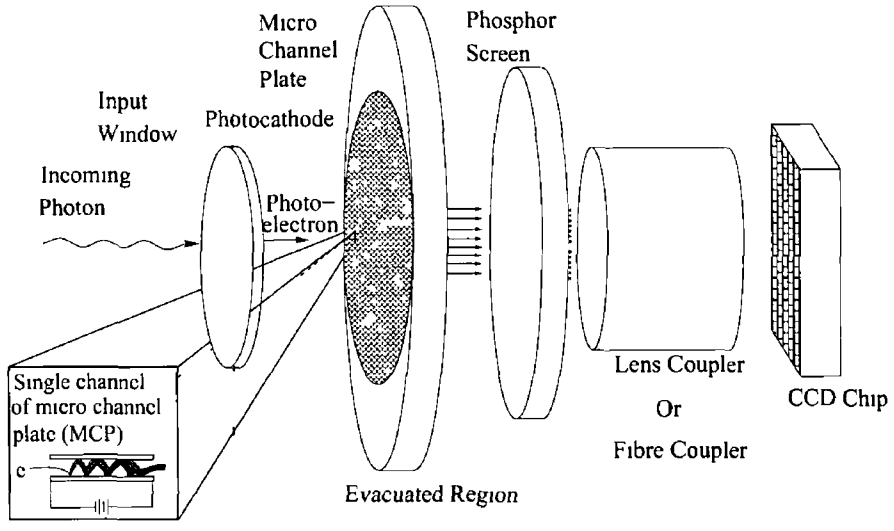

Figure 4 28 Schematic of ICCD intensifier attached to the Andor DH5H7 CCD camera [15]

secondary electrons that are released from the walls of the capillary and hence the gain of the system This enables the camera to operate at very low light levels [15]

The packet of secondary electrons that exit the MCP are subsequently swept across another small gap ($\sim$ 0 5 mm) by a very large potential ($\sim$ 6000 V) This large potential keeps the bunch tightly packed together and adds energy to the electron cloud before it strikes the phosphor screen and creates an image The resulting

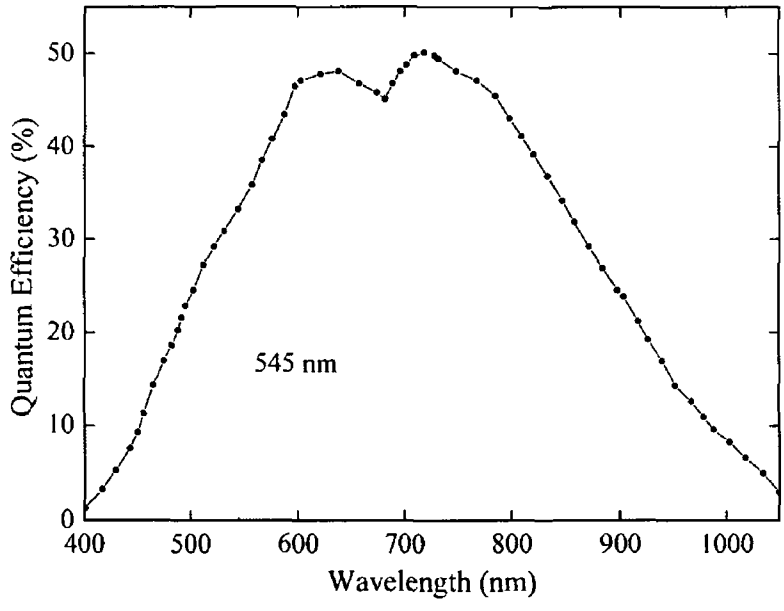

Figure 4 29 Quantum efficiency of the Andor DH5H7 CCD camera chip

image on the phosphor screen is directly coupled to the CCD chip using a fibre optic coupler

The quantum efficiency of the front illuminated CCD chip used in this camera is shown in figure 4 29 The more important factor for determining the useful wavelength range is the spectral response of the photocathode on the intensifier The photocathode material was bismuth, which allows the overall spectral response of the camera to be extended into the UV ($\sim$ 180 nm), figure 4 30 shows the quantum efficiency curve for the photocathode in the 200 to 900 nm spectral range

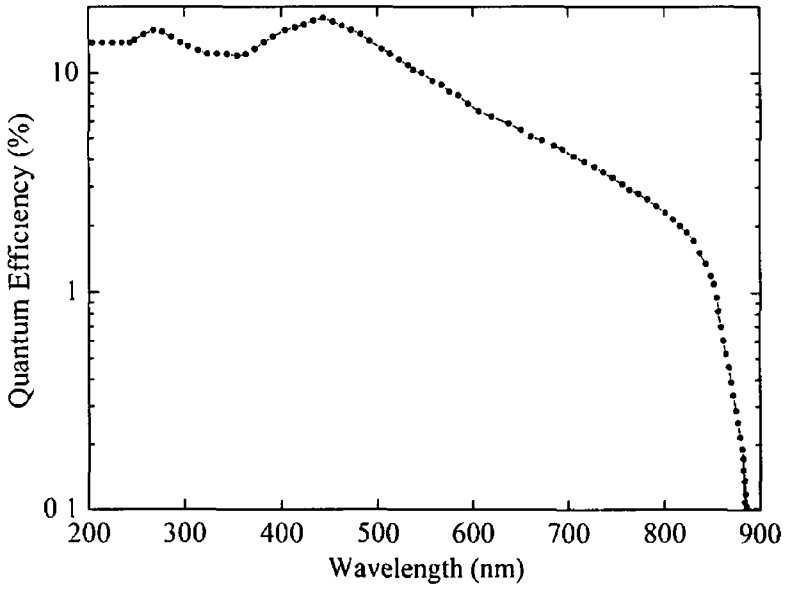

Figure 4 30 Quantum efficiency of the Andor DH5H7 Gen II photocathode

The photons emitted by the phosphor screen (type P43) have a narrow band yellow-green emission at 545 nm, indicated by the dotted vertical line on figure 4 29 The phosphor type was chosen to match the peak quantum efficiency of the CCD chip Fluorescence from the phosphor screen is relatively long lived, requiring 1 ms to fall below 10%, hence limiting the frame rate of the camera to less than 1 kHz

A Pentax zoom lens assembly was coupled to the ICCD camera and was used to image the plasma emission onto the input window of the intensifier The overall magnification of the imaging system was measured using a ruler section that was attached to the target holder inside the vacuum chamber The white curved trace shown on the image in figure 4 31 (a) shows a line-out taken along the white

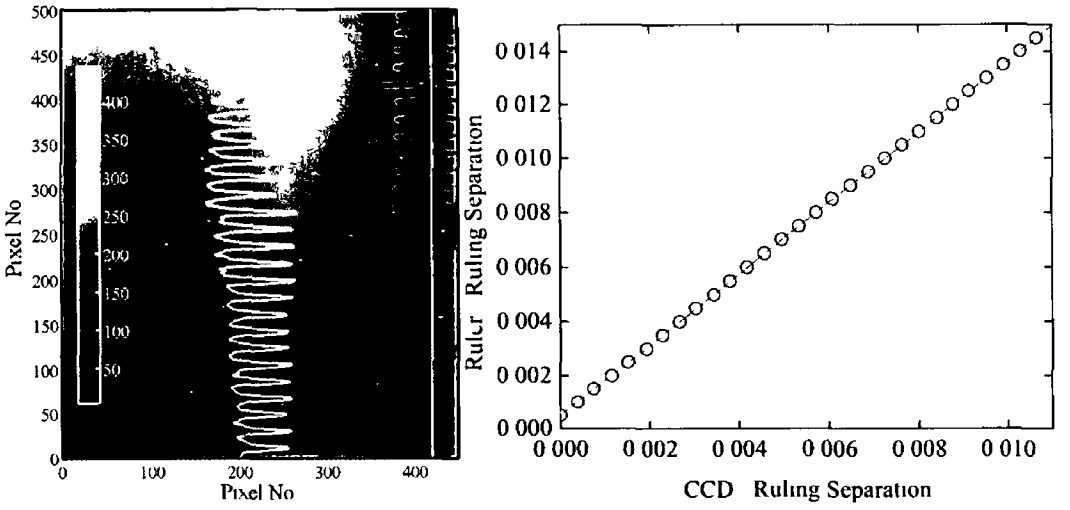

(a) Image of ruler in target chamber (b) Plot of measured vs actual ruling separation

Figure 4 31 Image of ruler for calculating the magnification of the ICCD imaging system

straight vertical line drawn on the graduated section of the ruler From the image presented in figure 4 31 (b) a magnification of 1 31 was calculated

4.10 Emission Imaging Spectroscopy

The ICCD spectroscopy setup may be used in tandem with the ICCD imaging setup described in the previous section It consists of a 0 5 m Chromex visible imaging spectrometer and a second Andor Technology ICCD camera The ICCD

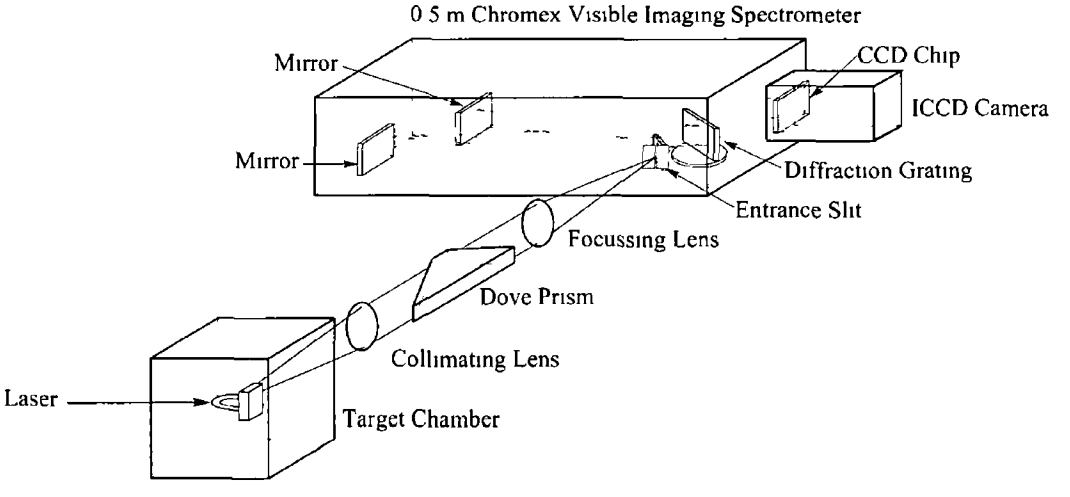

Figure 4 32 Schematic diagram of the emission imaging spectroscopy setup including imaging optics and dove prism

camera that is coupled to the spectrometer may be gated in the same manner as the imaging ICCD described in the previous section This allows us to perform simultaneous gated visible emission imaging and gated imaging spectroscopy of single and colliding plasma plumes over the same time-frames A schematic of the spectroscopy system is shown in figure 4 32 and a photograph of the spectrometer and ICCD are shown in figure 4 33

A plasma generated in the target chamber is imaged onto the entrance slit of the spectrometer using two 250 mm focal length achromatic doublet lenses A dove prism is placed between the two lenses at 45° in order to rotate the image of the plasma by 90°, so that the image of the plasma expands upwards (vertically) along the length of the entrance slit of the spectrometer

The spectrometer comprises a Czerny-Turner mount with toroidal collimating and focusing mirrors which enable aberration-corrected flat field stigmatic imaging A 1200 groove/mm diffraction grating blazed at 400 nm was used leading to a reciprocal linear dispersion of 1 6 nm/mm and a resolution of 0 07 nm (FWHM) limited by the spatial resolution of the ICCD Figure 4 34 shows the efficiency of the grating in the 190 to 700 nm spectral range

The instrument function of the spectrometer was determined using a Cadmium lamp (441 nm transition) The entrance slit of the spectrometer was varied from 1000 μm to 10 μm Gaussian functions were fitted to the recorded profiles Figure 4 35 shows a plot of the FWHM of the Gaussian fits as function of slit width

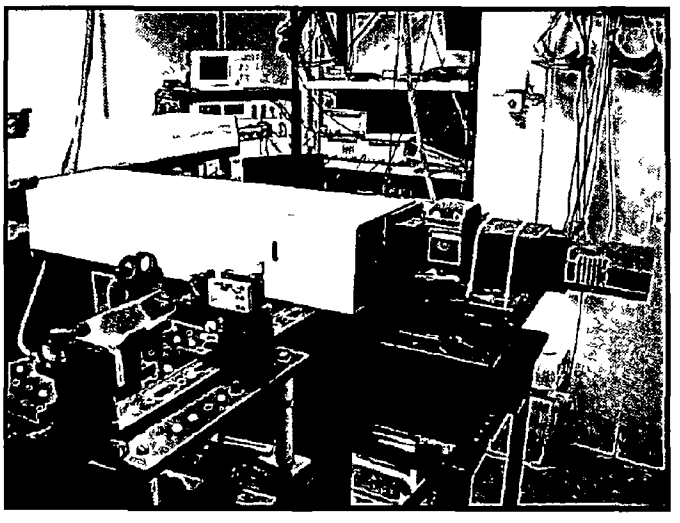

Figure 4 33 Photograph of the Chromex emission imaging spectrometer

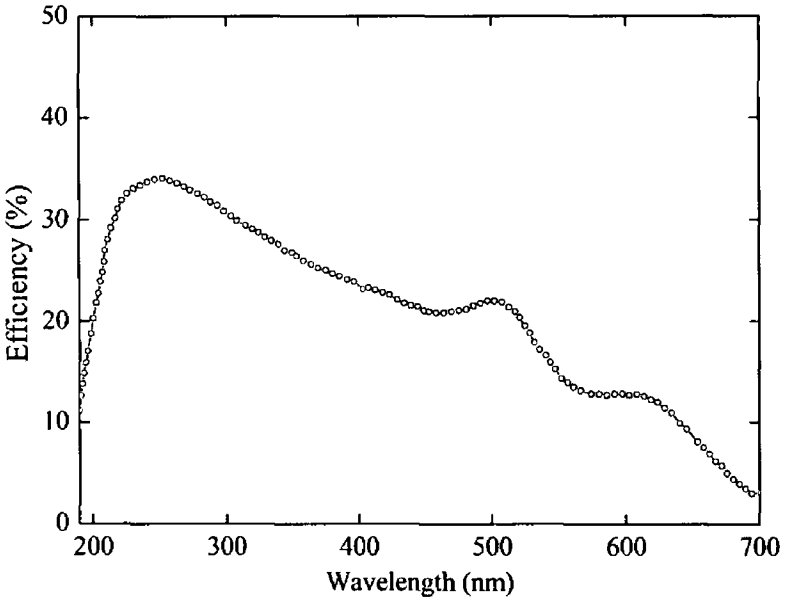

Figure 4 34 Grating efficiency curve for the 1200 grooves mm^{-1} supplied with the Chromex visible spectrometer

An optimum slit width of 60 μm was determined providing an instrument function of width 0 22 nm The results obtained for slit widths of 50 μm and below became very erratic and irreproducible This is possibly due to the spatial sampling frequency of the CCD approaching the Nyquist limit The best effective CCD pixel size achievable when using the image intensifier in front of the CCD camera was

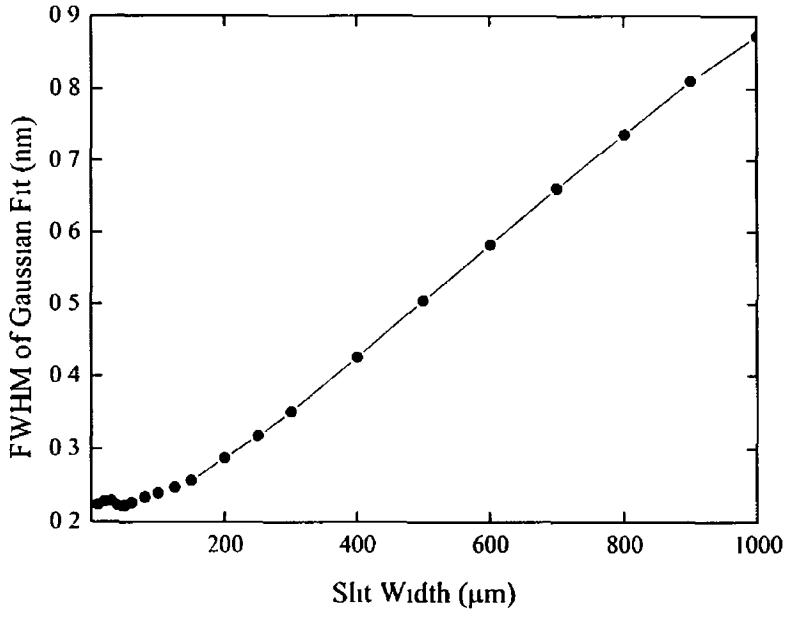

Figure 4 35 The instrument function of the Chromex IS-500 imaging spectrometer

~ 25 μm This was likely caused by spreading of the electron bunches exiting the channels of the MCP which are ~ 20 μm wide for this intensifier Therefore imaging a slit width of ~ 50 μm approaches the sampling limit of the ICCD Table 4 4 summarises the important details of the Chromex imaging spectrometer

Table 4 4 Chromex imaging spectrometer specifications

Configuration	Czerny-Turner
Aperture ratio	f/8
Wavelength range	180 - 900 nm
Reciprocal linear dispersion	1 6 nm/mm
Resolution	$\sim$ 0 08 nm
Slit widths	10 μm - 2 mm
Wavelength accuracy	$\pm$ 0 15 nm
Grating	1200 grooves/mm
Focal length	0 5 m

4 11 Summary

In this chapter the important features of the experimental systems used during the course of this work have been discussed The details of the three laser systems used were presented This was followed by an individual description of each element of the VUV photoabsorption imaging facility, as well as beam characterisation, timing and resolution The experimental setup for obtaining spectrally filtered emission images was then discussed, with particular emphasis on the capabilities if the ICCD camera used Finally the emission spectroscopy setup was described The capabilities and limitations of all of the equipment used has been outlined

In the next chapter experimental results obtained using the VPIF will be presented and discussed Equivalent width and column density image sets, acquired using different irradiation conditions will be analysed

Bibliography

[1] O Meighan *Photoabsorption Imaging of Laser Produced Plasmas* PhD thesis, School of Physical Sciences, Dublin City University, 2000

[2] Cormac McGuinness *The XUV Photoabsorption and Photoionisation Spectra of Selected Ions Techniques, Results and Theory* PhD thesis, University College Dublin, 1996

[3] J S Hirsch *Photoabsorption Imaging of Laser Produced Plasmas* PhD thesis, School of Physical Sciences, Dublin City University, 2003

[4] E T Kennedy, J T Costello, J -P Mosnier, and P van Kampen Vuv/euv ionising radiation and atoms and ions dual laser plasma investigations *Radiation Physics and Chemistry*, 70 291–321, 2004

[5] C Breton and R Papoular Vacuum-uv radiation of laser-produced plasmas *Optical Society of America*, 63 1225–1232, 1973

[6] O Meighan, A Gray, J -P Mosnier, W Whitty, J T Costello, C L S Lewis, A MacPhee, R Allott, I C E Turcu, and A Lamb Short-pulse, extreme-ultraviolet continuum emission from a table-top laser plasma light source *Applied Physics Letters*, 70 1497–1499, 1997

[7] J-P Mosnier, S Bac, R Barchewitz, E T Kennedy, M Collins, and J T Costello Measurements of extreme uv yields from nd-yag plasmas using a multilayer monochromator *Journal of Electron Spectra and Related Phenomena*, 80 295–298, 1996

[8] J S Hirsch, O Meighan, J-P Mosnier, P van Kampen, W W Whitty, and J T Costello Vacuum-ultraviolet resonant photoabsorption imaging of laser produced plasmas *Journal of Applied Physics*, 88 4953–4960, 2000

[9] O Meighan, C Danson, L Dardis, C L S Lewis, A MacPhee, C McGuinness, R O'Rourke, W Shaikh, I C E Turcu, and J T Costello Application of a picosecond laser plasma continuum light source to a dual-laser plasma photoabsorption experiment *Journal of Physics B Atomic, Molecular and Optical Physics*, 33 1159–1168, 2000

[10] D Colombant and G F Tonon X-ray emission in laser produced plasmas *Journal of Applied Physics*, 44 3524–3537, 1973

[11] M A Khater *Spectroscopic investigations of laser-produced steel plasmas in the vacuum ultraviolet* PhD thesis, School of Physical Sciences, Dublin City University, 2001

[12] H R Griem *Plasma spectroscopy* McGraw-Hill, New York, 1964

[13] J S Hirsch, E T Kennedy, A Neogi, and J T Costello Vacuum-ultraviolet photoabsorption imaging system for laser plasma plume diagnostics *Review of Scientific Instruments*, 74 2992–2998, 2003

[14] C S Williams and O A Becklund *Introduction to the optical transfer function* Wiley, New York, 1989

[15] A McKiernan *Study of Ga, GaN, Li and LiF laser ablation plumes using spectroscopic and fast imaging techniques* PhD thesis, School of Physical Sciences, Dublin City University, 2003

CHAPTER 5

PHOTOABSORPTION IMAGING

5.1 Introduction

As has been mentioned previously the vacuum ultraviolet photoabsorption imaging facility is a tuneable VUV light source This light source may be used to excite inner-shell and multiply excited resonances, which decay predominantly via autoionisation processes The fact that these states autoionise as opposed to decaying through fluorescence means that the attenuation of the intensity of the probe beam may be readily described by the Beer-Lambert law (section 3 2) This removes the need for a complete radiation transfer analysis along the line of sight through the plasma, which would be necessary if absorption and 'photon" re-emission cycles were taking place Additionally, the fact that the VUV beam may be used to populate autoionising states means that the photoabsorption images recorded by the VPIF are in fact maps of photoionisation occurring within the plasma [1, 2]

Calcium has been chosen as the most suitable material for photoabsorption imaging using the VPIF for a number of reasons Extensive photoabsorption studies have been undertaken on calcium by a number of authors [3, 4, 5, 6, 7] In particular 3p-3d transitions have received most attention The VPIF can access the 3p-3d transitions of Ca^0, Ca^+ and Ca^{2+} at 31 4, 33 2 and 34 7 eV respectively These three transitions may be uniquely selected using the quasi-monochromatic ($\Delta\lambda \sim$ 0 01 nm, at 50 nm) VPIF probe beam, without interference from transitions from neighbouring charge stages This may be seen in figure 5 2, which shows the

isonuclear photoabsorption spectra of calcium (Ca^0, Ca^+ and Ca^{2+}) in the 28 to 42 eV energy range, recorded by A Gray [8]

In this work only Ca^+ photoabsorption images will be presented, the photoionisation pathway followed by Ca^+ may be written as

$$Ca^+ (3p^6 4s\ ^2S) + h\nu \longrightarrow Ca^{+*}(3p^5 4s3d\ ^2P) \longrightarrow Ca^{2+}(3p^6\ ^1S) + e^- \qquad (5\ 1)$$

Ca^+ was chosen because the absolute photoionisation cross-section is known for this transition and hence column density maps for this ion may be determined from the photoabsorption image data The photoionisation cross section was measured by Lyon *et al* from 28 2 to 49 2 nm and is shown in figure 5 1

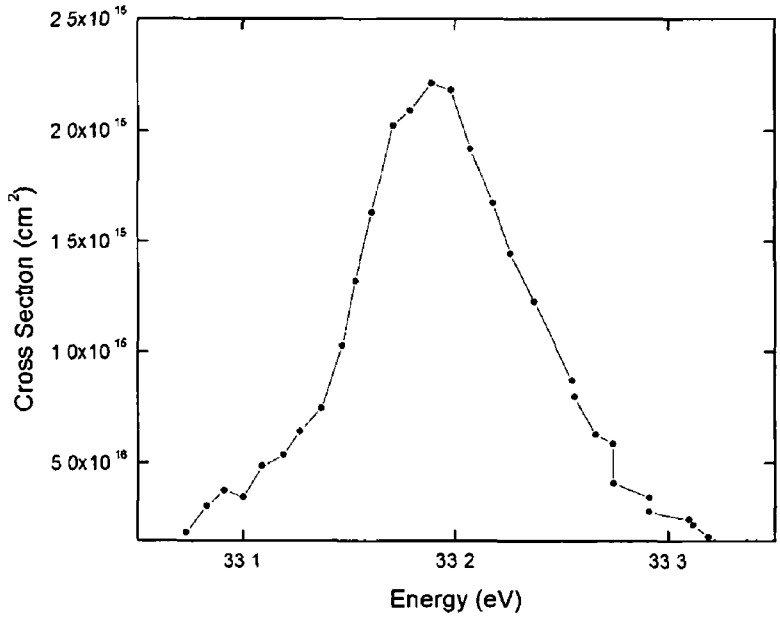

Figure 5 1 Absolute photoionisation cross section of the Ca^+ 3p-3d resonance centred at 33 19 eV (Lyon *et al* [3])

The sequence of this chapter is as follows We will first discuss the data acquisition procedure and the process by which equivalent width images are constructed (section 5 2) After that, four equivalent width image sets will be presented tracking the temporal evolution of Ca^+ in (i) single line plasmas, (ii) single point plasmas, (iii) colliding line plasmas on a flat surface and finally (iv) colliding line plasmas on an angled surface (section 5 3)

Having presented the equivalent width image sets and discussed general trends in the space-time evolution of this parameter, we will discuss the procedure that

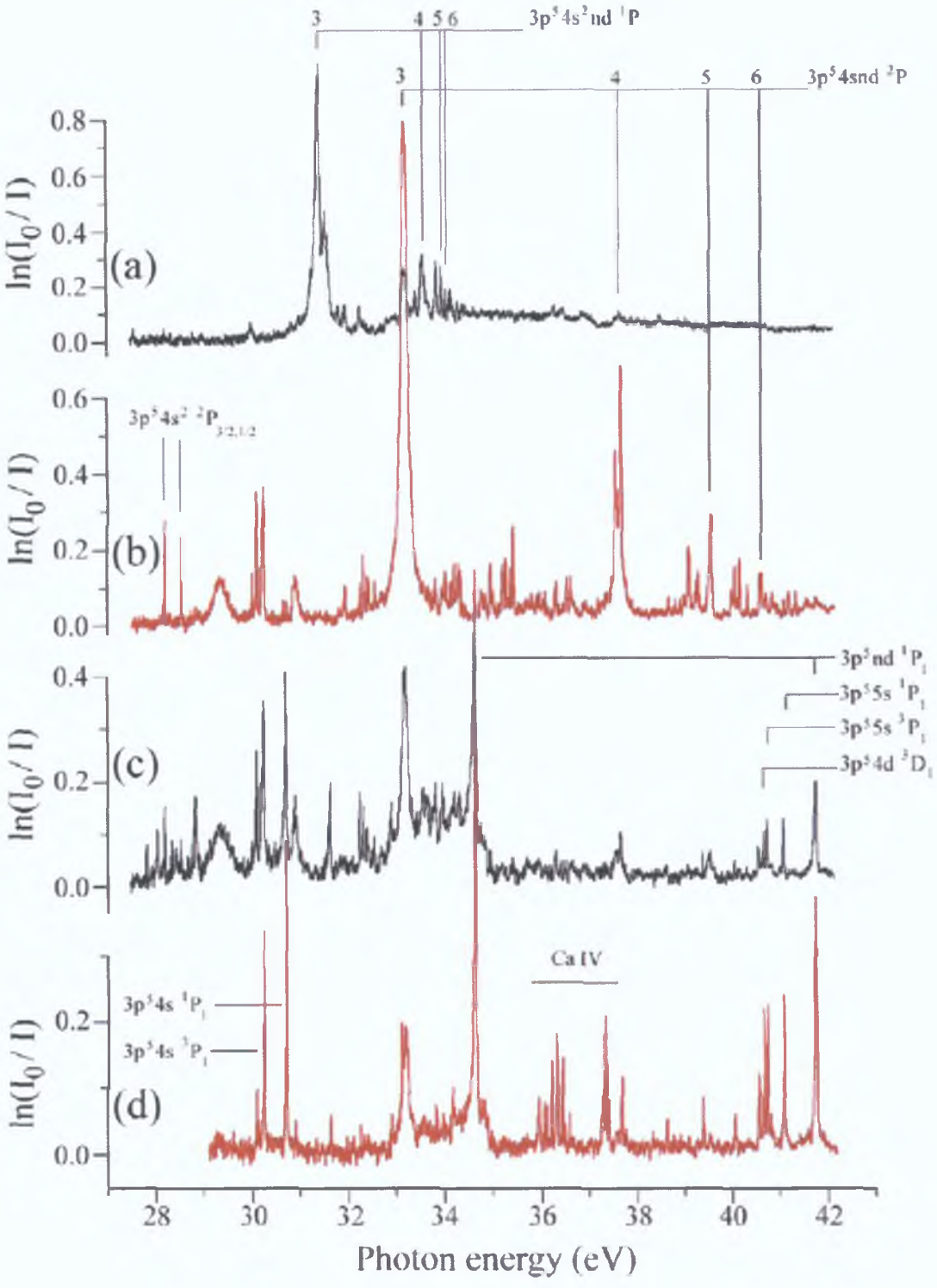

Figure 5.2: Calcium isonuclear sequence in photoabsorption where (a) is Ca^0 (Δt = 800ns, cylindrical lens), (b) is Ca^+ (Δt = 500ns, cylindrical lens), (c) is Ca^{2+} (Δt = 20ns, cylindrical lens) and (d) is Ca^{2+} (Δt = 45ns, spherical lens)(After Gray 1999 [8]).

allows us to convert equivalent width images into column density maps using the absolute photoionisation cross section of the Ca^+ 3p-3d resonance at 33.2 eV. All

four equivalent width image sets have been converted into column density maps and are presented in section 5.4.

In the final section of this chapter (section 5.5), expansion velocities are extracted from the single non-colliding line plasma images and the stagnation layers formed at the collision interface between the two colliding line plasma plumes. The velocities are compared with each other and an adiabatic expansion model.

5.2 Data Acquisition

A set procedure was devised and used to record all photoabsorption images with the VPIF. Each absorption image presented here has been constructed from ten individual images, each such image being composed of the accumulation of ten laser shots each.

The first step of the procedure is to record a background image (Bg:1) on the CCD camera in the absence of both source and sample plasmas (no lasers fired). This procedure yields a recording of the CCD thermal background level and its associated noise. Next the source plasma is generated and an image of the VUV beam is recorded at the desired monochromator wavelength (minus the thermal background image (Bg:1)). The source image (I_0) minus this thermal background may be represented by $\int_{\Delta\lambda} I_0(\lambda)d\lambda$ where $I_0(\lambda)d\lambda$ is the VUV fluence in Jcm^{-2} between λ the chosen wavelength of the monochromator and $\lambda + d\lambda$ the bandwidth of the VUV beam [9].

Next the sample plasma is generated by firing its associated laser only and the emission from this plasma is recorded and saved to disk as a second background image (Bg:2). The intensity of this background depends on the amount of emission from the sample plasma below $\sim$ 80 nm that passes through the Al filter and reaches the CCD. Minimising this background is very important to obtain a good signal-to-noise ratio in the final image.

Next an image is recorded with both lasers firing and the desired time delay inserted between generation of the sample and source plasmas. The second background (Bg:2, sample plasma emission) is then subtracted from this image and may be represented as $\int_{\Delta\lambda} I(\lambda)d\lambda$ where $I(\lambda)d\lambda$ is the transmitted VUV fluence between

λ and $\lambda + d\lambda$ [9].

This procedure is repeated five times for each time delay, alternating between source and sample images in order to minimise "apparent" absorption due to the decrease in source intensity (I_0) between successive shots as a result of backlighting plasma occlusion by cratering, as shown in figure 4.22 (section 4.7). Each source image (I_0) and source and sample image (I) is then summed to improve signal-to-noise ratio.

Maps of equivalent width are then calculated using equation 3.1 (section 3.2.1), repeated here for the reader's convenience, along with a simplified version written in terms of the images recorded.

$$W_\lambda = \Delta\lambda \left(\frac{\int_{\Delta\lambda} [I_\lambda(0) - I_\lambda(L)] d\lambda}{\int_{\Delta\lambda} I_\lambda(0) d\lambda} \right) = \Delta\lambda \left(\frac{I_0 - I}{I_0} \right) \tag{3.1}$$

Each individual image recorded was an accumulation of ten laser shots, which is determined by a CCD exposure time of one second. The bandwidth $\Delta\lambda$ of the VUV probe beam is determined by the entrance and exit slit widths of the monochromator; 100 μm slits yield a bandwidth of $\sim$ 0.1 nm at 50 nm. Figure 5.3

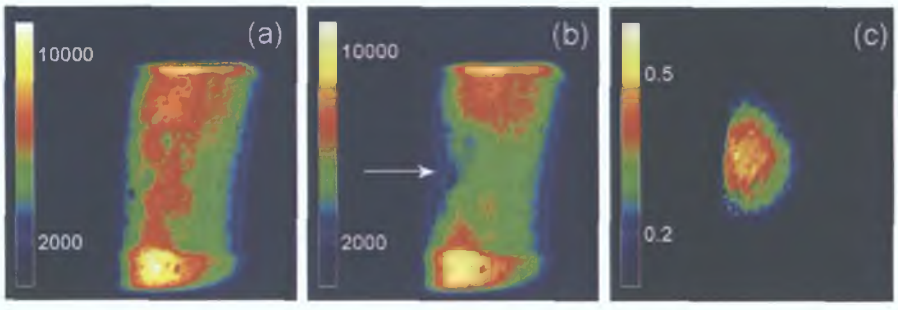

Figure 5.3: Processing procedure for VUV photoabsorption images

shows images obtained at each stage of the procedure just outlined. For figure 5.3 the monochromator wavelength was set to 37.34 nm corresponding to a photon energy of 33.2 eV, which can be used to excite the Ca^+ ($3p^6 4s\ ^2S$)$\rightarrow$($3p^5 4s3d\ ^2P$) states. The entrance and exit slits used for figure 5.3 were both set to 100 μm and the time delay between the two lasers was set to 40 ns, with an on-target (sample) irradiance of $\sim 1 \times 10^9$ Wcm^{-2}.

Figure 5.3 (a) is the summation of five individual source images (I_0), which are in themselves the accumulation of ten laser shots. The thermal background (Bg:1) has been subtracted from each image of the source prior to summation.

Figure 5 3 (b) shows the summation of five photoabsorption images (I), in which both source and sample plasmas are formed The front plasma emission (Bg 2) has been subtracted from each image before summation It is clear from figure 5 3 (b) that a portion of the beam passing through the centre of the field of view, but offset to the left-hand side is attenuated (indicated by the white arrow) This attenuation is caused by the absorption of the VUV photons in the sample plasma

Figure 5 3 (c) shows the equivalent width W_λ image, which is the result of equation 3 1 Since the majority of absorbed photons, result in emitted electrons only, this image can be considered a genre of "photoionisation image"

5.3 Equivalent Width Maps

In this section we will present time and space resolved maps of equivalent width W_λ, of expanding calcium plasmas, tracking the Ca^+ 3p-3d resonance transition at 37 34 nm Four image sets will be presented in this section

The first image set (figures 5 4 and 5 5) show the expansion dynamics of plasmas generated using 200 mJ pulses focussed to a line, with dimensions of $\sim$ 0 2 $\times$ 8 mm The laser pulse is propagating from right to left on the image and strikes the target surface The approximate position of the target face has been indicated by the vertical white line drawn on each image The plasma then expands away from the target surface (left to right on the images) The pixels on the CCD have been binned 6 $\times$ 6 and the CCD chip has been cooled to -20° C to improve SNR The entrance and exit slits of the monochromator were set to 100 μm each The knife edge (described in section 4 4 5), used to occlude the hottest part of the plume, at very early time delays, was positioned 200 μm in front of the target surface The image set tracks the plasma expansion from 40 to 1000 ns

The second image set (figures 5 6 and 5 7) show the expansion dynamics of point plasmas using the same parameters as the previous image set except for the fact that a spherical lens was used to focus the laser beam to a $\sim$ 0 2 mm diameter spot In order to compensate for the reduced spot size the laser energy was also reduced to 110 mJ using the Brewster angle polariser and half-wave plate Without doing this the source plasma emission (Bg 2) would totally saturate the CCD camera

making measurements impossible. This image set tracks the plasma expansion from 40 to 1000 ns.

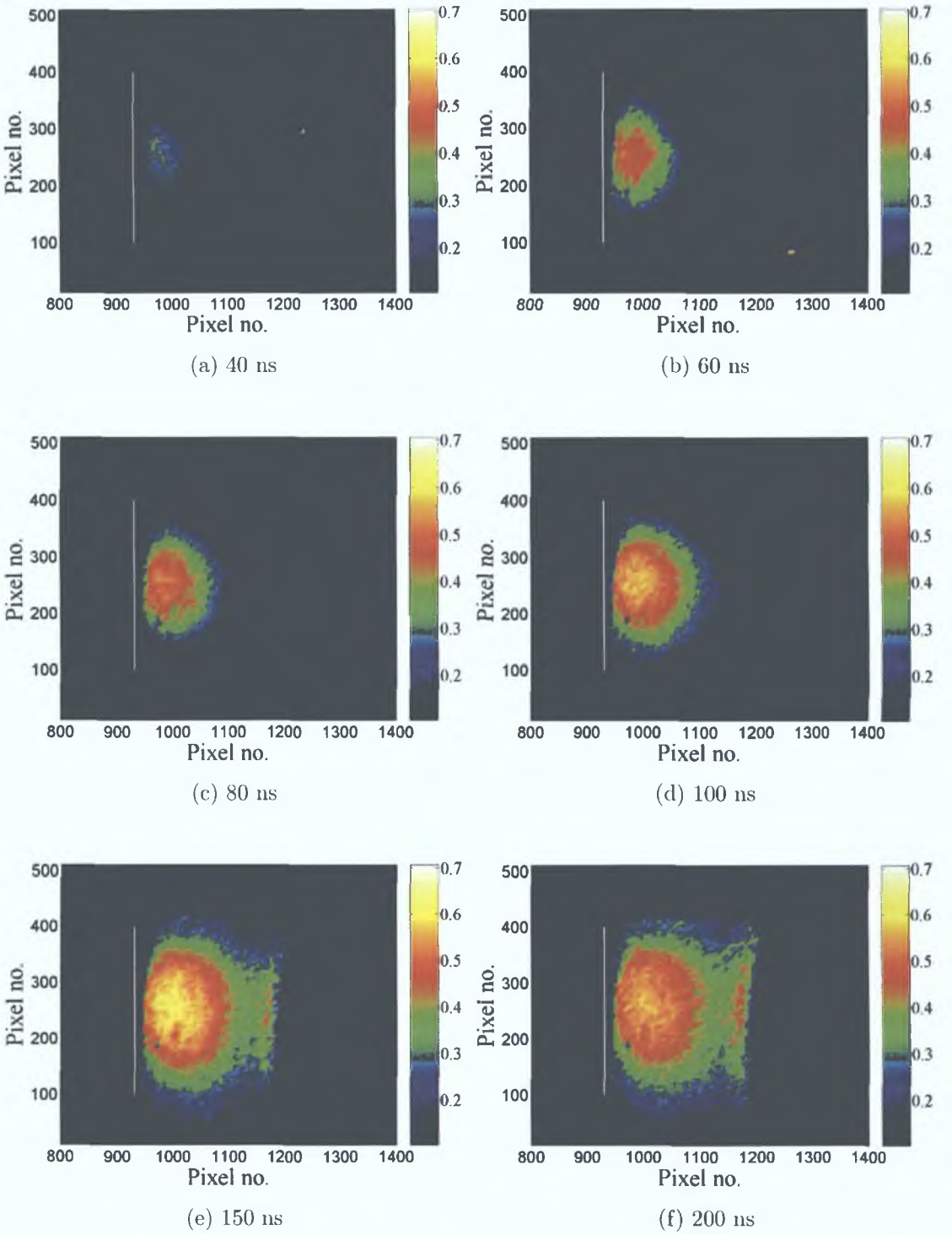

(a) 40 ns

(b) 60 ns

(c) 80 ns

(d) 100 ns

(e) 150 ns

(f) 200 ns

Figure 5.4: Time and space-resolved maps of equivalent width W_λ (in Angstroms), of a single expanding (line) plasma, tracking the Ca^+ 3p-3d resonance transition at 37.34 nm, from 40 to 200 ns.

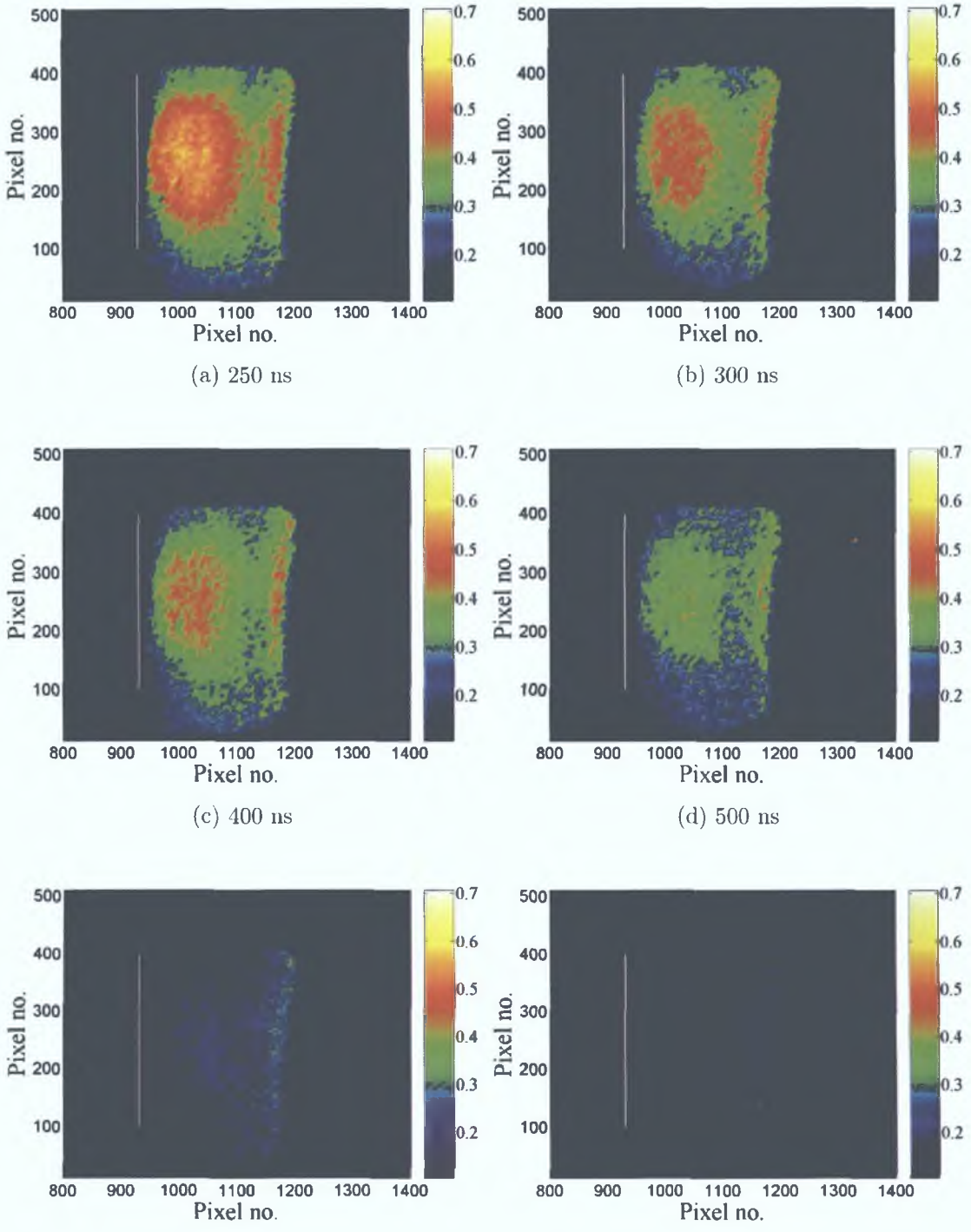

(a) 250 ns

(b) 300 ns

(c) 400 ns

(d) 500 ns

(e) 700 ns

(f) 1000 ns

Figure 5.5: Time and space-resolved maps of equivalent width W_λ (in Angstroms), of a single expanding (line) plasma, tracking the Ca^+ 3p-3d resonance transition at 37.34 nm, from 250 to 1000 ns.

The third image set (figures 5 8 and 5 9) show the expansion dynamics of two calcium plasmas generated next to each other on a flat surface The experimental parameters used are the same as those used in the first image set, except for the fact that the laser beam was split in two using a 1° wedge prism (as was shown in figure 4 13, section 4 4 5) This resulted in a separation between the two plasmas of approximately 0 75 mm In this image set it was also possible to retract the knife edge so that it protruded only some 100 μm in front of the target surface, without seriously increasing the background due to front plasma (Ca) emission (Bg 2) The image set tracks the plasma expansion from 40 to 700 ns The colour scales used on all images in the first three image sets have been kept the same to aid comparisons

The final image set (figures 5 10 and 5 11) show the expansion dynamics of two calcium plasmas generated on an angled target This geometry caused many difficulties, mainly due to the fact that the knife edge could not be used to block early time-scale plasma emission and still record the overlap region between the plumes For this reason the laser energy was reduced to 60 mJ and no knife edge was used, thereby severely reducing the amount of material ablated from the target and the time-scales over which an absorption signal could be detected The low particle density resulted in weak absorption signals The image set tracks the plasma expansion from 10 to 100 ns

If we begin by looking at figure 5 4, it may be seen that as time progresses an almost spherical plume cross-section is recorded on the CCD The transverse expansion velocity parallel to the target surface is similar in magnitude to the primary expansion axis perpendicular to the target surface The actual plume shape is more circular than that shown in the images in figure 5 4, it is somewhat like a circle touching the target surface at one point The flattened profile observed on the left hand side of each plume is caused by the protruding knife edge covering a portion of the plume The position of the target face is located slightly to the left of the white vertical line drawn on the image as a guide At approximately 150 ns (figure 5 4 (e)) the plume front has reached the far edge of the viewing window, limited by the width of the VUV probe beam cross-section At 250 ns (figure 5 5 (a)) almost the entire extent of the VUV probe beam, vertical and horizontal experiences attenuation due to the sample plasma From this time delay forward the density of Ca^+ species in the plume decreases until 1000 ns (figure 5 5 (f)) when

only residual absorption from the plume is observed (on this scale).

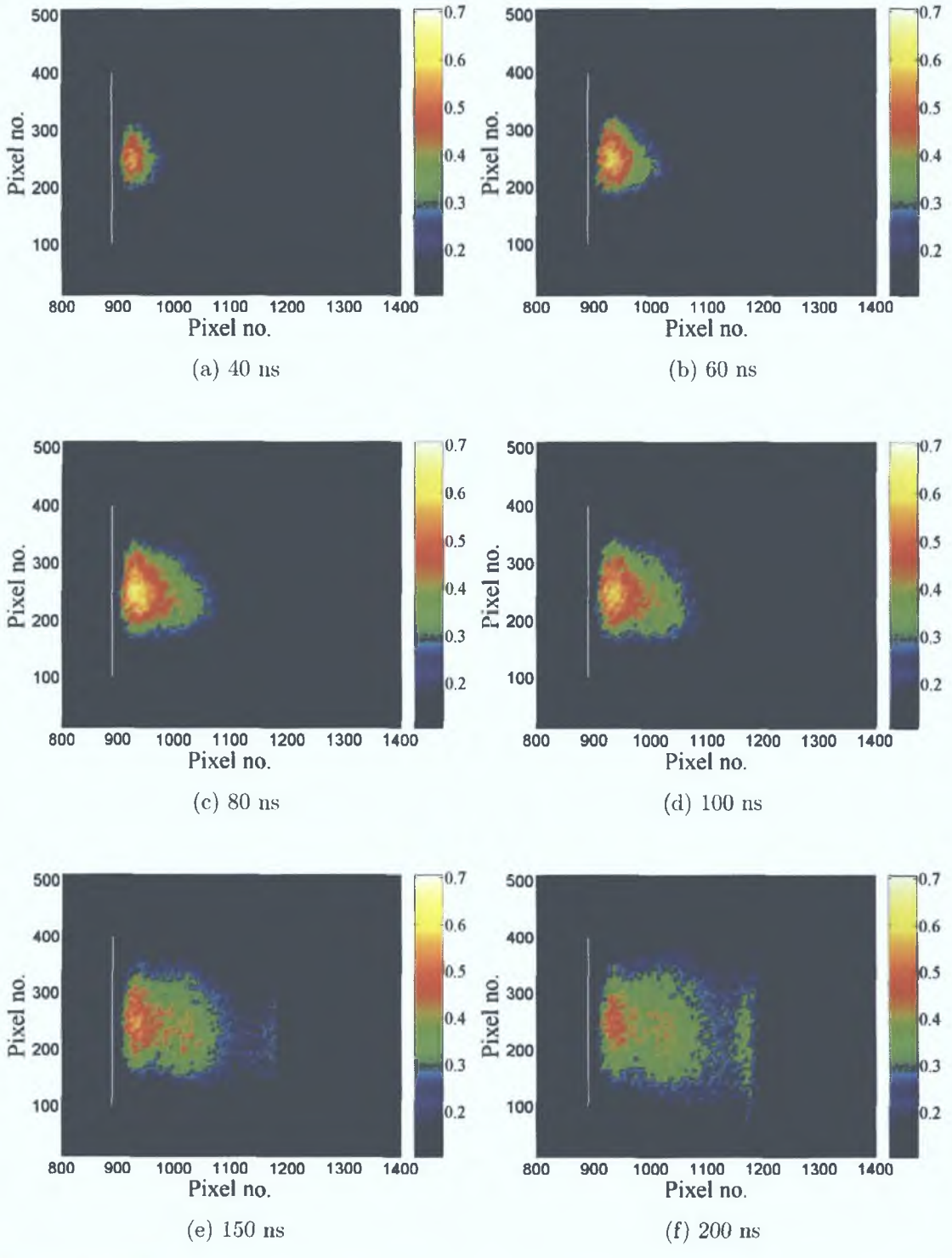

(a) 40 ns

(b) 60 ns

(c) 80 ns

(d) 100 ns

(e) 150 ns

(f) 200 ns

Figure 5.6: Time and space-resolved maps of equivalent width W_λ (in Angstroms), of a single expanding (point) plasma, tracking the Ca^+ 3p-3d resonance transition at 37.34 nm, from 40 to 200 ns.

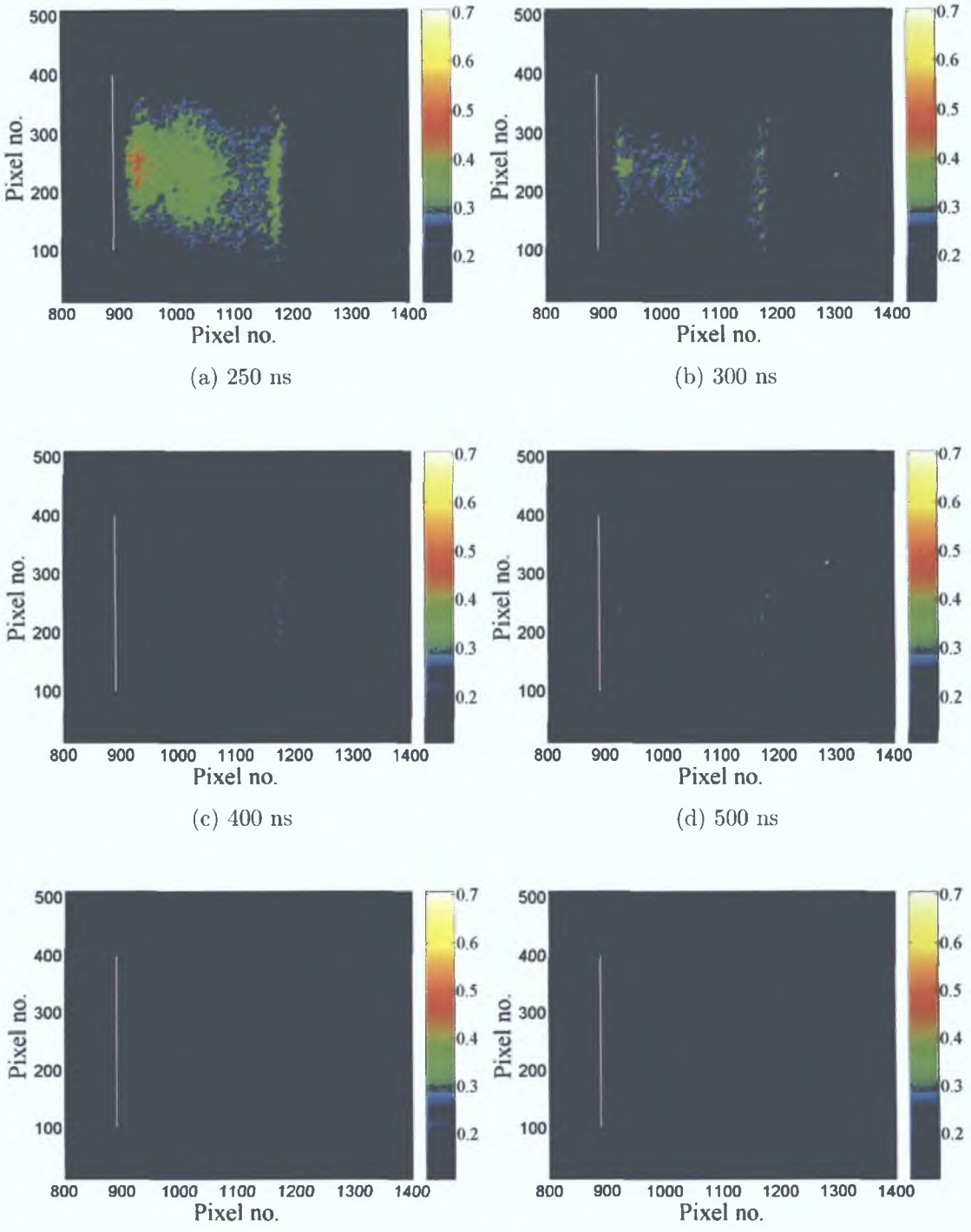

(a) 250 ns

(b) 300 ns

(c) 400 ns

(d) 500 ns

(e) 700 ns

(f) 1000 ns

Figure 5.7: Time and space-resolved maps of equivalent width W_λ (in Angstroms), of a single expanding (point) plasma, tracking the Ca^+ 3p-3d resonance transition at 37.34 nm, from 250 to 1000 ns.

Figure 5 6 shows the temporal evolution of a calcium plasma generated with a point focus The shape of the plume is quite different to that presented in figure 5 4 Here the expansion velocity is greater perpendicular to the target than the expansion velocity parallel to the target face This gives the plume a more pointed profile than the previous case (figure 5 4) however the overall expansion velocity appears to be smaller than that seen in figure 5 4 At 150 ns (figure 5 6 (e)) the plume front has not quite touched the far edge of the probe beam This is probably due to the lower on-target irradiance used in this case to prevent saturation of the CCD camera Figure 5 6 (f) shows the plume 200 ns after plasma initiation This is the point of maximum absorption, from this point on the magnitude of the absorption decreases rapidly, considerably faster than that of the line plasma shown in the previous data set Only minor absorption is evident after 400 ns (figure 5 7 (c))

Figure 5 8 shows the expansion of two calcium plasmas generated next to each other on a flat target The position of the protruding knife edge has been retracted to a distance of 100 μm in front of the target face For this reason the volume of plasma visible 40 ns after initiation is greater than that observed in the previously presented image sets At 40 ns (figure 5 8 (a)) the two calcium plumes already overlap yet no significant enhancement (or decrease) in the absorption signal is observed from the overlap region The individual plume shapes again appear to be quite circular at early time delays (figure 5 8 (a) and (b)), similar to the first image set (figure 5 4) This is unsurprising considering the same cylindrical lens was used to generate line plasmas in both cases The ratio of the incident laser energy between the two plumes was ~ 1 1 The amount of absorption observed and the volumes of the individual plumes appears to support that fact for the first few time delays (figure 5 8 (a), (b) and (c)) However as time progresses the upper plume appears to weaken while the lower plume remains strong It may be seen from figure 5 8 (c), taken 150 ns after plume initiation, that the spatial extent of the lower plume is considerably greater than that of the upper one This trend continues in figure 5 9 at later time delays It may be observed from figure 5 9 (a) that at this time delay only one plume can be seen This plume is considerably longer perpendicular to the target surface than it is wide (parallel to the target face) This behaviour is in contrast with the single line plasma plume at this time delay (figure 5 6 (a)), which completely covered the horizontal and vertical extent of the probe beam The laser energy supplied to the surface for both of these images was equivalent

The final image set (figure 5 10 and 5 11) was an attempt to use an angled target configuration to force the plasmas together with a higher relative collision velocity Numerous attempts were made to fine tune the irradiation conditions to balance front plasma emission with appreciable ablation volumes An angled knife edge setup using crossed blades was also tried to occlude early plasma emission, however accurate positioning was prohibited due to space restrictions in the vacuum chamber and the fact that micrometer control was available only on the horizontal axis

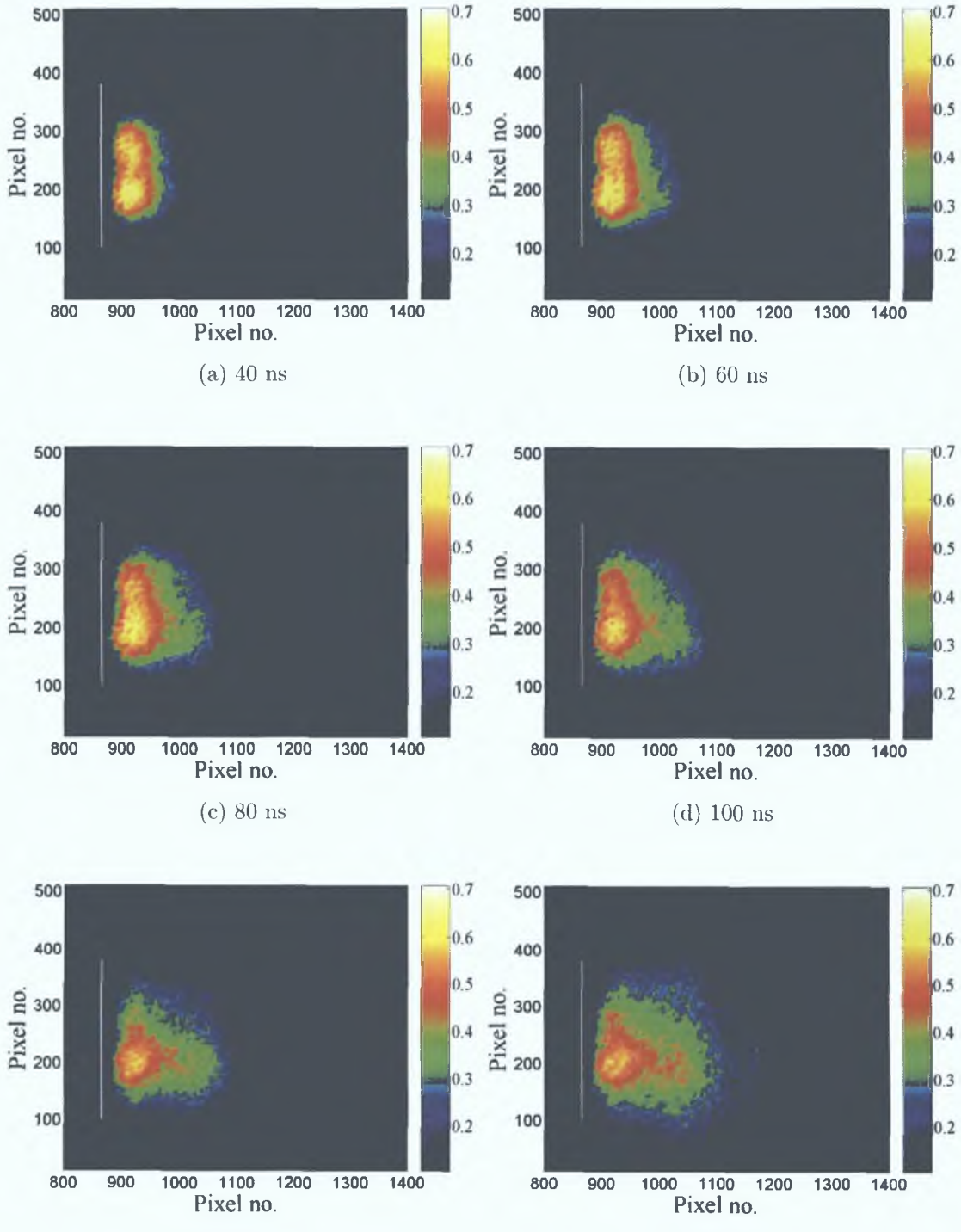

(a) 40 ns

(b) 60 ns

(c) 80 ns

(d) 100 ns

(e) 150 ns

(f) 200 ns

Figure 5.8: Time and space-resolved maps of equivalent width W_λ (in Angstroms), of colliding (line) plasmas on a flat target, tracking the Ca^+ 3p-3d resonance transition at 37.34 nm, from 40 to 150 ns.

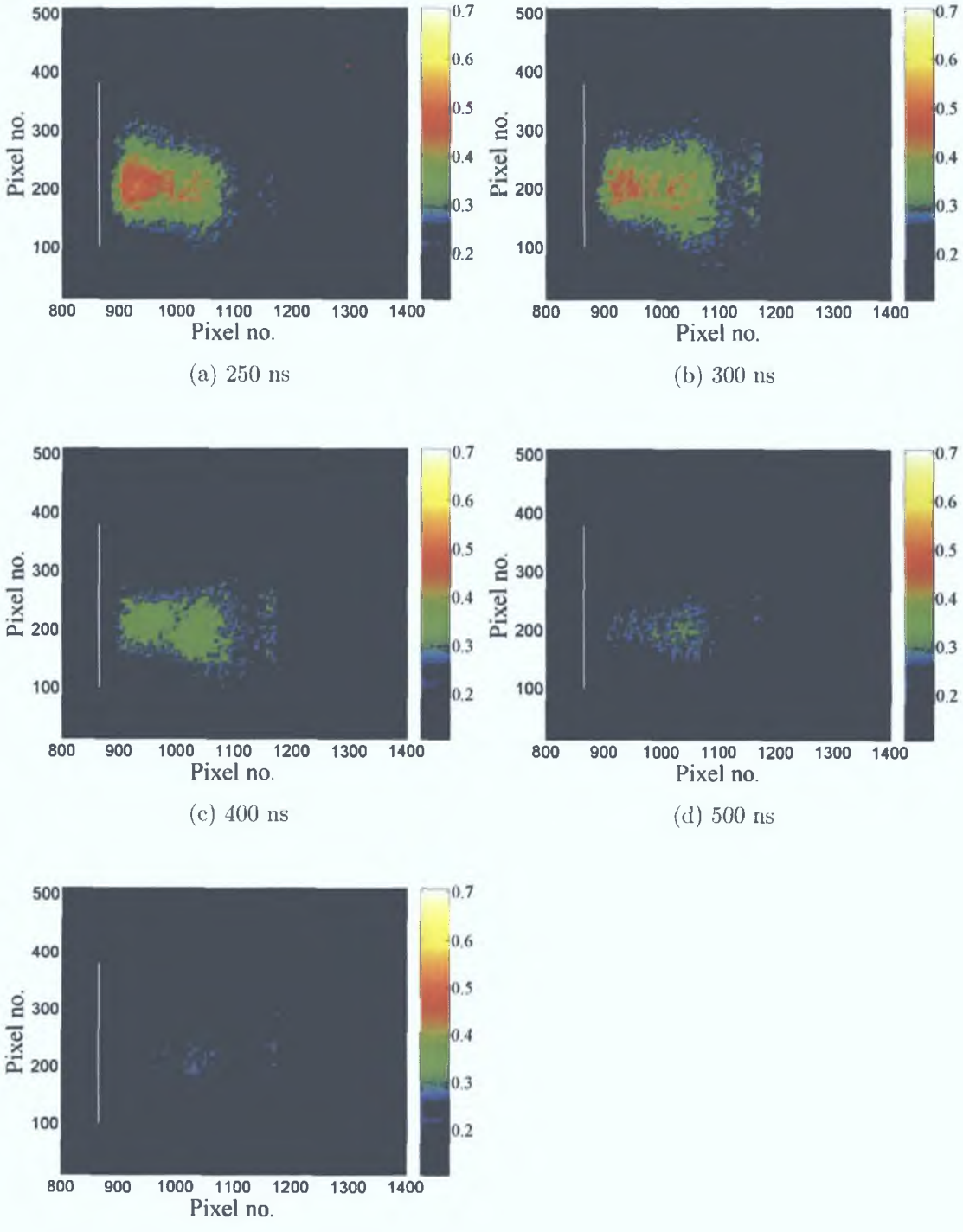

(a) 250 ns

(b) 300 ns

(c) 400 ns

(d) 500 ns

(e) 700 ns

Figure 5.9: Time and space-resolved maps of equivalent width W_λ (in Angstroms), of colliding (line) plasmas on a flat target, tracking the Ca^+ 3p-3d resonance transition at 37.34 nm, from 200 to 500 ns.

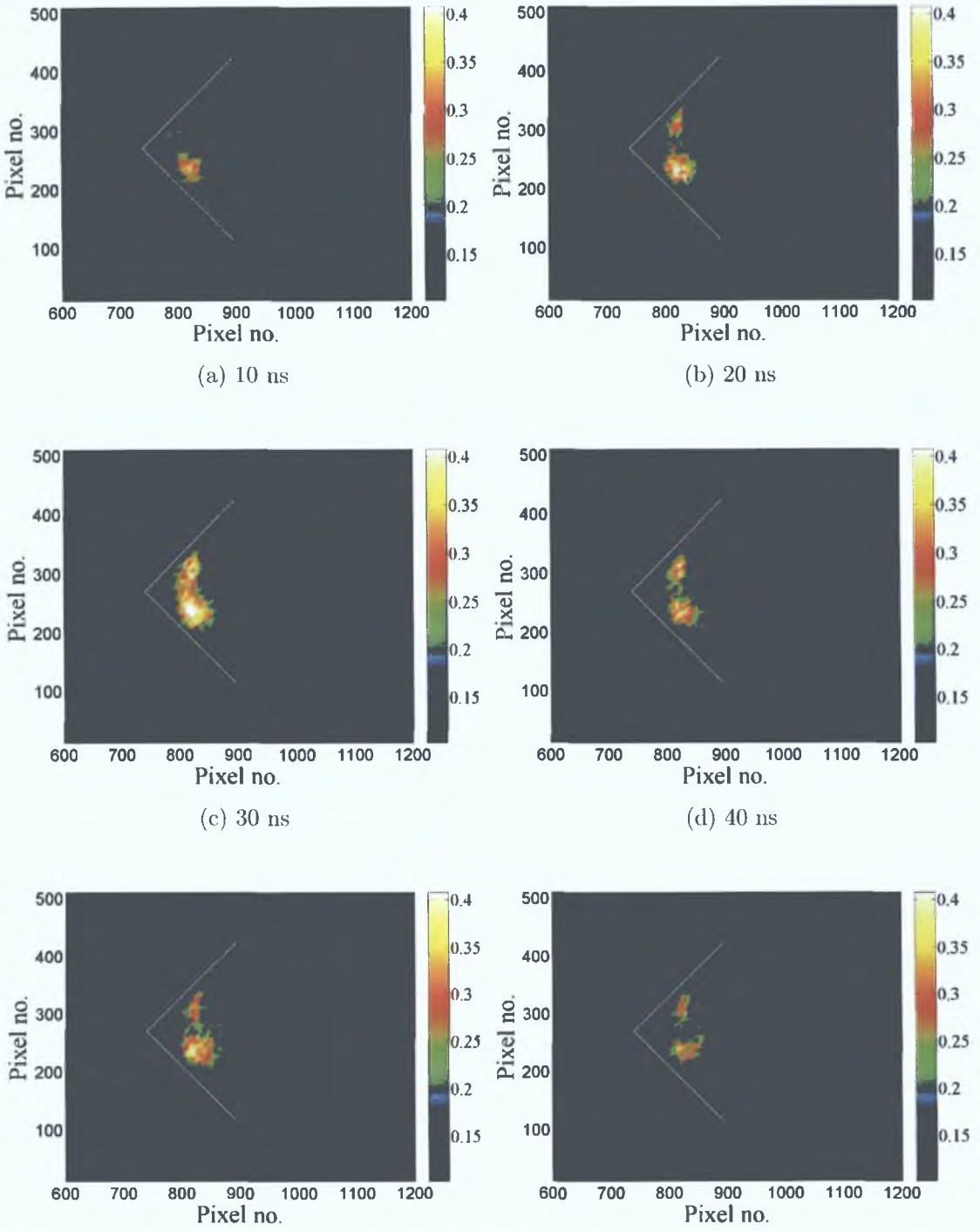

(a) 10 ns

(b) 20 ns

(c) 30 ns

(d) 40 ns

(e) 50 ns

(f) 60 ns

Figure 5.10: Time and space-resolved maps of equivalent width W_λ (in Angstroms), of colliding (line) plasmas on an angled target, tracking the Ca^+ 3p-3d resonance transition at 37.34 nm, from 10 to 60 ns.

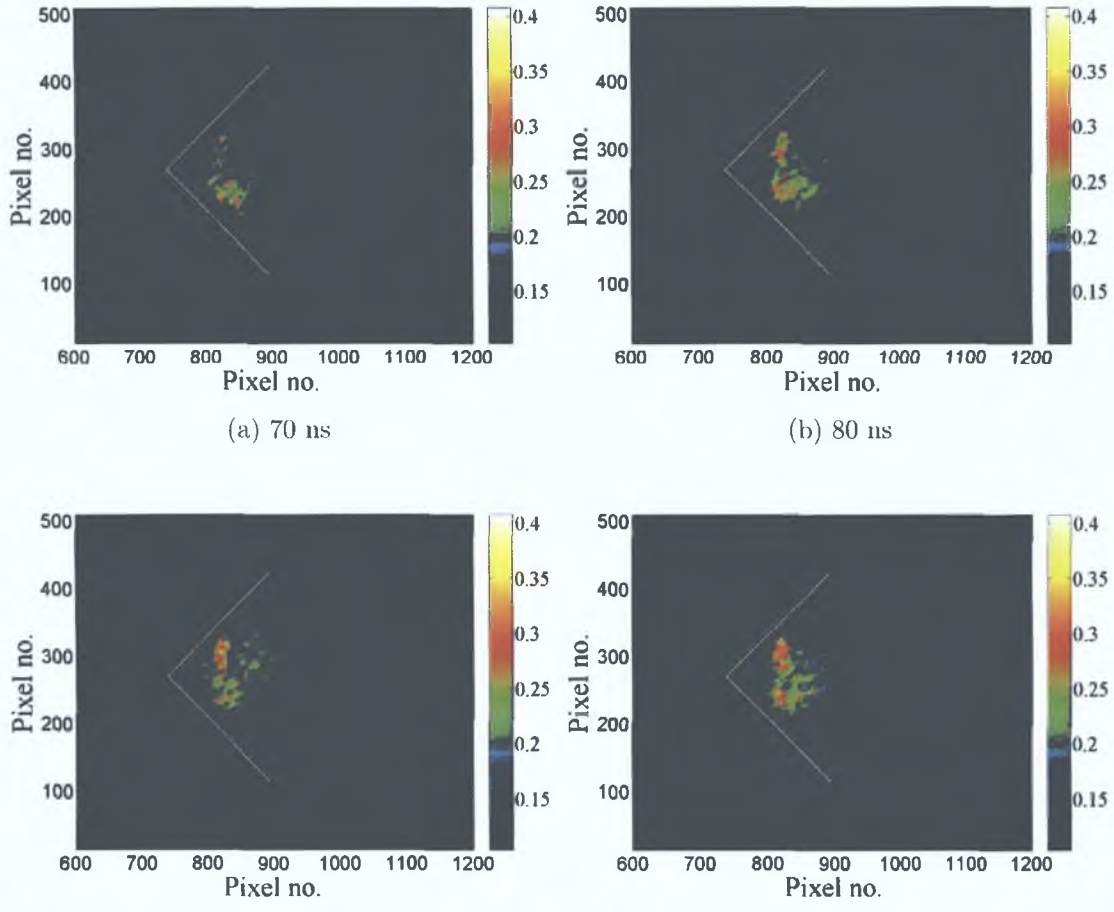

(a) 70 ns

(b) 80 ns

(c) 90 ns

(d) 100 ns

Figure 5.11: Time and space-resolved maps of equivalent width W_λ (in Angstroms), of colliding (line) plasmas on an angled target, tracking the Ca^+ 3p-3d resonance transition at 37.34 nm, from 70 to 100 ns.

5.4 Column Density Maps

In this section we will convert all of the equivalent width images presented in the previous section into maps of column density The general expression of the equivalent width given by Corney [10], written as a function of wavelength was used

$$W_\lambda = \int_{\Delta\lambda} (1 - exp(-NL \int_{\Delta\lambda} \sigma_\lambda d\lambda)) d\lambda \qquad (5\ 2)$$

where σ_λ is the absolute photoionisation cross section of Ca^+ 3p-3d resonance at 37 34 nm, shown in figure 5 1 measured by Lyon *et al* [3]

The equivalent width maps were converted into column density maps by graphically solving equation 5 2 The procedure is as follows A range of possible NL values was inserted into equation 5 2 and the equivalent width values associated with those column densities were calculated by performing the integration over the 3p-3d cross section Next a plot of NL versus equivalent width was constructed, this is shown in figure 5 12 Using this plot experimentally recorded equivalent width values are converted into column density values, pixel by pixel

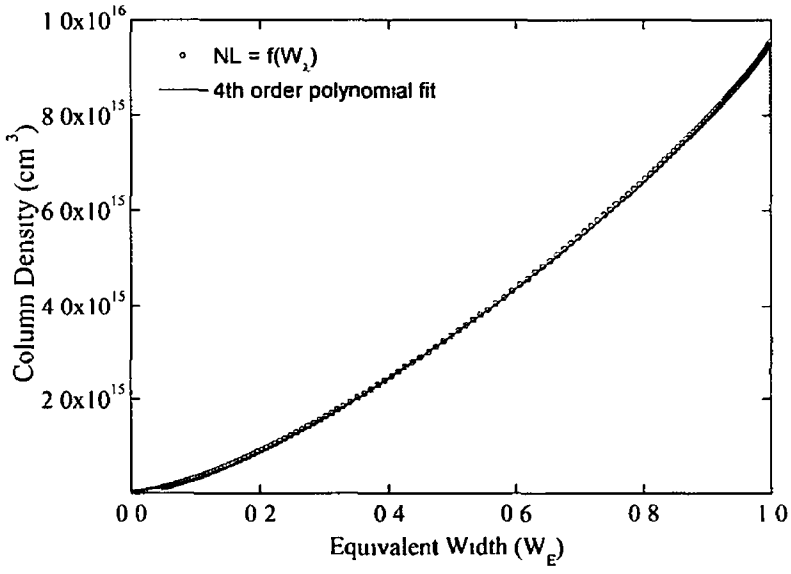

Figure 5 12 Relationship between the column density NL and the equivalent width W_λ for the Ca^+ 3p-3d resonance transition at 33 2 eV

This was achieved by fitting a polynomial function to figure 5 12 and then applying the polynomial to each W_λ image It was found that a 4^{th} order polynomial provided a good fit to this curve with residuals below 0 5 % The specific form of

the quartic equation that was fitted to figure 5 12 is given by

$$NL = C_1 + C_2 W_\lambda + C_3 W_\lambda^2 + C_4 W_\lambda^3 + C_5 W_\lambda^4 \quad (5\ 3)$$

the coefficients of which are given in table 5 1 Figure 5 13 and 5 14 show the column

Table 5 1 Coefficients of polynomial fit to plot of NL vs W_λ (figure 5 12)

Coefficient	Value ($\times 10^{10}$)
C1	$-7\ 055 \times 10^2$
C2	$1\ 735 \times 10^5$
C3	$1\ 698 \times 10^6$
C4	$-1\ 831 \times 10^6$
C5	$9\ 136 \times 10^5$

density maps for the single line plasma data set Figure 5 15 and 5 16 show the column density maps for the single point plasma data set Figure 5 17 and 5 18 show the column density maps for the flat target colliding plasmas data set, and finally the column density maps for the angled colliding plasma data set are shown in figure 5 19 and 5 20 The trends that were discussed in the previous section, when discussing the equivalent width image sets, are valid for all of the column density image sets presented in this section A different colour scale has been used for the column density maps in this section to avoid confusion with the equivalent width maps previously presented

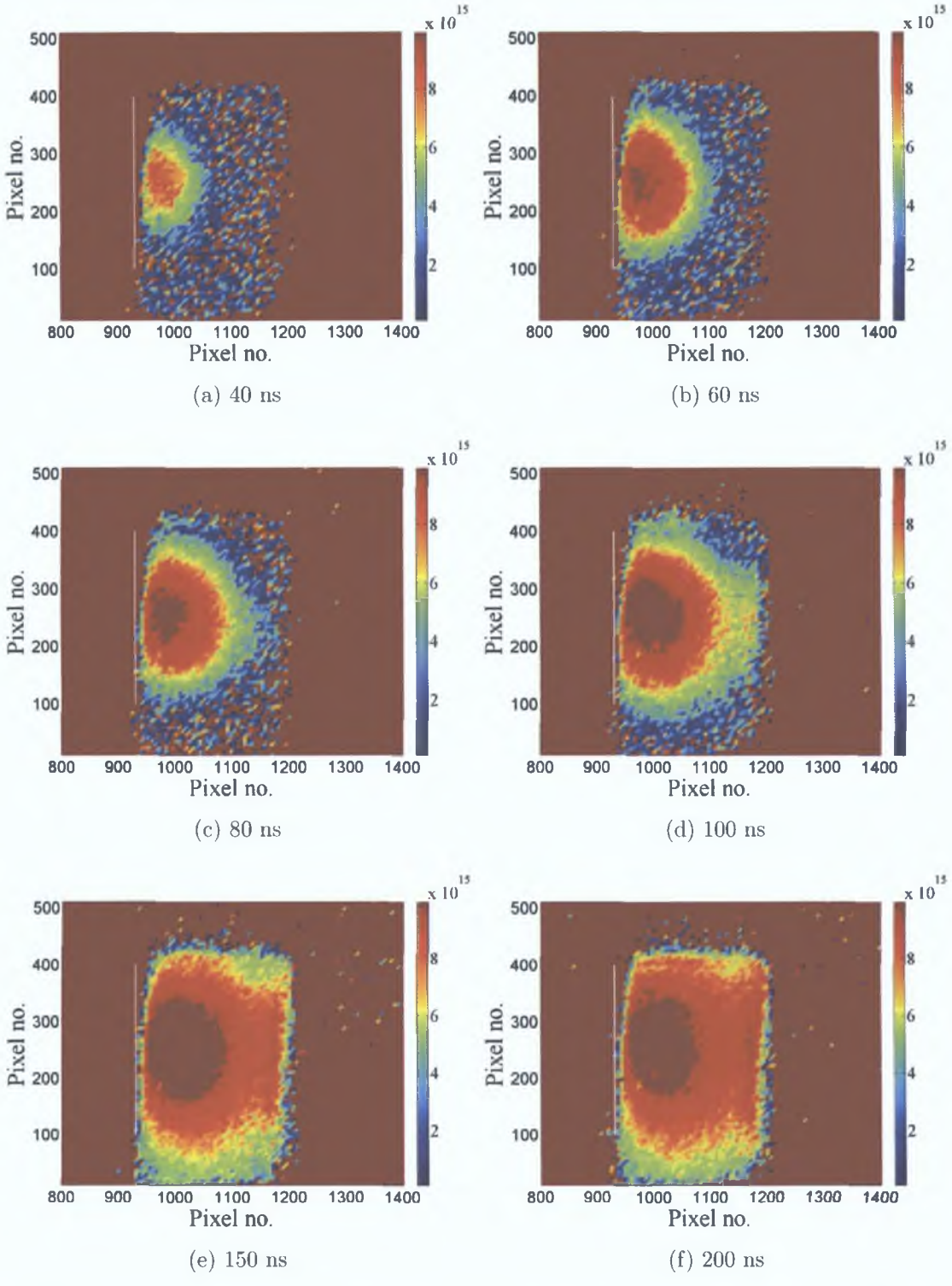

(a) 40 ns

(b) 60 ns

(c) 80 ns

(d) 100 ns

(e) 150 ns

(f) 200 ns

Figure 5.13: Time and space-resolved maps of column density NL, of a single expanding (line) plasma, tracking the Ca^+ 3p-3d resonance transition at 37.34 nm, from 40 to 200 ns.

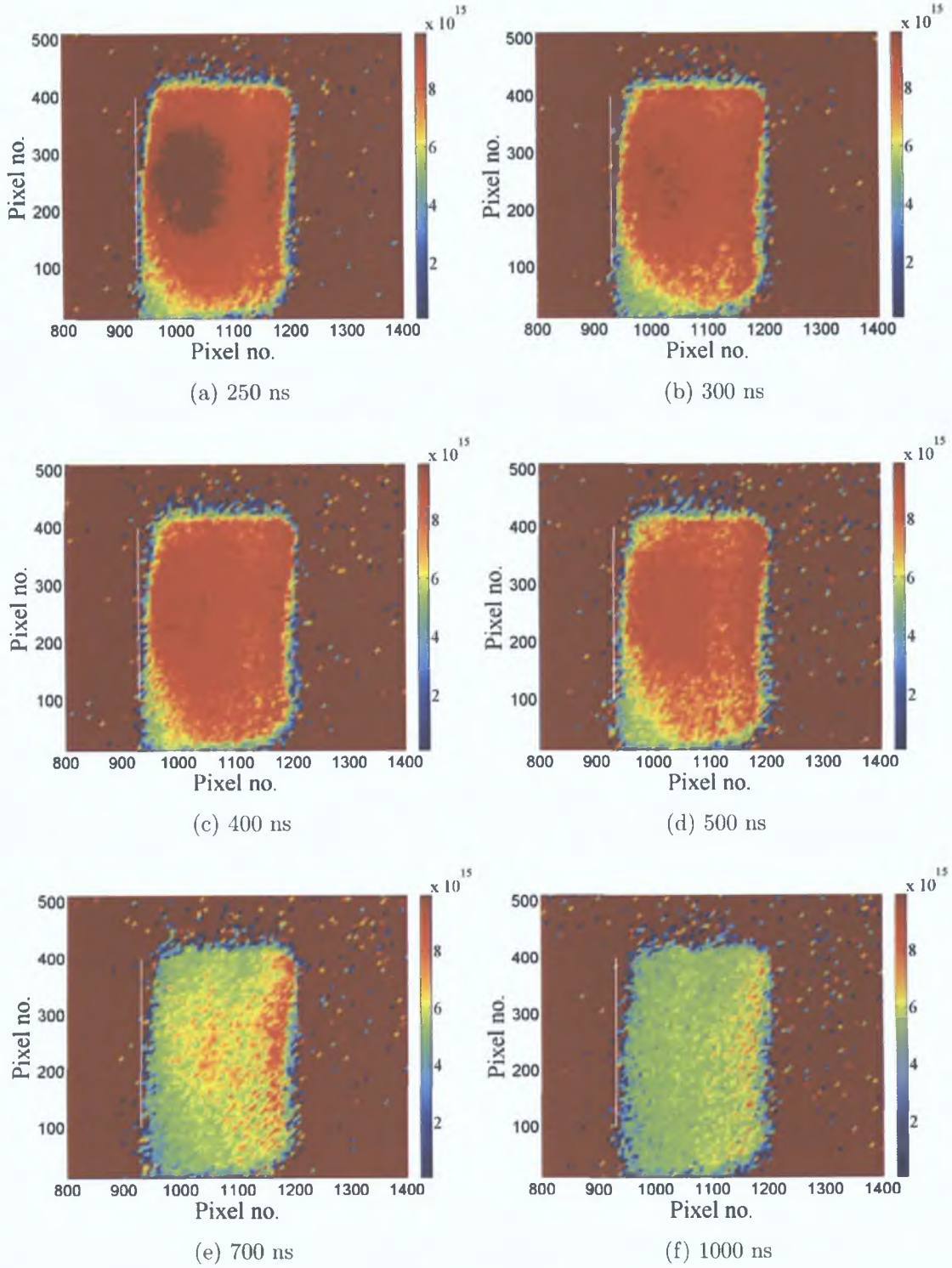

(a) 250 ns

(b) 300 ns

(c) 400 ns

(d) 500 ns

(e) 700 ns

(f) 1000 ns

Figure 5.14: Time and space-resolved maps of column density NL, of a single expanding (line) plasma, tracking the Ca^+ 3p-3d resonance transition at 37.34 nm, from 250 to 1000 ns.

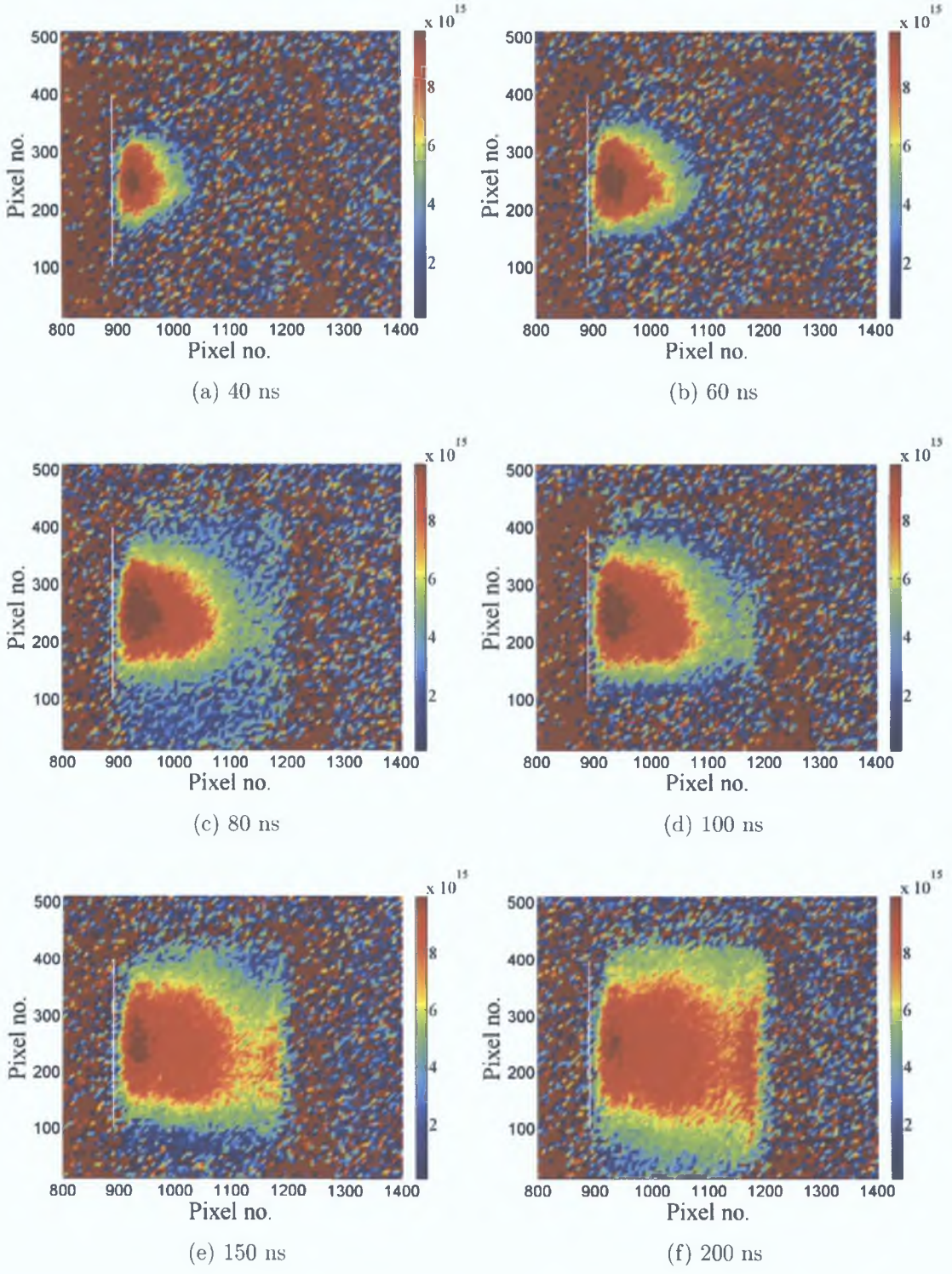

(a) 40 ns

(b) 60 ns

(c) 80 ns

(d) 100 ns

(e) 150 ns

(f) 200 ns

Figure 5.15: Time and space-resolved maps of column density NL, of a single expanding (point) plasma, tracking the Ca^+ 3p-3d resonance transition at 37.34 nm, from 40 to 200 ns.

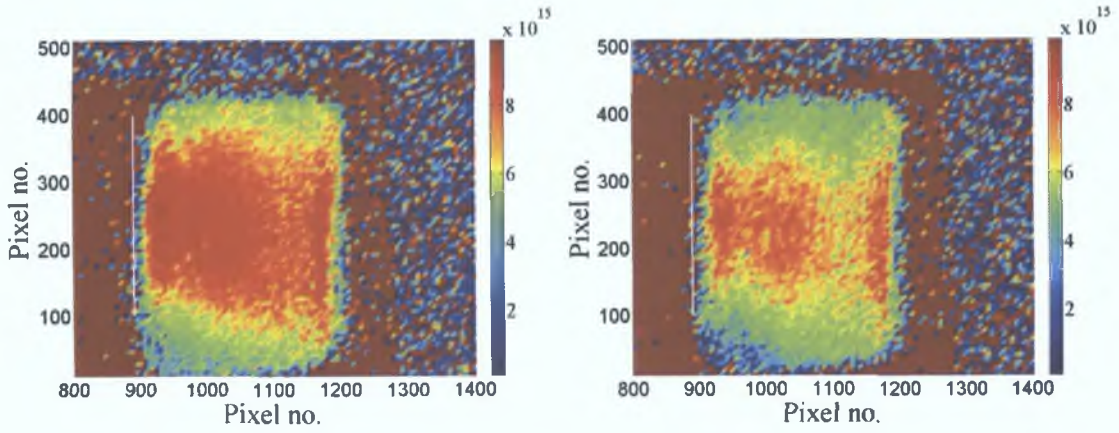

(a) 250 ns

(b) 300 ns

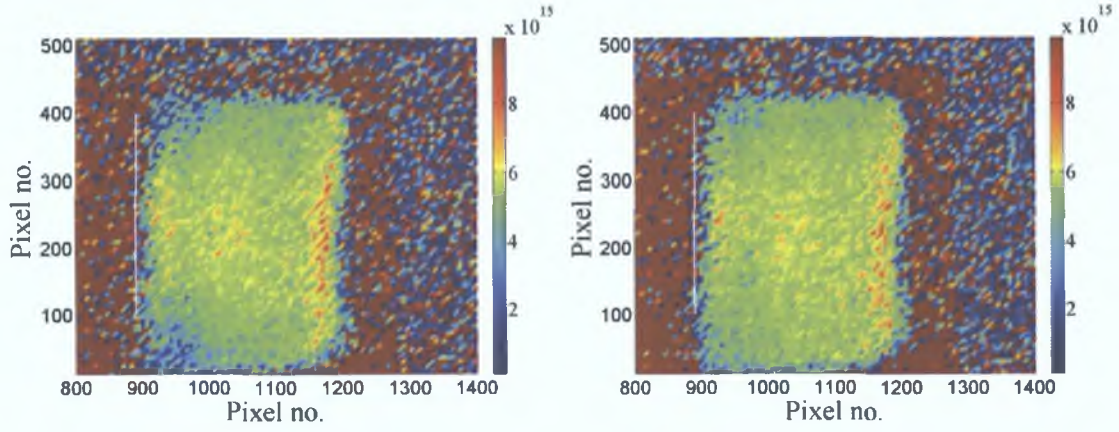

(c) 400 ns

(d) 500 ns

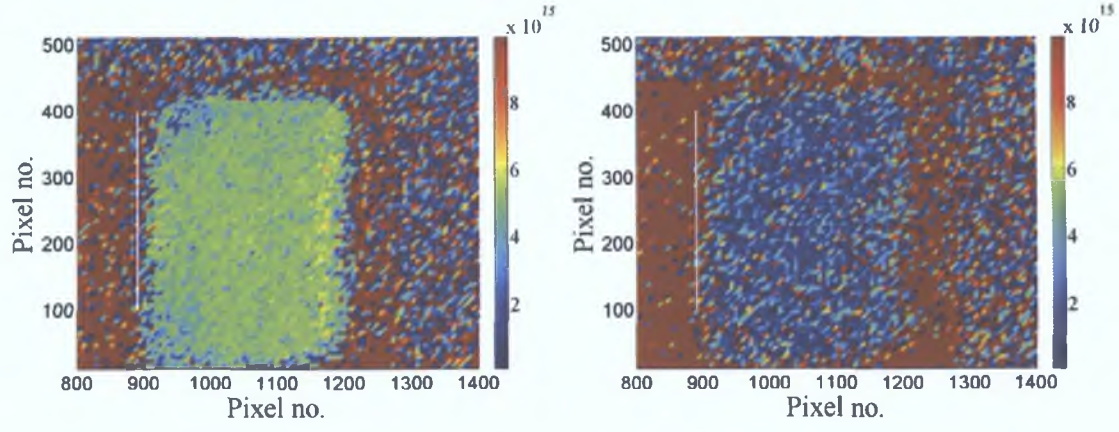

(e) 700 ns

(f) 1000 ns

Figure 5.16: Time and space-resolved maps of column density NL, of a single expanding (point) plasma, tracking the Ca^+ 3p-3d resonance transition at 37.34 nm, from 250 to 1000 ns.

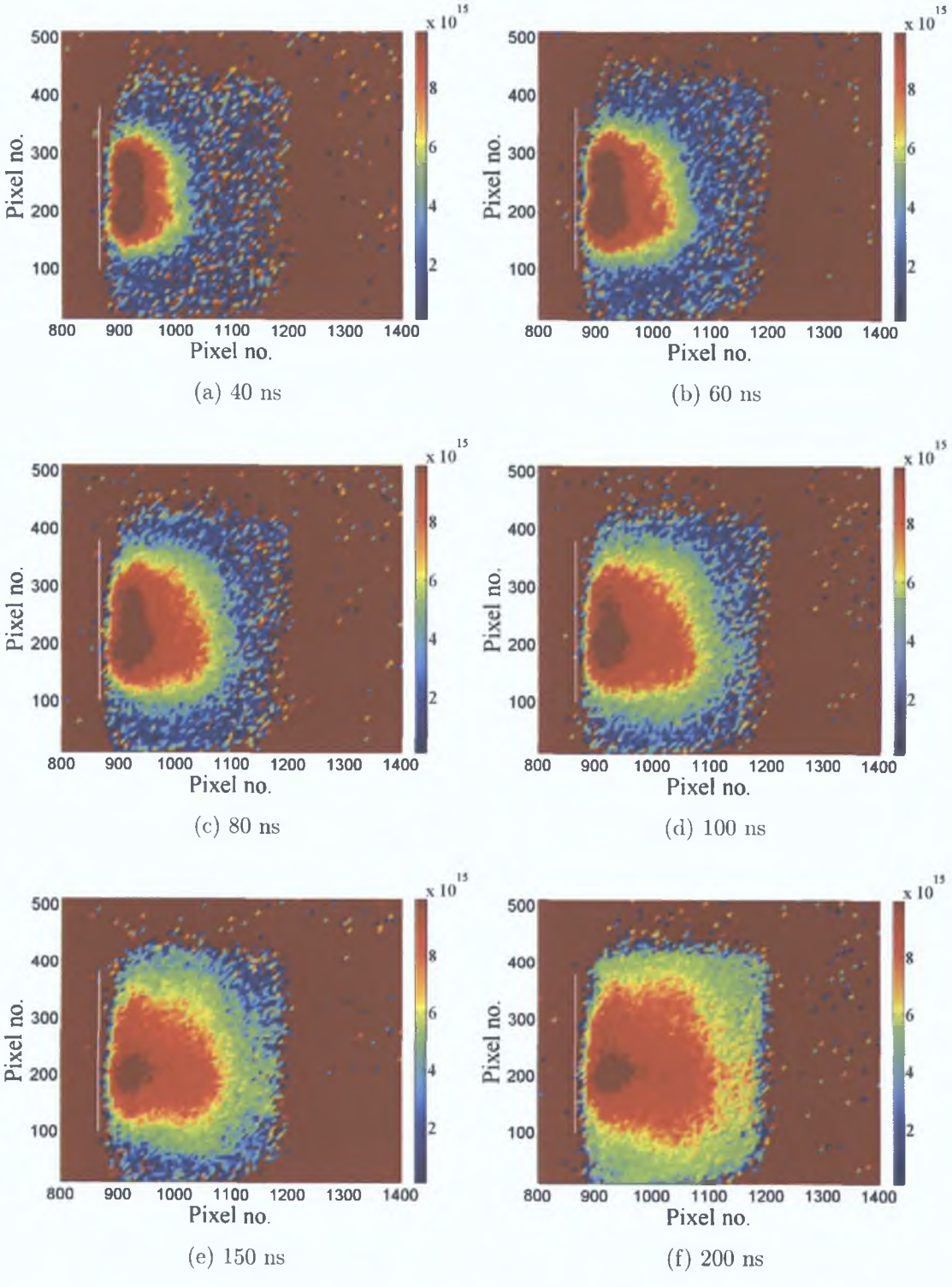

(a) 40 ns

(b) 60 ns

(c) 80 ns

(d) 100 ns

(e) 150 ns

(f) 200 ns

Figure 5.17: Time and space-resolved maps of column density NL, of colliding (line) plasmas on a flat target, tracking the Ca^+ 3p-3d resonance transition at 37.34 nm, from 40 to 150 ns.

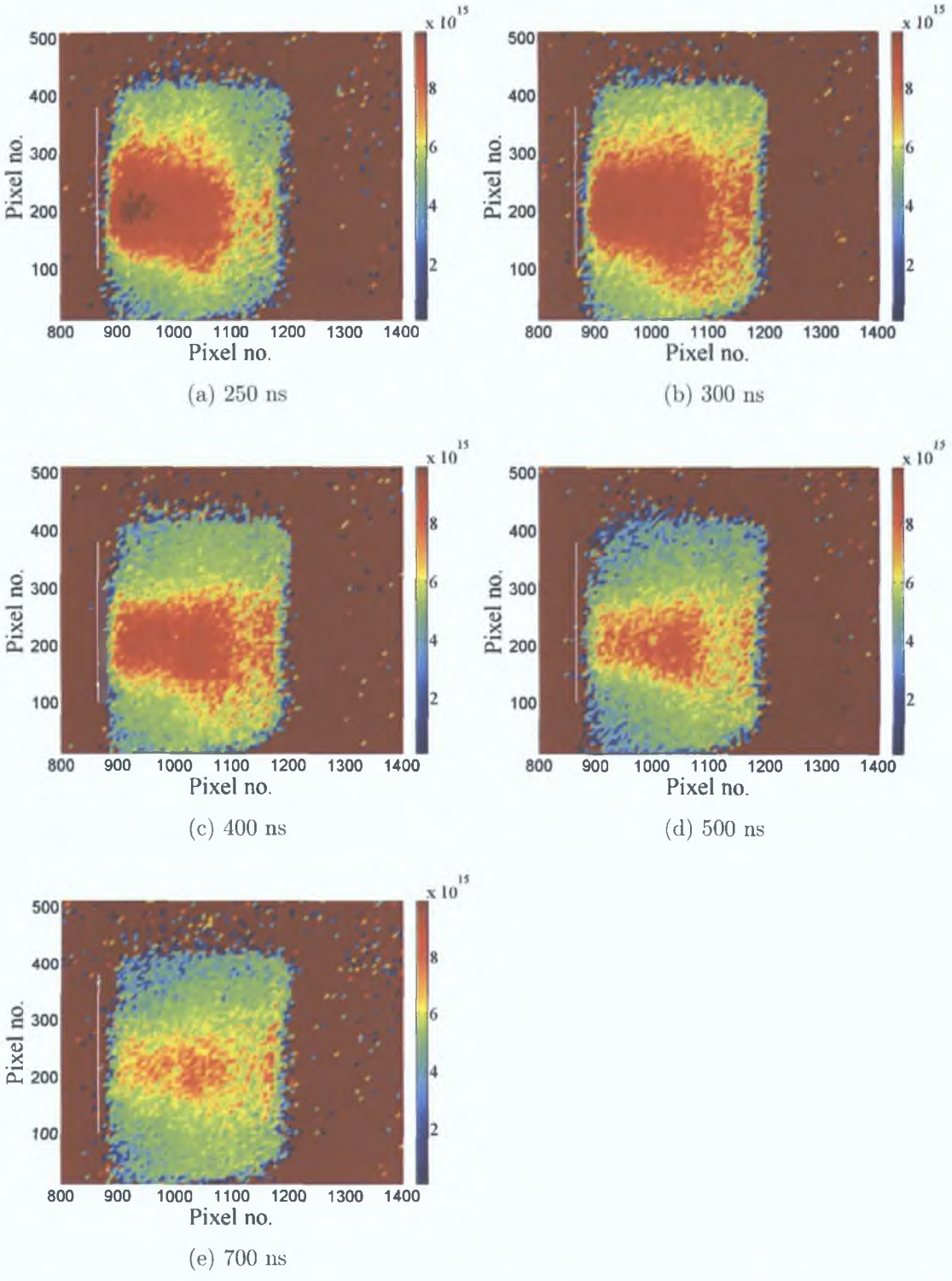

(a) 250 ns

(b) 300 ns

(c) 400 ns

(d) 500 ns

(e) 700 ns

Figure 5.18: Time and space-resolved maps of column density NL (in Angstroms), of colliding (line) plasmas on a flat target, tracking the Ca^+ 3p-3d resonance transition at 37.34 nm, from 200 to 500 ns.

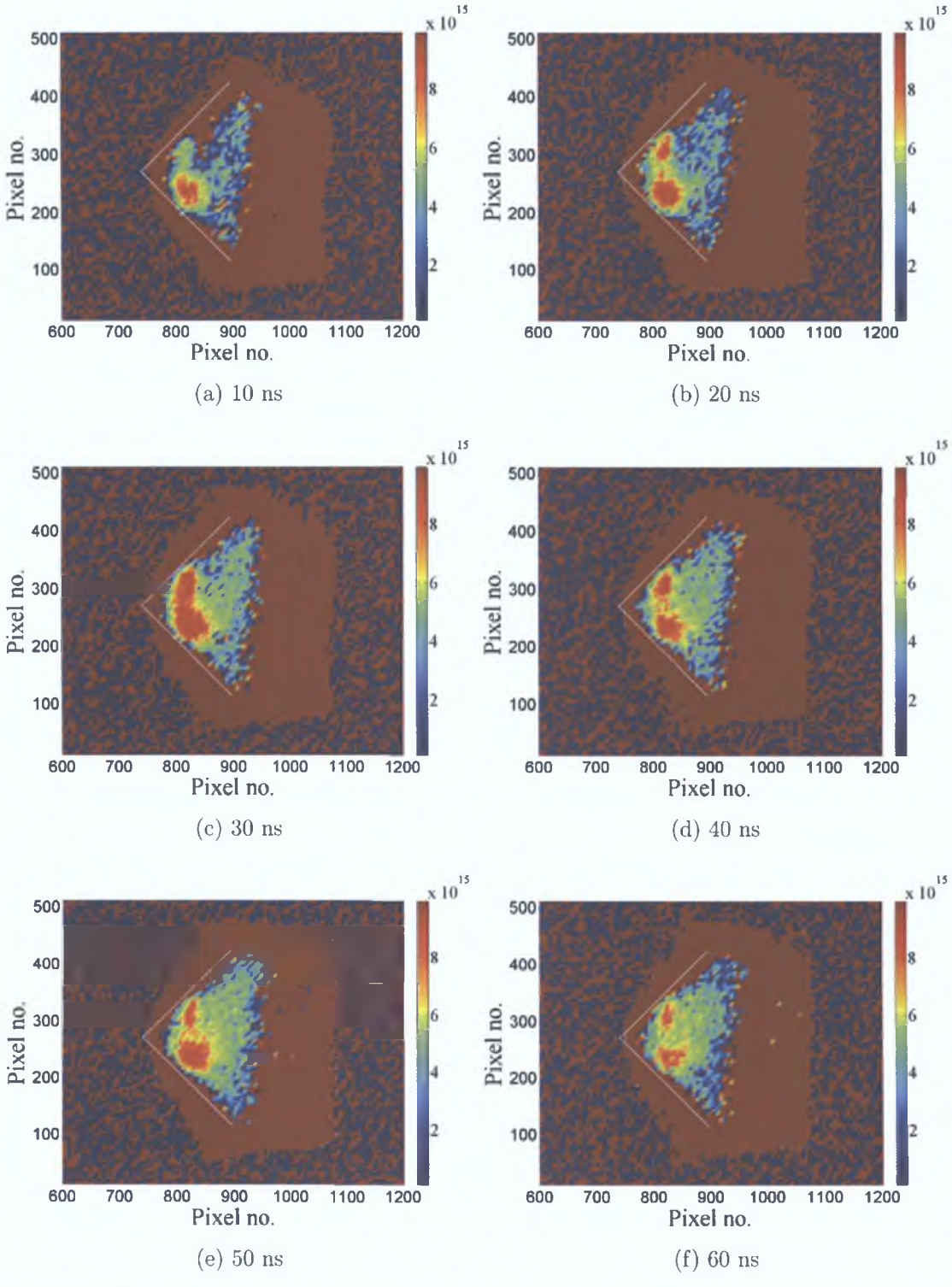

(a) 10 ns

(b) 20 ns

(c) 30 ns

(d) 40 ns

(e) 50 ns

(f) 60 ns

Figure 5.19: Time and space-resolved maps of column density NL, of colliding (line) plasmas on an angled target, tracking the Ca^+ 3p-3d resonance transition at 37.34 nm, from 10 to 60 ns.

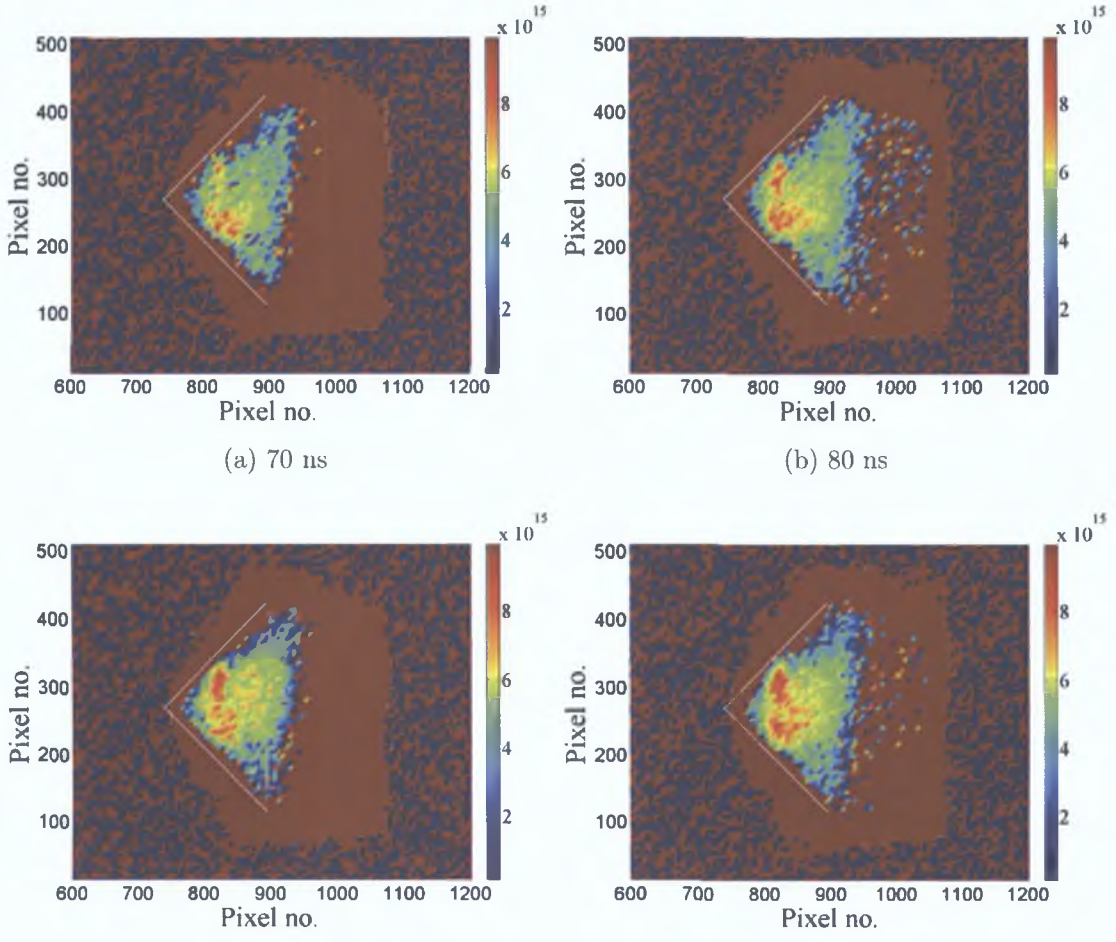

(a) 70 ns

(b) 80 ns

(c) 90 ns

(d) 100 ns

Figure 5.20: Time and space-resolved maps of column density NL, of colliding (line) plasmas on an angled target, tracking the Ca^+ 3p-3d resonance transition at 37.34 nm, from 70 to 100 ns.

5.5 Plasma Dynamics

In this section we extract information concerning the expansion dynamics of single and colliding Ca plasmas from the equivalent width images presented in section 5.3. We will compare our results with the adiabatic expansion model described in section 2.3 using a code developed previously [11].

As mentioned in section 2.3 the adiabatic expansion model best describes the motion of a high pressure, high temperature gas, which is suddenly allowed to expand in vacuum. For this reason comparing images of the Ca^+ component of the plasma, against the Singh and Narayan model [12], may be somewhat limited in applicability but it is nevertheless worthy of at least some comparison.

A number of difficulties present themselves when attempting to extract expansion velocities from the photoabsorption images. The most limiting of these problems is the relatively small viewing area dictated by the dimensions of the VUV probe beam. This translates into a short temporal window from which discernable plume fronts and motion in general can be extracted and analysed. This fact has limited the time delays covered here to the 40 to 150 ns range, after which the plasma has reached the boundary of the VUV beam and can no longer be followed.

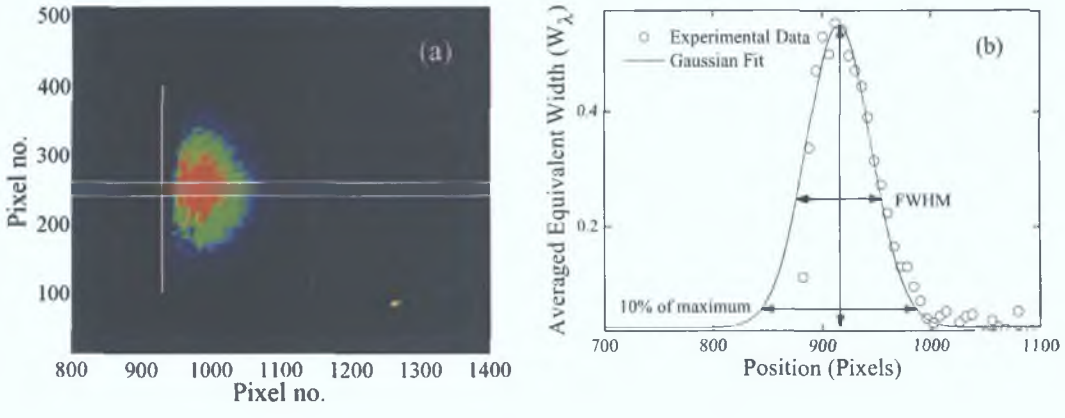

Figure 5.21: Expansion dynamics of a single expanding (line) plasma: (a) Ca^+ equivalent width image taken 40 ns after plasma initiation, (b) Gaussian fit to line-outs from image.

Another difficulty in determining the expansion velocity is deciding what point on the plasma image should be tracked, in order to extract a parameter which one

can credibly call the plume expansion velocity The expansion velocity will vary between the centre of the plume and the plume front Figure 5 21 illustrates the procedure used in this work to calculate expansion velocities from photoabsorption images Ten rows of pixels along the central expansion axis of the plasma were vertically summed and averaged for each time delay, this minimised the effect of random pixel fluctuations from looking along just one row The white horizontal lines shown on figure 5 21 (a) show the boundaries of the summed rows of pixels The averaged trace was then fitted with a Gaussian profile as is shown on figure 5 21 (b)

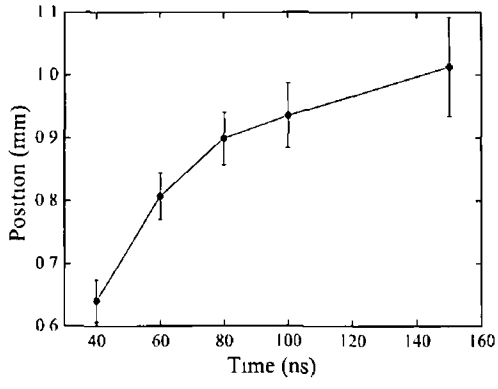

(a) Peak position of Gaussian fits to image line-outs, as a function of time delay

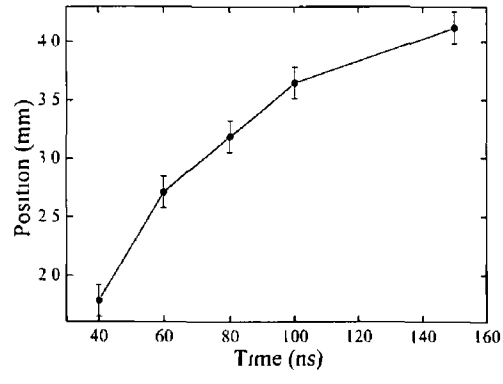

(b) Plasma plume front position as a function of time delay

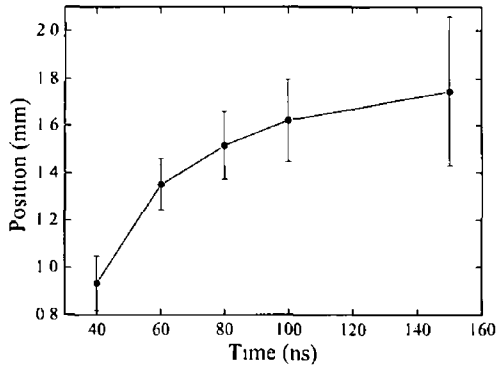

(c) FWHM of Gaussian fits to image line-outs, as a function of time delay

Figure 5 22 Expansion dynamics of a single expanding (line) plasma, extracted from Ca^+ equivalent width maps tracking the 3p-3d resonance transition at 37 34 nm, from 40 to 150 ns

Three parameters were then extracted from the Gaussian fits and plotted as a function of time delay. The first was the position of the centre of the Gaussian, corresponding to the position of maximum absorption. The second was the FWHM of the Gaussian, which gave an indication of how the profile of the plasma plume broadened with time; and the third was the position of 10% of the maximum value of the fit at the leading edge of the plasma, taken to be a measure of the plume front position. These values have been plotted along with the errors associated with the fitting procedure for single and colliding plasmas in figures 5.22 and 5.23.

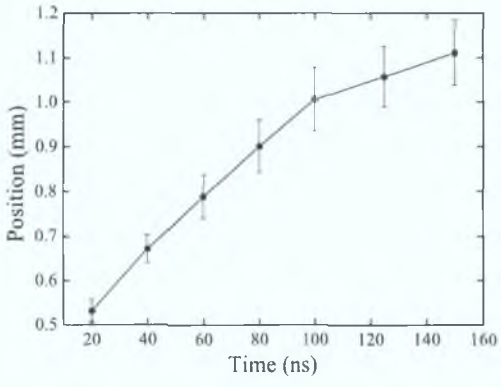

(a) Peak position of Gaussian fits to image line-outs, as a function of time delay.

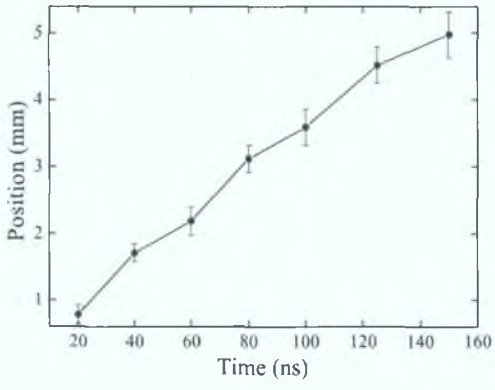

(b) Plasma plume front position as a function of time delay.

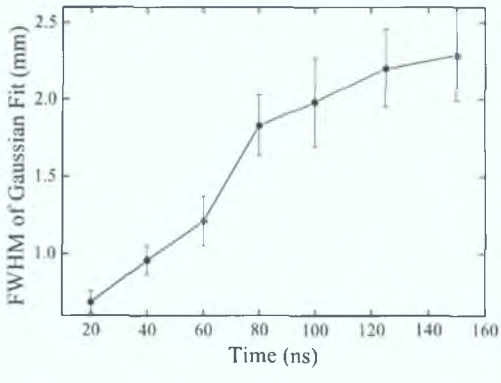

(c) FWHM of Gaussian fits to image line-outs, as a function of time delay.

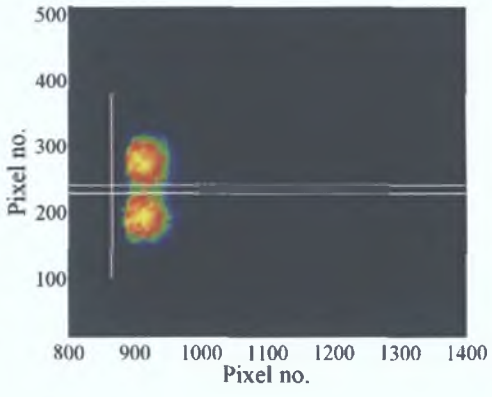

(d) Position of line-out used for colliding plasma expansion velocities

Figure 5.23: Expansion dynamics of a single expanding (line) plasma, extracted from Ca^+ equivalent width maps tracking the 3p-3d resonance transition at 37.34 nm, from 40 to 150 ns.

Figure 5 22 shows the results obtained from the equivalent width image set shown in figure 5 4, for a single expanding line plasma generated using a cylindrical lens Figure 5 21 (b) shows the position of the line-outs used for this data set It may be seen from figure 5 22 (a) and (b) that the plume front position moves considerably faster than that of the position of peak absorption within the plume This broadens the profile of the plume as is shown in figure 5 22 (c) with the increasing FWHM of the Gaussian fits It is interesting to note that in this image set the expansion velocity of the plume appears to be slowing with time This is contrary to what would be expected in simple adiabatic expansion in vacuum

Figure 5 23 shows the results obtained from line-outs taken between two colliding plasmas, corresponding to the equivalent width data sets shown in figures 5 8 and 5 9 The position of the line-outs between the two plasmas is illustrated in figure 5 23 (d) It is interesting to note that the expansion profiles for the overlap region between the two plumes is quite different to that of the single plume expansion The plume front position as a function of time (figure 5 23 (b)) appears to be almost linear, resulting in a constant velocity The peak position of the Gaussian fit is also more linear than the single plume case, even though the profile appears to turn over at $\sim$ 100 ns

Figure 5 24 shows the results obtained for four Ca plasma simulations using the adiabatic expansion model described previously (section 2 3) for varying initial temperatures Figure 5 24 (a) shows the calculated velocity profiles as a function of time for the four initial temperatures of 3×10^4, 4×10^4, 5×10^4 and 6×10^4 Kelvin Figure 5 24 (b) shows the plume front position as a function of time and figure 5 24 (c) shows how the plasma temperature falls off with time It should be noted from graphs (a) and (c) in figure 5 24 that the trend changes significantly at $\sim$ 16 ns This is the pulse length of the Spectron laser used in this work At this boundary the plasma expansion dynamics changes from an isothermal to an adiabatic one, as there is no longer an energy supply to the plasma

Figure 5 25 compares the model and experimental plume front positions as a function of time It may be seen that the single and colliding plasmas expand at near identical velocities over the time-scales observed here, but that the trends are different from that of the model, even though the absolute values are in good agreement

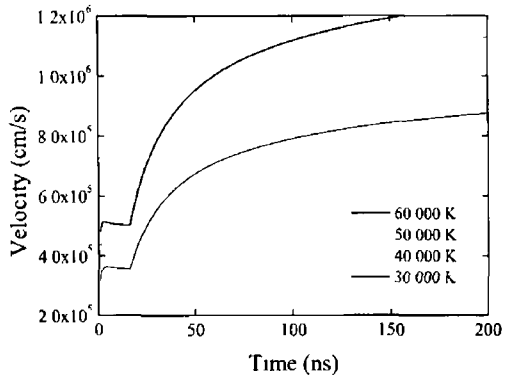

(a) Evolution of the calculated expansion velocity of a calcium plasma as a function of time

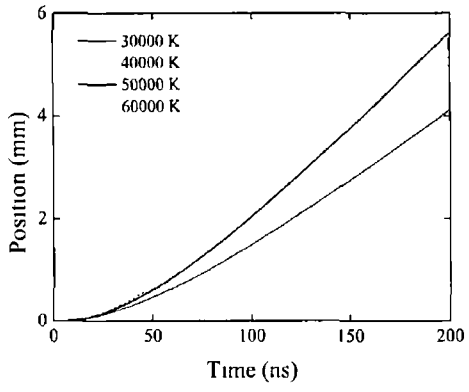

(b) Calculated plume front position as a function of time for a calcium plasma

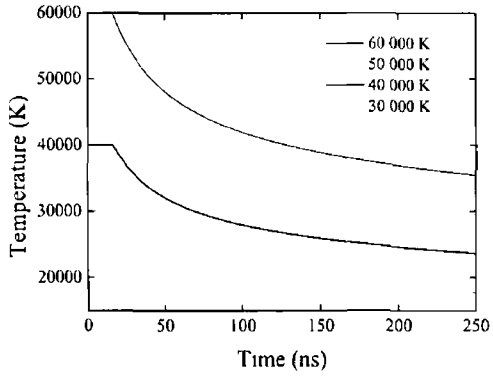

(c) Evolution of the plasma temperature as a function of time

Figure 5 24 Results obtained from the Singh and Narayan [12] adiabatic expansion model for four initial plasma temperatures

The average velocity during this temporal window is $\sim 1 \times 10^6$ cms^{-1} for the single expanding line plasma and the interaction region between the two line plasmas The average velocity extracted from the model for the four initial input temperatures varies from $\sim 6 \times 10^5$ to 2×10^6 cms^{-1}

The error bars shown in figures 5 22, 5 23 and 5 25 only indicate the errors associated with the fitting of the Gaussian profiles to the line-outs from the images There are however two other significant sources of error that should be considered in relation to the photoabsorption images The first is the error associated with

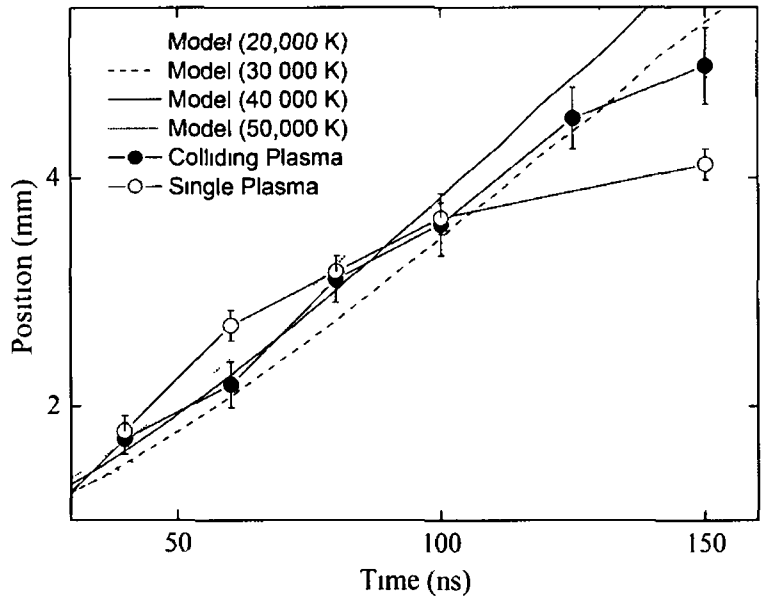

Figure 5 25 Comparison between experimentally observed plume front positions for single (figure 5 4) and colliding plasmas (figure 5 8) with an adiabatic expansion model [12]

measuring of the plasma dimensions from the images, an upper limit on this can be estimated to be the spatial resolution of the VUV probe beam (as described in section 4 6), which was determined to be $\sim$ 130 μm (horizontal) The second significant source of error comes from the trigger jitter between the Surelite and the Spectron lasers, this has been measured to be $<$ 1 ns Combining these error estimates, a value for the total experimental error associated with our plume expansion velocities of 1×10^6 cms^{-1} is $\sim$ 10%

5.6 Summary

In this chapter the manner in which photoabsorption images are acquired and processed has been described Equivalent width image sets from single and colliding calcium plasmas have been presented and discussed The procedure used to convert equivalent width values to column density values was subsequently described Using this procedure all of the equivalent width image sets were converted to column density maps Expansion velocities were extracted from equivalent width images of single line plasma plume expansion and the overlap region between two colliding line plasma plumes The results were then compared with an adiabatic expansion model [11, 12]

In the next chapter results obtained using the emission imaging and imaging spectroscopy setups will be presented and analysed Plasma parameters from the interaction region between two colliding calcium plumes will be presented and discussed

Bibliography

[1] J S Hirsch, K D Kavanagh, E T Kennedy, P Nicolosi, L Poletto, and J T Costello Tracking ground state Ba^+ ions in an expanding laser plasma plume using Vacuum-UV photoionization imaging *Laser and Particle Beams*, 2004

[2] J S Hirsch, E T Kennedy, A Neogi, and J T Costello Vacuum-ultraviolet photoabsorption imaging system for laser plasma plume diagnostics *Review of Scientific Instruments*, 74 2992–2998, 2003

[3] I C Lyon, B Peart, K Dolder, and J B West Measurements of absolute photoionisation cross sections of Ca^+ ions *Journal of Physics B Atomic and Molecular Physics*, 20 1471–1477, 1987

[4] M W D Mansfield and G H Newsom The Ca I absorption spectrum in the vacuum ultraviolet Excitation of the 3p-subshell *Proceedings of the Royal Society of London Series A, Mathematical and Physical Sciences*, 357 77–102, 1977

[5] Y Sato, T Hayaishi, Y Itikawa, Y Itoh, J Murakami, T Nagata, T Sasaki, B Sonntag, A Yagishita, and M Yoshino Single and double photoionisation of ca atoms between 35 and 42 nm *Journal of Physics B Atomic and Molecular Physics*, 18 225–231, 1985

[6] J M Bizau, D Cubaynes, M Richter, F J Wuilleumier, J Obert, J C Putaux, T J Morgan, E Kallne, S Sorensen, and A Damany First observation of photoelectron spectra emitted in the photoionization of a singly charged-ion beam with synchrotron radiation *Phys Rev Lett* , 67 576–579, 1991

[7] K Ueda, J B West, K J Ross, H Hamdy, H J Beyer, and H Klempoppen Angle-resolved photoelectron spectroscopy of ca in the 3p-3d giant-resonance region *Phys Rev A*, 48 R863–R866, 1993

[8] Andy Gray *XUV photoabsorption studies of calcium and the neon isoelectronic sequence* PhD thesis, School of Physical Sciences, Dublin City University, 1999

[9] J S Hirsch *Photoabsorption Imaging of Laser Produced Plasmas* PhD thesis, School of Physical Sciences, Dublin City University, 2003

[10] A Corney *Atomic and laser spectroscopy* Clarendon Press, New York, 1977

[11] W Whitty *A study of the expansion of a laser produced lithium plasma using spatially and temporally resolved imaging and spectroscopic techniques* PhD thesis, School of Physical Sciences, Dublin City University, 1998

[12] R K Singh and J Narayan Pulsed-laser evaporation technique for deposition of thin films Physics and theoretical model *Physical Review B*, 41 8843–8859, 1990

CHAPTER 6

EMISSION IMAGING & SPECTROSCOPY

6.1 Introduction

In this chapter results obtained during the study of the interaction of two counter-propagating laser-produced plasmas using simultaneous imaging and spectroscopic techniques will be presented. Spectrally-filtered time-gated ICCD imaging was used to obtain information about the spatial dynamics and temporal evolution of the collision process, while time-resolved imaging spectroscopy was used to determine the spatial and temporal distributions of electron temperature and density within the interaction region. We examine specifically the interaction of plasmas whose parameters match those typically used in pulsed laser deposition of thin films. These low temperature plasmas are highly collisional leading to the creation of a pronounced stagnation layer in the interaction region.

When two expanding plasmas collide several interactions may arise. These interactions may be either of collisionless type, in which case collective plasma effects should occur or, in contrast they may be collision dominated (CD) [1]. For example, considering two extreme cases where the ion-ion mean-free path is either bigger or smaller than the typical spatial dimension of the colliding plasmas system, we can expect two different behaviours to occur during the interaction of the two plasma plumes. In the first case, the expanding plasma plumes should interpenetrate and therefore the heating processes should be mostly driven by binary collisions between the species, as has been examined by a number of au-

thors [2, 3, 4] In the second case a quite different scenario is expected to occur once the two plasmas collide The region of interpenetration should be relatively small and the two plumes will decelerate rapidly and stagnate A quasi-stationary plasma should then be formed at the interface, where the translational (kinetic) energy of the plasma streams, is converted into thermal energy The increased temperature in the interaction region leads to increased emission as the colliding species become thermally excited This very localised heated region is frequently referred to as a stagnation layer

We have chosen three different laser irradiance conditions in order to study the effect that the initial conditions have on the formation of the interaction between the two plasma plumes Results will be compared from data obtained using (i) 355 nm 6 ns pulses, (ii) 1064 nm, 6 ns pulses and (iii) 1064 nm 16 ns pulses

6 2 Colliding Plasmas (355nm-6ns)

We will begin by examining the case in which the colliding plasmas are generated using laser pulses with a wavelength of 355 nm and a pulse duration of $\sim$ 6 ns The 3^{rd} harmonic of the Surelite laser system (discussed in section 4 2) was used to generate these pulses The laser beam from the Surelite was split in two using the wedge prism (figure 4 13, section 4 4 5) prior to being focussed to two spots of $\sim$ 200 μm diameter The intensity ratio of the two resulting laser beams was $\sim$ 1 1 leading to on-target irradiance of $\sim 3 \times 10^{10}$ Wcm^{-2} The separation d between the two foci on the target surface is determined by the acute wedge angle γ of the prism and the focal length of the lens used and is given by

$$d = f\gamma(n-1) \tag{6 1}$$

where $n = 1\,5$, the refractive index of glass and $f = 100$ mm, the focal length of the lens used In the case of the image sets presented in this chapter a 2° wedge prism was used to split the laser beam yielding an on-target separation of the foci of $\sim$ 1 5 mm

As was described in section 4 9 1 interference filters were employed to spectrally filter the plasma emission before being recorded on the time-resolved imaging ICCD camera For each of the initial irradiance conditions we will present images of the

transmission from three different interference filters at three different time delays Figure 6 1 shows the expansion and interaction of two colliding Ca plasmas at three time delays after plasma initiation (Δt = 100, 200 and 400 ns) Figure 6 1 (a), (d) and (g) are broadband "white" light images, which may be viewed as a measure of the spatial distribution of the bulk plasma material Figure 6 1 (b), (e) and (h) show the transmission through a narrow band (10 nm FWHM) interference filter with a central wavelength of 390 nm (figure 4 27, section 4 9 1) This filter allows us to selectively image the Ca^+ component in the plasma by tracking only the emission from the $3p^64s(^2S_{1/2})$-$3p^64p(^2P_{3/2,1/2})$ Ca^+ doublet at 393 36 and 396 47 nm Finally figure 6 1 (c), (f) and (i) show the transmission through an interference filter centered at 420 nm (10 nm FWHM), which allows is to image the neutral Ca plasma component by tracking the $3p^64s^2(^1S_0)$-$3p^64s4p(^1P_1)$ Ca^0 transition at 422 67 nm (figure 4 26, section 4 9 1) The intensities presented have been corrected for the differing percentage transmission through the respective interference filters The intensifier gate-width on the ICCD camera was set to the minimum value achievable (3 ns) for all of the emission images presented in this chapter

It is very important to exercise caution when interpreting the luminosity images recorded in this work The luminosity distributions presented here do not necessarily reflect the plasma density or temperature profiles Similarly the luminous boundary visible in these images may not accurately represent the actual effective boundary of the plasma [5] It should also be noted that the colour-scales differ from image-to-image in order to make the observed plasma boundaries perceptible over the large intensity ranges recorded

In figure 6 1 the laser-beam travels horizontally from right-to-left striking the angled target surface, whose position is located just in front of the black angled line drawn on each figure From the first row of images in figure 6 1 it may be seen that the intensity of the emission from the top plasma is greater than that of the lower one This is probably due to differing spot sizes caused by focussing aberrations, as the two off-axis laser-beams are focussed using the same lens onto the target surface In order to generate a symmetric interaction region about the apex of the target surface it was necessary to accurately position the spots on the target surface This was achieved by vertically translating the target with respect to the incident beams Slight changes in the positions of the foci resulted in large changes

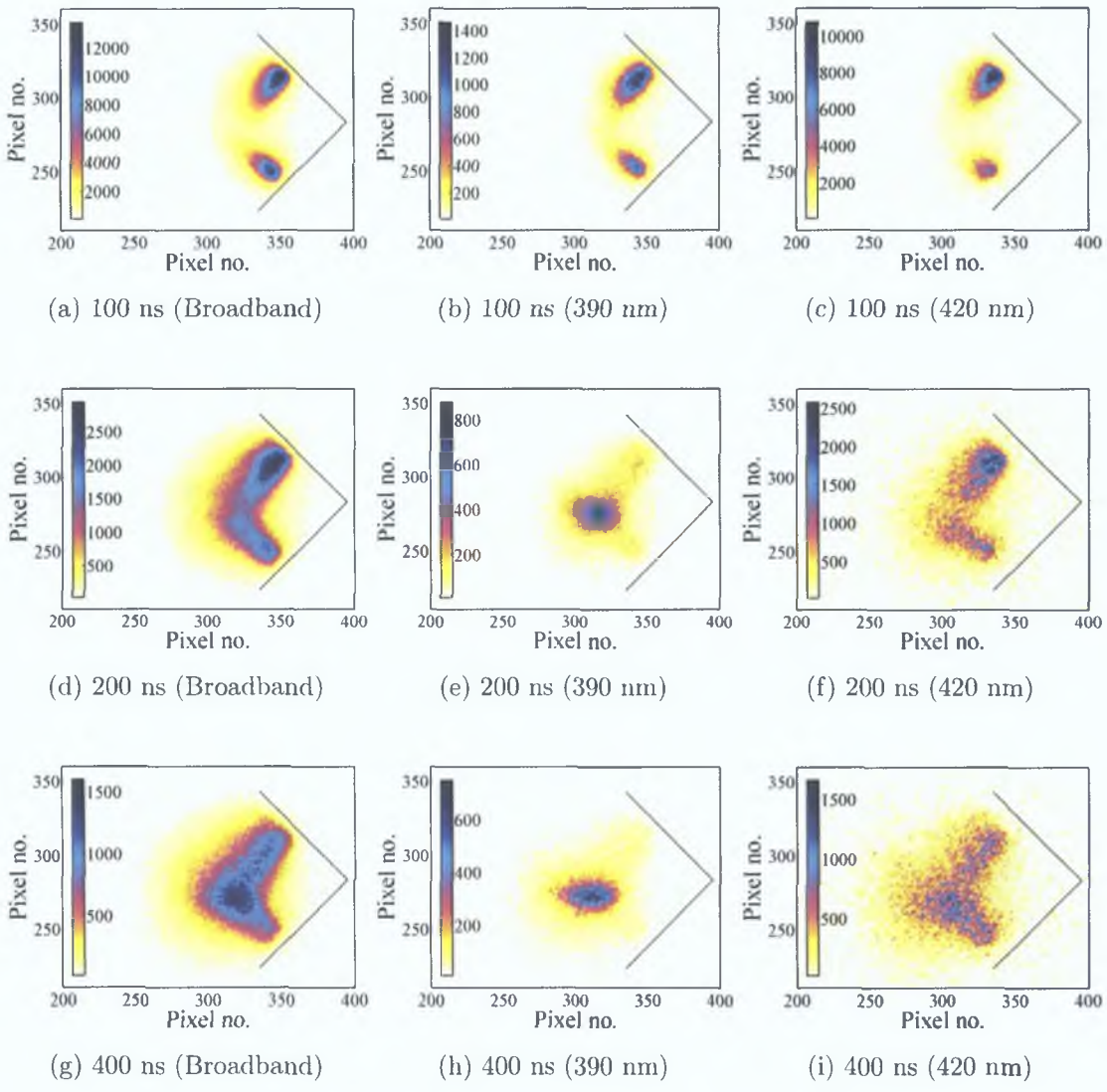

(a) 100 ns (Broadband) (b) 100 ns (390 nm) (c) 100 ns (420 nm)

(d) 200 ns (Broadband) (e) 200 ns (390 nm) (f) 200 ns (420 nm)

(g) 400 ns (Broadband) (h) 400 ns (390 nm) (i) 400 ns (420 nm)

Figure 6.1: Time-resolved emission images of colliding laser-produced plasmas using three different interference filters (i) a broadband, (ii) a 390 nm (10 nm FWHM) used to track the Ca^+ $3p^64s(^2S_{1/2})$-$3p^64p(^2P_{3/2,1/2})$ doublet, (iii) a 420 nm filter used to track the Ca^0 $3p^64s^2(^1S_0)$-$3p^64s4p(^1P_1)$ transition (355 nm - 6 ns).

in the overall evolution of the plumes. In this work we endeavoured to position the foci and distribute the laser energy evenly such that a horizontal stagnation layer was generated. This was necessary in our case in order that we may align the spectrometer entrance slit with this interaction region to perform spatially-resolved spectroscopy of this region. Cratering of the target surface also had a significant effect on the evolution and interaction of the plumes, all of the images presented here are integrated over five laser shots; thereby averaging-out shot-to-shot fluctuations. The target surface was then horizontally translated to a "fresh" surface for

the next time delay

It may be observed from the first row of images (figure 6 1) recorded using a 100 ns time delay that initially both plasmas expand freely, perpendicular to the target surface After approximately 120 ns a thin interaction region becomes visible in the Ca^+ image set and broadens until the near spherical emission profile (figure 6 1 (e)) is formed It should also be noted from figure 6 1 (e) that at this time delay (200 ns) the Ca^+ emission from the laser-generated or "primary" plasmas has all but dissipated This behaviour is quite different to what is observed in the broadband (figure 6 1 (d)) and the neutral (figure 6 1 (f)) images Here no visible emission enhancement is observed from the overlap region between the plumes and the primary emission persists It may be seen from figure 6 1 that the majority of the emission from the interaction region between the two plumes is from the Ca^+ plume component As time progresses the visible interaction region in the singly ionised calcium images broadens until it reaches a maximum width of $\sim$ 950 μm and a length of $\sim$ 1600 μm at approximately 300 ns It should be noted that the interaction region seen in figure 6 1 (e) and (f) is vertically broad and horizontally short compared to the stagnation layers presented later in this chapter This would lead us to believe that the collisionality of the system is relatively low, allowing the plasmas to interpenetrate to a certain degree without generating a well confined and narrow stagnation layer at the interaction front It is also worth reiterating that there is no apparent enhancement of neutral calcium emission due to stagnation in the interaction region This behaviour differs considerably to the long laser pulse (16 ns) image set to be presented later in this chapter (figure 6 13) The lifetime of emission from the interaction region compared with emission from the primary "feeding" plasmas is greater only in the case of the Ca^+ component Previous reports [6] in the XUV spectral range, integrated over all charge stages observed that the emission from the interaction region always outlived the primary plasma emission

Figure 6 2 shows a plot of three pixel values, taken at three different positions, as a function of time delay, from colliding plasma images One of the pixels was located near the centre of the top primary plasma, close to the target surface, the second was located near the centre of the bottom primary plasma close to the target surface, and the final pixel location was taken at the centre of the interaction region between the two plumes The image set used was the Ca^+ images, i e using

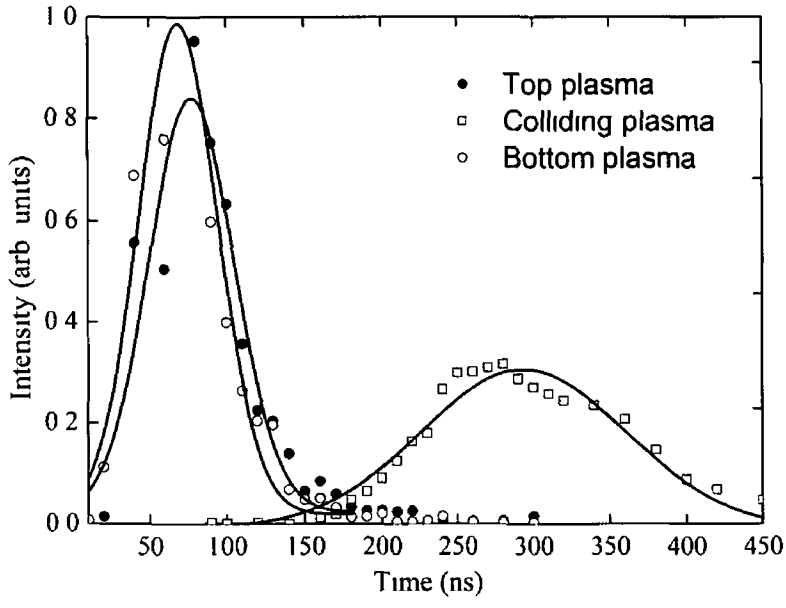

Figure 6 2 Emission intensity at three points as a function of time (355 nm - 6 ns)

the 390 nm filter (figure 6 1 (b, e and h)) It may be observed from figure 6 2 that the intensity of the Ca^+ emission from the two primary plasmas close to the target surface has all but extinguished 150 ns after initiation Around this time the emission from the interaction begins to increase until it reaches a maximum at $\sim$ 300 ns From this plot we may estimate the lifetime of the Ca^+ emission from the interaction region or stagnation layer to be of the order of 200 ns

In order to determine the velocities at which the primary plasmas interact, expansion velocities have been extracted from the broadband images Figure 6 3 illustrates the manner in which expansion velocities were extracted from the images The image used in figure 6 3 corresponds to the broadband image presented in figure 6 1 (a) Line-outs were taken along the primary expansion direction of each plasma, perpendicular to the target surface Figure 6 3 (a) shows the intensity of the pixels along the dashed line labelled (a) on the image Likewise figure 6 3 (b) shows the line-out along the dashed line labelled (b) on the image Fitting Gaussian functions to these traces in the same manner as was done during the analysis of the photoabsorption images was not practical for this situation This is mainly due to the fact that the traces are quite asymmetric, with a long tapered leading edge For this reason the position of 10% of the maximum luminosity value on the leading expansion edge was chosen to be the plume front position

Figure 6 4 shows the plume front position as a function of time for the first 120 ns

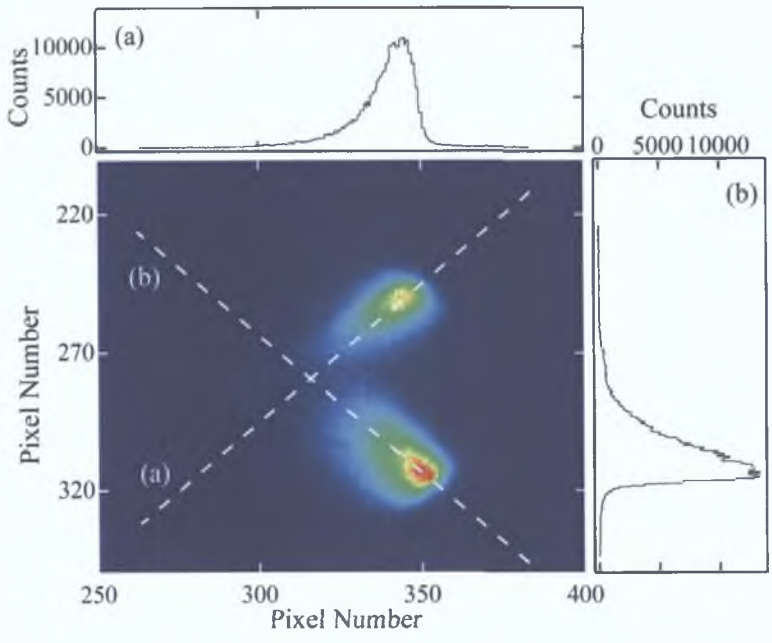

Figure 6.3: Position of line-outs used to extract expansion velocities from (broadband) colliding plasma images.

We are limited to this time-frame because after 120 ns the plume fronts begin to interact. Figure 6.4 also shows outputs from the Singh and Narayan [7] adiabatic expansion model (described in section 2.3) for three initial plasma temperatures: 50,000, 60,000 and 70,000 K. These temperatures are in good agreement with the initial plasma temperature approximation by Colombant and Tonon [8] using equation 4.1 (section 4.4.1). For the laser irradiances used, equation 4.1 predicts an initial plasma temperature of $\sim$ 4 eV (or $\sim 50,000$ K). Plume front velocities of $\sim 1 \times 10^6$ cms^{-1} were determined for the plasmas prior to interaction.

Using the spectroscopy setup described in section 4.10 the electron density and temperature present in the interaction region was determined. In order to perform spatially-resolved spectroscopy solely on the interaction region between the two plumes it was necessary to precisely align the stagnation layer with the entrance slit of the spectrometer. The optics used to image the plasma onto the entrance slit of the spectrometer (figure 4.32, section 4.10) were fixed in position and the entire spectrometer and ICCD camera were translated (vertically and horizontally) on a specially designed micrometer driven table in order to spatially select the desired region (figure 4.33, section 4.10).

The procedure used to position the spectrometer is illustrated in figure 6.5. A

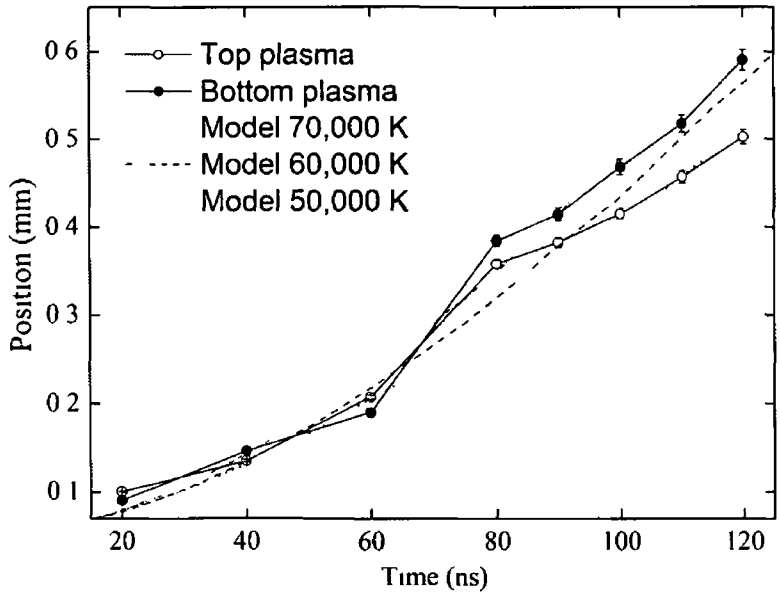

Figure 6 4 Plume front position as a function of time delay for primary (broadband) plume emission, as well as comparisons with an adiabatic expansion model [7]

very short time delay was set between plasma initiation and the gate on the ICCD camera connected to the spectrometer The spectrometer was then physically scanned across the image of the plasma When the image of the first plume was intercepted by the entrance slit of the spectrometer (figure 6 5 (a)), very strong continuum emission was recorded on the CCD Due to the short time delay used, this position may be considered to be the position of plasma initiation Moving the spectrometer either side of this position by tens of microns resulted in the emission intensity dropping to zero The spectrometer was then translated until the position of the second plasma was determined (figure 6 5 (a)) The spectrometer was subsequently moved to a position mid-way between these two positions (where the stagnation layer would be expected to form) and the time delay between the laser and CCD was increased to allow the plasmas time to reach the central position and interact with each other (figure 6 5 (b))

The electron density was calculated via an analysis of the profile of the Ca^+ $3p^64p(^2P_{3/2})$-$3p^65s(^2S_{1/2})$ transition at 373 69 nm Voigt functions were fitted to the emission line in order to take into account the various processes that contribute to the line broadening The Stark contribution to the broadening is described by the Lorentzian component and all other contributions, such as the Doppler effect ($\sim$ 0 005 nm for a plasma temperature of 1 eV) and the instrument function of $\delta \sim 0\ 22$ nm (section 4 10) were accounted for in the Gaussian component of the

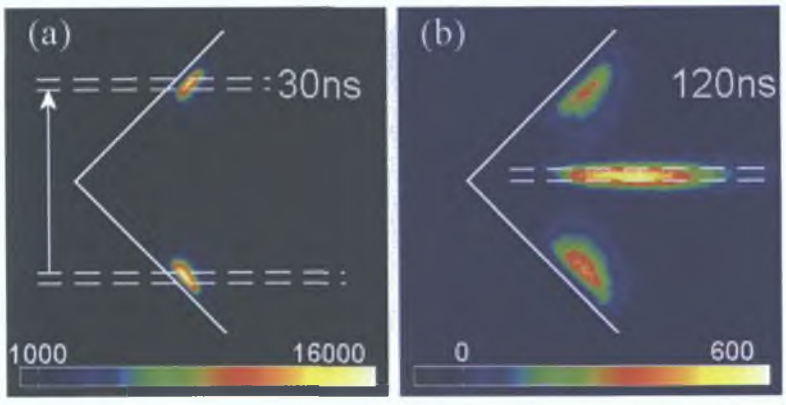

Figure 6.5: Positioning of the entrance slit of the imaging spectrometer.

Voigt profile [9, 10]. Therefore the electron density may be computed using equation 3.5 (section 3.4.3, repeated here for the reader's convenience) using only the Lorentzian component of the fitted Voigt profiles

$$\Delta\lambda_{width} = 2w\left(\frac{n_e}{10^{16}}\right) + 3.5A_i\left(\frac{n_e}{10^{16}}\right)^{\frac{1}{4}}\left[1 - 1.2N_D^{-\frac{1}{3}}\right]w\left(\frac{n_e}{10^{16}}\right) \qquad (3.5)$$

where the electron-impact parameter w, and the ionic-impact parameter A_i are taken from tabulated values [9] and N_D is the number of particles in the Debye sphere.

Figure 6.6 shows an example of a spectroscopic image of the interaction region taken 300 ns after plasmas initiation. The wavelength dispersion direction lies along the x-axis of the image and position along the y-axis. The trace shown in figure 6.6 (a) is a horizontal slice taken across the image, the white dashed horizontal line drawn on the image indicates its position. Similarly the trace shown in figure 6.6 (b) is a vertical slice indicated by the white dashed vertical line drawn on the image. In order to determine electron densities the spectroscopic image was broken into sections, vertically binning twenty rows of spectra before fitting the Voigt functions, as was described in Doria *et al* [11].

Using both the electron-impact and the quasi-static ion component of equation 3.5 introduces a temperature dependence incorporated in the Debye length term (equation 2.2, section 2.1). Assuming a temperature of 1 eV the electron density may be calculated for an experimentally observed linewidth by minimising equation 3.5 (section 3.4.3) in terms of n_e. The contribution that the ion broadening component provides to the overall electron density value (calculated using this method) was determined to be $<5\%$. For this reason only the first term in equation 3.5 (electron

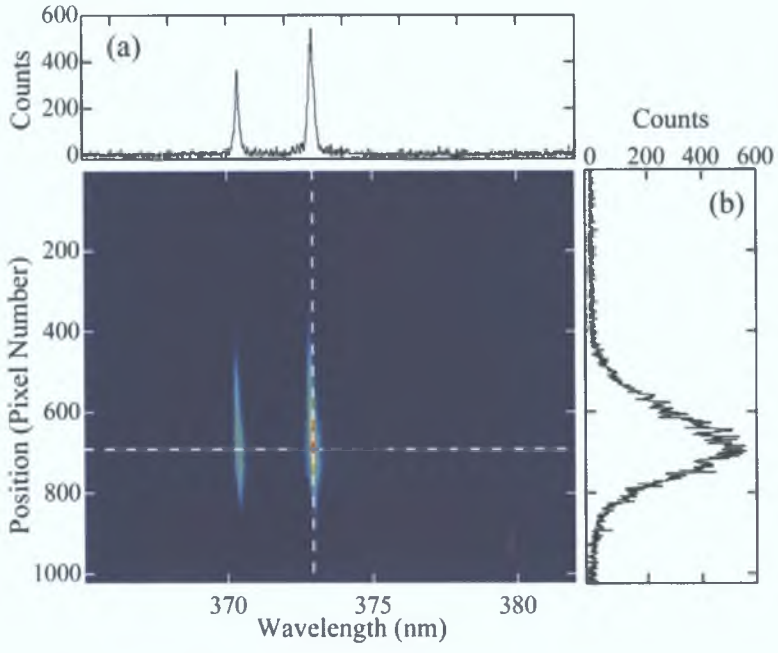

Figure 6.6: Example spectroscopic image, showing the Ca^+ $3p^64p(^2P_{1/2,3/2})$-$3p^65s(^2S_{1/2})$ doublet at 370.60 and 373.69 nm

impact) will be used in our calculations.

Figure 6.7 shows the spatial distribution of electron density for three time delays 300, 400 and 500 ns after primary plasma initiation. It may be seen that for this case the electron density is very similar in trend and absolute value for all three time delays. This result is unsurprising given the stationary nature of the interaction region as well as the continuous particle feeding into this region from the primary plasmas.

As was described in section 3.4.8, under the assumption of LTE the electron temperature in a plasma may be obtained from spectroscopic measurements by: (i) relative line-to-continuum intensity, (ii) relative intensity of lines from the same ionisation stage, and (iii) relative line intensity of subsequent ionisation stages.

The relative line-to-continuum method, although useful in the characterisation of early stages of a single plasma plume expansion, could not be used here due to the absence of continuum emission from the stagnation layer (a fact contrary to observations previously reported in the literature [1]). The relative intensity of lines from the same ionisation stage obtained from the ratio of the Ca II $3p^64s(^2S_{1/2})$-$3p^64p(^2P_{3/2,1/2})$ to the $3p^64p(^2P_{1/2,3/2})$-$3p^65s(^2S_{1/2})$ doublets, was avoided due to

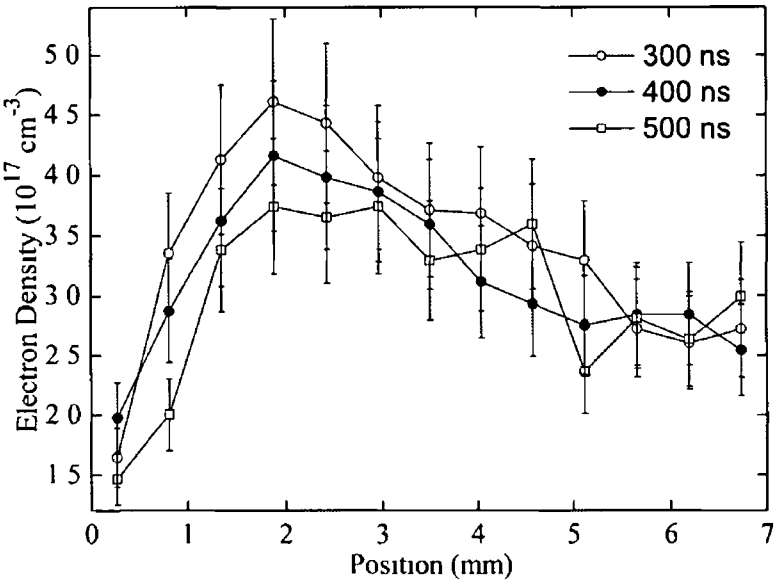

Figure 6 7 Spatially and temporally resolved electron density distributions of the interaction region (355 nm - 6 ns)

the presence of significant opacity in the $4s(^2S_{1/2})$-$4p(^2P_{3/2,1/2})$ transitions for our plasma conditions and due to errors associated with using small energy separations between transitions

The most applicable and accurate technique available to us, may be used when one observes two isolated lines from subsequent ionisation stages, λ and λ', emitted from the same atomic or ionic species, and if the energy level population is distributed according to the Boltzmann law, the line intensity ratio is given by [9]

$$\frac{I'}{I} = \frac{f'g'\lambda^3}{fg\lambda'^3}(4\pi^{3/2}a_0^3 n_e)^{-1}\left(\frac{kT}{E_H}\right)^{\frac{3}{2}} exp\left(\frac{E - E' - E_\infty}{k_B T}\right) \qquad (3\ 14)$$

where I, λ, g and f are total intensity (integrated over the profile), wavelength, statistical weight of the lower state of the line, and absorption oscillator strength, respectively, of the line related to the lower charge state transition and E its excitation energy and a_0 denotes the Bohr radius The subsequent ionisation stage is denoted by primed quantities, and E is the ionisation energy of the lower ionisation stage

Temperatures were obtained by solving equation 3 14 using a graphical method The right-hand side of equation 3 14 has been plotted against a range of possible values for the ratio of intensities, for five different values of the electron density as is shown in figure 6 8 The line intensity ratios were computed from the ratio of

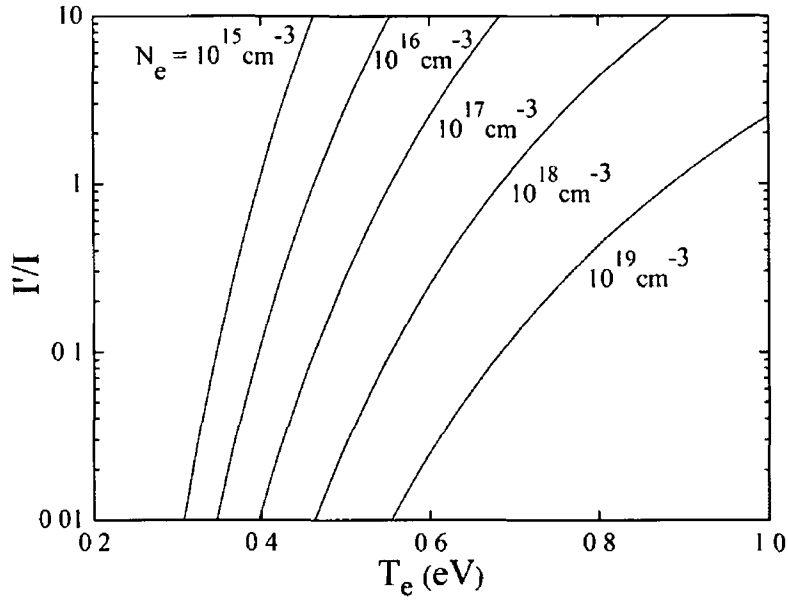

Figure 6 8 Solution to equation 3 14, used to calculate electron temperatures, for five electron densities

Ca^+ 373 69 nm and Ca^0 422 7 nm transitions This graphical method permits temperature determinations with accuracies ranging from 5 to 15%, for temperatures between $\sim$ 0 5 and 2 eV [9]

The method employed in this work to calculate the electron temperature was as follows First an average electron density was determined from figure 6 7 and inserted into equation 3 14 Using this density a plot similar to figure 6 8 was generated A ninth order polynomial function was then fitted to the calculated curves in an analogous procedure to the one performed in section 5 4 for column density calculations This allowed us to readily convert the integrated intensity ratios into electron temperature values Figure 6 9 shows the electron temperatures calculated using this procedure for three time delays 300, 400 and 500 ns as a function of position An approximately isothermal spatial and temporal distribution centered at $\sim$ 0 7 eV was determined The average temperature in the interaction region does not decrease in the same manner as that of a single plasma expanding in vacuum The Singh and Narayan expansion model predicts an $\sim$ 20% temperature decrease over the 300 $-$ 500 ns time range for a single plume generated with the same irradiance conditions used here It should also be noted that the spatial extent of the emission tracked using the imaging spectrometer was far greater than that observed using the imaging setup This would indicate that the spectroscopy setup was more sensitive to low light levels than the imaging system

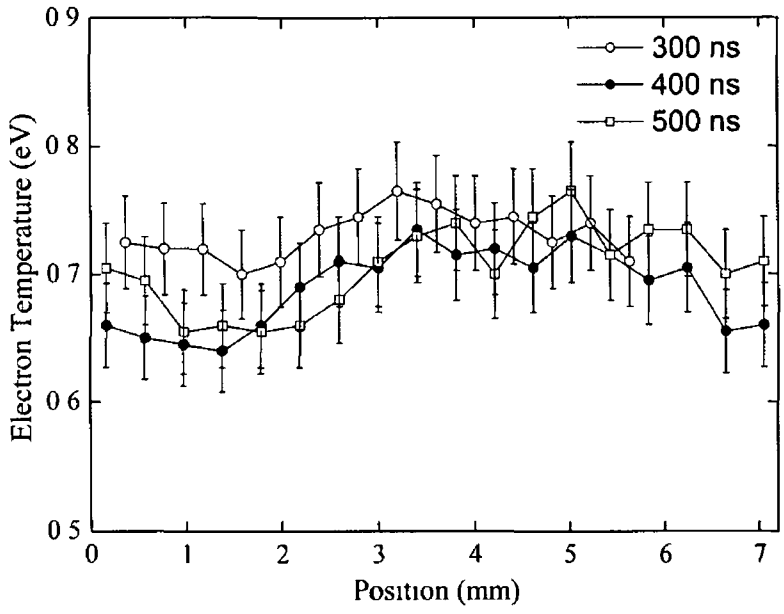

Figure 6 9 Spatially and temporally resolved electron temperature distributions of the interaction region (355 nm - 6 ns)

This could possibly be caused by the attenuation due to spectral filtering of the plasma emission and the less efficient fibre coupling of the intensifier to the CCD chip, compared to the lens coupling used in the spectroscopy ICCD camera

In this section the procedures used to acquire and calculate electron densities and temperatures have been discussed Spectrally filtered emission images have been presented for various acquisition time delays Temporally and spatially-resolved electron density and temperature distributions from the stagnation layers formed between two calcium plasma plumes have been presented and discussed

In the next two sections we will contrast results obtained on colliding laser-produced plasmas generated with different initial irradiation conditions The same procedures used for determining plasma parameters from experimentally obtained spectra described in this section, will be employed in the coming sections

6.3 Colliding Plasmas (1064nm-6ns)

In this section we will examine colliding plasma results obtained using the same experimental conditions used in the previous section except for the fact that the frequency doubling crystals on the Surelite laser have been removed. The output from the Surelite laser thus becomes 450 mJ in 6 ns at 1064 nm. This produces an on-target irradiance of $\sim 4 \times 10^{11}$ Wcm^{-2} for a 100 μm diameter spot size.

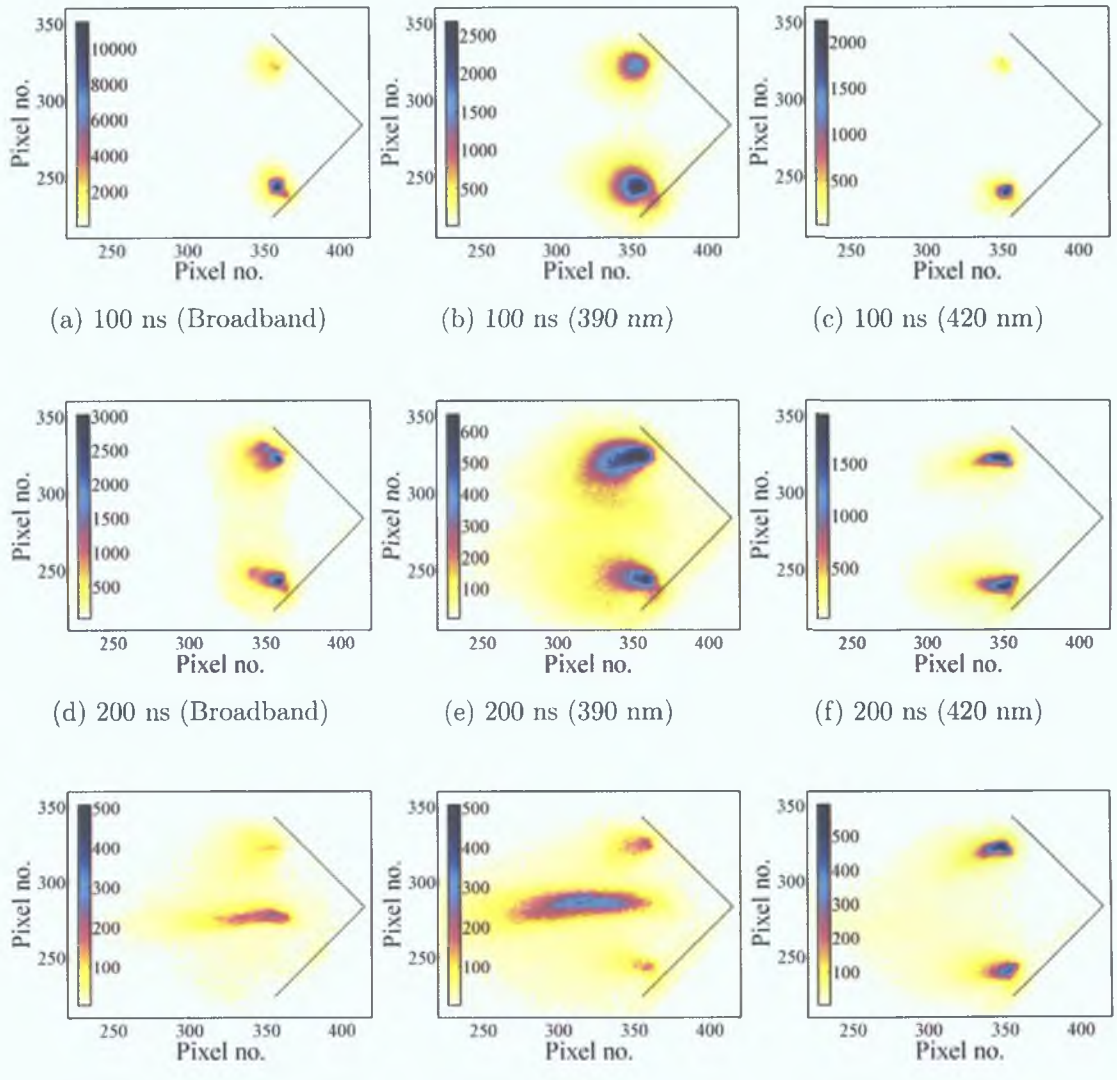

(a) 100 ns (Broadband) (b) 100 ns (390 nm) (c) 100 ns (420 nm)

(d) 200 ns (Broadband) (e) 200 ns (390 nm) (f) 200 ns (420 nm)

(g) 400 ns (Broadband) (h) 400 ns (390 nm) (i) 400 ns (420 nm)

Figure 6.10: Time-resolved emission images of colliding laser-produced plasmas using three different interference filters (i) a broadband, (ii) a 390 nm (10 nm FWHM) used to track the Ca^+ $3p^64s(^2S_{1/2})$-$3p^64p(^2P_{3/2,1/2})$ doublet, (iii) a 420 nm filter used to track the Ca^0 $3p^64s^2(^1S_0)$-$3p^64s4p(^1P_1)$ transition (1064 nm - 6 ns).

It may be seen from figure 6 10 that the focussing of the laser pulses appears to be much tighter in this image set compared to that of figure 6 1 A much greater proportion of the emission from the images taken 100 ns (first row, figure 6 10) after plasma initiation originate from Ca^+ species of the plume This would indicate a higher plasma temperature than that achieved in figure 6 1 This is unsurprising considering the higher on-target irradiance facilitated by the higher energy pulses achievable at the fundamental laser wavelength A further indication of a smaller spot size is the bulbous shape of the plumes at early time delays A large transverse (vertical on image) expansion velocity is evident caused by large pressure gradients at the target surface, while the plumes observed in figure 6 1 exhibit a more directed almost one-dimensional expansion perpendicular to the target surface In spite of the larger transverse expansion velocity evident in figure 6 10, the actual plume front velocity extracted perpendicular to the target surface, determined from the broadband images, is approximately the same as those determined for figure 6 1 ($\sim 2 \times 10^6$ cms^{-1})

Looking now at the second row of images (figure 6 10), it appears that the primary plumes have begun to turn towards the horizontal axis instead of expanding perpendicularly away from the target surface (as they appear to do for the first 130 ns) This turning of the plumes is seen most clearly in the case of the Ca^+ image at 200 ns (figure 6 10 (e)) A possible cause for this change in direction away from the expected one is due to momentum transfer to each plume from rapidly expanding (likely highly charged ions) from the opposite plume partner The structure of the plumes viewed through the broadband filter at 200 ns (figure 6 10 (d)) is disjointed and asymmetric Additionally, the plumes shown in figure 6 10 (f) appear flattened at the leading expansion edge of both plasmas A surprising feature of this image set is that even after 200 ns, when plasma overlap has definitely occurred, very little stagnation is evident This stands in stark contrast to the image set previously presented (figure 6 1) and the impending image set (figure 6 13) This would lead us to believe that considerable interpenetration may have occurred at early times delays

Finally moving on to the third row of images in figure 6 10, it may be seen that a pronounced elongated stagnation layer has been formed, comprising solely of Ca^+ constituents The neutral Ca image (figure 6 10 (i)) appears to show no emission from the interaction region However, approximately 600 ns after the primary

plasma initiation the stagnation layer between the plumes exhibits neutral Ca emission far from the target surface (> 4 mm) The dimensions of the stagnation layer extracted from the Ca^+ images, is significantly different from that of the interaction recorded using the 355 nm pulses The interaction region from the current data set is narrower (650 μm) and considerably longer (4 2 mm) at the same time delays

The density profiles extracted from the Stark broadening of the $3p^64p(^2P_{3/2})$-$3p^65s(^2S_{1/2})$ Ca^+ transition at 373 69 nm differs considerably from those previously presented in figure 6 7 Figure 6 11 shows the density profiles obtained from the collision region generated using the 1064 nm, 6 ns pulses for three time delays (Δt = 300, 400 and 500 ns) The 300 ns spatial profile is reasonably flat with a peak density occurring at ~ 3 5 mm from the beginning of the emission from the interaction region near the target surface At 400 ns the density observed in the interaction region reaches its maximum value with a pronounced peak closer to the target surface At 500 ns the stagnation layer density has decreased rapidly near the target surface, however at longer distances (> 4 mm) the overall density remains largely constant

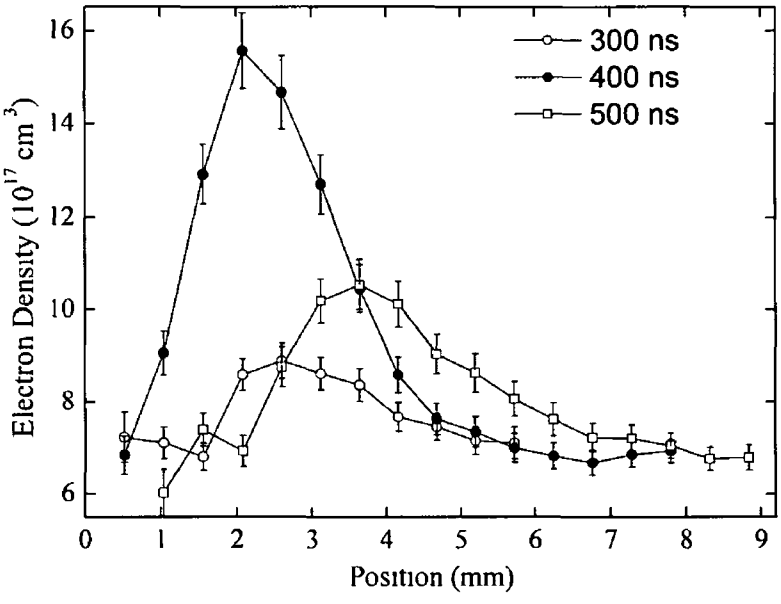

Figure 6 11 Spatially and temporally resolved electron density distributions of the interaction region (1064 nm - 6 ns)

The magnitudes of the electron temperatures obtained for this data set were very comparable to those previously presented (figure 6 9) Figure 6 12 shows the spa-

tial distribution of the electron temperature for three time delays Again the temperature remains spatially quite constant for each delay

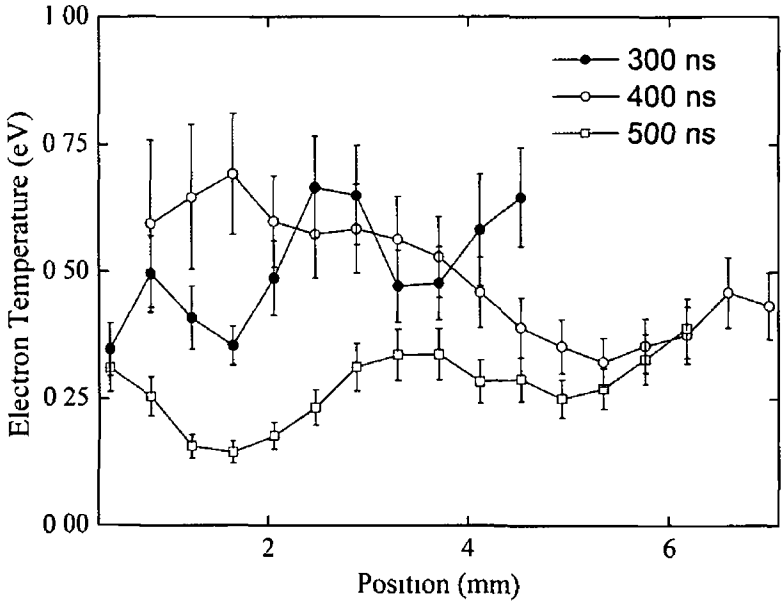

Figure 6 12 Spatially and temporally resolved electron temperature distributions of the interaction region (1064 nm - 6 ns)

6.4 Colliding Plasmas (1064nm-16ns)

In this section we will present the final data set on colliding plasmas. The plasmas here were generated using longer duration, lower energy laser pulses (16 ns, 300 mJ), produced by the Spectron laser system (section 4.3). The on-target irradiance is estimated to be $\sim 5 \times 10^{10}$ Wcm^{-2} for a spot size of ~ 200 μm.

It may be seen from figure 6.13 that the behaviour of the plasmas generated and

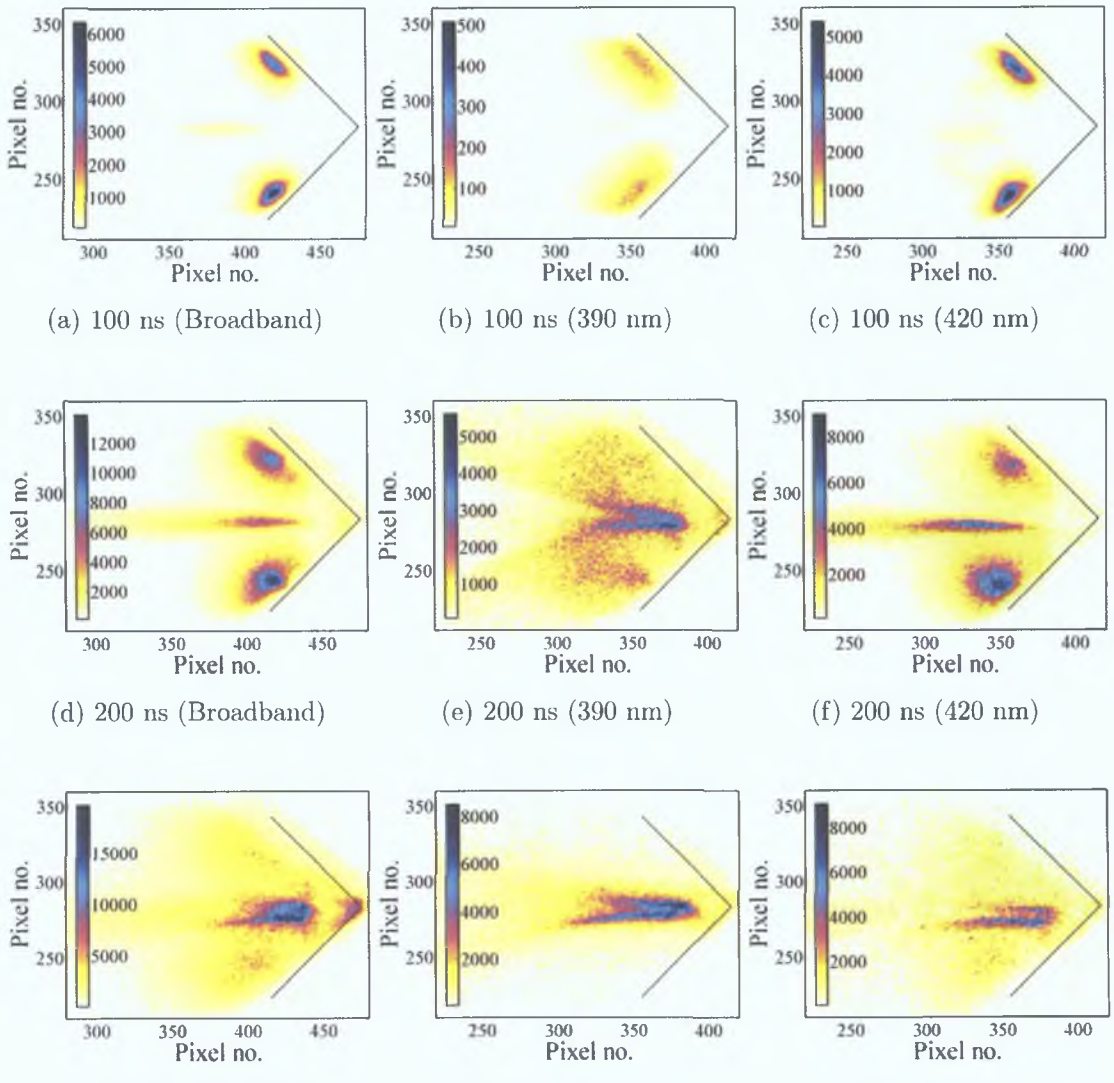

(a) 100 ns (Broadband) (b) 100 ns (390 nm) (c) 100 ns (420 nm)

(d) 200 ns (Broadband) (e) 200 ns (390 nm) (f) 200 ns (420 nm)

(g) 400 ns (Broadband) (h) 400 ns (390 nm) (i) 400 ns (420 nm)

Figure 6.13: Time-resolved emission images of colliding laser-produced plasmas using three different interference filters (i) a broadband, (ii) a 390 nm (10 nm FWHM) used to track the Ca^+ $3p^64s(^2S_{1/2})$-$3p^64p(^2P_{3/2,1/2})$ doublet, (iii) a 420 nm filter used to track the Ca^0 $3p^64s^2(^1S_0)$-$3p^64s4p(^1P_1)$ transition (1064 nm - 16 ns).

the interaction between the plasmas departs considerably from that of the two previous irradiation regimes The first point of note is the slight visible interaction that may be seen in the broadband image at 100 ns (figure 6 13 (a)) This emission appears to originate from the neutral Ca component, which has substantially higher counts at this time delay than singly ionised species in the plumes This feature has not been observed in the previous two data sets at such early time delays The shape of the primary plumes suggest a spot size comparable with the first image set (figure 6 1) The plumes appear horizontally broader than vertically long for the first time delay presented

As we move to the second row of images, taken 200 ns after plasma initiation the stagnation layer observed using the broadband filter (figure 6 13 (d)) becomes more intense and stretches for some distance away from the target surface The stagnation layer appears to be most dense in the region located directly between the plumes and tails off further from the surface The overall shape of the interaction region is narrower ($\sim$ 500 μm) and longer ($\sim$ 4 mm) when compared to the previous image sets, most notably when compared to the dimensions of the interaction region produced using the 355 nm pulses (figure 6 1) The emission recorded through the broadband filter (figure 6 13 (d)) appears to be dominated by neutral calcium emission, as the shape and intensity mirrors that recorded using the 420 nm filter (figure 6 13 (f)) The narrow interaction region between the plumes leads us to believe that the plasmas are highly collisional and stagnated very locally in space with minimal interpenetration This trend however is not followed by the emission from the Ca^+ plasma as is shown in figure 6 13 (e) Here the interaction region is broader and less well defined It also appears that the maximum intensity of the interaction is spatially offset from the maximum of the neutral interaction, which is located further from the target surface and slightly closer to the lower primary plume More surprising is the fact that the interaction region appears to be splitting as we move from right-to-left away from the position of maximum density (figure 6 13 (e))

Finally, as we look at the third row of images in figure 6 13, recorded 400 ns after plasma initiation, it may be seen that the splitting of the interaction region becomes more pronounced and now is visible through all three filters The compressed narrow emission region from the neutral collision region (figure 6 13 (f)) has become more fragmented and broader near the target surface (figure 6 13 (i)) The emission

from the primary plasmas has died away, whereas the interaction region continues to emit strongly An interesting feature may be observed in the broadband image at this time delay (figure 6 13 (g)) A certain amount of hot emitting plasma appears to have accumulated at the apex of the target surface This would suggest a wide angular scatter pattern from the initial primary plasmas resulting in a slow density build-up in this confined region It may also however be caused by plasma particles in the stagnation layer impacting on the target surface, thereby causing secondary emission from the surface The reason for the splitting of the interaction region is not completely clear It may be caused by un-even density gradients across the plasma fronts resulting from non-uniform irradiation of the target surface These density gradients would present varying levels of collisionality to the opposing plasma, thereby causing the stagnation of the plumes at differing spatial locations

A similar trend in the density of the interaction region to that observed in the previous data set was determined from spectroscopic measurements Figure 6 14 shows the spatial distribution of electron density for a range of time delays Again the absolute value of the density varies most significantly close to the target surface, with the peak density occurring at approximately 2 5 mm and a delay 400 ns At longer distances (> 4 mm) the density variation with time is smaller

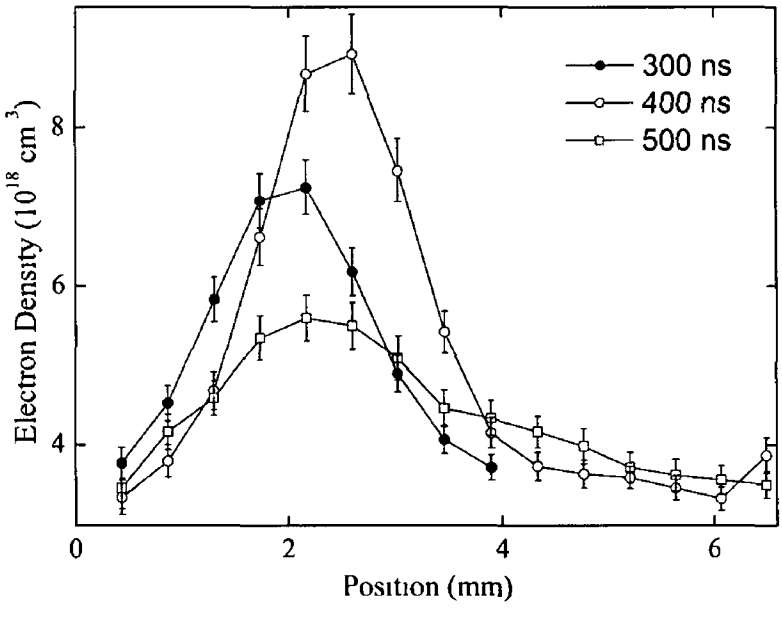

Figure 6 14 Spatially and temporally resolved electron density distributions of the interaction region (1064 nm - 16 ns)

Figure 6 15 shows the electron distribution along the interaction region for the same three time delays The maximum temperature achieved near the target surface at earliest time delay (300 ns) are slightly higher than those previously presented, however the overall trend and average values are in considerable agreement with the temperatures obtained using the other two irradiation conditions

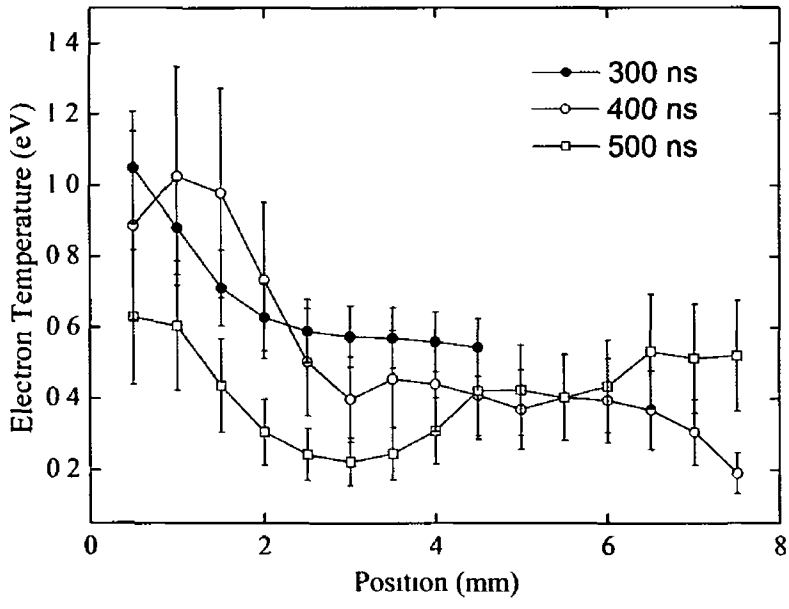

Figure 6 15 Spatially and temporally resolved electron temperature distributions of the interaction region (1064 nm - 16 ns)

6.5 Comparison of Emission Results

Spectrally and temporally resolved emission images as well as spatially and temporally resolved imaging spectra have been used to study the interaction of counter-propagating laser-produced plasmas The three image sets presented in this chapter showed a range of different behaviours in the interaction dynamics between the plumes, caused by differing initial conditions

The electron densities varied from an average of $\sim 4 \times 10^{17}$ cm^{-3} in the case of the 355 nm, 6 ns laser pulses (figure 6 7) to an average of $\sim 5 \times 10^{18}$ cm^{-3} in the case of the 1064 nm, 16 ns pulses (figure 6 14) The magnitude of the stagnation observed from the images appeared to follow this electron density trend, with the least amount of stagnation observed for the 355 nm, 6 ns pulses and the most stagnation observed for the 1064 nm, 6 ns pulses The images obtained using the 1064 nm, 6 ns pulses generated intermediate electron density values as well as an intermediate level of stagnation

The spatial temperature distribution along the stagnation layers have also been determined and presented in the case of the three differing irradiation conditions at time delays near the maximum brightness epoch of the interaction, namely 300, 400 and 500 ns after plasma initiation Our results show a nearly isothermal distribution of $\simeq 0$ 75 eV along the major axis of the longitudinal stagnation layer The temperatures achieved in the interaction region are largely unaffected by changes in the initial irradiation conditions of the primary plasmas, or the density of the interaction region The electron temperature is more strongly determined by the separation of the laser foci, or more specifically, on the relative velocity at which the two plumes collide This fact has been observed previously in the literature [12] and was also found to be independent of the amount of interpenetration involved in the interaction The initially available kinetic energy per particle was determined to be the dominant factor [12]

In contrast to stagnation layers formed by colliding relatively high temperature plasmas [1, 13], we do not observe any significant continuum emission from the stagnation layer even at early times after its formation Any continuum emission will result from either free-free (bremsstrahlung) or free-bound (recombination) processes and its absence here is an indication that we observe predominantly

stagnation with little interpenetration at long time delays (> 200 ns) A certain amount of interpenetration will however always occur at short time delays when the plume fronts meet with greatest velocity and lowest density

The results presented in this chapter may be understood by looking at the form of the collisionality parameter (ζ, described in chapter 1 2 [14, 15]) used to characterise the situation For a pair of colliding plasma the collisionality parameter ζ can be cast as the ratio of the characteristic geometrical scale length (D) to the ion-ion mean-free path (λ_{ii}) Therefore, for a plasma with high ion density ($n_i(x)$) and a gentle spatial rolloff (large plasma scale length - dn/dx) formed in close proximity to each other (small D), one can expect strong deceleration at the plasma-plasma collision front and the formation of a tight, well defined stagnation layer Since the ion-ion mean-free path (λ_{ii}) depends on the ratio (T^2/n_i) [16], low temperature plasmas will possess quite low values of λ_{ii} and concomitantly high values of ζ and hence almost no interpenetration can be expected Rough estimates for our case ($T_e \sim 0\ 75$ eV, $n_i \sim 10^{18}$ cm^{-3}) give ζ values of $\sim 10^4$, while for Harilal *et al* [1] the temperature can be expected to be > 30 eV (strong emission from Mg ions with charge $> 5^+$), and hence the collisionality parameter is likely to be < 10 and therefore interpenetration is expected, as was observed in their work

If opacity effects could be ignored and LTE assumed in the case of the image sets presented (figures 6 1, 6 10 and 6 13), an estimate of the plasma temperature could be inferred, using the ratio of the intensity of the species in the ground to first excited state using the ionisation balance calculated with the Saha equation in section 2 5 1 (figure 2 10) Opacity however cannot be neglected in the case of the images recorded using the 390 nm interference filter as the $3p^64s(^2S_{1/2})$-$3p^64p(^2P_{3/2,1/2})$ doublet that is transmitted by this filter is significantly affected by radiation trapping Spectroscopic analysis using this doublet was also avoided due to these opacity effects For a colliding plasma, a self-reversed profile was found to be present into a region localised near the maximum intensity / density However, temperatures obtained from regions where the self-reversal profile seemed not to be present, were still systematically smaller than those calculated using different transitions This can be regarded as an indication that part of the emission from the 393 36 / 396 84 nm doublet is still being reabsorbed by the cooler part of the plasma and that the dip in each profile is washed out by instrumental

broadening at lower densities and hence they were not used here for temperature determination. Figure 6.16 shows a spectroscopic image of the interaction region

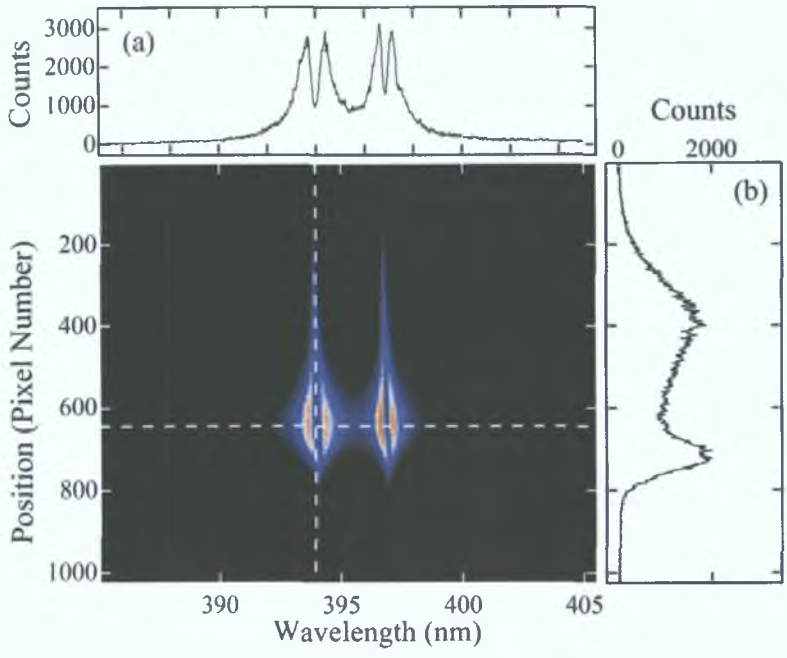

Figure 6.16: Spectroscopic image of the interaction region between two colliding laser-produced plasmas showing the Ca^+ $3p^64s(^2S_{1/2})$-$3p^64p(^2P_{3/2,1/2})$ doublet at 393.36 and 396.84 nm.

between two colliding plumes demonstrating the strength and spatial distribution of opacity along the length of the plume. Beginning from the bottom of the image in figure 6.16, one may see that both spectral lines begin at a narrow point before broadening considerably due to pressure / density effects. The extent of the broadening reaches its maximum value at approximately pixel number 620. This position is highlighted by the white dashed horizontal line drawn on the image; figure 6.16 (a) shows the line-out taken along this horizontal line. Figure 6.16 (b) shows the line-out taken along the white dashed vertical line drawn through the centre of the spectral line located at 393.36 nm. It may be seen that as we continue to move further up the image from the position of the horizontal line that both transitions begin to narrow again before reaching a point and disappearing. This behaviour is in good agreement with all of the density profiles presented in this chapter on the interaction region. In an attempt to understand the spectra shown in figure 6.16 and the processes involved in their formation, it was decided that a radiation transport model should be implemented to extract information from such optically thick transitions. This model and its application to Ca^+ transitions

in expanding plumes are presented in the next chapter

6.6 Summary

In this chapter we have presented and discussed spectrally and temporally-resolved emission images as well as spatially and temporally-resolved imaging spectra of colliding laser-produced plasmas Results were obtained from plasmas generated using three different laser pulse parameters Spatial distributions of electron temperature and density in the interaction region were presented and discussed

In the next chapter we will discuss the implementation of a computational radiation transport model used to describe the strong radiation trapping effects observed during the course of our spectroscopic studies of calcium plasmas

Bibliography

[1] S S Harilal, C V Bindhu, V P Shevelko, and H-J Kunze Xuv diagnostics of colliding laser-produced magnesium plasmas *Journal of Physics B Atomic, Molecular and Optical Physics*, 34 3717–3726, 2001

[2] F Ruhl, L Aschke, and H -J Kunze Selective population of the $n = 3$ level of hydrogen-like carbon in two colliding laser-produced plasmas *Physics Letters A*, 225 107–112, 1997

[3] V Henč-Bartolic, Z Andreic, D Gracin, L Aschke, F Ruhl, and H -J Kunze Spectral line enhancement in laterally colliding boron-nitride plasmas *Physica Scripta*, T75 279–299, 1998

[4] L Aschke Selective population of the n = 3 levels of lithium like aluminium in interpenetrating plasmas *Contrib Plasma Phys* , 40 72–76, 2000

[5] T Sakka, T Nakajima, and Y H Ogata Spatial population distribution of laser ablation species determined by self-reversed emission line profile *Journal of Applied Physics*, 92 2296–2303, 2002

[6] S S Harilal, C V Bindhu, and H -J Kunzea Time evolution of colliding laser produced magnesium plasmas investigated using a pinhole camera *Journal of Applied Physics*, 89 4737–4740, 2001

[7] R K Singh and J Narayan Pulsed-laser evaporation technique for deposition of thin films Physics and theoretical model *Physical Review B*, 41 8843–8859, 1990

[8] D Colombant and G F Tonon X-ray emission in laser produced plasmas *Journal of Applied Physics*, 44 3524–3537, 1973

[9] H R Griem *Plasma spectroscopy* McGraw-Hill, New York, 1964

[10] H R Griem *Principles of plasma spectroscopy* Cambridge monographs on plasma physics Cambridge University Press, New York, 1997

[11] D Doria, K D Kavanagh, J T Costello, and H Luna Plasma parametrization by analysis of time-resolved laser plasma image spectra *Measurement*

Science and Technology, 17 670–674, 2006

[12] C Chenais-Popovics, P Renaudin, O Rancu, F Gilleron, J -C Gauthier, O Larroche, O Peyrusse, M Dirksmoller, P Sondhauss, T Missalla, I Uschmann, E Forster, O Renner, and E Krousky Kinetic to thermal energy transfer and interpenetration in the collision of laser-produced plasmas *Physics of Plasmas*, 4 190–208, 1997

[13] A S Wan, T W Barbee, R Cauble, P Celhers, L B Da Silva, J C Moreno, P W Rambo, G F Stone, J E Trebes, and F Weber Electron density measurement of a colliding plasma using soft-x-ray laser interferometry *Phys Rev E*, 55 6293–6296, 1997

[14] C Courtois, R Grundy, A Ash, D Chambers, R Dendy, K Mcclements, and N Woolsey Experiment on colhsionless plasma interaction with applications to supernova remnant physics, *Astrophysics and Space Science,*, 298 93–98, 2005

[15] P W Rambo and J Denavit Interpenetration and ion separation in colliding plasmas *Physics of Plasmas*, 1 4050–4060, 1994

[16] S Eliezer *The interaction of high-power lasers with plasmas* Institute of Physics Publishing, Bristol, 2002

CHAPTER 7

RADIATION TRANSPORT MODELLING

7.1 Introduction

Radiation emitted from LPP's, or any light source, must in general travel from some interior point within the source to the exterior As the radiation travels through the source from its emission point to the perimeter of the source it may be absorbed by atomic constituents in its path The absorption of radiation by atoms or ions on this path is usually by the same species as the emitter, hence the term 'self-absorption" [1] This has the effect of suppressing the intensity of the radiation exiting the source Therefore if the absolute or relative intensity of spectral lines are being used to determine parameters such as the oscillator strengths or as a diagnostic tool to characterise the source then special care should be taken to account for self-absorption

A plasma, for which the re-absorption / trapping of radiation cannot be neglected is said to be optically thick Radiation trapping complicates the use of spectroscopic diagnostics that are based on a linear relationship between the plasma's emission coefficient and the observed line intensity Determining the effect that opacity has on the intensity of a measured spectral line is very difficult The strength of the absorption will vary between spectral lines from the same source, and will even vary with wavelength across a single spectral line In many circumstances a plasma may be optically thin (radiation trapping may be neglected) at all frequencies except for resonance transitions Under certain circumstances the influence of the radiation

field on the population density of the atomic levels must also be considered [2]

In laser-produced plasmas steep radial density gradients exist between the centre of the plasma and its periphery The hot central core consists of a high density of excited species leading to large amounts of emission, whereas the cooler low density peripheral regions contain a much larger proportion of less excited atoms, which may absorb photons emitted by the core

The emission profile from the hot, dense central core of the plasma is broadened and shifted by Stark effects due to the high electron density On the other-hand the absorption profile nearer the plasma's edges is less broadened and more concentrated at the centre frequency of the transition For this reason the majority of the absorption occurs at the centre of the emission line profile Under certain circumstances this may lead to a special case of self-absorption known as "line-reversal" When this happens the intensity of the centre of the profile has been attenuated to such an extent that it is lower than the wings of the profile, resulting in a dip at the central frequency of the transition [3, 4]

The profile of a spectral line, as observed outside a plasma, depends chiefly on the distribution of the emitting and absorbing atoms along the line-of-sight through the plasma [5] Line-reversal only occurs in a spectral line if the distribution of the absorbing or lower level state atoms is longer than that of the emitting excited state distribution (inhomogeneous plasma) In the case where the two distributions are equivalent (homogeneous plasma), the intensity attenuation caused by self-absorption will not lead to a self-reversed profile, nevertheless the effect will be to invalidate any data on plasma diagnostics obtained using the intensity of such lines [6, 7]

The effect of self-absorption is felt most strongly in high oscillator strength transitions, such as resonance transitions This is so because of the tendency of large populations to accrue in the ground state or lower level of these transitions in the cooler extremities of a laser plasma plume, hence providing a strong base for the re-absorption of photons exiting the plasma It is for this reason that resonance transitions are ideal candidates to study the extreme self-absorption case, line-reversal [8, 9] Determining plasma parameters from optically thick plasmas (or transitions) can be very difficult because they can not be placed into any of the thermodynamic equilibrium models discussed in section 2 5 All four models

described require that the plasma be optically thin at all frequencies This also precludes the application of the majority of the spectroscopic diagnostic techniques discussed in section 3 4 because most of them assume a state of local thermodynamic equilibrium

This difficulty in determining parameters from optically thick plasmas may be tackled by the careful study of self-reversed line profiles The depth of reversal, of line profiles, is very sensitive to changes in the excited and lower level distributions as well as the plasma temperature This makes them a powerful diagnostic for determining such parameters

As was mentioned previously in chapter 6 we have observed experimentally line-reversal in the Ca^+ $3p^64s(^2S_{1/2})$-$3p^64p(^2P_{3/2,1/2})$ doublet at 393 36 and 396 48 nm In an attempt to further understand the observed spectra we decided to adapt and implement a model developed by Sakka *et al* [3] for comparison with the experimental results The model generates synthetic spectra by solving the one-dimensional equation of radiative transfer [10, 11] introduced in section 2 6

7.2 Details of Sakka model

In this section we will discuss the details of the self-absorption model proposed by Sakka *et al* [3] We will discuss the model *ab initio* in the order in which the quantities should be calculated Important parameters will be plotted and presented to aid in the description of the model

A critical component in the determination of the profile of a self-reversed spectral line is the relationship between the width of the upper and lower level population distributions More specifically, the profile is determined by the ratio of the density of emitters-to-absorbers, which is closely related to the source function $S(x, \nu)$ along the line-of-sight [5]

$$S(\tau, \nu) = \frac{\epsilon(x, \nu)}{\kappa(x, \nu)} \tag{7 1}$$

where $\epsilon(x, \nu)$ and $\kappa(x, \nu)$ are the position-dependent emission and absorption coefficients from equations 2 35 and 2 36 in section 2 6 In this model Gaussian functions are used to describe the radial population distributions along the line-of-sight perpendicular to the expansion direction of the plasma This geometry is

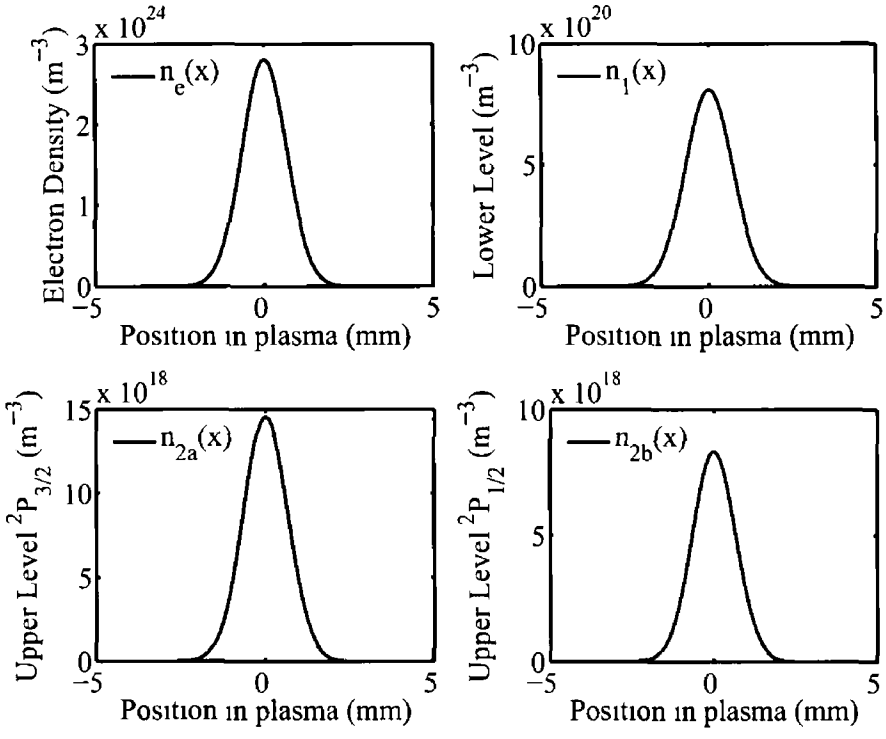

Figure 7 1 Spatial distributions of (a) electron density, (b) ground state population, (c) excited state $^2P_{3/2}$ and (d) excited state $^2P_{1/2}$

equivalent to the emission spectroscopy setup described in section 4 10 and illustrated in figure 4 32, where we recorded spatially-resolved spectra perpendicular to the plasma expansion direction

Three population distribution functions are required to describe the general case of a single spectral line These distributions are the lower level $n_1(x)$, the upper level $n_2(x)$ and the electron density $n_e(x)$ The electron density spatial distribution is used to improve the fit to the experimental data by introducing a space dependent asymmetric broadening and shift to the line profiles that could not be accounted for in terms of radiative transfer alone [3] When applying the model to the neutral Al^0 $3s^23p(^2P^o_{3/2,1/2})$-$3s^24s(^2S_{1/2})$ doublet (as was implemented by Sakka *et al*), two lower level distributions are required to represent the doublet, while conversely when applying the model to the Ca^+ $3p^64s(^2S_{1/2})$-$3p^64p(^2P_{3/2,1/2})$ transitions that were experimentally observed during the course of this work, two excited state distributions are required The four distribution functions for the Ca^+ case are

given by

$$n_{2a}(x) = N_{2a} exp\left(-\frac{x^2}{\sigma_{2a}^2}\right) \tag{7 2}$$

$$n_{2b}(x) = N_{2b} exp\left(-\frac{x^2}{\sigma_{2b}^2}\right) \tag{7 3}$$

$$n_1(x) = N_{10} exp\left(-\frac{x^2}{\sigma_1^2}\right) \tag{7 4}$$

$$n_e(x) = N_{e0} exp\left(-\frac{x^2}{\sigma_e^2}\right) \tag{7 5}$$

where σ_{2a}, σ_{2b}, σ_1 and σ_e are the widths of the distribution for the two upper, lower and electron distributions respectively N_{2a}, N_{2b}, N_{10} and N_{e0} are the maximum values of the population parameter for the four distributions at the centre of the plasma

A Boltzmann population distribution is assumed in order to provide an approximation of the excited levels populations Therefore using a static plasma temperature T_0, only one (upper or lower) population parameter is required as an input to the model The population of the other level would then be calculated using the Boltzmann relation

$$\frac{N_{20}}{N_{10}} = \frac{g_2}{g_1} exp\left(-\frac{h\nu_0}{k_B T_0}\right) \tag{7 6}$$

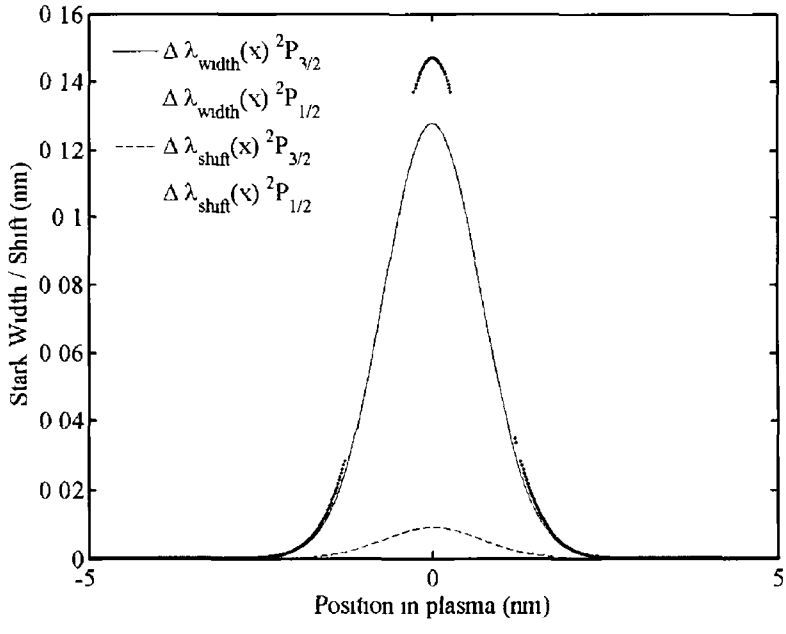

Figure 7 2 Stark width and shift of spectral lines as a function of position in the plasma where "0" corresponds to the plasma core

where g_1 and g_2 are the relevant state degeneracies and ν_0 is the central frequency of the transition. In the case of a doublet with closely lying levels, denoted a and b we can write that

$$\frac{N_a}{N_b} = \frac{g_a}{g_b} \tag{7.7}$$

For example in Ca^+ we can write the $3p^6 4p\ ^2P_{3/2}$ state as a and the $3p^6 4p\ ^2P_{1/2}$ state as b. The assumption of a Boltzmann population distribution in the peripheral region of the plasma may be somewhat questionable in the case of certain plasmas (radiation dominated), as it does not take into account the effect that reabsorption may have on the population of the excited levels. However, radiation trapping should not seriously affect the population of excited states in laboratory plasmas, which are almost always collision dominated. A plasma is said to be collision dominated when the excitation and ionisation of particles is predominantly caused by particle impacts rather than by radiative processes [2].

Figure 7.1 shows the population distributions of the energy levels and the electrons as a function of space for the Ca^+ case, where the centre of the plasma is denoted by position 0 mm. From the electron distribution $n_e(x)$, the magnitude of the Stark width $\Delta\lambda_{width}(x)$ and shift $\Delta\lambda_{shift}(x)$ as a function of space may be calculated. In this case the non-linear functions presented in section 3.4.3 (equations 3.5 and 3.6)

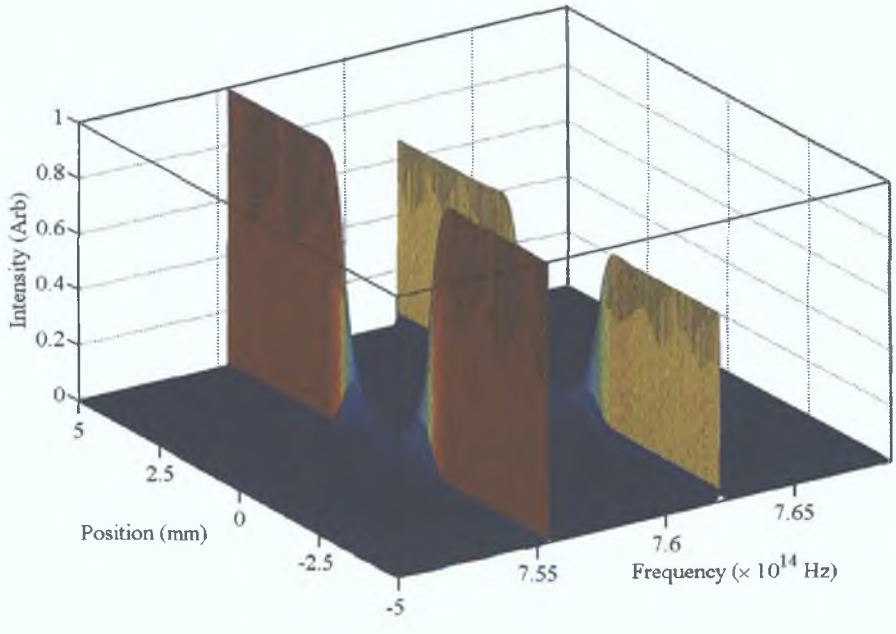

Figure 7.3: Normalised position-dependent spectral distribution function for the Ca^+ $3p^6 4s$-$3p^6 4p$ doublet.

have been approximated as linear functions given by

$$\Delta\lambda_{width}(x) = wn_e(x) \tag{7.8}$$

$$\Delta\lambda_{shift}(x) = dn_e(x) \tag{7.9}$$

where w and d are experimentally determined width and shift parameters obtained from literature [17, 18]. The validity of this approximation was discussed in section 6.2; for singly charged ions the effect of the ion-broadening component on the overall linewidth was calculated to be $< 5\%$. This value would be smaller for the neutral Al transition used by Sakka *et al* [3]. Figure 7.2 shows how the magnitude of the width and shift varies through the plasma for both transitions.

The position-dependent width and shift distributions are subsequently used to formulate a position-dependent spectral distribution function $f(x, \nu)$ given by

$$f(x,\nu) = \frac{1}{\pi}\frac{\Delta\nu_{width}(x)/2}{[\Delta\nu_{width}(x)/2]^2 + [\nu + \nu_0 + \Delta\nu_{shift}(x)/2]^2} \tag{7.10}$$

this function is then normalised over the frequency range being used such that

$$\int_{-\infty}^{\infty} f(x,\nu)d\nu = 1 \tag{7.11}$$

The normalised position-dependent spectral distribution function is plotted in figure 7.3. The spectral distribution function $f(x, \nu)$ is subsequently used in the

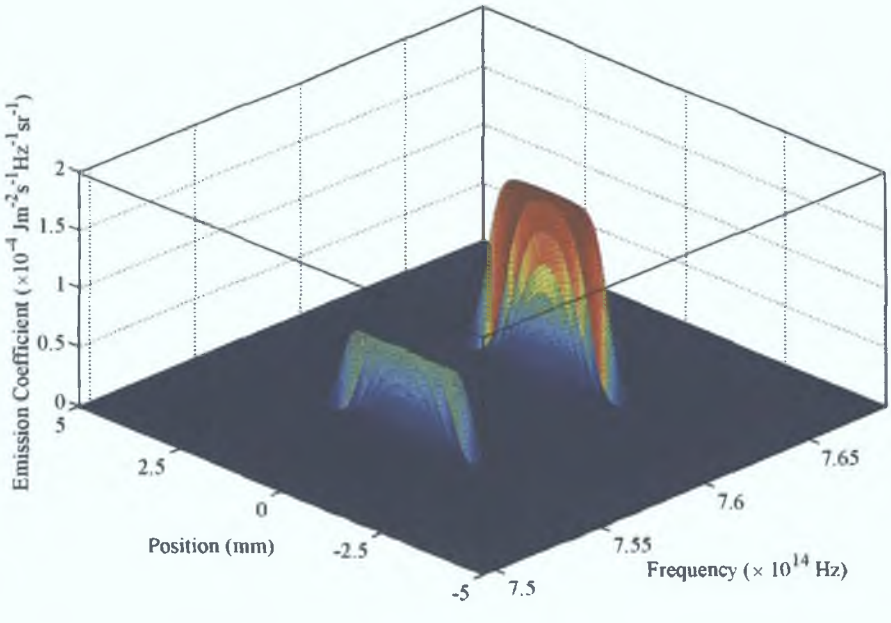

Figure 7.4: Position-dependent spectral emission coefficient.

formulation of the position dependent emission $\epsilon(x,\nu)$ and absorption $\kappa(x,\nu)$ coefficients that were discussed in section 2.6 and will be expanded on below. However before these may be calculated the Einstein coefficients for spontaneous emission A_{ba}, absorption B_{ba} and stimulated emission B_{ba} must be calculated from equations 2.32, 2.33 and 2.34 respectively, as they were presented in section 2.6.1.

Having calculated Einstein's coefficients, the position dependent emission coefficient may now be calculated by inserting the Einstein coefficient for spontaneous emission, the upper level population distribution function and the Stark broadened and shifted spectral distribution function into equation 2.35, repeated here for the reader's convenience.

$$\epsilon(x,\nu) = \frac{A_{ba} n_b(x) h\nu f(x,\nu)}{4\pi} \tag{2.35}$$

Similarly the position-dependent absorption coefficient can be calculated by inserting the upper and lower level population distributions, as well as the Einstein coefficients for absorption and stimulated emission, along with the spectral distribution function into equation 2.36, also repeated here for convenience.

$$\kappa(x,\nu) = \frac{[B_{ab} n_a(x) - B_{ba} n_b(x)] h\nu f(x,\nu)}{c} \tag{2.36}$$

The spectral emission and absorption coefficients as a function of space are plotted in figures 7.4 and 7.5 respectively. At this stage all of the factors required to solve

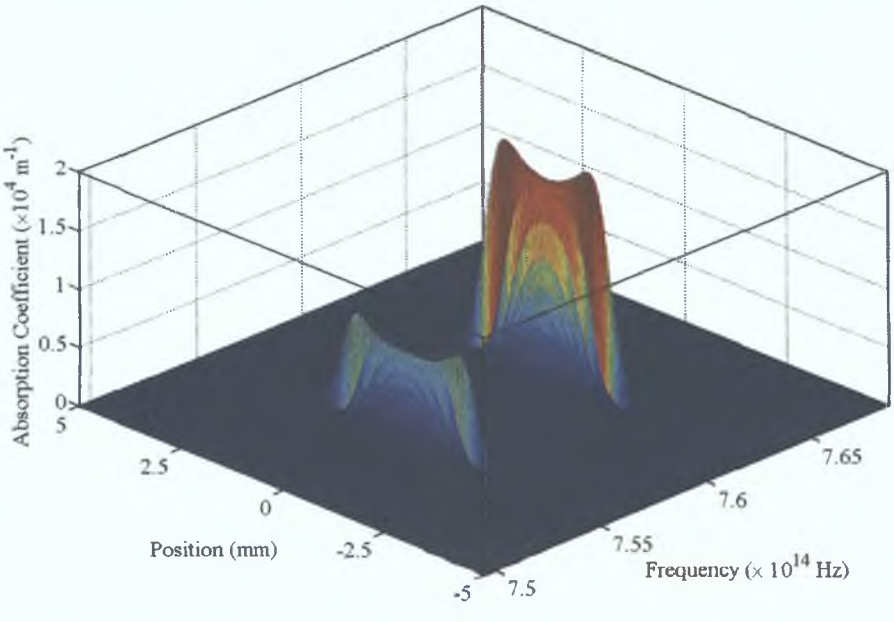

Figure 7.5: Position-dependent spectral absorption coefficient.

the general form of the equation of radiative transfer (discussed in section 2.6.4)

have been calculated The far field radiant flux density $I(\nu)$, which is the intensity profile of the radiation observed at a position outside of the plasma, is thus given by

$$I(\nu) = \frac{1}{\phi(\infty, \nu)} \int_{-\infty}^{\infty} \phi(x, \nu)\epsilon(x, \nu)dx \tag{7 12}$$

where

$$\phi(x, \nu) = exp\left[\int_{-\infty}^{x} \kappa(x, \nu)\right] \tag{7 13}$$

$I(\nu)$ for the Ca^+ doublet is plotted in figure 7 6 over a 10 nm spectral window using all of the input parameters listed in table 7 2 (next section 7 3)

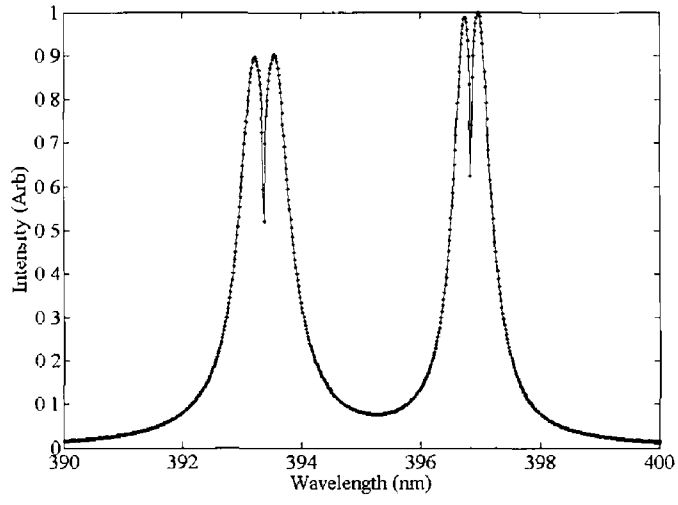

Figure 7 6 The far-field radiant flux density I_ν for the Ca^+ $3p^6 4s(^2S_{1/2})$-$3p^6 4p(^2P_{3/2,1/2})$ doublet using the input parameters from table 7 2

A grid spacing of $1\ 67\times10^{-2}$ nm was used over the 10 nm wavelength range of interest, while a $1\ 67\times10^{-2}$ mm grid cell size was used over a 10 mm spatial line-of-sight range This was the case for all of images presented in this chapter These computational grid spacings were chosen to balance detail with computational efficiency, providing only slightly more spatial and spectral resolution than that of the experimental observations

Before comparisons are made between the calculated spectrum $I(\nu)$ and the experimental spectra, the instrument function of the spectrometer used to record the experimental data should be convolved with the far-field radiant flux density $I(\nu)$

$$I_{calc}(\nu) = \int_{-\infty}^{\infty} I(\mu)g(\nu - \mu)d\mu \tag{7 14}$$

where $g(\nu)$ is a normalised ($\int_{-\infty}^{\infty} g(\nu)d\nu = 1$) Gaussian function, whose FWHM corresponds to the resolution of the entire optical system, optics, spectrometer and detector In order to compare the calculated spectra with the experimental results the calculated model spectrum was splined and re-sampled in order that the sampled wavelength values coincided with the CCD experimental pixel positions, and the dispersion of the spectrometer thus allowing the straightforward calculation of residuals

A goodness of fit (r-squared) parameter was then calculated to the determine the extent of correlation between the experimental and calculated data sets The r-squared factor is calculated using

$$R^2 = \left(\sum_{i=1}^{n}(\hat{y}_i - \bar{y})^2\right)\left(\sum_{i=1}^{n}(y_i - \bar{y})^2\right)^{-1} \tag{7 15}$$

where $\hat{y}$ is the difference between the predicted and actual values, $\bar{y}$ is the grand mean of the data-set and y_i is the model data The r-squared value may be described as, the ratio of the sum of squares of the difference between the predicted values and the grand mean, to the sum of the squares of the difference between the model data and its grand mean

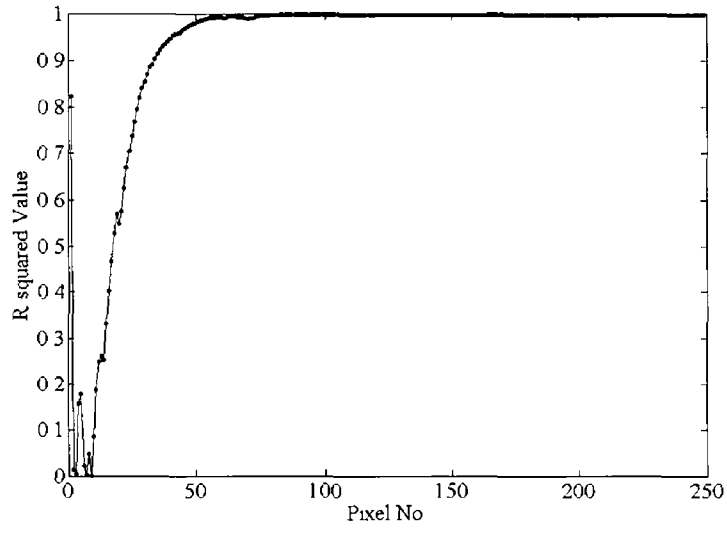

Figure 7 7 Cumulative r-squared values for one model-experiment comparison

A plot of the cumulative r-squared value as a function of data-point is shown in figure 7 7 This shows how the r-squared value improves for one model-experiment comparison as more and more data points are considered The last value in figure 7 7 is the total r-squared value of the comparison between the two data sets

This value is outputted to the minimisation function An r-squared value of 1 would signify complete correlation between the calculated and experimental values The model was fitted to the experimental data by iteratively varying three adjustable input parameters (i) the lower level population distribution N_{10}, (ii) the excited state distribution width σ_2 and (iii) the electron population parameter N_{e0}

The fitting procedure attempts to maximise the correlation between the model and the experimental data by minimising an output factor $(1 - R^2)$ The fitting procedure robustly converged to the same values (within 0 5%) provided the initial input parameters are within 10% of the best fit solution

Two versions of the model were implemented in this work, one model simulating the Al^0 $3s^2 3p(^2P^o_{3/2,1/2})$-$3s^2 4s(^2S_{1/2})$ as was presented by Sakka *et al*, and the other model simulating the Ca^+ $3p^6 4s(^2S_{1/2})$-$3p^6 4p(^2P_{3/2,1/2})$ which was experimentally observed in this work Grotrian diagrams for these two systems are shown in figure 7 8 The Al(I) case was implemented so that it could be compared with results presented in the paper of Sakka *et al* Three figures were presented in that paper demonstrating the effect of varying the three adjustable input parameters These three figures are presented here as figure 7 9 (a), (b) and (c) The results generated using the same input parameters as those presented by Sakka *et al* [3] (table 7 1), using the Al model implemented in this work are shown (with normalised intensities) as figure 7 9 (d), (e) and (f)

Figure 7 9 (a) shows the effect that the width of the ground state distribution

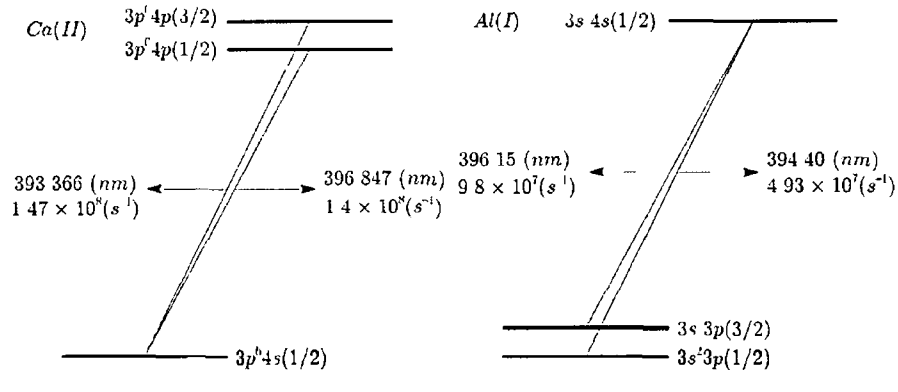

(a) Ca(II) Doublet (b) Al(I) Doublet

Figure 7 8 Grotrian diagrams for the Ca(II) and Al(I) doublets

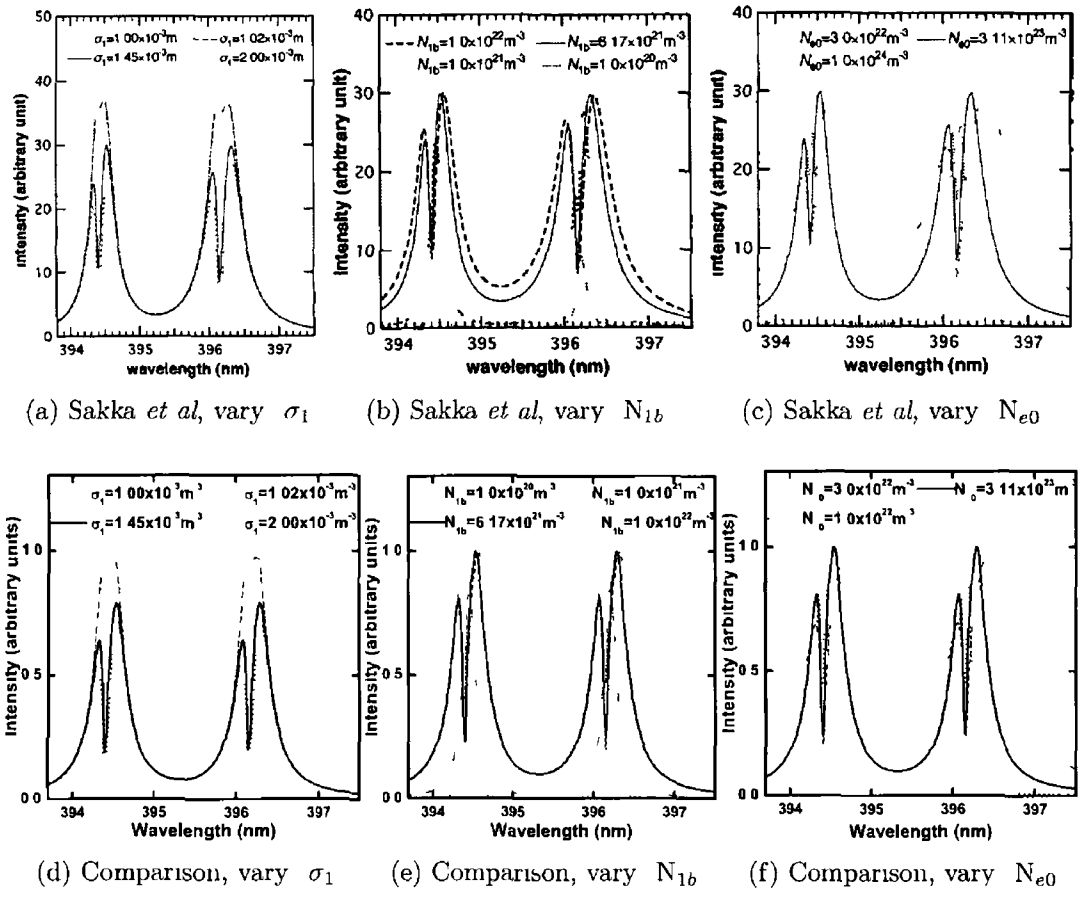

(a) Sakka *et al*, vary σ_1 (b) Sakka *et al*, vary N_{1b} (c) Sakka *et al*, vary N_{e0}

(d) Comparison, vary σ_1 (e) Comparison, vary N_{1b} (f) Comparison, vary N_{e0}

Figure 7 9 Comparison of results obtained from the modelling of the 394 401 nm ($^2P^\circ_{1/2}$ - $^2S_{1/2}$) and the 396 152 nm ($^2P^\circ_{3/2}$ - $^2S_{1/2}$) of neutral Al, with those presented by Sakka *et al* [3]

has on the profile Four representative spectra are presented for four different σ_1 values, all of the other parameters are fixed at the values presented in table 7 1 The excited state distribution width (σ_2) does not vary As σ_1 increases relative to σ_2, the calculated emission profile begins to develop a dip at the central frequency of the transition As the difference between the ground and excited state distribution width is further increased the self-reversal structure becomes more pronounced It should however be noted that the effect of varying σ_1 is limited only to the central or self-reversing portion of the line profile The wings of the lines are unaffected by the values of σ_1 It may be seen from figure 7 9 (a) that even a very slight disparity (2%) between the upper and lower distribution widths leads to the formation of a self-reversed spectral feature Consequently, the experimental observation of the self-reversed spectra would be a sensitive measure for the purpose of obtaining information on the inhomogeneity in the population-density distribution of the

Table 7.1: Parameters used for the simulation of $^2P^\circ$–^2S self-reversed spectra of Al(I) (After Sakka *et al* [3])

Symbol	Definition	Value (Unit)
A_{2a}	radiative rate for $^2P^\circ_{3/2} - ^2S_{1/2}$ transition	$9.8\text{x}10^7(\text{s}^{-1})$
A_{2b}	radiative rate for $^2P^\circ_{1/2} - ^2S_{1/2}$ transition	$4.93\text{x}10^7(\text{s}^{-1})$
g_a	degeneracy of $^2P^\circ_{3/2}$ level	4
g_b	degeneracy of $^2P^\circ_{1/2}$ level	2
g_2	degeneracy of $^2S^\circ_{1/2}$ level	2
λ_{a0}	origin of the $^2P^\circ_{3/2} - ^2S_{1/2}$ transition	396.152 (nm)
λ_{b0}	origin of the $^2P^\circ_{1/2} - ^2S_{1/2}$ transition	394.401 (nm)
w	Stark width parameter	$4.22\text{x}10^{-25}$ $(\text{nm}/\text{m}^{-3})$
d	Stark shift parameter	$2.42\text{x}10^{-25}$ $(\text{nm}/\text{m}^{-3})$
T_0	temperature parameter	4000 (K)
N_{e0}	electron density parameter	$3.11\text{x}10^{23}$ (m^{-3})
N_{1a}	population parameter of $^2P^\circ_{3/2}$ state	$1.23\text{x}10^{22}$ (m^{-3})
N_{1b}	population parameter of $^2P^\circ_{1/2}$ state	$6.17\text{x}10^{21}$ (m^{-3})
N_{20}	population parameter of ^2S state	$6.68\text{x}10^{17}$ (m^{-3})
σ_e	distribution parameter of the electrons	$1.00\text{x}10^{-3}$ (m)
σ_1	distribution parameter of the $^2P^\circ$ state	$1.45\text{x}10^{-3}$ (m)
σ_2	distribution parameter of the ^2S state	$1.00\text{x}10^{-3}$ (m)

lower and excited states [3].

Figure 7.9 (b) shows four calculated spectra in which the ground state population parameter N_{1b} is varied. It may be seen that this parameter has a strong effect on the emitted line profile. In particular three distinct features arise while varying this parameter: (i) the width of the profiles increases with increasing N_{1b}, (ii) the depth of self reversal structure increases with increasing N_{1b}, but disappears for values below $\sim 5 \times 10^{20}$ m^{-3}, (iii) and finally, that the intensities of the doublet do not increase any further for N_{1b} values $> 1 \times 10^{21}$ m^{-3}.

The final variable input parameter to the model is the electron density parameter N_{e0}. Figure 7.9 (c) shows the effect that the electron density has on the calculated profile. By varying the values of N_{e0}, the position and the width of the peak changes significantly. This is due to Stark shifting and broadening of the profiles. The position and the width of the self-reversal hole are however largely unchanged

when the electron density parameter is increased This is due to the fact that the absorbing atoms lie at the periphery of the plasma where the value of the electron density distribution is low For this reason the absorption profile is affected to a lesser extent than the emission emanating from the hot plasma core

7.3 Parameters used to model Ca(II) spectra

In order to make the comparison between our experimental measurements and the output of the radiation transport model, it is very important to match the model's input parameters to our experimental conditions

In the next section we will analyse in detail two space and time resolved Ca^+ spectral images, taken at 80 and 260 ns after plasma initiation These will be used to demonstrate the usefulness of the model as a diagnostic tool

Figure 7 10 shows line-outs from two broadband Ca emission images recorded at the same time delays as the spectral images that will be analysed in the next section The emission images were taken using the imaging setup described in section 4 9

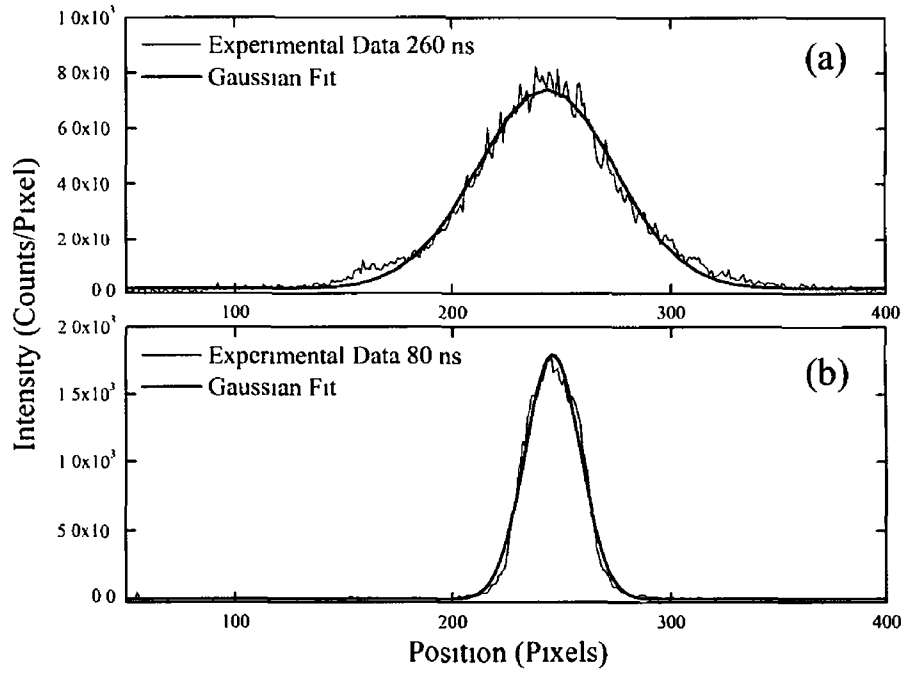

Figure 7 10 Broadband emission image line-outs for (a) 260 ns delay plasma image, (b) 80 ns delay plasma image

Table 7 2 Parameters used for the simulation self-reversed spectra of Ca(II)

Symbol	Definition	Value (Unit)
A_{2a}	radiative rate for $^2S_{1/2} - ^2P^\circ_{3/2}$ transition	1 47x10^8(s^{-1})
A_{2b}	radiative rate for $^2S_{1/2} - ^2P^\circ_{1/2}$ transition	1 40x10^8(s^{-1})
g_{2a}	degeneracy of $^2P^\circ_{3/2}$ level	4
g_{2b}	degeneracy of $^2P^\circ_{1/2}$ level	2
g_{10}	degeneracy of $^2S_{1/2}$ level	2
λ_{a0}	origin of the $^2P^\circ_{3/2} - ^2S_{1/2}$ transition	393 366 (nm)
λ_{b0}	origin of the $^2P^\circ_{1/2} - ^2S_{1/2}$ transition	396 847 (nm)
w	Stark width parameter	See table 7 3
d	Stark shift parameter	See table 7 3
T_0	temperature parameter	10,000/8000 (K)
N_{e0}	electron density parameter	Adjusted
N_{1a}	population parameter of $^2P^\circ_{3/2}$ state	Calculated
N_{1b}	population parameter of $^2P^\circ_{1/2}$ state	Calculated
N_{20}	population parameter of ^2S state	Adjusted
σ_e	distribution parameter of the electrons	Adjusted
σ_1	distribution parameter of the $^2P^\circ$ state	Expt determined
σ_2	distribution parameter of the ^2S state	Adjusted

The line-outs were taken at the broadest point of the emissivity perpendicular to the plasmas expansion direction Gaussian functions have been fitted to the line-outs and their widths extracted

The FWHM of the fitted Gaussian profile in figure 7 10 (a) (260 ns) is 63 pixels Given a CCD pixel size of 25 5 μm and a magnification of 1 3 (from figure 4 31 (a), section 4 9), the FWHM of the plasma is $\sim$ 1 25 mm The FWHM of the fit to the 80 ns profile (figure 7 10 (b)) is 24 pixels, which gives us a value of $\sim$ 0 5 mm

Table 7 3 Ca(II) Stark parameters (After Konjevic *et al* [18])

λ (nm)	T (K)	N_e (cm^{-3})	Broadening (nm)	w (nm/m^{-3})
393 36	13,350	1 32 $\times$ 10^{17}	0 018	1 3939 $\times$ 10^{-25}
	12,240	0 8 $\times$ 10^{17}	0 009	1 1425 $\times$ 10^{-25}
396 68	13,350	1 32 $\times$ 10^{17}	0 016	1 2197 $\times$ 10^{-25}
	12,240	0 8 $\times$ 10^{17}	0 009	1 0575 $\times$ 10^{-25}

These widths are used as input parameters to generate the ground state distributions σ_1 The excited state and electron density distributions are varied around this point in order to generate the best fit to the experimental data Most of the parameters required to model the Ca^+ $3p^6 4s(^2S_{1/2})$-$3p^6 4p(^2P_{3/2,1/2})$ doublet are given in table 7 2 The Stark parameters used were obtained from the literature [18]

7.4 Application of model to Ca(II) imaging spectra

As was mentioned previously, analysis of optically thick profiles strongly prohibits their application using standard plasma diagnostics [19] However, using the radiation transport model described in section 7 2 and the experimental spectroscopic setup outlined in section 4 10 we may use optically thick transitions to temporally and spatially infer information such as population distributions, densities and to a lesser extent temperature

As was previously discussed when dealing with optically thick transitions the relationship between the observed emission intensity and the plasma parameters, such as the emission coefficient or the oscillator strength of the transition becomes more complicated In optically thin transitions where re-absorption can be neglected the intensity of the observation can be directly related to the number density of the emitters and the oscillator strength of the transition This leads to a situation where given the same number of emitters, the transition with the highest oscillator strength will produce the strongest spectral line

However in the case where re-absorption of photons cannot be neglected, as in optically thick transitions, this relationship between intensity and oscillator strength does not necessarily hold The emission intensity of an observed transition is directly proportional to the number density N of emitters and the oscillator strength f of the transition

$$I_{Emission} \propto Nf \tag{7 16}$$

However the absorption intensity is proportional to the exponential of the population number density by the oscillator strength by the path length l

$$I_{Absorption} \propto e^{-Nfl} \tag{7 17}$$

Therefore as the number density increases the emission increases linearly, whereas the absorption increases exponentially. This may lead to the situation where the transition with the highest oscillator strength and the same population, is less intense than a lower oscillator strength transition, due to the increased absorption.

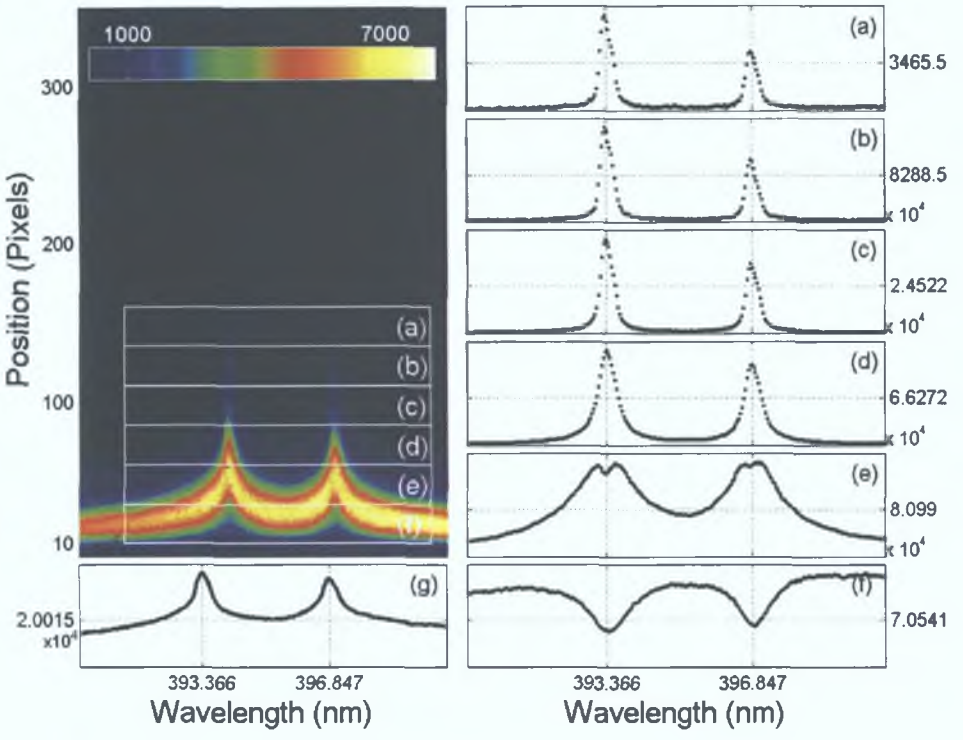

Figure 7.11: Spectral image showing the $3p^6 4s(^2S_{1/2})$-$3p^6 4p(^2P_{3/2,1/2})$ transitions at 393.36 and 396.84 nm recorded 80 ns after plasma initiation with a 15 ns gate width.

This relationship between the oscillator strength, density, opacity and path length was experimentally observed using our space resolved spectroscopy setup (as outlined in section 4.10). Figure 7.11 shows a spectroscopic image of the Ca^+ $3p^6 4s$ $(^2S_{1/2})$-$3p^6 4p(^2P_{3/2,1/2})$ doublet taken 80 ns after plasma initiation, with an ICCD gate width of 15 ns. Partial vertical binning of the image has been performed, on the image. Six boxes have been drawn on the image in figure 7.11. The contents of the six boxes labelled (a)-(f) (containing 25 rows of pixels each) have been summed and plotted in the graphs to the right of the image labelled (a)-(f). The graph labelled figure 7.11 (g) located directly below the image, shows the profile obtained if the entire image was fully vertically binned. This trace is what would be experimentally recorded if spatially integrated spectroscopy was performed. It is clear that all evidence of self-reversal in these transitions is masked by such integration.

The box labelled (f) on the image covers the area closest to the target surface where the density is highest. Strong Bremsstrahlung emission can be observed across the wavelength range of the image, as well as strong absorption at the transition wavelengths. This may be seen more clearly in graph (f), where it may be observed that absorption strongly dominates over emission at the transition wavelengths, leading to a deep dip in the continuum emission.

Moving to the box and graph labelled (e), where the density is lower, the magnitude of the absorption has decreased rapidly, leading to recognisable emission features with self-reversed peaks. The peaks are broadened significantly by the large electron density close to the target. It should be noted that at this point both peaks exhibit approximately the same intensity, the 396.847 nm line ($3p^6 4s(^2S_{1/2})$-$3p^6 4p(^2P_{1/2})$) being slightly more intense.

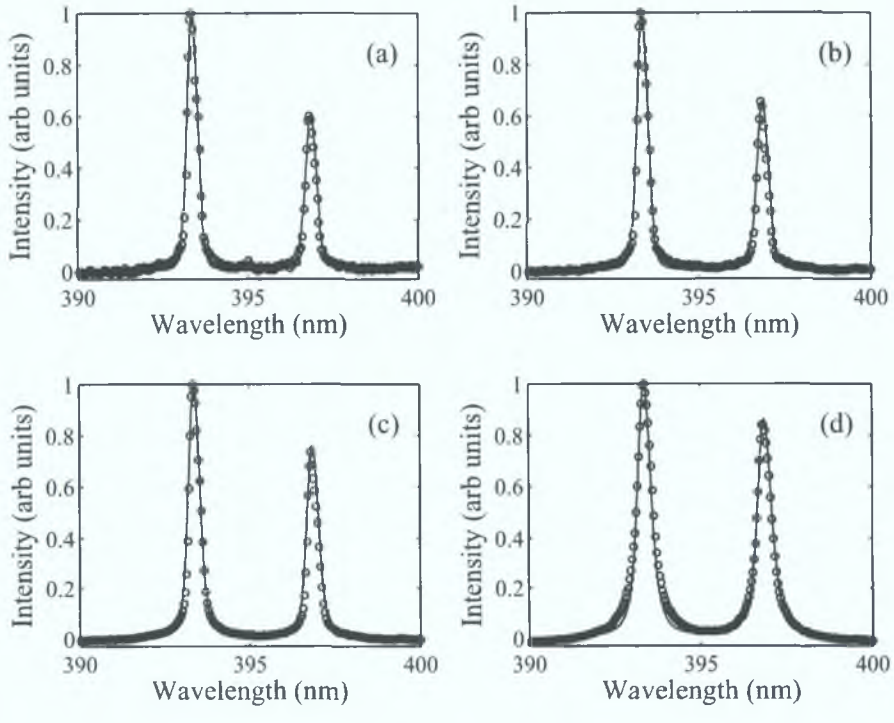

Figure 7.12: Experimental data (o) reproduced from figure 7.11, graphs (a)-(d) (normalised), as well as model fits (-) to data.

Looking now at the next four boxes and graphs (d), (c), (b) and (a) of figure 7.11, i.e. moving further and further away from the target surface and concomitantly to progressively lower density, it may be observed that the ratio of the intensity between the two spectral lines changes, with the longer wavelength line weakening relative to its shorter wavelength companion. Eventually the intensity ratio should

Table 7.4: Output parameters generated during the fitting of data presented in figure 7.12

Box label	σ_2 (m)	N_{1b} (m^{-3})	N_{e0} (m^{-3})
(a)	9.10×10^{-4}	1.56×10^{19}	4.84×10^{24}
(b)	8.75×10^{-4}	1.58×10^{19}	4.95×10^{24}
(c)	8.30×10^{-4}	1.63×10^{19}	5.44×10^{24}
(d)	6.25×10^{-4}	2.62×10^{19}	6.50×10^{24}

approach the statistical value of the two levels $g(\frac{3}{2})/g(\frac{1}{2}) = 2$. This is so because the absorption coefficient, for the two differing oscillator strengths, has decreased more rapidly with the density gradient than the linear emission relationship as mentioned previously. This feature can be simulated using the radiation transport model described in section 7.2. Figure 7.12 shows fits obtained for the data contained within the four graphs (a)-(d) in figure 7.11. The fitted parameters extracted from the model are presented in table 7.4.

This example powerfully illustrates how a model based on radiation transport can be used to determine parameters from optically thick transitions even in the case where no line-reversed features are evident. The model accurately fitted the

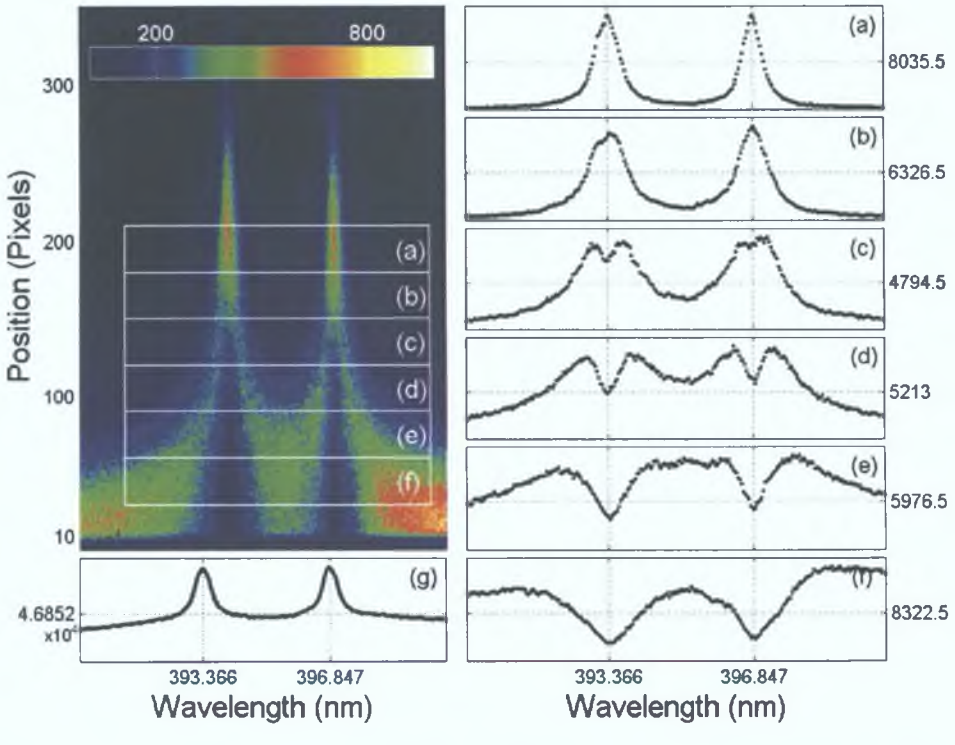

Figure 7.13: Spectral image showing the $3p^6 4s(^2S_{1/2})$-$3p^6 4p(^2P_{3/2,1/2})$ at 393.36 and 396.84 nm recorded 260 ns after plasma initiation with a 30 ns gate width.

intensity ratio variation between the two emission lines as a function of opacity

It should be noted from table 7 4, that in addition to the density drop moving further from the target surface, the excited state distribution width σ_2 changes between fits This parameter also strongly affects the intensity ratios, as it has an important effect on path length l, given in equation 7 17 The ground state distribution used here was fixed to the width extracted from the plasma image recorded at 80 ns (figure 7 10 (b))

In the second case we will examine another spectroscopic image, figure 7 13, recorded on the same day under the same experimental conditions but taken 260 ns after plasma initiation At this delay the plasma has expanded considerably and the continuum emission near the target surface has all but died away

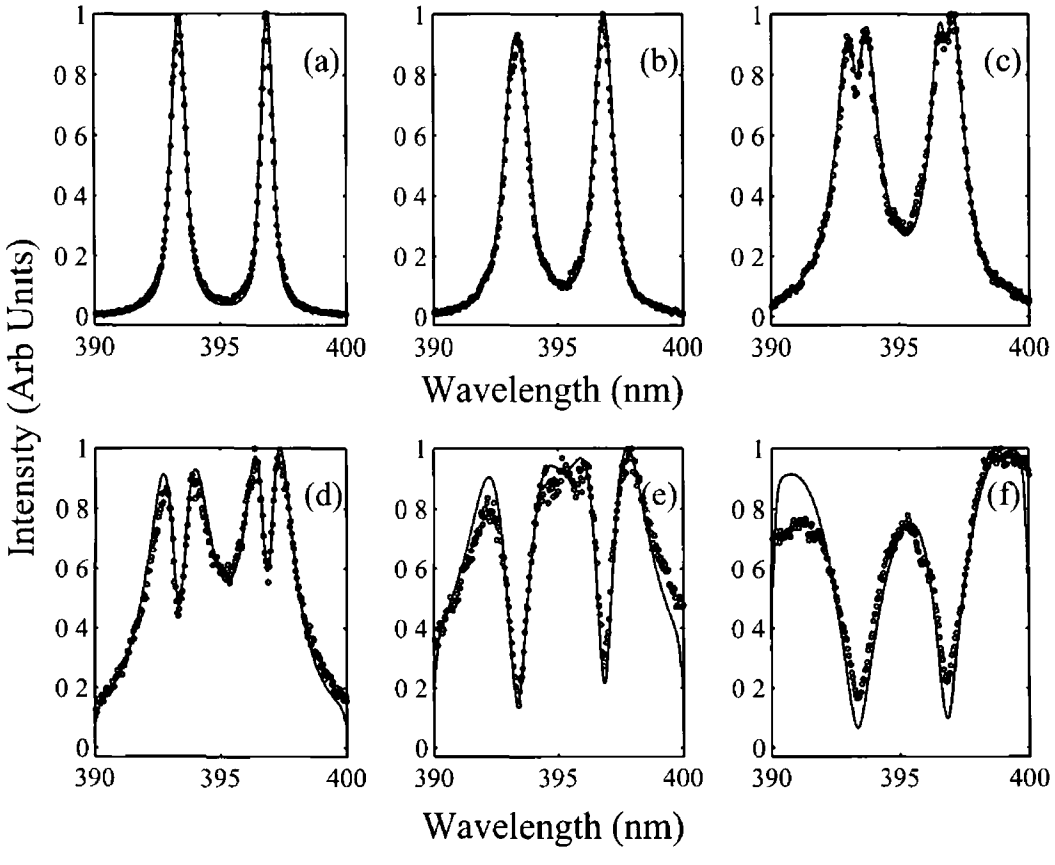

Figure 7 14 Experimental data reproduced from figure 7 13, graphs (a)-(f) (normalised) as well as model fits to data

It may be seen from the image in figure 7 13 that absorption (the dark area) at the centre wavelength of the two transitions extends for some distance along the

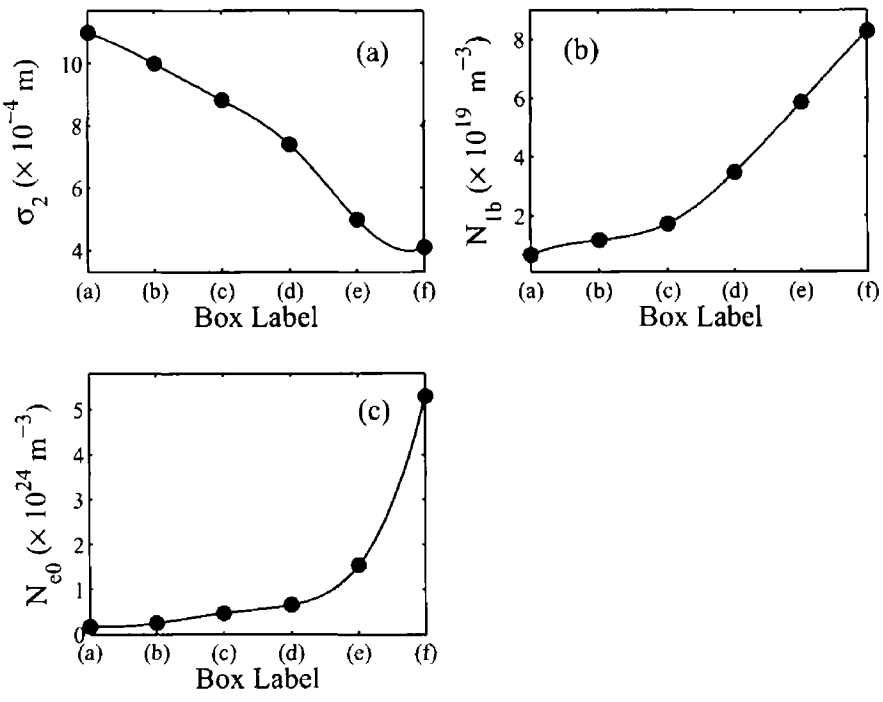

Figure 7 15 Best-fit input parameters calculated during the model comparison with a 260 ns spectroscopic image (figure 7 13)

plasma expansion direction Again the image has been divided into six boxes with corresponding graphs to facilitate a spatial analysis of the image Each box in this case contains 40 rows of pixels The box sizes were chosen such that the progression from highly self-reversed to non-reversed spectra could be presented The time delay of 260 ns was chosen here to balance the complicating issues of poor signal-to-noise ratio and underlying continuum emission near the target surface

It may be seen from the graph (f) (figure 7 13), that the emission profile emanating from the region in box (f), is dominated by the absorption coefficient This leads to a large absorption profile and no discernable emission "peak" Again as we move to the next box and graph labelled (e) the density has dropped somewhat allowing the emission profile to emerge as the absorption drops off with greater rapidity

Figure 7 14 shows the synthetic spectra fits to the experimental data presented in graphs (a)-(f) from figure 7 13 using the radiation transport model The r-squared value for each fit presented in figure 7 14 is $> 0\ 98$ Figure 7 15 shows the outputs from the fitting procedure, i e the input parameter values yielding greatest correlation between the model and experimental data sets

It may be seen from figure 7 15 (a) that the excited state distribution σ_2 decreases

almost linearly as one moves closer to the target surface This distribution predominantly affects the depth of the reversed feature as it moves relative to the static ground state distribution width extracted from figure 7 10 (a)

The ground state population parameter N_{1b} results are shown in figure 7 15 (b) Over the first three spatial boxes (a) to (c) the value of N_{1b} increases only slightly This is unsurprising due to the relatively long time delay (260 ns) of the image, where strong spatial density gradients have decreased significantly From box (c) to (f) the density increases more rapidly as we approach the target surface The effect that the population parameter has on the calculated profiles is to vary the ratio of the emission intensities between the two spectral lines as well as the ratio of the depth of the self-absorption holes This may be clearly seen from the profiles (a) to (f) in figure 7 14

Finally the results from the model fits to the experimental data for the electron density parameter are shown in figure 7 15 (c) Here we see that the electron density decreases rapidly along the primary expansion axis of the plasma, moving away from the target surface The contribution of the electron densities to the profiles can be seen in figure 7 14 (a) to (f) as it broadens and shifts the emission profiles as we move closer to the target surface

The first two spectroscopic images (figures 7 11 and 7 13) presented and analysed in this chapter have been obtained from single calcium plasma expansion in vacuum In both cases the position of the target surface may been clearly seen at the bottom of each image Partial binning of the spectroscopic images showed that the magnitude of the radiation trapping was greatest near the target surface (dark area within emission lines) and that it decreased the further we looked along the length of the plume Indications of opacity within these spectral lines were seen to be lost when the image was fully vertically binned, as was shown in the graph labelled (g) in figures 7 11 and 7 13

Figure 7 16 shows a spectroscopic image of the interaction / stagnation layer between two colliding calcium plumes showing the $3p^6 4s(^2S_{1/2})$-$3p^6 4p(^2P_{3/2,1/2})$ Ca^+ doublet at 393 36 and 396 84 nm, taken 400 ns after primary plasma initiation This image was obtained using the same procedure outlined in section 6 2 The primary plasma plumes were generated using 1064 nm, 16 ns pulses from the Spectron SL-404 laser system (section 4 3) The data was acquired on the same day,

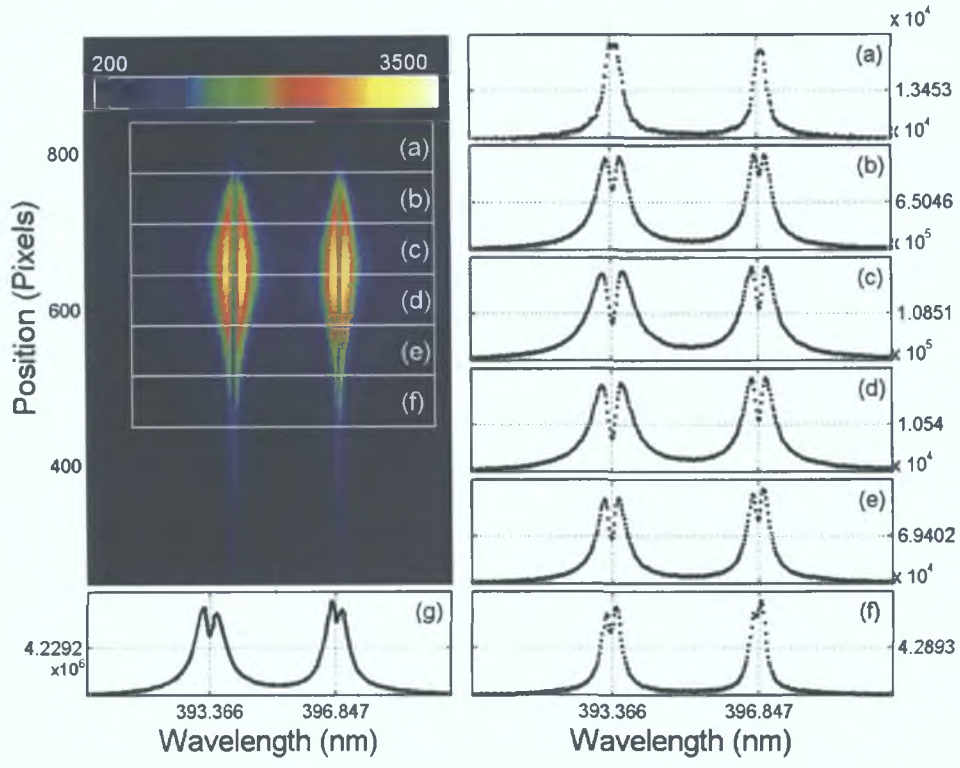

Figure 7.16: Spectral image showing the $3p^6 4s(^2S_{1/2})$-$3p^6 4p(^2P_{3/2,1/2})$ at 393.36 and 396.84 nm recorded 400 ns after plasma initiation with a 30 ns gate width.

using the same experimental conditions as the imaging and spectroscopic data presented in section 6.4. This, therefore provides an opportunity to corroborate the outputs from the computational model with the independently extracted plasma parameters.

Images of the stagnation layer (figure 6.13, section 6.4) were used to provide an estimate of the length of the line-of-sight through the interaction region. This provided an estimate of the ground state population distribution width σ_1. It may be seen from the image in figure 7.16 that the spatial distribution of the emission is quite different to that of the two previously presented spectral images (figures 7.11 and 7.13). In this case the plume is not connected to the target surface and the effect of radiation trapping may be seen along the entire length of the plume. Two important points however should be noted about this spectral image when comparing it with the other two previously presented (figures 7.11 and 7.13). Firstly the spatial scale shown on the image has been changed in order to fit the long interaction region and secondly the expansion direction on this image (figure 7.16) moves from top to bottom, whereas in figures 7.11 and 7.13 the

plumes expand from the bottom up

Again six boxes (a)-(f) have been overlayed onto the spectroscopic image and the contents have been summed and plotted in graphs (a)-(f) to the right of the image If we look sequentially at these six graphs beginning at graph (a) (closest to the target surface and the feeding plasmas), we see that the line profiles are relatively narrow with minimal visible line-reversal As we move to graph (b) we see that both lines have broadened considerably and that the depth of the line reversal has increased This trend continues into graph (c) with further broadening of the profiles and increased reversal depth Around this point we have reached the maximum density of the interaction region From here the profiles narrow and the depth of self-reversal decreases until graph (f), which displays similar features to graph (a)

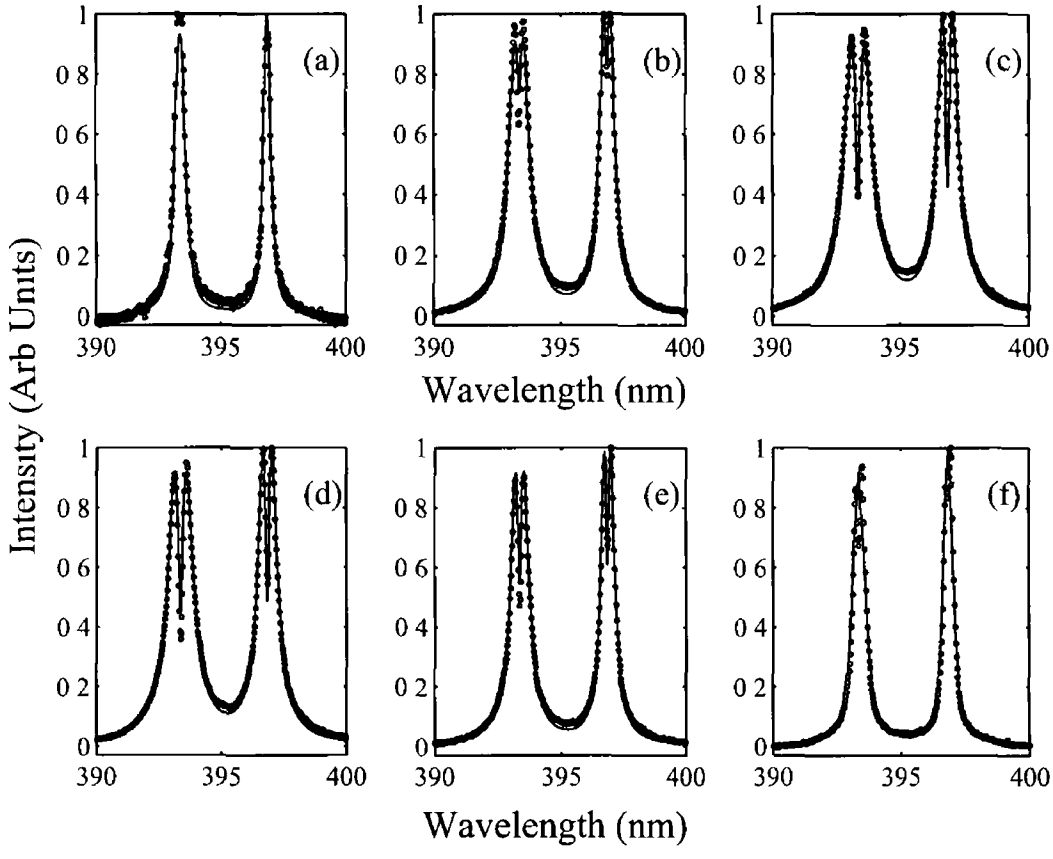

Figure 7 17 Experimental data reproduced from figure 7 13, graphs (a)-(f) (normalised), as well as model fits to data

An interesting point to note may be seen in graph (g) (figure 7 16), which is the fully vertically binned trace of the entire image In this graph a self-reversed profile may

be clearly seen This is in contrast to both single plume spectral images presented previously in this chapter In those images the strong absorption at the transition wavelength near the target surface was masked by the emission at this wavelength that was not absorbed, at positions far from the surface The fact that this does not happen in the image of the interaction region (figure 7 16) may indicate the more symmetric and uniform density distribution along the length of the plume

The profiles shown in graphs (a)-(f) on figure 7 16 have been re-plotted along with fits from the radiation transport model Theses are shown in graphs (a)-(f) on figure 7 17 The best fit values for the three adjustable input parameters, used to generate the synthetic spectra, have been plotted in figure 7 18

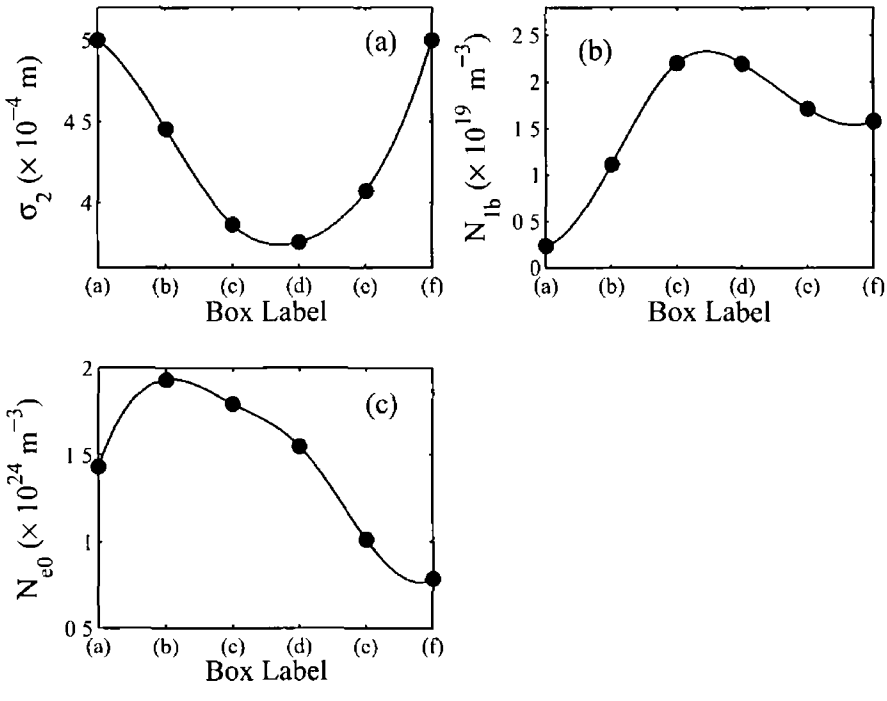

Figure 7 18 Best-fit input parameters calculated during the model comparison with a 400 ns spectroscopic image (figure 7 16)

It may be seen from figure 7 18 (a) that the width of the excited state distribution decreases to a minimum value between box (c) and (d) At this point the difference between the ground state distribution and the excited state distribution is greatest This means that the effective absorption path length is longest, leading to a strongly absorbed profile The ground state population parameter as a function of position is plotted in figure 7 18 (b) The ground state population varies from a minimum in box (a) to a maximum between boxes (c) and (d) before slowly tapering off

The spatial distribution of electron density as a function of position is shown in figure 7 18 (c) An average electron density value of $\sim 1\,4 \times 10^{24}$ m^{-3} can be compared with an average of $\sim 6 \times 10^{24}$ m^{-3} from figure 6 14 in section 6 4

7.5 Summary

In this chapter we have discussed in detail the implementation of a radiation transport model used to simulated radiation trapping in optically thick plasmas Examples of experimentally obtained spectroscopic images showing the Ca^+ $3p^64s(^2S_{1/2})$-$3p^64p(^2P_{3/2,1/2})$ resonance transitions at 393 36 and 396 48 nm were analysed by fitting the radiation transport model for different spatial regions of the plasma The model can be used to simulate the effect that opacity has on the relative line intensities, it may also be used to extract plasma parameters from self-reversed line profiles Due to the fact that a Boltzmann distribution is employed to populate the energy levels, the quality of the fit may also be considered an indication of how close the plasma may be to local thermodynamic equilibrium In the next chapter conclusions and suggestions for future work will be discussed

Bibliography

[1] R D Cowan and G H Dieke Self-aborption of spectrum lines *Reviews of Modern Physics*, 20 418–455, 1948

[2] W Lochte-Holtgreven *Plasma diagnostics* AIP Press, New York, 1995

[3] T Sakka, T Nakajima, and Y H Ogata Spatial population distribution of laser ablation species determined by self-reversed emission line profile *Journal of Applied Physics*, 92 2296–2303, 2002

[4] H Furusawa, T Sakka, and Y H Ogata Characterization of ablated species in laser-induced plasma plume *Journal of Applied Physics*, 96(2) 975–982, 2004

[5] D Karabourniotis and J van der Mullen Numerical validation of a self-absorption model for plasma radiation *Journal of Physics D Applied Physics*, 38 3016–3027, 2005

[6] J Hermann, C Boulmer-Leborgne, and D Hong Diagnostics of the early phase of an ultraviolet laser induced plasma by spectral line analysis considering self-absorption *Journal of Applied Physics*, 83 691–696, 1998

[7] S Fujioka, H Nishimura, K Nishihara, A Sasaki, A Sunahara, T Okuno, N Ueda, T Ando, Y Tao, Y Shimada, K Hashimoto, M Yamaura, K Shigemori, M Nakai, K Nagai, T Norimatsu, T Nishikawa, N Miyanaga, Y Izawa, and K Mima Opacity effect on extreme ultraviolet radiation from laser-produced tin plasmas *Physical Review Letters*, 95 235004, 2005

[8] G Tondello, E Jannitti, and A M Malvezzi Line broadening and self-absorption of be iv in a laser-produced plasma *Physical Review A*, 16 1705–1714, 1977

[9] J Siegel, G Epurescu, A Perea, F J Gordillo-Vazquez, J Gonzalo, and C N Afonso Temporally and spectrally resolved imaging of laser-induced plasmas *Optics Letters*, 29 2228–2230, 2004

[10] J P Apruzese, J Davis, K G Whitney, J W Thornhill, P C Kepple, and R W Clark The physics of radiation transport in dense plasmas *Physics of*

Plasmas, 9 2411–2419, 2002

[11] H R Griem *Principles of plasma spectroscopy* Cambridge monographs on plasma physics Cambridge University Press, New York, 1997

[12] H R Griem *Plasma spectroscopy* McGraw-Hill, New York, 1964

[13] R H Huddlestone and S L Leonard *Plasma diagnostic techniques* Academic Press, New York, 1965

[14] D Salzmann *Atomic Physics in Hot Plasmas* Oxford University Press, New York, 1998

[15] A Corney *Atomic and laser spectroscopy* Clarendon Press, New York, 1977

[16] T P Hughes *Plasmas and laser light* Hilger, Bristol, 1975

[17] N Konjevic, M S Dimitrijevic, and W L Wiese Experimental stark widths and shifts for spectral lines of neutral atoms (a critical review of selected data for the period 1976 to 1982) *Journal of Physical and Chemical Reference Data*, 13 619–647, 1984

[18] N Konjevic and W L Wiese Experimental stark widths and shifts for spectral lines of neutral and ionized atoms *Journal of Physical Chemistry and Reference Data*, 19 1307, 1990

[19] P A Miller, G A Hebner, R L Jarecki, and T Ni Optical self-absorption technique for qualitative measurement of excited-state densities in plasma reactors *Journal of Vacuum Science & Technology A Vacuum, Surfaces, and Films*, 16 3240–3246, 1998

CHAPTER 8

CONCLUSIONS AND FUTURE WORK

The work that has been presented in this thesis has been concerned with the expansion and interaction dynamics of laser-produced colliding plasmas VUV photoabsorption imaging, spectrally filtered time-resolved emission imaging and spatially / temporally-resolved emission imaging spectroscopy have been used as diagnostic tools to study collisions between expanding calcium plumes

Using the pulsed tuneable VUV probe beam supplied by the VPIF, the temporal evolution of the spatial distribution of ground-state Ca^+ species within the plume was tracked This was achieved by tuning the wavelength of the VUV beam to the 3p-3d resonance at 37 34 nm Equivalent width image sets were presented for a number of target and irradiation conditions The equivalent width images were subsequently converted to column density values using the absolute photoionisation cross section of the 3p-3d Ca^+ resonance measured by Lyon *et al* [1] The expansion dynamics of the plumes were extracted from the equivalent width images and discussed with respect to an adiabatic expansion model [2]

Numerous improvements have been made to the VPIF during the course of this work however a few additional modifications would considerably enhance the systems performance A gateable CCD camera would allow much more flexibility to the sample plasma irradiation conditions At the moment the CCD camera accumulates all of the VUV emission that is transmitted through the aluminium filter during a one second acquisition time The protruding knife edge is the only obstacle preventing the CCD camera from being saturated by emission from the

hot central core of the sample plasma at early time delays The knife edge would not be required with a gated CCD because the camera could be set to acquire $\sim$ 40 ns after plasma initiation when strong VUV ($<$ 80 nm) emission from the core has dissipated Another improvement that would enhance the performance of the VPIF would be the design of a new, more flexible target chamber The current chamber offers very limited space to incorporate a high precision target holder This is necessary for stability and reproducibility as the target must be regularly translated to offer a fresh" surface to the incident laser pulses Motorised translational stages would provide the most control in this situation If motorised stages were employed, then the target position could be precisely horizontally translated with respect to the VUV beam, this could be used to increase the distance which the plasma plume must travel before intercepting the probe at long time delays This would allow the plume front to be followed at much longer time delays than the 150 ns currently imposed by the spatial extent of the probe beam

Additional experiments that could be performed using the VPIF include broadband imaging of plasma plumes If the monochromator grating was set at zero order a broadband VUV beam (from the continuum plasma source) could be used to probe a plume Interpretation of the recorded images would be much more complicated but the SNR would be substantially improved due to the larger photon fluxes An estimate of the photoionisation cross-section at wavelengths in which it is not currently known could be determined in a reverse process to that outlined in section 5 4 If an accurate value of the column density for specific irradiation conditions is known using the Lyon cross-section, then the photoionisation cross-section at a different wavelength could be calculated using that NL value and the magnitude of the equivalent width of a plasma under the same conditions at the new wavelength

During the absorption imaging studies it was decided that emission imaging of the plasma plumes should be performed in order that they may be compared with the absorption results The results obtained from those preliminary emission imaging were very interesting and were quite different to the photoabsorption results The pronounced stagnation layer observed in the emission images and the dearth of information in the literature on plasmas generated with similar irradiance conditions led us to improve the imaging setup and to develop experimental systems to perform spectroscopy on the interaction region

Results obtained using these systems were presented in chapter 6 for plasmas generated using three different laser pulse parameters The plume expansion and interaction dynamics were quite different for the three data sets presented Two processes in particular played important roles in altering the interaction dynamics in these data sets The first was the greater absorption efficiency of the short wavelength pulses (355 nm) at the target surface which created higher kinetic energy plumes even though the laser pulse energy was lower The second process was the increased Inverse Bremsstrahlung absorption of the longer wavelength pulses (1064 nm) in the plume, leading to higher excitation temperatures within the plume and reduced particle ablation rates due to shielding of the target surface Combining these two processes leads to highly excited, low velocity plumes generated from pulses with long wavelengths and high velocity, lowly excited plumes from short wavelength pulses These facts may be used to explain why the short wavelength pulses generated plumes interpenetrated each other to a greater degree than the plumes generated with long wavelength pulses The ion-ion mean-free path is related to the relative collision velocity of the plume [3] The higher the relative velocity, the longer the ion-ion mean-free path The more excited slowly moving plumes generated using the long wavelength pulses had a shorter ion-ion mean-free path thereby generating a more pronounced stagnation layer in the interaction region All of these factors contributed to the complicated interaction dynamics observed

When two plasma plumes collide the transfer of directed kinetic energy from the primary plumes into thermal energy in the interaction region occurs through ion collisions For this reason an independent measure of the ion temperature in the interaction region would be a very useful addition to our current diagnostics setup It is not known if the electron and ion temperatures in the interaction region are equivalent Additionally energy transfer from ions to electrons in plasmas is a slow process of the order of hundreds of nanoseconds [4] and may be longer for the low density plumes used in this work This may explain the relatively isothermal (in space and time) electron temperature profiles recorded A slow transfer of thermal ion energy generated during ion-ion collisions at the interface could be continuously heating the stagnated electron cloud in the interaction region More reliable measurements of electron density and temperature will be performed in the near future on the interaction region as a Thompson scattering setup is currently being developed in the laboratory Two new diffraction gratings have also been purchased

and are awaiting installation in the imaging spectrometer These gratings have line densities of 2400 and 3600 mm^{-1} These gratings will significantly improve the spectral resolution of the system, which is very important when determining electron densities in low density plumes where Stark broadening of spectral lines is small

The geometry used in our experimental setup, does not provide us with the flexibility to systematically alter the plasma parameters (i e the collisionality of the system) to a sufficient degree to quantitatively study the change from stagnation to interpenetration in the interaction region A head-on target geometry, where the inter-target distance can be accurately varied is a must for further study Using this the collision velocity may be accurately varied, and the densities may be varied by controlling the on-target irradiance Using a system like this will provide full control over the collisionality of the plasma Another advantage provided by a head-on target geometry is that results may be readily compared with 1-D computational models of colliding plasmas Just such a model was recently developed in DCU by Dr Mark Stapleton based on the multifluid model developed by Rambo and Denavit [5]

A considerable amount of work on imaging and spectroscopy of laterally colliding calcium plasmas was undertaken during the course of this work but not presented in this thesis In this case plasmas were generated next to each other on flat targets To compare the effect that the atomic weight has on the interaction we also performed experiments on colliding lithium plumes When using lithium it was difficult to form an appreciable stagnation layer between the plumes This was most likely due to the much faster expansion velocity of lighter lithium ions leading to significant interpenetration An example image set for laterally colliding lithium plumes is shown in figure 8 1 A narrowband interference filter centered at 610 nm (10 nm FWHM) was used to image the $1s^2 2p$-$1s^2 3d$ Li^0 transition at 610 3 nm Figure 8 1 (a) and (b) show images of the top and bottom plasmas being generated individually Figure 8 1 (c) shows the interaction when both plasmas are generated at the same time and figure 8 1 (d) shows the result of numerically summing the figure 8 1 (a) and (b)

Composite targets have also been constructed during this work Half calcium and half lithium, in which one plasma was generated on the calcium half and one on the lithium half By using interference filters to select transitions from

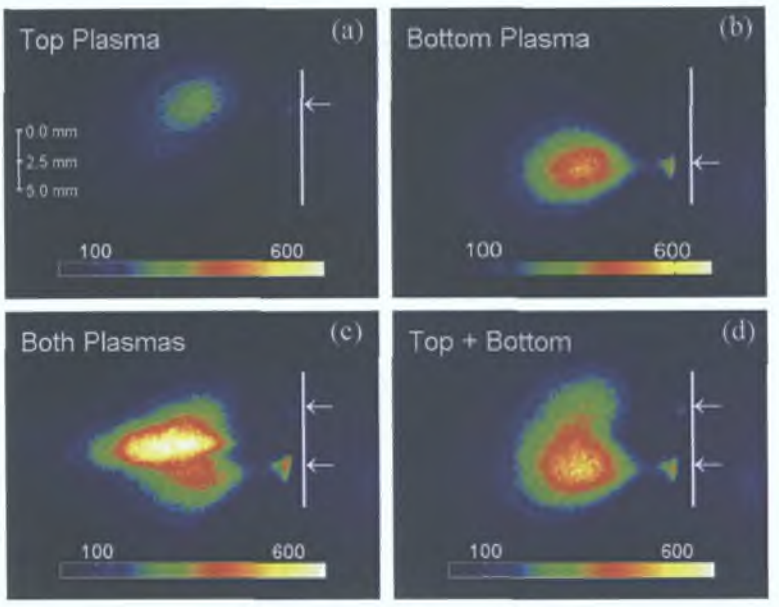

Figure 8.1: Colliding lithium plasmas generated on a flat surface imaged using a narrow-band filter centered at 610 nm (10 nm FWHM).

each material the spatial distribution of each plume could be imaged separately. The target preparation for these experiments was very difficult. The soft lithium metal could not be machined therefore moulds were constructed and the lithium was compressed into these moulds to provide flat and angled target geometries. To prevent oxidisation of the lithium surface the compression of the targets was performed in an argon atmosphere. A limited number of laser shots could be fired on these targets before the required re-moulding. However, further study using these multi-material targets should be performed despite these difficulties.

A distinct advantage of using two target materials is that it is possible to determine the extent of the interpenetration between two plasmas of differing material using the imaging spectrometer. This can be achieved by positioning the entrance slit of the spectrometer such that it views the interaction region parallel to the target face (i.e. by removing the dove prism). Then if a spectral window is selected containing emission lines from both materials the spatial overlap of the emission lines from the different materials will be the distance in which the two plumes have interpenetrated into each other. Using this technique the interpenetration depth versus relative velocity of the collision could be explored.

Finally in chapter 7 a radiation transport model was implemented to help understand radiation trapping and the effect that it has on our spectroscopic work.

The model was used to analyse three spatially and temporally-resolved calcium spectroscopic images Plasma parameters were extracted from the images by fitting the transport model to the spectra by iteratively varying three adjustable input parameters The experimentally observed spectra were in excellent agreement with the calculated synthetic spectra The results obtained from the fitting of the spectral images was presented and discussed Further automation of the fitting algorithm should be performed to enable automatic fitting of all 1024 spectra contained within each spectral image This would provide much more spatial information than the partial binning into six boxes, as has been performed here

Bibliography

[1] I C Lyon, B Peart, K Dolder, and J B West Measurements of absolute photoionisation cross sections of Ca^+ ions *Journal of Physics B Atomic and Molecular Physics*, 20 1471–1477, 1987

[2] R K Singh and J Narayan Pulsed-laser evaporation technique for deposition of thin films Physics and theoretical model *Physical Review B*, 41 8843–8859, 1990

[3] C Chenais-Popovics, P Renaudin, O Rancu, F Gilleron, J -C Gauthier, O Larroche, O Peyrusse, M Dirksmoller, P Sondhauss, T Missalla, I Uschmann, E Forster, O Renner, and E Krousky Kinetic to thermal energy transfer and interpenetration in the collision of laser-produced plasmas *Physics of Plasmas*, 4 190–208, 1997

[4] P T Rumsby, J W M Paul, and M M Masoud Interactions between two colliding laser produced plasmas *Plasma Physics*, 16 969–975, 1974

[5] P W Rambo and J Denavit Interpenetration and ion separation in colliding plasmas *Physics of Plasmas*, 1 4050–4060, 1994

Appendix A

Reference Material

A.1 List of symbols

Chapter 1

λ_{ii}	Ion-ion mean free path	10
ζ	Collisionality parameter	10
D	Scale length (inter-target separation)	10

Chapter 2

n_e	Electron density	16
z	Charge stage	16
n_z	Ion density of charge z	16
λ_D	Debye length	16
ϵ_0	Permitivity of free space	17
k_B	Boltzmann constant	17
L	Plasma length	17
N_D	Debye sphere	17
m_e	Electron mass	17
e	Electron charge	17
δ	Skin depth	18
ω	Angular frequency	18
μ	Magnetic permeability	18

σ	Conductivity	18
L_{th}	Heat penetration depth	18
D_f	Heat diffusion coefficient	18
ρ	Mass density	18
c	Speed of light	18
τ_p	Laser pulse length	18
ΔZ_ν	Ablation depth	19
F_L	Laser fluence	19
F_{th}	Laser fluence ablation threshold	19
L_ν	Latent heat	19
A_s	Surface absorbance	19
K_{IB}	Inverse Bremsstrahlung absorption coefficient	20
$ln\Lambda(\omega)$	Coulomb logarithm for particle collisions	20
k_p	Wave propagation constant	20
λ	Wavelength	20
n_c	Critical electron density	20
t	Time	21
T	Plasma temperature	21
T_0	Plasma temperature at termination of laser pulse	22
m	Particle mass	22
γ	Ration of specific heat capacities	22
$e_{1,2}$	Electron kinetic energy	24
$A^z_{i,j}$	Bound electron, occupying level i/j of an ion of charge z	25
h	Planck's constant	25
ν	Frequency	25
$E_{i,j}$	Energy of level i/j	25
χ_{max}	Highest ionisation potential	32
T_e	Electron temperature	32
U_z	Partition function of ion of charge z	33
I_z^{eff}	Effective ionisation energy for $z \rightarrow (z+1)$	33
g_k	Degeneracy of level k	33
$S(Z, T_e)$	Electron-impact ionisation rate	34
$\alpha_r(z, T_e)$	Radiative recombination rate	34
χ_z	Ionisation potential of charge stage z	34
ξ_z	Number of electrons in the outermost shell	34
$\alpha_{3b}(z, T_e)$	3-body recombination rate	35

n_T	Total population of all charge stages	36
A_{ab}	Einstein's coefficient for spontaneous emission	37
B_{ba}	Einstein's coefficient for stimulated emission	37
B_{ba}	Einstein's absorption coefficient	37
f	Oscillator strength	37
$\epsilon(\lambda, \nu)$	Emission coefficient	38
$\kappa(x, \nu)$	Absorption coefficient	38
$f(\lambda, \nu)$	Spectral distribution function	38
$n_a(x)$	Population distribution of level a	38
Ω	Divergence angle	38
$\tau_\nu(x)$	Optical depth	40

CHAPTER 3

σ_a	Absorbance	47
σ_λ	Absolute photoionisation cross-section	51
W_λ	Equivalent width	50
$\mathcal{L}(\omega)$	Lorentzian profile	54
w	Electron-impact broadening parameter	55
A_i	Ion-broadenmg parameter	55
v_x	Velocity of emitting particle	56
$\mathcal{G}(\omega)$	Gaussian profile	57
$\mathcal{V}(\omega)$	Voigt profile	57
I_{ab}	Integrated line profile intensity	60
A	Oscillator strength	60
l_{sight}	Line of sight through plasma	60
E_∞	Ionisation energy of the lower of the two ion stages	61
ΔE_∞	Ionisation potential lowering factor	61
G	Free-free Gaunt factor	62
ξ	Free-bound continuum correction factor	62

CHAPTER 4

A_n	Atomic number	74
ϕ	Laser irradiance	74
Q_E	Quantum efficiency	81

N_C	Counts per detected photon	81
W_l	Line spread function	86
W_e	Edge trace function	86
a	Slit width	88
D_{sc}	Slit to CCD distance	88

CHAPTER 6

d	Separation of foci	141
γ	Acute wedge angle	141
n	Refractive index	141
δ	Instrument function	147

CHAPTER 7

$S(x, \nu)$	Source function	169
$n_e(x)$	Electron density distribution	170
N_{e0}	Electron density population parameter	171
N_{10}	Ground state population parameter	171
$N_{2a,b}$	Excited state population parameter	171
σ_e	Electron distribution width	171
σ_1	Ground state distribution width	171
$\sigma_{2a,b}$	Excited state distribution width	171
I_ν	Far-field radiant flux density	175

A.2 List of Abbreviations

LPP	Laser-produced plasma	3
VUV	Vacuum ultraviolet	3
PLD	Pulsed laser deposition	3
MC-PIC	Monte-Carlo Particle-In-Cell	10
VPIF	Vacuum ultraviolet photoabsorption imaging facility	1
IB	Inverse Bremsstrahlung	19
UV	Ultra-violet	20
VIS	Visible	20
IR	Infrared	20
m f p	Mean-free path	27
CT	Complete thermodynamic equilibrium	30
LTE	Local thermodynamic equilibrium	31
CE	Corona equilibrium	31
CR	Collisional radiative equilibrium	31
DLP	Dual-laser plasma	48
CCD	Charged coupled device	49
FWHM	Full width half maximum	57
SNR	Signal-to-noise ratio	81
FVB	Full vertical binning	87
FHB	Full horizontal binning	87
ICCD	Intensified charged coupled device	93
MCP	Micro channel plate	95
CD	Collision Dominated	140